GDAŃSK UNIVERSITY OF TECHNOLOGY

The Author of the doctoral dissertation: Omid Ekhlasiosgouei

Scientific discipline: Materials Engineering (IM_a)

DOCTROAL DISSERTATION

Title of doctoral dissertation: **Electrophoretic deposition of protective coatings for high temperature applications of steel interconnects**

Supervisor Signature
Prof. Sebastian Molin

Gdansk, 2025

Załącznik nr 2/2
do Zarządzenia Rektora PG nr 30/2022 z 14 kwietnia 2022 r.

POLITECHNIKA GDAŃSKA

STATEMENT

The author of the doctoral dissertation: Omid Ekhlasiosgouei

I, the undersigned, declare that I am aware that in accordance with the provisions of Art. 27 (1) and (2) of the Act of 4th February 1994 on Copyright and Related Rights (Journal of Laws of 2021, item 1062), the university may use my doctoral dissertation entitled:
Electrophoretic deposition of protective coatings for high temperature applications of steel interconnects
for scientific or didactic purposes.[1]

Gdańsk, 23.11.2025

Omid Ekhlasiosgouei
signature of the PhD student

Aware of criminal liability for violations of the Act of 4th February 1994 on Copyright and Related Rights and disciplinary actions set out in the Law on Higher Education and Science (Journal of Laws 2021, item 478), as well as civil liability, I declare, that the submitted doctoral dissertation is my own work.

I declare, that the submitted doctoral dissertation is my own work performed under and in cooperation with the supervision of Prof. Sebastian Molin.

This submitted doctoral dissertation has never before been the basis of an official procedure associated with the awarding of a PhD degree.

All the information contained in the above thesis which is derived from written and electronic sources is documented in a list of relevant literature in accordance with Art. 34 of the Copyright and Related Rights Act.

I confirm that this doctoral dissertation is identical to the attached electronic version.

Gdańsk, 23.11.2025

Omid Ekhlasiosgouei
signature of the PhD student

I, the undersigned, agree/do not agree* to include an electronic version of the above doctoral dissertation in the open, institutional, digital repository of Gdańsk University of Technology.

Gdańsk, 23.11.2025

Omid Ekhlasiosgouei
signature of the PhD student

*delete where appropriate

[1] Art 27. 1. Educational institutions and entities referred to in art. 7 sec. 1 points 1, 2 and 4–8 of the Act of 20 July 2018 – Law on Higher Education and Science, may use the disseminated works in the original and in translation for the purposes of illustrating the content provided for didactic purposes or in order to conduct research activities, and to reproduce for this purpose disseminated minor works or fragments of larger works.

2. If the works are made available to the public in such a way that everyone can have access to them at the place and time selected by them, as referred to in para. 1, is allowed only for a limited group of people learning, teaching or conducting research, identified by the entities listed in paragraph 1.

Acknowledgements

I extend my deepest gratitude to my supervisor, Prof. Sebastian Molin, for his unwavering support and insightful critiques throughout my research journey. His deep commitment to academic excellence and meticulous attention to detail have significantly shaped this dissertation.

I am equally thankful to Prof. Piotr Jasinski, for his constructive feedback and essential suggestions that enhanced the quality of my research.

This thesis is a reflection of the unwavering support and boundless love I received from my family and friends during this challenging academic pursuit. I owe an immense debt of gratitude to my parents, who nurtured my curiosity and supported my educational endeavors from the very beginning.

Finally, I dedicate this thesis to all those who have supported and believed in me. This achievement would not have been possible without you.

Contents

List of abbreviation:

SOCs	Solid oxide cells
SOFCs	Solid oxide fuel cells
TEC	Thermal expiation coefficient
TPB	Three-phase boundary
EPD	Electrophoretic deposition
AFC	Alkaline fuel cell
DMFC	Direct methanol fuel cell
PAFC	Phosphoric acid fuel cell
SAFC	Sulfuric acid fuel cell
PEMFC	Proton-exchange membrane fuel cell
MCFC	Molten carbonate fuel cell
PCFS	Protonic ceramic fuel cell
YSZ	Yttria-stabilized zirconia
GDC	Cerium doped gadolinium
SDC	Cerium doped samarium
LSGM	Lanthanum strontium gallium magnesium
BYO	Bismuth yttrium oxide
Mn-Co	$MnCo_2O_4$
Mn-Fe-Cu	$Mn_{1.7}CuFe_{0.3}O_4$
FSS	Ferritic stainless steel
Cr	Chromium
CO_2	Carbone dioxide
NO_x	Nitrogen oxide

XRD	X-Ray diffraction
EDS	Energy Dispersive Spectroscopy
ASR	Area specific resistance
σ	Electrical conductivity
σ_m	corrected electrical conductivity
σ_0	Pre-exponential factor
T	Temperature
K	Boltzmann's constant
E_a	Activation energy
P	Porosity
V	Velocity
A	Deposition area
t	Time
M	Mass
μ	Electrophoretic mobility
E	Electrical field
C_s	Solid concentration
G	Gibbs free energy
ΔG^0	Gibbs free energy of formation
R	Gas constant
P_{O2}	Oxygen partial pressure

Abstract

In solid oxide cells (SOCs), metallic interconnects play a pivotal role in providing electrical connections between individual cells and assisting in the distribution of reactant gases. Due to the high operating temperature in SOCs, stainless-steel metallic interconnects encounter challenges such as increased oxidation, reduced electrical conductivity, and enhanced chromium diffusion, which leads to the formation of a dense chromia layer. To address these issues, ceramic protective coatings are essential for metallic interconnects, as they help restrict oxidation rates and inhibit the migration and evaporation of chromium from the interconnects to the oxygen electrodes. Additionally, ceramic protective coatings play a critical role in reducing degradation and enhancing the durability of SOCs when applied to stainless steel. The ideal protective materials should possess high electrical conductivity, a low thermal expansion coefficient (TEC), and the ability to block oxygen and chromium.

In this thesis, Electrophoretic Deposition (EPD) is selected to deposit $MnCo_2O_4$ (Mn-Co) and $Mn_{1.7}CuFe_{0.3}O_4$ (Mn-Cu-Fe) spinel materials on stainless-steel metallic interconnects to investigate electrical conductivity, chromium (Cr) diffusion, and the quality of the coating, including uniformity, density, and crack-free characteristics, under different configurations, such as dual-layer and hybrid coatings. The various sections of this thesis are outlined as follows:

- To achieve a uniform, dense, and crack-free coating, various suspension parameters such as stability, zeta potential, iodine concentration, solid content, solvents, and suspension conductivity are examined. Additionally, process parameters, including applied voltage and deposition time, are also investigated.
- A novel Mn-Co/Mn-Cu-Fe dual-layer coating configuration, along with Mn-Co and Mn-Cu-Fe single-layer coatings, is deposited using EPD method on complex-shaped metallic interconnects. The quality of the coatings, including their uniformity, densification, and cracks-free, is evaluated. Furthermore, the densification behaviour of sintered dual and single layers in oxidation treatment, as well as reduction treatment followed by oxidation treatment, is analysed. Additionally, the undetermined phases composition at Mn-Co/Mn-Cu-Fe coatings interface and the coating/substrate interface are investigated using confocal Raman spectroscopy.

- A novel Mn-Co: Mn-Cu-Fe hybrid coating with varying weight ratios (1:0, 1:3, 1:1, 3:1, and 0:1) is deposited on metallic interconnects using EPD method. The quality of the sintered hybrid coatings is examined under oxidation treatment and reduction treatment followed by oxidation treatment. The electrical conductivity of the oxide spinel material mixtures and chromium (Cr) diffusion from the substrate to the hybrid coating are analyzed. Additionally, new phases and phase compositions in the hybrid materials are investigated using X-ray diffraction (XRD) and Raman spectroscopy.

Keywords: Electrophoretic deposition, Complex-shaped metallic interconnect, stainless steel, Spinel materials, Dual-layer coating, Hybrid coating, Electrical conductivity

Abstrakt

W stosach tlenkowych ogniw (SOCs, ang. Solid Oxide Cells) metaliczny interkonektor odgrywa kluczową rolę w zapewnianiu połączeń elektrycznych pomiędzy poszczególnymi ogniwami oraz we wspomaganiu dystrybucji reagentów gazowych. Ze względu na wysoką temperaturę pracy w SOC, interkonektory ze stali nierdzewnej napotykają problemy, takie jak zwiększone utlenianie, obniżona przewodność elektryczna oraz nasilona dyfuzja chromu, która prowadzi do powstawania gęstej warstwy tlenku chromu. Aby rozwiązać te problemy, niezbędne są ceramiczne powłoki ochronne na metalicznych interkonektorach, ponieważ ograniczają one szybkość utleniania oraz hamują migrację i parowanie chromu z interkonektorów do elektrod tlenowych. Ponadto ceramiczne powłoki ochronne odgrywają istotną rolę w redukcji degradacji i zwiększeniu trwałości SOC w przypadku zastosowania ich na stali nierdzewnej. Idealne materiały ochronne powinny charakteryzować się wysoką przewodnością elektryczną, niskim współczynnikiem rozszerzalności cieplnej (TEC) oraz zdolnością do blokowania dyfuzji tlenu i chromu.

W niniejszej pracy wybrano metodę osadzania elektroforetycznego (EPD, *Electrophoretic Deposition*) do nanoszenia materiałów spinelowych $MnCo_2O_4$ (Mn-Co) i $Mn_{1.7}CuFe_{0.3}O_4$ (Mn-Cu-Fe) na metaliczne interkonektory ze stali nierdzewnej w celu zbadania przewodności elektrycznej, dyfuzji chromu (Cr) oraz jakości naniesionej warstwy, obejmującej jednorodność, gęstość i spękalność. Warstwy naniesiono w różnych konfiguracjach, takich jak warstwy dwuwarstwowe i hybrydowe. Poszczególne części pracy przedstawiają się następująco:

- W celu uzyskania jednorodnej, gęstej i pozbawionej pęknięć powłoki zbadano różne parametry zawiesiny, takie jak stabilność, potencjał zeta, przewodność zawiesiny, zmianę stężenia jodu, zmianę zawartości fazy stałej oraz zmianę rozpuszczalników. Dodatkowo przeanalizowano parametry procesu, w tym przyłożone napięcie i czas osadzania.

- Zaproponowano nową konfigurację warstwy ochronnej dwuwarstwowej Mn-Co/Mn-Cu-Fe, a także powłoki jednowarstwowe Mn-Co i Mn-Cu-Fe, naniesione metodą EPD na złożonych kształtach metalicznych intekonektorów. Oceniono jakość powłok, w tym ich jednorodność, gęstość i spękalność. Ponadto przeanalizowano zagęszczanie

spieczonych powłok dwu- i jednowarstwowych w procesie utleniania, a także w procesie redukcji poprzedzającym utlenianie. Dodatkowo niezidentyfikowany skład fazowy na granicy powłok Mn-Co/Mn-Cu-Fe oraz na granicy powłoka/podłoże zbadano za pomocą konfokalnej spektroskopii Ramana.

- Zaproponowano nową hybrydową powłokę Mn-Co:Mn-Cu-Fe o różnych proporcjach wagowych (1:0, 1:3, 1:1, 3:1 oraz 0:1) osadzono na metalicznych interkonnectorach metodą EPD. Zbadano jakość spieczonych powłok hybrydowych w procesie utleniania oraz redukcji poprzedzającej utlenianie. Przeanalizowano przewodność elektryczną mieszanin materiałów spinelowych tlenków oraz dyfuzję chromu (Cr) z podłoża do powłoki hybrydowej. Ponadto nowe fazy i ich skład w materiałach hybrydowych zbadano przy użyciu dyfrakcji rentgenowskiej (XRD) oraz spektroskopii Ramana.

Słowa kluczowe: osadzanie elektroforetyczne, metaliczne interkonektory o złożonych kształtach, stal nierdzewna, materiały spinelowe, powłoka dwuwarstwowa, powłoka hybrydowa, przewodnictwo elektryczne

1. Introduction

Fuel cells directly convert chemical energy from gas into electrical and thermal energy through an electrochemical reaction between the fuel and the oxidant agent (oxygen from the air) through electrode and via an ion conducting electrolyte. In order to decrease pollutants as nitrogen oxide (NO_x) and produce energy with higher efficiency. Accordingly, fuel cells have seen as more ideal energy sources in transport, stationary, and distributed power generators[1–3].

Fuel cells are generally classified by the chemical properties of the electrolyte used as the ionic conductor in the cells. The different types of fuel cells include [4]:

- Alkaline fuel cell (AFC)

The electrolyte used in this system is potassium hydroxide (KOH), and it operates at a temperature range of 50–200°C. The fuel source is either pure hydrogen or hydrazine, while oxygen acts as the oxidant.

- Direct methanol fuel cell (DMFC)

This system uses a polymer electrolyte and operates at temperatures between 60–200°C. It runs on liquid methanol as the fuel, with oxygen serving as the oxidant.

- Phosphoric acid fuel cell (PAFC)

This system uses phosphoric acid as the electrolyte and operates at a temperature range of 160–210°C. The fuel is hydrogen derived from hydrocarbons and alcohol, while oxygen acts as the oxidant.

- Sulfuric acid fuel cell (SAFC)

This system utilizes sulfuric acid as the electrolyte and operates at a temperature range of 80–90°C. It uses alcohol or impure hydrogen as the fuel, with oxygen serving as the oxidant.

- Proton-exchange membrane fuel cell (PEMFC)

  This system uses a polymer and proton exchange membrane as the electrolyte, operating at a temperature range of 50–80°C. The fuel source is less pure hydrogen derived from hydrocarbons or methanol, while oxygen serves as the oxidant.

- Molten carbonate fuel cell (MCFC)

This system uses molten salts, such as nitrates, sulfates, and carbonates, as the electrolyte and operates at a high temperature of 630–650°C. It can run on various fuels, including hydrogen, carbon monoxide, natural gas, propane, and marine diesel. The oxidant can be either oxygen or carbon dioxide (CO_2).

- Protonic ceramic fuel cell (PCFC)

This system uses a thin membrane of barium cerium oxide as the electrolyte and operates at a temperature range of 600–700°C. It utilizes hydrocarbons as the fuel, with oxygen serving as the oxidant.

- Solid oxide fuel cell (SOFC)

This system uses a ceramic electrolyte, such as stabilized zirconia or doped perovskite, and operates at temperatures ranging from 600 to 1000°C. It runs on natural gas or propane as the fuel, with oxygen acting as the oxidant.

SOFCs use an oxide-ion conducting electrolyte that provides multiple benefits as compared to other fuel cell technologies. SOFCs benefit from cheap materials and show reduced sensitivity to fuel impurities while delivering extremely high efficiency. Since SOFCs can operate directly on hydrocarbon fuels they avoid the need for hydrogen conversion which lowers system complexity and expenses.

1.1. Solid oxide fuel cells (SOFCs)

Solid oxide fuel cells (SOFCs) have become a prominent choice in high-temperature fuel cell technology recently. These systems use solid ceramic electrolytes to function at extremely high temperatures. The elevated operating temperature of SOFCs facilitates internal reforming and accelerates electrocatalysis with non-precious metals while producing high-quality byproduct heat suitable for co-generation applications. SOFCs reach up to 70% efficiency levels and can extend this to 90% by capturing and recovering heat. The lengthy time required to reach operating temperatures limits SOFC research to utility power generation applications [5].

An SOFC consists of three primary components which include an anode, cathode and a solid electrolyte. The fuel serves as an essential primary parameter but becomes independent from other components after conversion to hydrogen. SOFCs have the ability to utilize high-purity hydrogen yet they function independently from it as a fuel source because hydrogen generation is expensive and handling this gas presents difficulties.

1.2. Materials for cell components

The properties and materials used for the anode, cathode, and electrolyte in solid oxide fuel cells (SOFCs) are as follows:

1.2.1. Electrolyte

At present, there is a wide range of ceramic materials available for the electrolyte of solid oxide fuel cells (SOFCs) such as the more advanced and commonly utilized, stabilized zirconia which is particularly yttria-stabilized zirconia (YSZ). YSZ exhibits purely oxygen ionic conduction without any electronic conduction [6]. The other oxide-based ceramic materials are also used as electrolytes in SOFCs such as cerium oxide doped with gadolinium (GDC), cerium oxide doped with samarium (SDC), lanthanum strontium gallium magnesium (LSGM), bismuth yttrium oxide (BYO), and so on. As shown in Fig. 1, ionic conductivity of these electrolytes undergoes a transition over a range of operating temperatures. The electrolyte must be dense in order to separate the air and fuel compartments, must possess high ionic conductivity in order to allow easy migration of oxygen anions, and must be an electronic insulator [7–9].

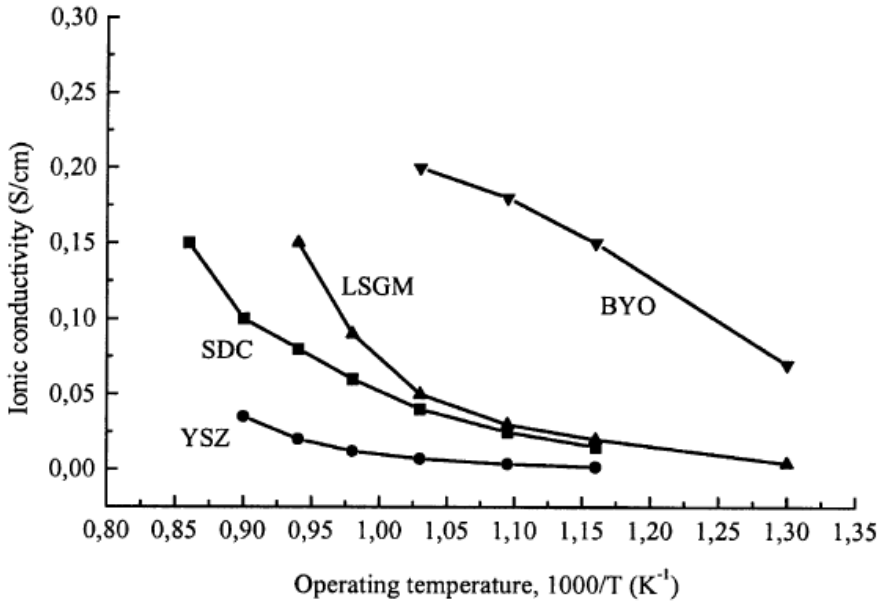

Fig. 1. The ionic conductivity of electrolyte as a function of operating temperature [7].

1.2.2. Anode electrodes

because of the reducing conditions of the fuel gas, metals are utilized as anode materials in solid oxide fuel cells (SOFCs). These metals have to avoid oxidation during the entire operation of the cell as well. Anodes usually consist of composite powders such as electrolyte materials YSZ, GDC, SDC and nickel oxide. Cermet anodes contain nickel which contributes to electronic conductivity as well as to the catalytic activity needed for the direct oxidation and steam reforming of methane. The electrolyte materials serve to inhabit sintering of the metal particles and to provide a thermal expansion coefficient comparable to those of other cell materials [10,11]. The anode is built with 20-40% porosity for effective mass transfer of reactant and product gases. Fig. 2 illustrates this region between the electrolyte and anode where the TPB exists. The reaction happens exclusively on the TPB where the oxygen ion conductor (electrolyte), electron-conducting metal, and gas phase all meet together [3,12].

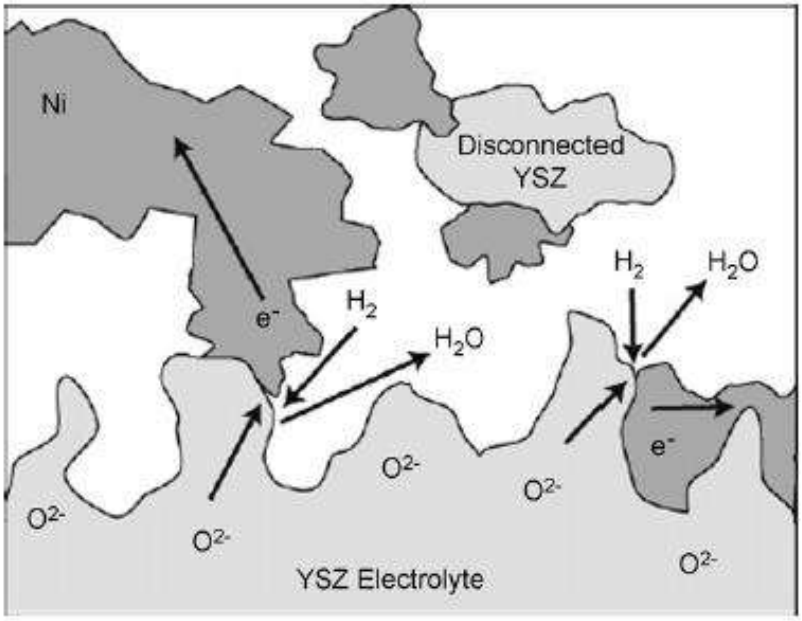

Fig. 2. A schematic illustration of three-phase boundary at Ni/YSZ anode [3].

1.2.3. Cathode electrodes

The cathode must be capable of effectively dissociating O_2 and conducting electrons. The most common cathode material is Sr-doped $LaMnO_3$ (LSM). In addition, there are lots of mixed ionic-electronic conductors, which can be used as cathode $LaCaMnO_3$ (LCM), (LaSr) $(CoFe)O_3$ (LSMF), (LaSr) $(Fe)O_3$ (LSF) and so on. The ideal cathode materials should readily dissociate molecular oxygen, have high electronic and ionic conductivities, and have a coefficient of thermal expansion that matches of the electrolyte. The incorporation of electrolyte material into the cathode material has been shown to improve electrode performance at lower temperature by increasing the volume of active sites available for electrochemical reaction. Similar to anode electrode, the cathode has a porous structure to facilitate rapid mass transport of reactant and product gases [13–16].

1.3. Mechanism of SOFC

Fig. 3 shows the schematic illustration of operating principles of SOFC. At cathode, molecular O_2 is first reduced to oxygen anions. In other words, oxygen gas reacts with electron to form oxide ions according to:

$$\tfrac{1}{2}\, O_2 + 2e^- \longrightarrow O^{2-} \qquad (1)$$

The oxide ions migrate through the electrolyte to combine with the fuel (H_2) at the anode electrode:

$$H_2 + O^{2-} \longrightarrow H_2O + 2e^- \quad (2)$$

The electrons released during the reaction between the fuel and oxide ions flow through the external circuit to the cathode, where they can be used to generate electricity. As shown in Fig. 2, when hydrogen is used as the fuel, the only by-product is water. However, SOFCs can also operate with hydrocarbons like methane or carbon monoxide as fuel, in which case carbon dioxide (CO_2) becomes an additional by-product [2,10,12,17].

By stacking several cells together in series, a more usable power output is easily achievable. Metallic interconnects are then used between the cathode and anode of adjacent cells to provide a current path and separate the anode and cathode gasses.

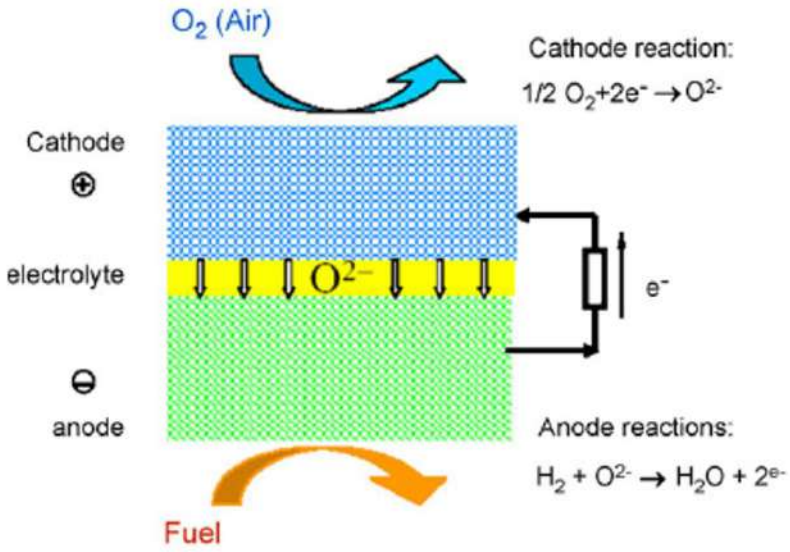

Fig. 3. The schematic illustration of mechanism of SOFC [12].

1.4. Metallic interconnect

The metallic interconnects are as electrical connectors between the different cells and also a physical barrier between the fuel (anode) and oxidant gases (cathode). Fig. 4 comparison of planar and tubular designs for solid oxide fuel cell. One typical single cell is with a dense electrolyte sandwiched between two porous electrodes. Then, interconnects layer many

single cells in a planar or tubular architecture and connect cells in series to combine voltage output into an electrochemical power source. Anode-supported tubular SOFCs can achieve high power densities, but planar SOFCs are more economical to manufacture with lower cell cost. But the commercialization of planar solid oxide fuel cells (SOFCs) suffers from a number of issues, technical hurdles in developing highly ionic conductive electrolyte material at the cell operating temperature, electrodes with appropriate catalytic activity and conductivity and cost-effective production of metallic interconnects [18,19].

Metallic interconnect must possess specific properties to meet the demands of the operating environment[20–22]:

- High electrical conductivity
- Chemical stability
- Mechanical strength
- Thermal compatibility
- Cost-effective
- Sufficient thermal conductivity

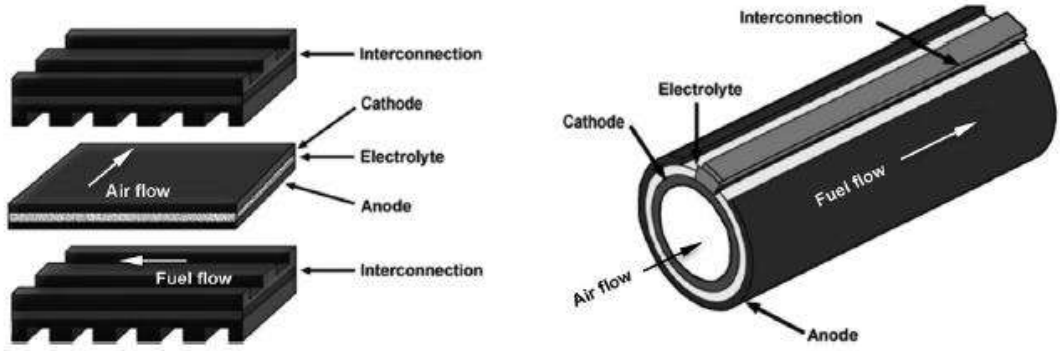

Fig. 4. The planar design versus tubular design of solid oxide fuel cells [18].

Ferritic stainless steels (FSS) including Crofer 22 APU [23,24], Crofer 22 H [25,26], 441 AISI [27,28], and 430 SUS [29,30] are used as metallic interconnect due to relatively low cost, their high-temperature stability, corrosion resistance, excellent mechanical properties, improved thermal expansion coefficient matched with the other cell components. Ferritic stainless steels present two major limitation, rapid Cr_2O_3-scale growth at elevated

temperature, which increases electrical resistance over time, and evaporation/ migration of Cr (VI) species from interconnects into cathode, which drastically deteriorates cell performance [31–36].

The properties of stainless-steel metallic interconnects, including oxidation resistance, chromium evaporation/migration, and electrical conductivity, are described as follows:

1.4.1. Oxidation resistance

Even with the presence of air, Oxygen can cause severe degradation of metallic materials, especially under high temperatures, in a phenomenon known as high-temperature corrosion. In order to better understand high temperature corrosion mechanisms, which would ultimately improve corrosion resistance and material longevity under harsh conditions, it is vital to understand these mechanisms. The mechanisms are controlled both by thermodynamics and kinetics of the system.

The high-temperature performance of a metallic material is related to the formation of a protective oxide scale. It acts as a diffusion barrier, separating the substrate material from the corrosive atmosphere. To be protective, however, the oxide scale has to meet certain conditions. For example, it must be dense, homogeneous and stable, have similar thermal expansion rate as the substrate and stay adherent to the substrate. These conditions must be fulfilled in order to provide protection for the entire surface of the material. Thus, it is not enough to consider only the chemical evolution of the oxide scale but also the mechanical evolution must be taken into account [37–40].

1.4.1.1. Thermodynamics

Metals and alloys naturally tend to degrade under corrosive conditions, driven by the thermodynamic forces of the reaction. When exposed to oxygen, a metal or alloy element forms an oxide, as outlined in the following equation 3:

$$2a/b\ M\ (s) + O_2\ (g) \longrightarrow 2/b\ M_aO_b\ (s) \quad (3)$$

When the metal reactant and the oxide product are considered to be pure, the Gibbs free energy expression for reaction 3 can be derived, as shown in equation 4:

$$G=\Delta G^0 + RTLn\ (1/P_{O2}) \quad (4)$$

Where G is Gibbs free energy, ΔG^0 Gibbs free energy of formation, T the temperature, R the gas constant, and P_{O2} the oxygen partial pressure. As equilibrium is reached, $G = 0$ and then the expression can be rewritten as equation 5:

$$\mathrm{Ln}P_{O2} = \Delta G^0/RT \quad (5)$$

At a given temperature, an oxygen partial pressure exists below which no oxidation occurs and above which the material will oxidize. This is used for the plotting of an Ellingham diagram. These types of diagrams are typically used for the comparison of the thermodynamic stability of oxides derived from a variety of metals (as shown in Fig. 5). Although thermodynamics can tell us if a reaction is possible or not, actual systems do not always achieve equilibrium, which limits the predictive usefulness of thermodynamic calculations [7].

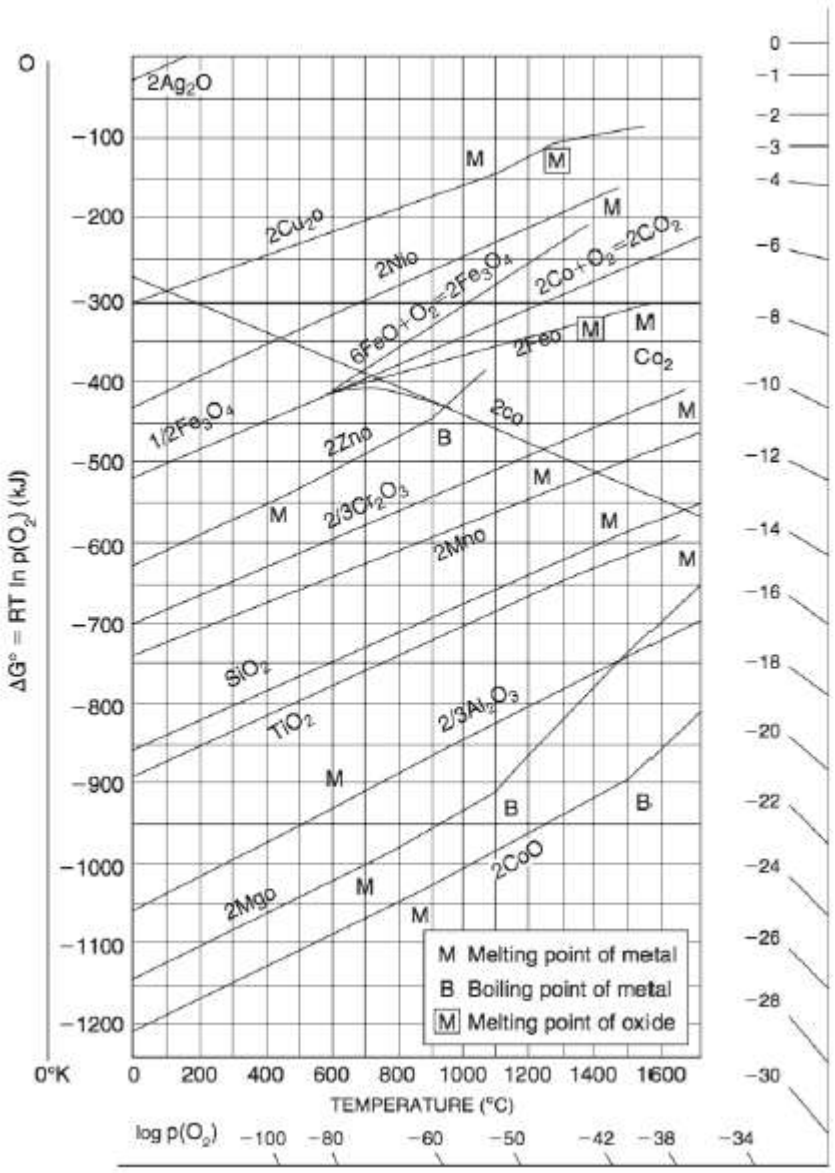

Fig. 5. The Ellingham-Richardson diagram for a selection of oxides showing the standard Gibb's energy of oxide formation as a function of temperature [7].

1.4.1.2. Kinetics

Kinetics gives further information that is complementary to the thermodynamic predictions. Reaction kinetics give information on the rate of oxidation, which can be expressed as mass gain versus time. The reaction between a metal surface and oxygen resulting in oxide scale formation and growth, is controlled by complex mechanisms. These stages consist of adsorption of oxygen on the metal surface, dissolution and nucleation of oxide, growth of oxide scale, internal oxidation, and formation of porosity, cavity, and crack, and macrocrack

formation as the last stage and, possibly, evaporation of oxide. Two oxide layers in general exist: an adherent dense oxide layer and a porous oxide layer. The porous oxide may also be poorly adhered, and this leads to spallation of the oxide. Porous or poorly adhered oxide scales always have access to oxygen, and this means the growth of the oxide is controlled by gaseous diffusion. This gives a linear mass gain-time relationship, which is a non-protective scale. On the other hand, adherent dense oxide coatings have a parabolic mass gain-time relation since they are effective protectors of the substrate material. Such an oxide scale is protective since it inhibits oxygen penetration to the metal surface and its growth is limited by ionic diffusion outward instead [41–44].

Reisert et al. [45] investigated the oxidation behavior of porous P434L ferritic stainless steel for metal-supported solid oxide fuel cells. They found that the oxidation rate in an air atmosphere was higher than in humid hydrogen at temperatures above 700 °C. During oxidation in both environments, a dense chromium layer formed on the porous stainless steel. Additionally, they found that a silica oxide layer developed at the metal-scale interface. Koszelow et al. [46] examined the corrosion properties of porous Fe22Cr stainless steel in air at temperatures ranging from 700 °C to 900 °C over a period of 100 h. The results indicated that a temperature of 700 °C is suitable for stainless steel with 30% porosity. However, the microstructure of the porous stainless steel underwent significant changes at the elevated temperature of 700 °C for 100 h. At 900 °C for 100 h, the porous stainless steel was completely oxidized. Additionally, the presence of a chromium-enriched area at the higher temperatures limited the lifespan of the porous stainless steel. Palcut et al. [39] investigated a dual-layer coating of $Co_3O_4/La_{0.85}Sr_{0.15}MnO_{3-\delta}$ applied to various alloys, including Crofer 22 APU, Crofer 22 H, E-Brite, and Al 29-4C, using a spray method. Their results demonstrated a significant increase in oxidation resistance for the stainless steel. They noted that a reaction and cation inter-diffusion layer formed at the interface between the coating and the oxide scale. Talic et al. [24] investigated the mass gain of bare and coated Crofer 22 APU at various oxidation temperatures. The mass change of the bare and spinel-coated Crofer 22 APU during oxidation in air at 700°C and 800°C is presented in Fig. 6. The mass change as a function of time obeys parabolic kinetics, which suggests that scale growth is limited by solid-state diffusion. Additionally, it was reported that the constant for the

parabolic oxidation rate was reduced by greater than four-fold compared to that of the bare alloy.

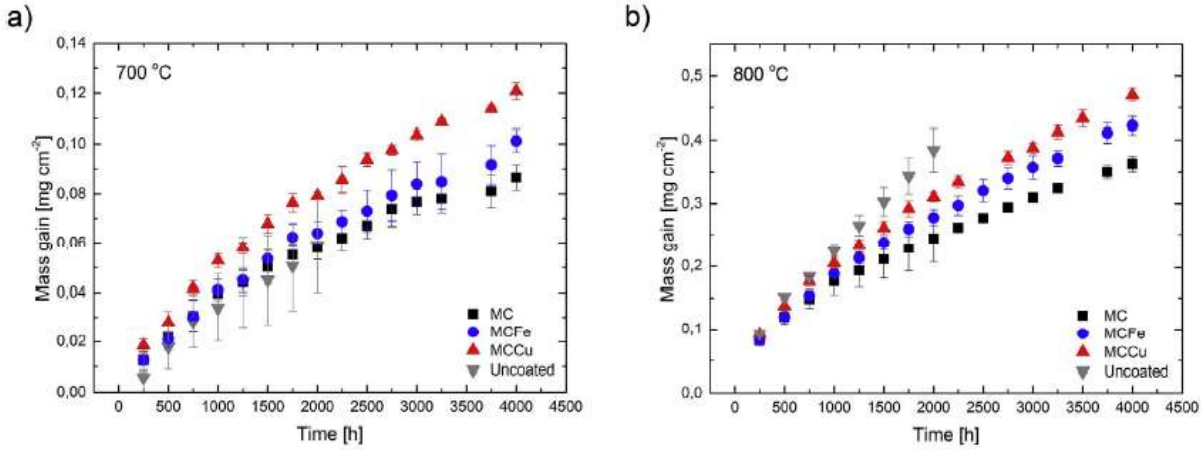

Fig. 6. Mass gain of uncoated and spinel (iron and cupper doped $MnCo_2O_4$) coated Crofer 22 APU during discontinuous oxidation in air at: a) 700 °C, and b) 800 °C [24].

1.4.2. Cr evaporation/migration

A layer of chromium oxide (Cr_2O_3) is formed on the metallic interconnect during oxidation. The chromium oxide layer immediately after its formation is well adhered to the surface and is gas-impermeable. Thus, it serves as a barrier layer for the diffusion of oxygen gases from the cathode to the interconnect. It hence retards the oxidation rate of the metallic interconnect under operating conditions [29,47].

Nevertheless, the chromium oxide layer still reacts with oxygen and volatilizes when it comes in contact with water vapor in the air under the cathodic condition. Chromium poisoning species like CrO_3 and $CrO_2(OH)_2$ are formed through the volatilization. Thermodynamic stability of the perovskite cathodes is impacted by chromium poisoning. The Cr_2O_3 migration to the TPB has been recognized as the primary source of chromium poisoning. The cathode's oxygen catalytic activity has been shown to be greatly influenced by deposition of such chromium poisoning species. The electrochemical reduction of Cr to gaseous chromium and the oxygen reduction reaction are competitive, and Cr_2O_3 deposits at the TPB. The following are the equations for the formation of chromium poisoning species [48]:

$$2Cr_2O_3\,(s) + 3O_2 \longleftrightarrow 4CrO_3\,(g) \qquad (6)$$

$$2Cr_2O_3\,(s) + 3O_2 + 4H_2O \longleftrightarrow 4CrO2(OH)_2\,(s) \quad (7)$$

$$Cr_2O_3\,(s) + O_2 + H_2O \longleftrightarrow 2CrO_2(OH)_2\,(g) \quad (8)$$

When Cr_2O_3(s) comes in contact with dry air and high temperature over 500 °C, CrO_3 (g) is easily formed on the surface of Cr_2O_3 (s). Moreover, even with only minimal presence of water vapor in air would subsequently increase the vapor pressure of Cr species and hence develops the formation of gaseous chromium oxide (CrO_3(g)) and oxy-hydroxide species ($CrO_2(OH)_2$). These chromium poisoning species travel to the cathode surface and precipitate at the cathode interface [41,49–51].

Yoo et al. [52] examined a double-layer coating of $La_{0.8}S_{0.2}MnO_3$ and $Mn_{1.5}Co_{1.5}O_4$ applied to Crofer 22 APU stainless steel through electrophoretic deposition. Their findings indicated that this double-layer coating effectively prevented chromium diffusion at the interface between the coating and the substrate while also exhibiting excellent long-term stability and electrical performance. Liu et al. [53] investigated a Ni/$NiFe_2$ dual-layer coating deposited on pre-oxidized SUS 430 stainless steel for 50 h using magnetron sputtering. This coating comprises three layers: a Cr_2O_3 oxide scale (inner), a NiO layer (middle), and an outer $NiFe_2O_4$ layer. The results revealed that chromium diffused into the outer layer, leading to the formation of a Cr_2O_3 oxide scale at the interface between the coating and the substrate. Goeble et al. [54] studied the long-term degradation behavior of Ce/Co coatings on AISI 441 stainless steel applied via PVD method. The results indicated that, after 37,000 h of oxidation at 800°C, the Cr evaporation rate remained consistent with its initial rate. Talic et al. [37] investigated the impact of $MnCo_{1.7}Fe_{0.3}O_4$ spinel coating density on oxidation resistance and chromium evaporation. The oxide spinel coating was applied to Crofer 22 APU using EPD method. The sintered coating processed solely in static air was more porous than the sintered coating subjected to reduction and re-oxidation heat treatment, which resulted in higher chromium evaporation.

Grolig et al. [55] studied the evaporation of chromium from cerium/cobalt-coated metallic interconnects and bare AISI 441 stainless steels. They found that the amount of evaporated chromium was reduced by about 90% in the coated interconnects compared with the uncoated substrate.

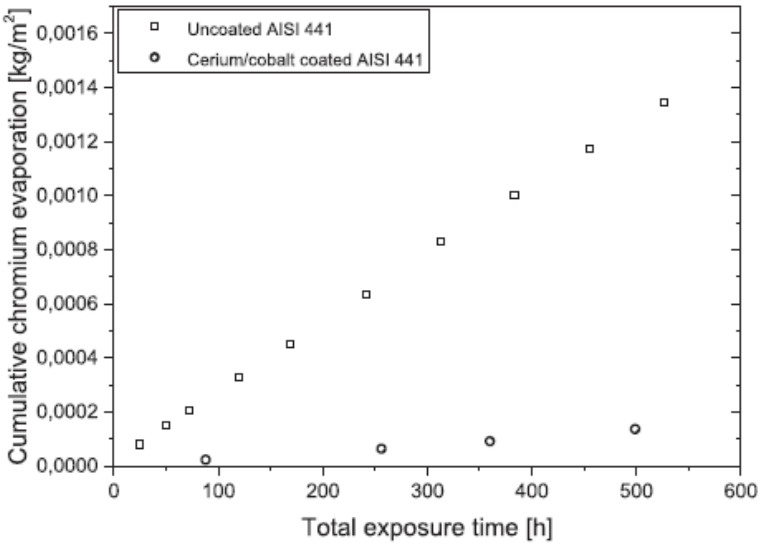

Fig. 7. Cumulative chromium evaporation of uncoated and cerium/cobalt coated AISI 441 stainless steels [55].

1.4.3. Electrical conductivity

The main function of the interconnect material is to establish electrical connection between the anode and the cathode of neighboring cells, and hence the electrical conductivity of the interconnect is very important. This is usually quantified in terms of contact or area-specific resistance (ASR). As the ASR of a metal interconnect is determined by the thickness and resistivity of the oxide scale, it should ideally show the same time dependence as the growth rate of the oxide scale. The oxide scale that developed on the metallic interconnect is Cr_2O_3 and possibly $(Mn, Cr)_3O_4$. The electrical conductivity of $(Mn, Cr)_3O_4$ is usually a little greater than that of Cr_2O_3 [53,56–58]. Sun et al. [59] examined the $Mn_{1.8}CuO_4$ spinel coating on Crofer 22 APU plates and Crofer 22 H mesh, which were uniformly and densely deposited using electrophoretic deposition method. The results revealed the presence of a $(Cu,Mn,Cr)_3O_4$ interaction layer between the spinel coating and the Cr oxide scale. The electric conductivity of Cr_2O_3 can be separated into two ranges of temperature:

1. At high temperature (>1000°C), Cr_2O_3 is an n-type intrinsic conductor independent of oxygen partial pressure [60].
2. At low temperature (<1000°C), pure Cr_2O_3 is a p-type extrinsic conductor with partial dependence on the oxygen partial pressure [61].

Thus, electrical conductivity of ferritic stainless steel is connected with the development of the oxide scale.

Shen et al. [49] studied a Co_3O_4/Sm-doped CeO_2/Co_3O_4 trilayer coating on AISI stainless-steel interconnects, which was deposited using both electrodeposition and electrophoretic deposition methods. The results revealed that the area specific resistance of the trilayer-coated stainless steel was lower compared to that of uncoated stainless steel after undergoing oxidation treatment at 800 °C for 400 h. Cheng et al. [62] examined a double-layer Co-Mn-O spinel coating applied to 430 stainless steels using a double glow plasma alloying process (DGPA), followed by a peroxidation treatment in static air. The outer layer of this double-layer coating consists of a thick $MnCo_2O_4$ spinel coating, while the inner layer is a thin mutual-diffused $(MnCoFe)_3O_4$ coating. The results indicated that the area specific resistance of the coated samples was significantly lower than that of the uncoated samples after 408 h of oxidation. Grolig et al. [55] examined the electrical properties of Ce/Co double-layer coatings on AISI 441 metallic interconnects applied using PVD method. The ASR was measured using both in-situ and ex-situ methods. The results revealed that the ex-situ ASR value was 15 mΩ.cm^2 after 1500 h of oxidation. In contrast, the in-situ ASR measurement indicated corrosion damage to the substrate, with the value reaching 35 mΩ.cm^2 after 500 h of oxidation. Wolff et al. [63] studied the $MnCo_{1.9}Fe_{0.1}O_4$ spinel coating on Crofer 22 APU, which was applied using a wet powder spraying technique. The results demonstrated that this method produced a dense coating with excellent adhesion and a thin layer. The ASR measurement indicated a value of 10 mΩ.cm^2 after 1000 h of oxidation at 800°C. Stevenson et al. [44] examined the area-specific resistance of uncoated and coated AISI 441 stainless steels. They noticed that ASR of uncoated samples was much greater than that of coated samples as a result of stainless-steel oxidation. In addition, the coated samples exhibited much greater stability compared to uncoated samples.

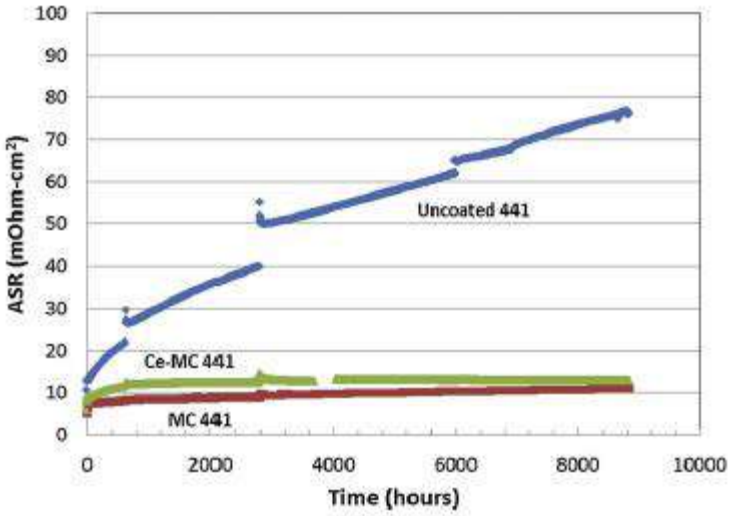

Fig. 8. Area specific resistance (ASR) of uncoated and coated AISI 441 stainless steels [44].

1.5. Protective coating

Protective coating is an effective method for avoiding chromium poisoning. In order to inhibit the formation of the Cr_2O_3 layer, outward chromium diffusion and inward oxygen ion diffusion, which are the driving forces for chromium oxidation, must be avoided. Besides, the coating material should be very conductive electrically so that the passage of electricity from the interconnector to the external circuit is not hindered. The TEC of the coating material should also be compatible with the TEC of the interconnect, preferably within a difference of 10%. This is important for the durability of the coating because thermal expansion mismatch outside this range can cause spallation and cracking. Apart from this, the coating material must possess a dense microstructure to minimize the diffusion of chromium and oxygen ions. The coating must consist of nano size particles with little agglomeration for the formation of a dense, well-distributed, and adherent layer [64–67]. Oxide spinel coating and oxide perovskite coatings are widely applied and studied.

1.5.1. Oxide spinel coating

Cubic spinel of the general composition AB_2O_4 is a stable and good protective coating material. Oxide spinel have been a significant area of study as interconnect protective coatings. The selection of the transition metals at the A and B positions is cation and ratio dependent. The octahedral and tetrahedral site cations of the cubic oxide spinel structure

are usually divalent, trivalent, or quadrivalent cations, as shown in Fig. 9. The ratio of A and B cations are adjusted as to match the electrical conductivity and thermal expansion. These cations are the binary spinel comprising of Al, Fe, Mn, Cr, Co, Ni, Mg, and Zn. Cubic spinel is proven to be good electronic conductor, and its thermal expansion coefficient matches with that of ferritic stainless steel. Transition metal oxides in the form of individual layers, like Co_3O_4, have been proven, while addition of transition metals like copper (Cu), nickel (Ni), and cerium (Ce) was seen to increase electrical conductivity while still optimizing the thermal expansion coefficient fit. Composite spinel coatings have successfully restrained volatilization of Cr_2O_3 on the scale surface and have been found to be nearly equal to thermal expansion coefficient of FSS. Mn-Co spinel oxide coating has been used widely due to its uniformity and superior oxidation resistance. The electrical conductivity of most of the oxide spinel coatings, however, should be further developed. The obstacle for spinel oxide coating is the synthesis of the binary spinel and adjustment ratio of A and B cations. Research into the synthesis process is required to obtain the correct spinel oxide formula (AB_2O_4) and an optimum cation ratio for the optimization of spinel coating performance [19,58,68–71].

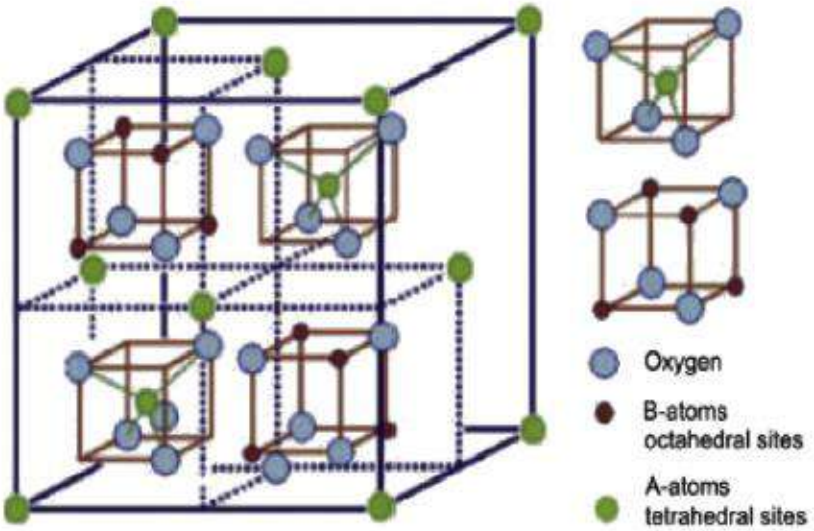

Fig. 9. Typical AB_2O_4 spinel oxide structure [19].

1.5.2. Perovskite coating

Cathode materials have often been used as protective coatings for stainless-steel interconnectors, but perovskite materials, which are more utilized in SOFCs for cathode development, are mentioned in only a few studies. The fundamental perovskite structure

follows the general formula ABO_3, where the total charge of A and B cations adds up to +6 [72]. The A cations are typically low-valence elements such as La, Sr, Ca, and Pb, with larger particle sizes, and are coordinated with twelve oxygen anions. On the other hand, the B cations are higher-valence elements like Ti, Co, Fe, and Ni . Fig. 10 illustrates the cubic perovskite structure. Most A-site cations in perovskite oxides for cathodes come from rare earth and alkaline earth elements such as La, Sr, Ca, or Ba, while B-site cations are a mix of reducible transition metals like Mn, Fe, Co, and Ni. Perovskite cathode composites are considered promising protective coatings due to their p-type electronic conduction in oxidizing environments. Examples of such materials include lanthanum strontium chromite (LSCr), lanthanum strontium cobaltite (LSC), and lanthanum strontium ferrites (LSF) [73]. However, the area-specific resistance (ASR) of these early perovskite coatings exceeds 0.1 $\Omega \cdot cm^2$, which is the required threshold for coating materials. Additionally, the coatings are often not dense, exhibiting cracks and pores. Used perovskite coatings like LSF and LSCr on various ferritic steel substrates have been studied, but coatings formed via radio frequency sputtering have been found to be inadequate due to structural flaws such as cracks and pores. If perovskite material is employed as a protective coating on interconnects, it is essential that the coating must be dense and well adhered to the interconnect surface so that chromium should not diffuse out and react with oxygen diffusing in. For this purpose, A and B site cations could be enhanced through doping by larger metal ions in an attempt to reduce the oxygen ion mobility and the self-diffusion coefficient through adjusting the composition ratio of the perovskite material [58,65,74,75].

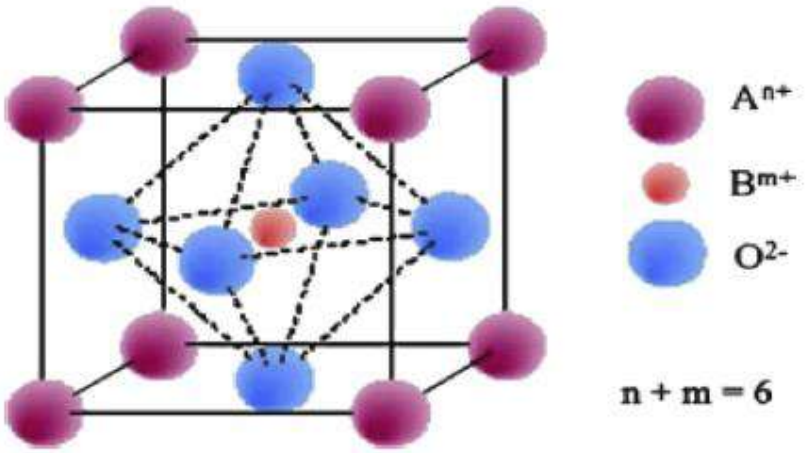

Fig. 10. Typical ABO_3 perovskite structure [72].

1.6. Properties of oxide spinel coating

The electrical conductivity and thermal expansion coefficient of oxide spinel coatings are described as follows:

1.6.1. Area specific resistance (ASR)

Area specific resistance (ASR) is the electrical property of the materials. Chromia scale presence indicates high ASR, and low electrical conductivity is indicated by it. With time, the oxide layer forms and grows thicker on the interconnect in the oxidizing environment, and the ASR rises and leads to interconnect degradation. ASR measurements are taken under constant current for coated interconnects that are exposed to air oxidation at 800 °C. Metallic interconnects require a reduced ASR such that they are able to carry electricity effectively [2,20,24,76]. The coated interconnect must have an ASR value of less than 0.1 $\Omega \cdot cm^{-2}$ [74]. Manganese cobalt oxide ($Mn_{1.5}Co_{1.5}O_4$) spinel coatings have been well researched due to their effective chromium diffusion suppression properties, with excellent resistance to chromium poisoning [77]. However, $Mn_2Co_2O_4$ is more resistant to oxidation but less thermally stable, although it is highly electrically conductive. This means that the composition of the elements in spinel coatings is crucial to their performance. ASR value needs to be low, so cubic spinel coatings are good electrical conductors and form strong, crack-free, adhesive protective films on interconnects [78]. Copper manganese oxide ($Cu_{1.3}Mn_{1.7}O_4$) has also been reported to have a very low ASR value of 0.0063 $\Omega \cdot cm^2$ after oxidation for 185 h, which is the lowest among spinel coatings [72].

Zhang et al. [79] investigated the electrophoretic deposition of $(Mn,Co)_3O_4$ spinel protective coating on T 441 stainless-steel metallic interconnect. $(Mn,Co)_3O_4$ spinel coating exhibited stable, long-term performance in an H_2/H_2O atmosphere, with the formation of a thin Cr oxide scale. Additionally, ASR measurements indicated that the sintered spinel coating in the H_2/H_2O atmosphere had lower resistance compared to the coating sintered in air. The ASR of $(Mn,Co)_3O_4$ spinel coating sintered in the H_2/H_2O atmosphere was 59 $m\Omega.cm^2$ after 500 h of oxidation. Shaigan et al. [80] examined ASR values of bare and Co/$LaCrO_3$-coated AISI 430 stainless steel at 800 °C in air as a function of time. Bare AISI 430 had a sharp rise in ASR with oxidation time, following parabolic behavior until approximately 50 h. Co/$LaCrO_3$-

coated samples showed very low resistance for approximately 165 h. The ASR of the coated samples began to increase parabolically after approximately 600 h, and at 900 h, no increase was observed. The sudden increase in ASR beyond 160 h resulted from the formation of porosity at the metal-scale interface that reduces the contact area between the substrate and the scale (as shown in Fig. 11).

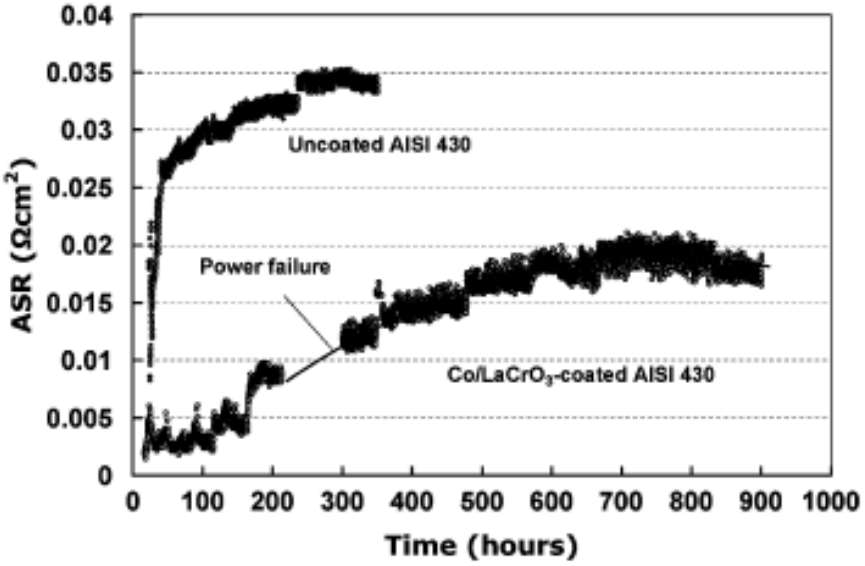

Fig. 11. ASR values for $Co/LaCrO_3$-coated and -uncoated AISI 430 stainless steel at 800 °C in air as a function of time [80].

1.6.2. Thermal expansion coefficient (TEC)

Among the important factors, the thermal expansion response defines the variation in size with temperature that is undergone by the coating material; this response has been quantified by the coefficient of thermal expansion, an essential material property in all SOFC components, and also in the interconnect. Because of their high operating temperatures, both coating material and the interconnect tend to expand due to the rising temperature. It has to be matching in TEC for ferritic stainless steel and coating material for uniform expansion without the creation of structural issues. Differential thermal stress and strain due to thermal shock may appear when different materials expand at different rates under thermal energy. If the induced stress is greater than the strength of the material, cracks or structural failure may appear [65,81,82]. In SOFC, high difference in thermal expansion coefficient between two materials causes another material which has higher TEC to exert higher thermal stress over the other material. The high thermal stress would exceed the

strength of the other material's strength. Hence, causing spallation and cracking. The average TEC for ferritic stainless steels is 11-14.5*10^{-6} K^{-1}. An acceptable TEC mismatch for these adjacent SOFC components should not be more than 10%, such as between the ferritic stainless steel and coating material [78,83,84]. Talic et al. [34] investigated the thermal expansion behavior of Fe- and Cu-substituted $MnCo_2O_4$ spinel coatings. Their results showed that increasing Fe substitution decreased thermal expansion in a nearly linear, while Cu substitution increased the TEC overall, although the expansion behavior was more complex and did not follow a clear trend. The effect of increasing temperature on increasing TEC was believed to be due to the spin state transition of Co^{3+} from low spin to high spin. Fe substitution resulted in more linear expansion with respect to temperature and overall lower TEC. Substitution by Cu probably affected the expansion behavior due to precipitation of CuO secondary phases, hence showing slightly higher TEC values compared to $MnCo_2O_4$.

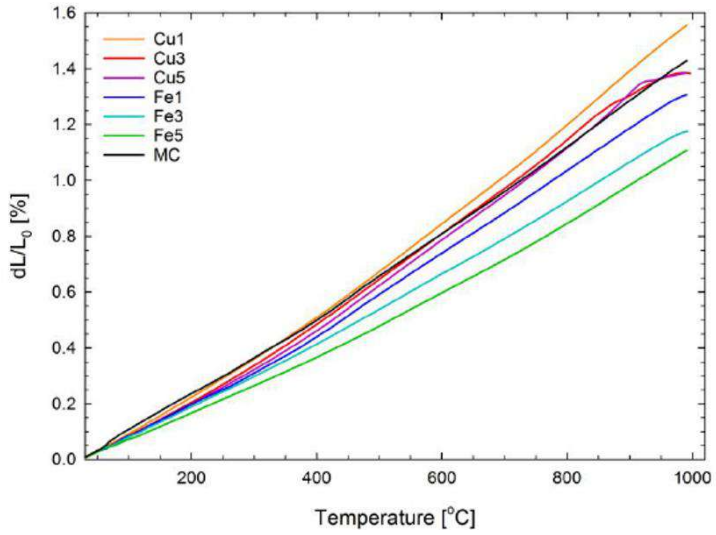

Fig. 12. Thermal expansion measured by dilatometry during heating in air [34].

1.6.3. Densification of coating

To obtain dense layer on substrate, it is necessary to sinter the coating material on the substrate. Sintering parameters, including temperature, time, and atmosphere, are important to the densification of the coating. The optimization of sintering parameters helps to decrease the stress on the coated substrate, resulting in the prevention of cracks. In addition, by increasing the densification of coated stainless steel, the protective coating

blocks oxygen diffusion and prevents the formation of a chromia layer, resulting in an increased lifespan of metallic interconnects in SOFC applications [44,85]. To increase the densification of the coated stainless steel, the coating was sintered under oxidation treatment (air atmosphere) and reduction treatment (pure hydrogen atmosphere), followed by oxidation treatment (air atmosphere). The first method is sintering under oxidation conditions (static air), in which the sintering of the coated metallic interconnect occurs through solid-state diffusion. In this condition, the densification of the coated metallic interconnect is slower, and some residual porosity remains, allowing oxygen to diffuse through these paths and form a continuous oxide layer on the stainless steel. Furthermore, operating at high temperatures for prolonged periods can lead to the growth of a chromia layer, forming a thick layer that decreases coating adhesion and reduces electrical conductivity [86,87]. The second method is sintering in a reduction treatment (including pure H_2, N_2+H_2, or Ar+H_2) followed by oxidation treatment (static air). During the reduction step, part of the spinel material is reduced to lower-valence oxides or metallic states, which increases atomic mobility through oxygen vacancies and cation defects. In the oxidation step, these defects and vacancies enhance diffusion, promote pore shrinkage, and facilitate grain rearrangement, thereby increasing the densification of the coating. Furthermore, the highly dense coating can prevent oxygen diffusion and chromia layer formation, reducing the risk of delamination or spallation of the coating [88,89].

Talic et al. [37] studied the effect of sintering parameters on the oxidation behavior of $MnCo_{1.7}Fe_{0.3}O_4$ spinel protective coating on Crofer 22 APU stainless-steel metallic interconnect. Improving the coating densification decreases the K_p because it limits the diffusion path of oxygen. The oxidation rate for uncoated sample 800 °C for 1000 h was, 4.2×10^{-11} mg^2 cm^{-4} s^{-1}. In addition, The oxidation rate for coating sintered in air (O900), coating sintered in reduction followed by air (R900+O800), and coating sintered in reduction followed by static air (R1100+O800) in an air atmosphere at 800 °C for and 5000 h were, 1.4×10^{-11}, 1.3×10^{-11}, and 0.34×10^{-11} mg^2 cm^{-4} s^{-1}, respectively. Increasing the coating densification on stainless-steel metallic interconnect through sintering conditions decreased oxidation rate. Zanchi et al. [90] investigated the area specific resistance (ASR) value of sintered $MnCo_2O_4$ spinel protective coating under different sintering conditions. After the applying of the Mn-Co spinel material by EPD method, the samples were sintered under

oxidation treatment (EPD_Ox) and reduction treatment, followed by oxidation treatment (EPD_R1000 and EPD_R1120). The area specific resistance (ASR) values of the EPD_Ox, EPD_R1120, and EPD_R1000 samples after 1500 h of oxidation were 30.3, 16.5, and 12.7 $m\Omega \cdot cm^{-2}$, respectively. The ASR value of the spinel protective coating sintered in oxidation treatment was higher than the samples sintered in reduction treatment. This difference is attributed to Cr diffusion from the chromia layer to the coating surface, as well as the growth of the oxide layer. Furthermore, achieving a dense layer through the sintering process on stainless steel prevents oxygen diffusion and the formation and growth of the chromia layer on the substrate, resulting in an increased lifespan of the metallic interconnect in SOFC applications.

1.7. Doping of active rare earth elements in spinel

Rare earth element doping in spinel is used for enhancing the properties of coatings over metallic interconnects, like electrical conductivity, oxidation resistance, coating densification, and matching the thermal expansion coefficient of the spinel coating with stainless steel [91–93]. These can be further optimized by incorporating rare earth and transition elements such as Fe [94], Ni [95], and Ce [96,97]. Qing et al. [96] studied Cu- and Ce-doping of $MnCo_2O_4$ spinel coatings on SUS430 stainless steel substrates deposited by a sol-gel technique and electrophoretic deposition. The oxidation rate at 800 °C for 500 h was 1.35 mg/cm^3. Under the same conditions, the ASR of the doped $MnCo_2O_4$ spinel coating was determined to be around 9.8 $m\Omega \cdot cm^2$. The research showed that the doping of rare earth metals enhanced the oxidation resistance considerably, as compared to both uncoated stainless steel and $MnCo_2O_4$ spinel coatings without doping. In addition, the ASR of the coating with co-doping was much lower when compared to SUS430 stainless steel and $MnCo_2O_4$ coatings. Zanchi et al. [94] investigated the oxidation performance of Fe-doped $Mn_{1.5}Co_{1.5}O_4$ coatings on metallic interconnects. Their findings showed that the oxidation rate of the Fe-doped Mn-Co spinel coating was lower than that of both the $Mn_{1.5}Co_{1.5}O_4$ spinel coating and uncoated stainless steel. Mazur et al. [95] studied Ni- and Fe-doped $Mn_{1.7}Cu_{1.3}O_4$ coatings on metallic interconnects. Their findings revealed that the electrical conductivity of $Mn_{1.7}Cu_{1.3}O_4$ increased with Ni doping levels of 0.3 or higher, while Fe doping at the same level led to a decrease in conductivity compared to $Mn_{1.7}Cu_{1.3}O_4$. Additionally, the oxidation resistance of the Cu-Mn-Ni-O spinel coating on stainless steel after 2000 h at 800°C was

significantly lower than that of bare stainless steel. Sabato et al. [51] investigated in-situ Cu-doped Mn-Co spinel coatings for metal interconnects by using electrophoretic deposition. Their results are presented in Fig. 13 show the densification of doped and undoped spinel coatings. Additions of Cu significantly improved densification in the as sintered state. While some residual open porosity was present in both the undoped and 5CuMCO samples, the 10CuMCO sample had largely closed porosity, which should be beneficial for protecting against gaseous chromium transport (as shown in Figs. 13a, b and c).

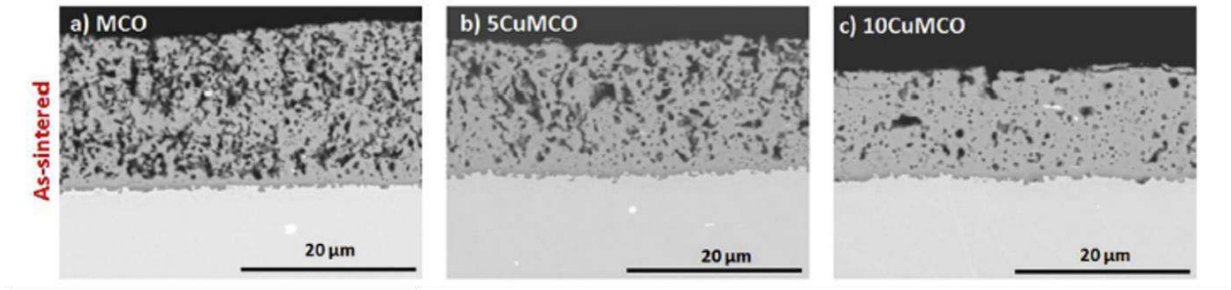

Fig. 13. Cross section SEM images of the coated samples: a) Mn-Co coating, c and d) Cu doped Mn-Co spinel coating with different ratio [51].

1.8. Electrophoretic deposition (EPD) method

Several deposition techniques have been developed to coat the metallic interconnect surfaces with spinel protective coatings, including electrophoretic deposition (EPD) [24,59,64,98], electrolyte deposition (ELD) [99–101], dip coating [102–106], plasma spraying [107–110], screen printing [111–113], spin coating [97], and magnetron sputtering [53,76,109,114]. Among them, EPD is quite effective in providing a homogeneous and dense spinel coating on metallic interconnects. Advantages of this technique include simplicity, low cost, rapid deposition, low-temperature processing, homogeneous microstructure, suitability for complex-shaped substrates, and easy control of coating thickness. On the other hand, disadvantages of EPD include compatibility with substrates, limitation to thick coatings, and optimization of many parameters carefully. These factors include parameters related to the suspension, such as particle size, zeta potential, suspension stability, and suspension conductivity. Additionally, process parameters, such as voltage, deposition time, solid concentration, and substrate conductivity, also play a critical role in the successful formation of the coating. EPD can operate both with aqueous and non-aqueous solvents.

Aqueous solvents are preferable due to their low cost, environmental friendliness, and possibility to work at lower voltages. On the other hand, non-aqueous are more expensive, toxic, flammable solvents, and higher voltages are required for deposition [27,33,115–118].

Aznam et al. [119] studied the zeta potential of $(Cu,Mn,Co)_3O_4$ spinel materials in different solvents, as illustrated in Figs. 14a and 14b. Among the tested suspensions, the highest zeta potential and most stable $(Cu,Mn,Co)_3O_4$ suspension were achieved using a 50/50 isopropanol–acetylacetone mixture, compared to using isopropanol or acetylacetone alone. This optimized solvent mixture resulted in a well-dispersed suspension, making it highly suitable for electrophoretic deposition (EPD). As shown in Fig. 14b, the deposition masses of the $(Cu,Mn,Co)_3O_4$ suspensions prepared in isopropanol, acetylacetone, and the 50/50 mixture all exhibited a linear increase over time. During EPD, the charged particles were discharged and deposited onto SUS430 steel substrates, forming an insulating layer that eventually slowed and inhibited further deposition. The suspension prepared using the 50/50 isopropanol–acetylacetone mixture resulted in a higher deposition mass than the suspension in isopropanol alone. This effect is likely due to the higher zeta potential in the mixed solvent, which enhances deposition efficiency. In addition to the suspension solvent, the applied voltage plays a crucial role in achieving a uniform and dense coating through EPD. The influence of voltage on deposition mass was investigated using the optimized 50/50 isopropanol–acetylacetone suspension. As depicted in Fig. 14c, increasing the applied voltage (40, 60, 80, and 100 V) and deposition time led to an increase in deposition mass. However, the deposition mass did not increase linearly, as the formation of an insulating layer on the substrate eventually hindered further deposition.

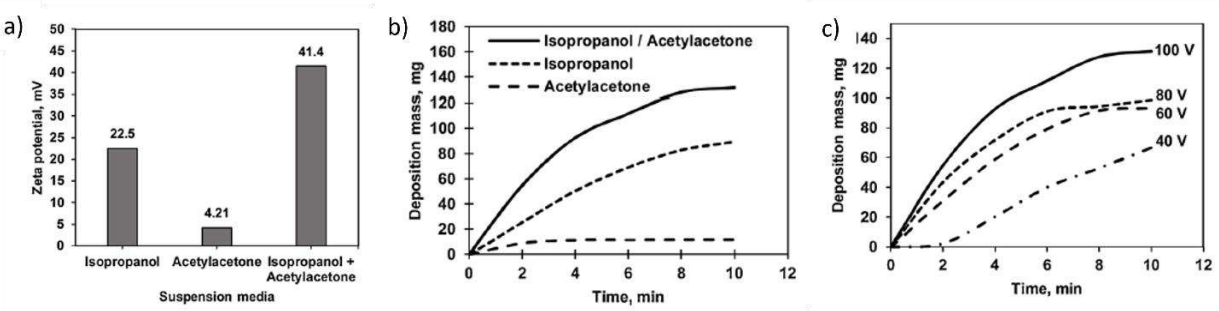

Fig. 14. a) Zeta potential values of the $(Cu,Mn,Co)_3O_4$ suspension in different suspension solvent, b) Deposition mass over time for different suspension solvent at the constant voltage of 100 V, and c) Deposition mass of $(Cu,Mn,Co)_3O_4$ coatings at different applied voltages over time by using a mixture of 50/50 isopropanol and acetylacetone solvent [119].

Talic et al. [120] studied the application of $Mn_{1.5}Co_{1.5}O_4$ spinel coatings on Crofer 22H stainless steel grids using EPD method. They demonstrated that uniform spinel coatings were achieved on the concave corners of the substrate, while cracks formed on the convex corners of the stainless-steel grid. These cracks in the convex corners were attributed to the coating thickness, sintering conditions, and the curvature radius of the substrate. Furthermore, they found that sintering the coating in a reducing atmosphere, followed by an oxidation treatment, was more likely to result in cracks compared to sintering only in an oxidation treatment. Zanchi et al. [90] studied the application of $MnCo_2O_4$ spinel coatings on complex-shaped stainless steel (SUS 445 ferritic stainless steel) using EPD method. They observed that a uniform coating was successfully deposited on the complex-shaped metallic interconnects via this technique. Furthermore, they found that sintering in a reducing atmosphere at 1000 °C for 2 h, followed by an oxidation treatment at 800 °C for 5 h in static air, effectively prevents chromium diffusion and evaporation. Shen et al. [121] studied the application of $Mn_{1.8}CuO_4$ spinel coatings on low-cost porous stainless steel using EPD method. They demonstrated that the $Mn_{1.8}CuO_4$ spinel coating significantly reduced chromium evaporation by up to 80% compared to uncoated porous stainless steel. Additionally, they found that EPD is the most effective method for minimizing chromium diffusion and evaporation from porous stainless steel.

2. Objective, hypotheses, and novelty of research

To increase the lifetime of metallic interconnects, the spinel protective coating plays a crucial role in enhancing oxidation resistance, improving electrical conductivity, and preventing Cr diffusion and evaporation, thereby increasing the durability and efficiency of metallic interconnects in solid oxide cells (SOCs) application. Accordingly, in this thesis, different configurations of spinel coatings, including single-, dual-layer and hybrid coatings, were used to improve the properties of stainless-steel metallic interconnects.

2.1. Objective of research

The objective is to develop deposition method through applying single-layer, dual-layer, and hybrid spinel coatings on flat and complex-shaped stainless-steel metallic interconnects using electrophoretic deposition (EPD) method. In addition, the microstructure of spinel protective coating with SEM and confocal optical microscope, surface roughness with confocal optical microscopy, phase and structural analysis with XRD, composition analysis with confocal spectroscopy, electrical conductivity of spinel materials with Van der Pauw method and the diffusion of chromium from the substrate into the oxide spinel coatings with energy-dispersive X-ray spectroscopy (EDX) were investigated.

To better understand the spinel protective coating on stainless-steel metallic interconnects using electrophoretic deposition (EPD) method, the following questions have been posed for each manuscript:

1. Which solvent type (pure ethanol or ethanol: water mixture) is more effective for achieving non-agglomerated suspension, higher suspension stability, higher zeta potential, and higher suspension conductivity? What iodine concentration in the solvent is required to obtain optimal zeta potential and suspension conductivity? What is the optimal concentration of solid spinel particles to control deposition yield or coating thickness on the substrate? How does varying applied voltage and deposition time affect the behavior of spinel particles in the solvent, in terms of achieving optimal coating thickness, uniformity, and crack-free morphology?
2. Which applied voltage and deposition time are optimal to deposit uniform, crack-free single-layer and dual-layer coatings on complex-shaped steel substrates? How does

changing the sintering atmosphere (from oxidation treatment to reduction followed by oxidation treatments) affect the microstructure and densification of the coating? What is the phase composition at the interface of Mn–Co and Mn–Cu–Fe spinel coatings after sintering? How does chromium diffusion behave in single-layer and dual-layer spinel protective coatings on stainless steel?

3. At what iodine concentration do Mn–Co and Mn–Cu–Fe spinel powders exhibit identical zeta potentials, ensuring a consistent ratio of both powders in the coating? How does chromium diffusion behave in hybrid spinel protective layers on stainless steel? What are the phase composition and structure of hybrid spinel coatings after sintering? How does the electrical conductivity of mixed spinel materials vary with different material ratios?

2.2. Hypotheses

On the basis of the preceding information, the following hypotheses are proposed for this PhD thesis.

1. Electrophoretic deposition can be effectively employed to sequentially fabricate high-quality dual-layer coatings with well-defined interfaces.
2. Electrophoretic deposition enables controlled co-deposition of distinct spinel materials, allowing the tailoring of their combined structural and functional properties.

2.3. Novelty of research

Due to the high oxidation rate, significant chromium diffusion, and low electrical conductivity observed in single-layer coated stainless-steel metallic interconnects, dual-layer and hybrid spinel coating configurations are proposed.

In Manuscript I, to obtain a well-dispersed suspension, various suspension parameters including solid loading, iodine concentration, zeta potential, suspension stability, and solvent type are optimized to deposit uniform, dense, and crack-free coatings on the substrate. Additionally, the microstructure and surface roughness of the oxide spinel coating on stainless steel are analyzed, as a uniform protective coating plays a crucial role in preventing the formation and growth of the chromia layer.

In Manuscript II, a novel Mn-Co/Mn-Cu-Fe dual-layer coating is applied to metallic interconnects using EPD method. Two main reasons support the selection of a dual-layer oxide spinel coating for metallic interconnects. First, the $Mn_{1.7}CuFe_{0.3}O_4$ spinel coating offers superior electrical conductivity compared to the $MnCo_2O_4$ spinel coating, making it an ideal outer layer to facilitate electrical conductivity between adjacent cells. Second, the $MnCo_2O_4$ spinel coating demonstrates significantly higher oxidation resistance than $Mn_{1.7}CuFe_{0.3}O_4$, serving effectively as an inner layer to reduce oxidation rates and inhibit chromium migration and evaporation from the interconnects to the oxygen electrodes.

In Manuscript III, a novel hybrid coating with varying weight ratios (1:0, 1:3, 1:1, 3:1, and 0:1) is deposited on metallic interconnects via EPD method. The hybrid coatings are selected due to the superior oxidation resistance of Mn-Co spinel materials, the higher electrical conductivity of Mn-Cu-Fe spinel materials, and the absence of new phases between these two oxide spinel materials. By utilizing these innovative Mn-Co: Mn-Cu-Fe hybrid spinel materials, simultaneously improve both electrical conductivity and oxidation resistance.

3. Manuscripts

In Chapter 3, the experimental methods and results, including materials, suspension preparation, spinel material deposition, sintering conditions, and characterization, are presented to address the research questions, hypotheses, objectives, and novelty of the study. The publications included in this thesis are listed as follows:

3.1. Manuscript I

Omid Ekhlasiosgouei, Federico Smeacetto, Sebastian Molin, "**Suspension and process parameters selection for electrophoretic deposition of Mn–Co spinel coating on steel interconnects**," International Journal of Hydrogen Energy, vol. 60, pp. 1054-1067, 2024**.** https://doi.org/10.1016/j.ijhydene.2024.02.252.

3.2. Manuscript II

Omid Ekhlasiosgouei, Maciej Bik , Sebastian Molin, "**Preparation of Mn-Co and Mn-Cu-Fe single-layer, and novel Mn-Co/Mn-Cu-Fe dual-layer spinel protective coatings on complex-shaped metallic interconnects by EPD method**," International Journal of Hydrogen Energy, vol. 83, pp. 563-576, 2024. https://doi.org/10.1016/j.ijhydene.2024.07.447.

3.3. Manuscript III

Omid Ekhlasiosgouei, Maciej Bik, Federico Smeacetto, Piotr Jasinski, Sebastian Molin, "**Electrophoretic deposition of novel hybrid $MnCo_2O_4$: $Mn_{1.7}CuFe_{0.3}O_4$ spinel protective coating on stainless-steel metallic interconnects for SOFCs application**,".

3.1. Manuscript I

Title: **Suspension and process parameters selection for electrophoretic deposition of Mn–Co spinel coating on steel interconnects.**

This study delved into the promising application of electrophoretic deposition (EPD) as a method for coating the surface of Crofer 22 APU alloy with a Mn-Co spinel layer. The investigation evaluated suspension and process parameters, aiming to achieve a coating that is uniform, dense, smooth, and free of cracks. The evaluation of the Mn-Co coating's attributes—quality, adhesion, and thickness on the substrate—was a central focus to attain a uniform and consistent layer. Results underscored the clear superiority of the pure ethanol solvent over the H_2O: ethanol mixture (40:60 %Vol) for Mn-Co particles. The pronounced agglomeration observed in the latter was approximately seven times more than that in the former, highlighting the critical role of solvent selection in achieving optimal coating characteristics. Detailed study of the sintered Mn-Co coating's morphology and surface roughness, conducted through SEM and confocal laser scanning microscopy (CLSM), respectively, provided valuable insights. The application of a uniform and dense coating was achieved by utilizing a pure ethanol solvent with a solid concentration of 10 g/L, along with 0.5 g/L of iodine as a disperser. The deposition process, executed at a voltage of 30V for 20 s, yielded a coating with a thickness measuring 7.4±0.3 μm and a surface roughness of 0.75±0.5 μm. This study not only highlights the suitability of EPD for Mn-Co spinel coating on Crofer 22 APU alloy but also emphasizes the critical role of solvent choice and process parameters in determining the quality and characteristics of the deposited coatings. The resulting coating's uniformity and controlled attributes hold promising implications for applications requiring resistance to chromium migration and oxidation.

The research highlighted are outlined as follows:

- Dispersed Mn-Co particles in ethanol were more appropriate for EPD process.
- A uniform and crack-free coating applied onto Crofer 22 APU using EPD method.
- The optimal voltage and deposition time for EPD method were 30 V and 20 s.
- The optimal coating thickness and surface roughness were 7.4±0.3 and 0.75±0.5 μm.

Table 1. CRediT author statement of manuscript I.

Author	CRediT author statement	Signature
Omid Ekhlasiosgouei	Methodology, Investigation, Formal analysis, Data curation, Writing– original draft	
Federico Smeacetto	Data curation, Writing- review and editing	
Sebastian Molin	Resources, Conceptualization, Supervision, Writing- review and editing	

International Journal of Hydrogen Energy 60 (2024) 1054–1067

Contents lists available at ScienceDirect

International Journal of Hydrogen Energy

journal homepage: www.elsevier.com/locate/he

Suspension and process parameters selection for electrophoretic deposition of Mn–Co spinel coating on steel interconnects

Omid Ekhlasiosgouei [a,*], Federico Smeacetto [b], Sebastian Molin [a]

[a] Advanced Materials Center, Faculty of Electronics, Telecommunications and Informatics, Gdansk University of Technology, Gdansk, Poland
[b] Department of Applied Science and Technology, Polytechnic di Torino, Italy

ARTICLE INFO

Handling editor: Suleyman I. Allakhverdiev

Keywords:
Interconnect
EPD
Crofer 22 APU
Mn–Co spinel coating
Crack-free

ABSTRACT

Metallic interconnect coatings, consisting of $MnCo_2O_4$ spinel, were effectively applied to Crofer 22 APU using the electrophoretic deposition (EPD) method in both H_2O: ethanol and pure ethanol solvents. The primary goal of this method was to prevent chromium migration, minimize evaporation, and control the oxidation rate. The study aimed to assess the quality, adhesion, and thickness of the Mn–Co coating, with the objective of achieving a consistent and uniform layer. The results indicated a preference for pure ethanol solvent over H_2O: ethanol (40:60 %Vol) for Mn–Co particles. Furthermore, the agglomeration of Mn–Co particles was notably lower (approximately 7 times) in ethanol compared to H_2O: ethanol. The morphology and surface roughness of the sintered Mn–Co coating on the alloy were examined using scanning electron microscopy (SEM) and confocal laser scanning microscopy (CLSM). A uniform and dense coating was successfully attained using pure ethanol solvent at a solid concentration of 10 g/L, with 0.5 g/L of iodine serving as a disperser. The deposition process, carried out at a voltage of 30V for 20 s, resulted in a coating with a thickness of 7.4 ± 0.3 μm and a surface roughness of 0.75 ± 0.5 μm.

1. Introduction

In solid oxide fuel cells (SOFCs), electrical energy is generated by converting chemical energy from gases through an electrochemical reaction involving fuel and oxygen. Metallic interconnects in SOFC stacks physically separate the cathode air from the anode fuel and facilitate energy transfer to an external circuit [1]. Various materials, including ferritic stainless steel (FSS) [2,3], Ni-based superalloy [4], and Inconel 600 [5], serve as metallic interconnects due to their excellent chemical stability, gas tightness, high thermal and electrical conductivity, durability, mechanical strength, and cost-effectiveness. Ferritic stainless-steel alloys, in particular, are widely used as metallic interconnects due to their suitable chromium content, affordability, excellent corrosion resistance at 600–800 °C, low coefficient of thermal expansion, and significant electrical conductivity [1,6]. However, when stainless steel is employed as a metallic interconnect without protective-conducting coatings, it may lead to chromium poisoning. This occurs when chromium species diffuse to the cathode, causing a decrease in electrical conductivity [7–9].

Interconnect degradation can be prevented by applying ceramic coatings to metallic interconnects [5,6]. The deterioration of metallic interconnections poses a significant challenge to the durability of solid oxide cells [7]. It is crucial to have protective-conductive coatings on metallic interconnects to reduce corrosion, minimize chromium evaporation, and control oxidation rates in solid oxide cells [9–12]. An ideal protective-conductive coating for metallic interconnects should possess high electronic conductivity, a low thermal expansion coefficient, and the ability to block chromium and oxygen [1,13–16]. However, thin-film coating on metallic interconnects plays a vital role. Various methods are available for depositing ceramic protective materials onto metallic interconnects, including screen printing [17,18], painting [19], spray [20], dip coating [21], sputtering [22], electrophoretic deposition (EPD) [23–33], electrolytic deposition (ELD) [34–39], sol-gel [40–43], slurry [44,45], plasma spraying [46–49], physical vapor deposition (PVD) [50]. Electrophoretic deposition (EPD) proves to be a highly efficient technique for applying uniform and dense spinel coatings to metallic interconnects. The EPD process relies on specific suspension and process factors to achieve a uniform, dense, and crack-free coating. These factors include parameters related to the suspension, such as particle size, zeta potential, suspension stability, and suspension conductivity. Additionally, process parameters, such as voltage, deposition time, solid concentration, and substrate conductivity, also play a critical

* Corresponding author.
E-mail address: omid.ekhlasiosgouei@pg.edu.pl (O. Ekhlasiosgouei).

https://doi.org/10.1016/j.ijhydene.2024.02.252
Received 18 December 2023; Received in revised form 24 January 2024; Accepted 19 February 2024
Available online 25 February 2024

Table 1
Composition of spinel coating material, suspension, and process parameters for the electrophoretic deposition (EPD) process, along with sintering parameters for spinel-coated metallic interconnects.

Composition (Wt.%)	Substrate	Electrodes Distance (mm)	Suspension Condition			EPD Condition		Zeta Potential (mV)	Sintering Condition (Temperature/Time/ Atmosphere)		Year	Ref
			solvent	Solid Load (g/L)	I_2 (g/L)	Voltage (V)	Time		Step1: Reduction	Step 2: Oxidation (air)		
$CuMn_{1.8}O_4$	Crofer22APU	15	EtOH ACE	–	–	20	10 min	–	1000 °C- 12h/2% H_2+Ar	750 °C- 100h	2019	[21]
$Mn_{1.5}Co_{1.5}O_4$	Crofer22APU	10	60 EtOH 40H_2O	37.5	–	50	20s	–	–	1000 °C- 2 h	2019	[8]
$MnCo_2O_4$	AISI 430 AISI 441 Crofer 22 H	15	50 EtOH 50 IPOH	–	0.5	60	60s	–	–	900 °C- 2h	2019	[3]
$Mn_{1.5}Co_{1.5}O_4$ $Mn_{1.5}Co_{1.5}O_4$ (95) CuO (5) $Mn_{1.5}Co_{1.5}O_4$ (90) CuO (10)	Crofer 22 APU	10	60 EtOH 40H_2O	37.5	–	50	20s	+13 (MCO) +6 (CuO)	900 °C- 2h/ 5% H_2+Ar	900 °C- 2h	2019	[57]
$Cu_{0.2}Mn_{1.4}Co_{1.4}O_4$	430 SUS	–	100 IPOH 100 ACAC 50 IPOH+ 50 ACAC	10	–	40–140	2–10 min	+22.5 +4.21 +41.4	800 °C 2h/ 5% H_2 + N_2	800 °C- 4 h	2020	[24]
$Mn_{1.5}Co_{1.5}O_4$	Crofer 22 APU	10	–	37.5	–	50	60s	–	900 °C- 2h/ 1% H_2 + N_2	900 °C 2 h	2021	[26]
$Mn_{1.5}Co_{1.5}O_4$	Crofer22APU	10	60 EtOH 40H_2O	37.5	–	50	20s	–	1000 °C- 2h/5% H_2 + Ar	900 °C 2 h	2021	[58]
$CuNi_{0.2}Mn_{1.8}O_4$	Porous 430 SUS	–	EtOH/ ACE	–	–	±20V	15 min	–	950 °C- 2h/ pure H_2	750 °C- 24h	2021	[59]
$(MnCo)_3O_4$	SS430	–	50 EtOH 50H_2O	10	–	30–50V	20s	–	–	800 °C- 90 min	2021	[52]
$Mn_{1.4}Co_{1.6}O_4$ $Mn_{1.1}Co_{1.5}Cu_{0.4}O_4$ $Mn_{1.2}Co_{1.5}Fe_{0.3}O_4$ $Mn_{1.2}Co_{1.5}Cu_{0.2}Fe_{0.2}O_4$	AISI 430	10	EtOH	10	0.15	30 V	5–7 min	–	–	800 °C 2 h	2022	[53]
$Cu_{1.35}Mn_{1.65}O_4$	460FC	10	EtOH	10	0.5–3.5	20–60V	30–120s	78	800 °C- 2h/ 5% H_2 + N_2	700 °C	2022	[56]
$CuMn_2O_4$ $CuNi_{0.2}Mn_{1.8}O_4$ $MnCo_2O_4$ $MnFe_{0.34}Co_{1.66}O_4$	SUS430	15	25 EtOH 75 ACE	4.5	1.09	20	5 min	–	950 °C- 6h/ pure H_2 900 °C- 2h/ pure H_2	750 °C- 24h	2022	[11]
$MnCo_2O_4$	SUS445	15	50 EtOH 50 ACE	15	0.5	50	30s	–	1000 °C 2h/2% H_2 1120 °C- 15min/5% H_2 –	800 °C- 5 h 800 °C- 5 h 800 °C- 5 h	2023	[54]
$Cu_{1.25}Mn_{1.65}Ni_{0.1}O_4$	Nirosta 4016/ 1.4016	10	25 EtOH 75 ACE	10	1.5	60	60s	–	1000 °C- 6h/10% H_2+ Ar	850 °C- 6 h	2023	[55]

role in the successful formation of the coating [51]. Table 1 provides a summary of the composition of the spinel coating material, suspension and process parameters used in the Electrophoretic Deposition (EPD) process. It also includes the sintering parameters necessary for spinel coating on metallic interconnects. During the EPD process for Mn–Co and Mn–Cu spinel coatings on metallic interconnects, various solvents such as ethanol, acetone, aqueous solutions, isopropanol, acetylacetone, and mixtures of these solvents were employed with different solid and iodine concentrations [3,8,11,24,26,28,52–59]. The EPD method offers various benefits, including its swift and uncomplicated nature, cost-effectiveness, high deposition rate, low-temperature processing, uniform microstructure, capability to deposit on complex-shaped substrates, and ease of thickness control. However, drawbacks of this method encompass substrate restrictions, limitations in achieving substantial coating thickness, and the intricacies involved in optimizing parameters. The EPD method utilizes two categories of solvents: aqueous and non-aqueous. Aqueous solvents offer benefits such as affordability, eco-friendliness, and the application of low voltage. Conversely, non-aqueous solvents present drawbacks, including toxicity, higher cost, the requirement for elevated voltage, and flammability [60–65]. A study by Zanchi et al. [10] explored the impact of adding Cu and Fe to Mn–Co spinel coatings on metallic interconnects. The findings highlighted the significance of carefully selecting doping levels to achieve the desired properties. Doping with Cu and Fe had

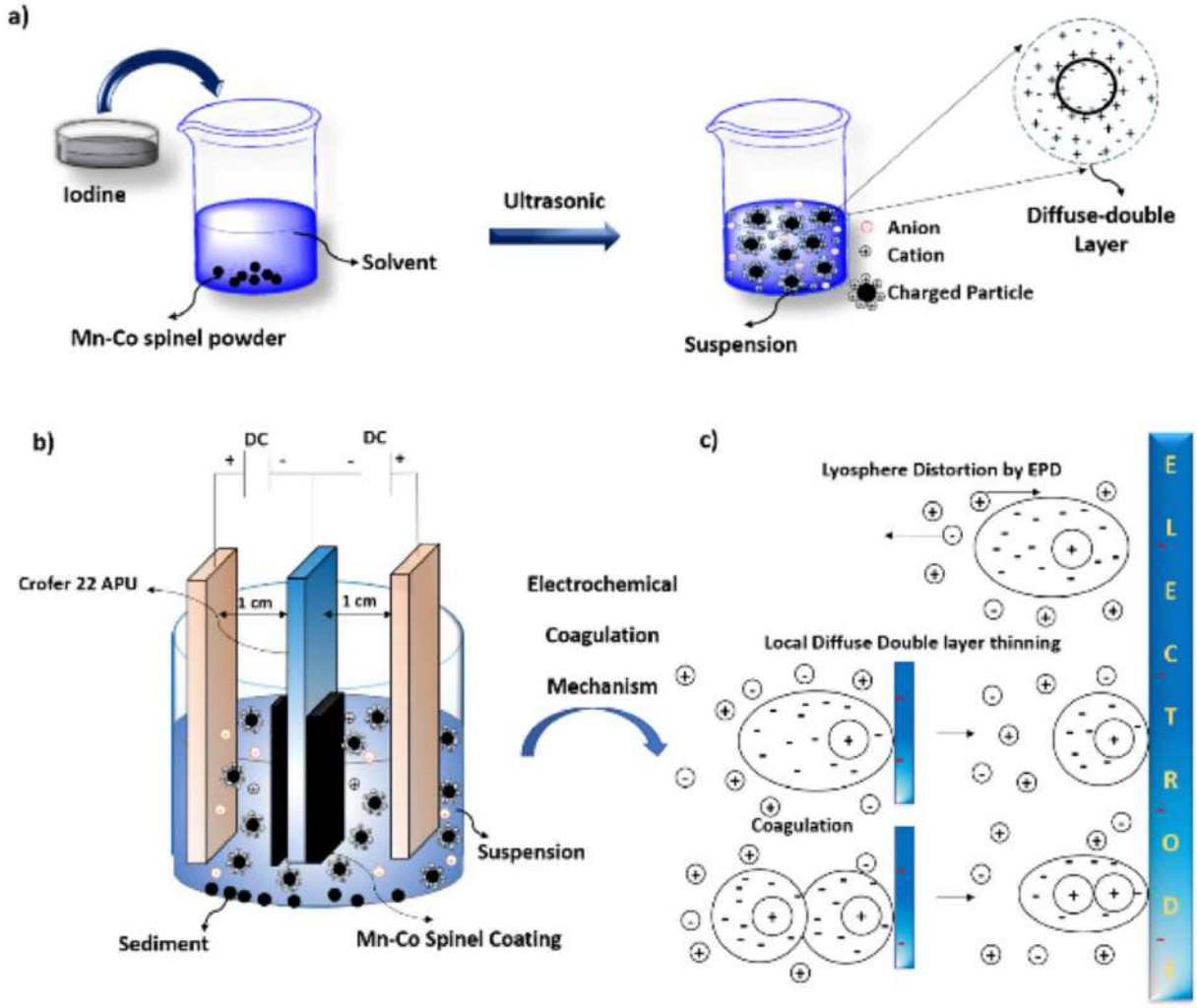

Fig. 1. The schematic illustration of the procedural steps in this research: a) electrostatic stabilization, b) EPD setup, and c) electrochemical coagulation mechanism.

significant effects on microstructural, thermo-mechanical, and corrosion properties. The researchers observed that doping Fe and Cu in Mn–Co spinel had different effects on the thermal expansion coefficient, with Fe increasing it and Cu decreasing it. Additionally, they demonstrated that doping Fe and Cu in Mn–Co spinel improved the densification and stabilization of the $MnCo_2O4$ cubic phase. The study also revealed that Fe and Cu doping enhanced the corrosion resistance of the coatings, particularly at high temperatures of 750 °C. Another study conducted by Zhu et al. [11] compared Cu–Mn and Mn–Co spinel coatings, deposited by electrophoretic deposition, on a SUS 430 substrate. The researchers examined phase stability, microstructural stability, and conductivity for four spinel coatings: $CuMn_2O_4$, $CuNi_{0.2}Mn_{1.8}O_4$, $MnCo_2O_4$, and $MnFe_{0.34}Co_{1.66}O_4$. The results indicated that the $CuNi_{0.2}Mn_{1.8}O_4$ spinel coating was the most suitable for use as a coating on the SUS 430 substrate in intermediate temperature solid oxide cell interconnects. This particular coating exhibited excellent sinterability, the highest conductivity, and the lowest area specific resistance (ASR). Furthermore, the study found that doping Ni in Cu–Mn spinel increased the conductivity of the spinel coating, while adding Fe in Mn–Co spinel decreased its conductivity. In a study by Zhang et al. [12] researchers investigated the effects of Ce doping on the oxidation behavior and electrical properties of Ni–Mn spinel coatings deposited on a SUS 430 substrate using electrophoretic deposition. The study focused on adding varying levels of Ce content to $NiMn_2O_4$ spinel powder and examining the resulting changes in structure, crystallinity, grain size, oxidation resistance, and electrical conductivity of the coatings. The findings revealed that adding Ce content up to 0.05 mol/L resulted in Ce-doped $NiMn_2O_4$ spinel powder with a stable structure, high crystallinity, and fine grain size. Furthermore, Ce doping in Ni–Mn spinel coatings on metallic interconnects improved oxidation resistance and electrical conductivity. Talic et al. [66] conducted a study on the influence of coating density ($MnCo_{1.7}Fe_{0.3}O_4$ spinel coating) on the oxidation resistance and chromium evaporation of the Crofer 22 APU alloy used as an interconnect. The results showed that a two-step reduction and pre-oxidation heat treatment resulted in higher coating density than an air-only heat treatment. Furthermore, dense coatings exhibited lower oxidation rates and chromium evaporation than porous coatings. Hua et al. [43] studied the oxidation behavior (in air, at 800 °C for 200 h) and electrical conductivity of $NiCo_2O_4$ spinel coatings on SUS 430 ferritic stainless steel. The presence of protective coatings improved alloy oxidation resistance and electrical conductivity. This improvement can be attributed to preventing the growth of the Cr_2O_3 layer and the formation of spinel oxide within the chromia layer by the protective coating.

Even though EPD has been used more extensively in recent times, very limited studies concerning the selection of proper suspensions/solvents have been conducted. The primary objective of this paper is to investigate the influence of suspension parameters, including stability, particle size distribution, zeta potential, and suspension conductivity, on

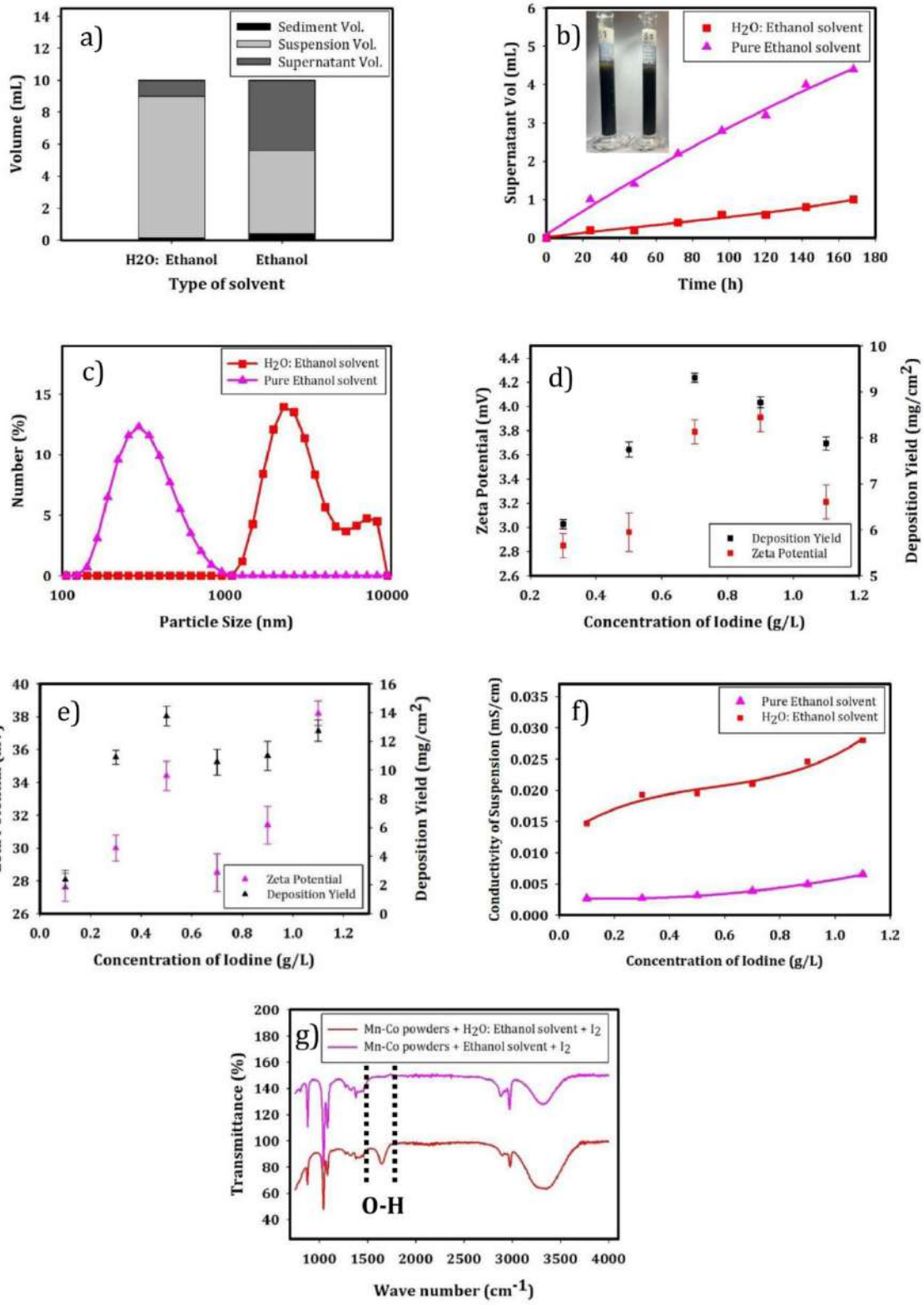

Fig. 2. a) volume of suspensions, b) volume of supernatant liquids for suspension stability; c) Particle size distribution; d) Zeta potential and deposition yield in H_2O: ethanol solvent; e) Zeta potential and deposition yield in ethanol solvent; f) Conductivity of suspension as a function of the iodine concentration; and g) FTIR-ATR spectra of Mn–Co particles.

$MnCo_2O_4$ spinel powders in H_2O: ethanol and pure ethanol solvents, and their impact on coating quality. The study seeks to comprehend the role of suspension parameters in achieving uniform and dense coatings on the substrate. Additionally, the research explores the effects of electrophoretic deposition (EPD) process parameters such as solid concentration, voltage, and deposition time on deposition yield and the quality of the Mn–Co layer. The goal is to determine the optimal EPD process conditions that result in Mn–Co coatings of the highest quality, characterized by properties like high density and uniformity. This study not only highlights the suitability of EPD for Mn–Co spinel coating on Crofer 22 APU alloy but also emphasizes the critical role of solvent choice and process parameters in determining the quality and characteristics of the deposited coatings. The resulting coating's uniformity and controlled attributes hold promising implications for interconnect applications requiring resistance to chromium migration and oxidation.

2. Experimental

2.1. Materials

In this study, Crofer 22 APU, a commercial ferritic stainless steel (FSS), was selected as the substrate for deposition. Crofer 22 APU (VDM Metals, Verdohl, Germany) consists of 22 wt% Cr, 0.45 wt% Mn, 0.1 wt % La, 0.06 wt% Ti, and less than 0.05 wt% each of Si and Al, with the balance being Fe. The sheets were cut into 20 × 20 mm^2 with a thickness of 0.3 mm. Prior to coating, the substrate was cleaned by rinsing it in acetone and ethanol (supplied by POCH, Gliwice, Poland) using an ultrasonic bath for 10 min to eliminate contaminants. For the deposition of the conductive protective coating on the metallic interconnects, a commercial $MnCo_2O_4$ spinel powder (supplied by Marion Technologie, France) was employed. Ethanol and distilled water were utilized as solvents, with iodine as a disperser, to prepare the Mn–Co suspension intended for the electrophoretic deposition process.

2.2. Preparation of suspension

Stable Mn–Co suspensions were investigated using two different solvents: EtOH: H_2O (60:40 %Vol) and pure ethanol, with a solid concentration of 10 g/L. Iodine was added to the Mn–Co suspension to enhance the surface charge. The stability of the Mn–Co suspension was evaluated by pouring it into graduated cylinders and measuring the volume of transparent liquid formed after 7 days. In Fig. 1a, a schematic illustration depicts the stability mechanism through which Mn–Co particles are stabilized via electrostatic and van der Waals forces. In the absence of iodine, Mn–Co particles cannot absorb the necessary H^+ ions to remain stable in the suspension. However, the addition of iodine enables the solvent to generate protons during ultrasonic treatment, which the Mn–Co particles can absorb to create a diffuse-double layer on their surface. This layer increases the electrostatic repulsion force and promotes the stability of the particles in the suspension. The stability of the Mn–Co suspension was further assessed by analyzing particle size distribution and zeta potential in various solvents. A NanoZeta Malvern Dynamic Light Scattering device (Zetasizer nano ZS, Malvern) was used to measure the particle size and zeta potential of the Mn–Co suspension in different solvents, while keeping the solid concentration constant at 10 g/L and varying the iodine concentration from 0.1 to 1.1 g/L. The electrical conductivity of H_2O: ethanol and pure ethanol solvents, with a solid concentration of 10 g/L Mn–Co and iodine concentrations ranging from 0.1 to 1.1 g/L, was also studied. The optimal solid concentration of Mn–Co spinel in H_2O: ethanol and pure ethanol solvents was determined by varying the solid concentration from 5 to 40 g/L, while keeping the iodine concentration constant at 0.5 g/L. After adding Mn–Co spinel powders and iodine to the solvents, the suspension was homogenized using an ultrasonic bath for 20 min.

2.3. Electrophoretic deposition

To deposit Mn–Co spinel particles on the substrate, the Crofer 22 APU served as the cathode and anode, positioned vertically and in parallel during the EPD process. The distance between the anode and cathode in the cell was maintained at 1 cm. The schematic of the cell used for Mn–Co powder deposition is shown in Fig. 1b. The deposition yield of the Mn–Co coating on the Crofer 22 APU was investigated at different voltages and deposition times. Fig. 1C illustrates the mechanism of electrochemical coagulation, examining the migration of positively charged particles toward the cathode within an EPD cell. After coating, Mn–Co green layers were dried at room temperature for 24 h and sintered at 800 °C for 2 h with a heating rate of 3 °C/min in an air atmosphere.

2.4. Characterization

The surface and cross-sections of the Mn–Co coatings were analyzed using a scanning electron microscope (SEM) with an acceleration voltage of 20 kV. FTIR spectra of H_2O: ethanol and ethanol solvents were acquired using an FT-IR spectrometer (Spectrum 100, PerkinElmer), covering the range of 750–4000 cm^{-1}. The instrument was equipped with an attenuated total reflection (ATR) module, employing a diamond with one reflection at a 45° angle. All measurements were performed at room temperature. The confocal microscope (Olympus LEXT OLS4000) was employed to examine the surface roughness and morphology of the sintered Mn–Co spinel coating.

3. Results and discussion

3.1. Parameters related to the suspension

3.1.1. Stability of suspension

In Fig. 2a, suspensions are observed over 7 days, tracking the volume of supernatant liquid and sedimentation. The Mn–Co powders remain stable in different solvents for up to 5 h. However, as time progresses, the volume of supernatant liquid increases, indicating a larger portion of liquid on top of the graduated cylinder. This suggests that the positively charged surfaces of the Mn–Co suspended particles lose their charge, leading to gravitational forces overpowering the repulsive forces between the particles. Consequently, sedimentation occurs after 5 h. Fig. 2b presents a seven-day evaluation of the volume of supernatant liquid in different suspensions. It was observed that the volume of supernatant liquid in ethanol solvent is greater than that in H_2O: ethanol solvent. This difference can be attributed to the higher amount of released H^+ ions in H_2O: ethanol solvent.

Fig. 2c presents the particle size distribution of Mn–Co spinel powders in H_2O: ethanol and ethanol solvents. The particle size distribution varies depending on the solvent and disperser used, indicating the presence of particle agglomeration in the suspension. In H_2O: ethanol solvent, a bimodal distribution of Mn–Co particles suggests the existence of agglomerated particles. Consequently, sedimentation occurs as the gravitational force overcomes the repulsive force between the agglomerated Mn–Co particles. Furthermore, it is evident that the coating of the agglomerated Mn–Co particles on the substrate is not uniform and dense. In contrast, the narrow monomodal distribution of Mn–Co particles in pure ethanol solvent indicates that the particles in the suspension have similar sizes. The average particle size of Mn–Co suspended in H_2O: ethanol and pure ethanol suspensions is 2.8 and 0.37 μm, respectively. Consequently, to achieve a uniform and dense Mn–Co coating on the substrate through EPD, it is crucial to prepare a well-dispersed Mn–Co suspension to minimize shrinkage during the sintering process. As a result, Mn–Co particles in pure ethanol solvent are better suited for electrophoretic deposition.

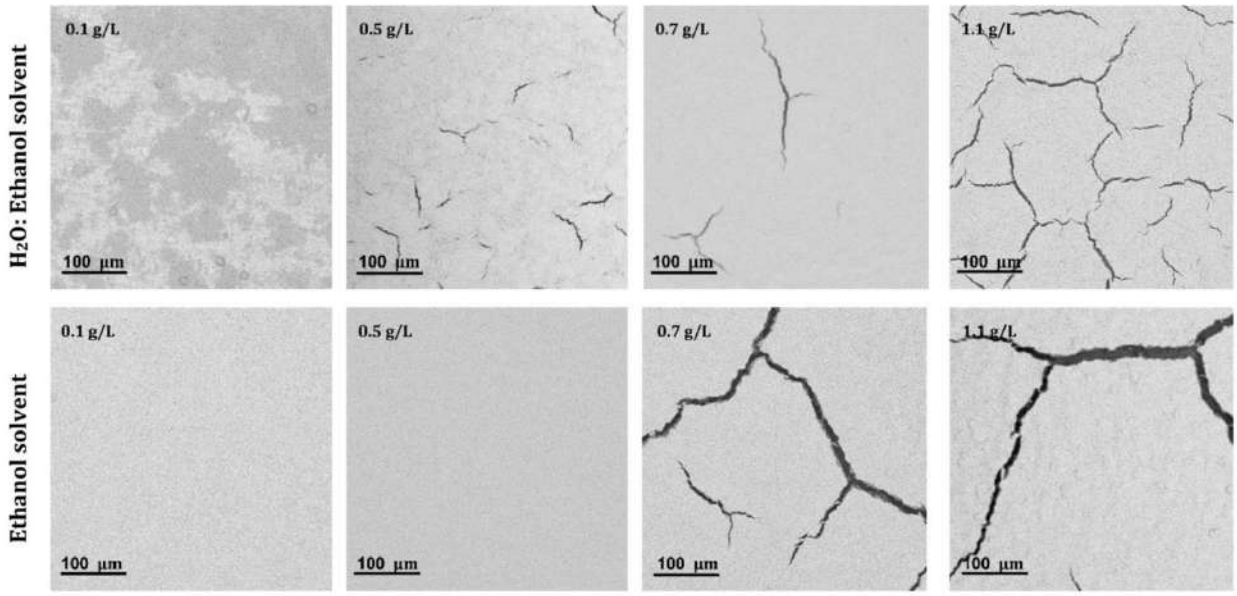

Fig. 3. SEM images of the surface of sintered Mn–Co spinel coatings subjected to oxidation treatment at 800 °C for 2 h with a solid concentration of 10 g/L in H_2O: ethanol and pure ethanol solvents, each at different iodine concentrations (0.1, 0.5, 0.7, and 1.1 g/L).

3.1.2. Zeta potential

Fig. 2d and e illustrate the zeta potential of Mn–Co particles and the deposition yield in H_2O: ethanol and pure ethanol solvents, respectively, as a function of iodine concentration ranging from 0.1 to 1.1 g/L. According to Equations (1) and (2), the reaction of iodine with pure ethanol and H_2O: ethanol solvents produce H^+ ions in the suspension, as outlined below:

$$C_2H_5OH + I_2 \rightarrow C_2H_5OI + I^- + H^+ \quad (1)$$

$$C_2H_5OH + H_2O + I_2 \rightarrow C_2H_5OI + I^- + 2H^+ \quad (2)$$

Mn–Co particles in the solvent absorb protons produced by iodine, leading to the formation of a positively charged surface around the particles. In Fig. 2d and e, it is observed that as the iodine concentration increases, the zeta potential rises due to the greater release of H+ ions in the Mn–Co suspension. The zeta potential of Mn–Co particles in the H_2O: ethanol solvent is lower due to the additional released H^+ ions in the suspension, which reduce the thickness of the electrical double layer. The zeta potential of Mn–Co particles in the H_2O: ethanol solvent increases from +0.76 to +3.9 mV as the iodine concentration in the suspension rises from 0.1 to 0.9 g/L. However, at iodine concentrations greater than 0.9 g/L, the zeta potential decreases from +3.9 to +3.2 mV. On the other hand, the zeta potential of Mn–Co particles in pure ethanol increases from +27 to +34 mV with an increase in the iodine concentration from 0.1 to 0.5 g/L. However, beyond 0.5 g/L of iodine, the zeta potential decreases from +34 to +28 mV. It is observed that the zeta potential tends to decrease when the quantity of released H^+ ions in the suspension increases, resulting in the compression of the electrical double layer. Furthermore, the amount of Mn–Co deposition yield increases with an increase in the zeta potential. Moreover, the deposition yield of Mn–Co particles in pure ethanol is significantly higher compared to that in the H_2O: ethanol solvent due to its higher zeta potential.

3.1.3. Conductivity of suspension

Fig. 2f presents the conductivity of Mn–Co particles in H_2O: ethanol and pure ethanol solvents as a function of iodine concentration, ranging from 0.1 to 1.1 g/L. With an increase in iodine concentration, the conductivity of the Mn–Co suspension exhibits an almost linear increase, attributed to the greater release of H^+ ions in the solvents. Furthermore, the conductivity of Mn–Co particles in H_2O: ethanol solvent is significantly higher compared to that in pure ethanol solvent. This difference can be explained by the excess amount of released H^+ and OH^- ions in H_2O: ethanol solvent. Consequently, it appears that as the amount of free H^+ and OH^- ions in the suspension increases, the deposition yield of Mn–Co particles on the substrate decreases. The presence of free H^+ and OH^- ions in the suspension carries electrical charges. Since the mobility of H^+ and OH^- ions is considerably higher than that of Mn–Co particles, the deposition yield is lower.

To further evaluate the additional presence of OH^- and H^+ ions in H_2O: ethanol solvent compared to pure ethanol, FTIR spectra were used. Fig. 2g displays the FTIR spectra of Mn–Co particles in H_2O: ethanol and pure ethanol solvents. By comparing the FTIR-ATR spectra, the addition of H_2O to the ethanol solvent results in an additional peak at 1642 cm^{-1}, attributed to the presence of OH^- ions. This indicates that H2O: ethanol solvent contains more H^+ ions compared to pure ethanol solvent. The presence of an OH^- peak at 1642 cm^{-1} provides evidence of greater H^+ adsorption on Mn–Co particles, observed at 3364 cm^{-1} with significantly higher intensity than the ethanol solvent spectrum. The wave numbers 3364 cm^{-1}, 2968 cm^{-1}, and 2877 cm^{-1} correspond to the stretching vibration of OH^- bonds. The wave number 1377 cm^{-1} is associated with the bending vibration of OH^- bonds, whereas the wave numbers 1050 cm^{-1} and 1091 cm^{-1} are indicative of the stretching vibration of C–O bonds. The wave number 874 cm^{-1} is related to the stretching vibration of C–H bonds. According to Equations (1) and (2), the addition of H_2O to the ethanol solvent leads to an increased concentration of H^+ and OH^- ions in the suspension, resulting in higher conductivity of the H_2O: ethanol suspension compared to pure ethanol (as shown in Fig. 2f). The increased H^+ ions also decrease the thickness of the diffuse double layer as Mn–Co particles in the suspension absorb more H^+. As a result, the zeta potential of Mn–Co particles in the H_2O: ethanol solvent is lower than that of Mn–Co particles in the ethanol solvent (as shown in Fig. 2d and e). Additionally, the H_2O: ethanol solvent contains a significant amount of OH^- ions, which are absorbed by Mn–Co particles during the suspension preparation. This leads to the deposition of Mn–Co particles on the surface of the anode electrode, affecting the morphology of the Mn–Co coating on the cathode electrode.

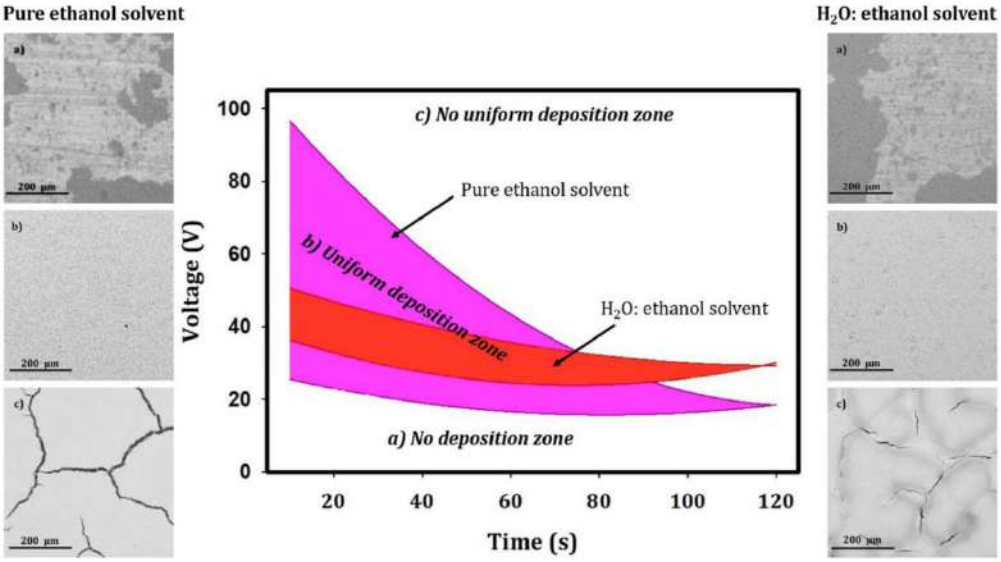

Fig. 4. The windows in which uniform and non-uniform coatings can be obtained during the electrophoretic deposition (EPD) of Mn–Co suspension in H_2O: ethanol and pure ethanol solvents: a) no deposition zone, b) smooth and uniform deposition zone, and c) non-uniform deposition zone.

3.1.4. Effect of iodine concentration on the microstructure

Fig. 3 depicts SEM images of the surface of sintered Mn–Co spinel coatings, deposited for 90 s at a voltage of 70V in H_2O: ethanol and pure ethanol solvents at different iodine concentrations. The results indicate that at an iodine concentration of 0.1 g/L in H_2O: ethanol solvent, the Mn–Co particles do not fully cover the surface due to low zeta potential. However, increasing the iodine concentration to 1.1 g/L results in the appearance of cracks on the surface of the Mn–Co coating. This phenomenon may be attributed to the agglomeration of Mn–Co particles in the suspension, leading to a less homogeneous coating on the substrate. At high iodine concentrations, many cracks appear on the coating's surface due to the high deposition yield on the substrate. Nonetheless, at an iodine concentration of 0.7 g/L, fewer cracks appear on the surface, which could be due to the higher zeta potential, indicating a better dispersion of the particles in the suspension. In pure ethanol solvent, a uniform, smooth, and crack-free coating is obtained when using iodine concentrations of 0.1 and 0.5 g/L. The Mn–Co particles are evenly dispersed in the suspension, creating a uniform and dense coating on the substrate. However, the zeta potential of Mn–Co particles is significantly higher at an iodine concentration of 0.5 g/L compared to 0.1 g/L, resulting in a denser coating. Thus, Mn–Co suspension with 0.5 g/L iodine concentration is chosen to achieve a uniform and crack-free coating on the substrate in this present study. Moreover, increasing the iodine concentration from 0.5 to 1.1 g/L results in the formation of cracks on the coating surface due to the high deposition rate.

3.2. Parameters related to the process

3.2.1. Quality of Mn–Co coating

Fig. 4 depicts a graph illustrating the variation of applied voltage with deposition time for the uniform deposition of Mn–Co in H_2O: ethanol and pure ethanol solvents. This experiment aims to determine a suitable range of voltage and deposition time parameters for depositing uniform Mn–Co coatings. In both solvents, the behavior of Mn–Co coatings varies significantly in three different zones. In zone a, there is a lower limit below which no deposition occurs. It appears that when the voltage is low, the motion of Mn–Co particles in the suspension is inadequate to reach the opposite electrodes and deposit on the substrate. Additionally, increasing the deposition time does not effectively promote the deposition of Mn–Co particles from the suspension onto the substrate, likely due to the insufficient mobility of the particles in the suspension. Furthermore, the morphology of the coatings reveals that the Mn–Co coatings are not entirely uniform on the substrate. In the voltage and deposition time range of zone b, uniform and crack-free Mn–Co coatings can be achieved in both suspensions. It appears that Mn–Co particles possess enough mobility and time to uniformly and smoothly deposit onto the substrate. The microstructure of coatings shows that Mn–Co coatings are smooth, uniform, and crack-free on substrates. In zone c, it is observed that deposits tend to be non-uniform and contain cracks in both suspensions when the upper limit is exceeded. Increasing the voltage and time results in thicker Mn–Co coatings on the substrate. Subsequently, during solvent drying, nano-cracks develop on the surface of Mn–Co coatings. These nano-cracks then grow and transform into micro-cracks on the coating's surface after sintering at 800 °C for 2h in static air. When the deposition time is short, the range of voltage is wider compared to longer deposition times in both suspensions. This makes it easier to control the deposition yield and achieve coatings that are uniform and free of cracks. As a result, voltage and deposition time in the EPD process play a crucial role in obtaining smooth, uniform, and crack-free coatings.

3.2.2. Effect of applied voltage and deposition time

3.2.2.1. Deposition yield. Fig. 5a shows the variation in deposition yield versus deposition time from 30 to 180 s at different voltages (50, 70, and 90 V) in H_2O: ethanol and pure ethanol solvents with a solid concentration of 10 g/L Mn–Co and 0.5 g/L iodine. It appears that the deposition yield variation versus deposition time in H_2O: ethanol and pure ethanol solvents is roughly linear up to 120 s, after which non-linear variations are observed. This is likely due to the formation of an insulating deposition layer on the substrate surface, hindering further deposition. The deposition yield of the Mn–Co suspension in both solvents increases with the deposition time and voltage. This is likely because increasing the deposition time allows more Mn–Co particles to deposit onto the substrate, while increasing the voltage exerts more force on the particles, enabling more particles to reach the electrode simultaneously, resulting in a higher deposition yield.

3.2.2.2. Electrophoretic velocity. Electrophoretic velocity is measured to understand and control the deposition process, and the deposition

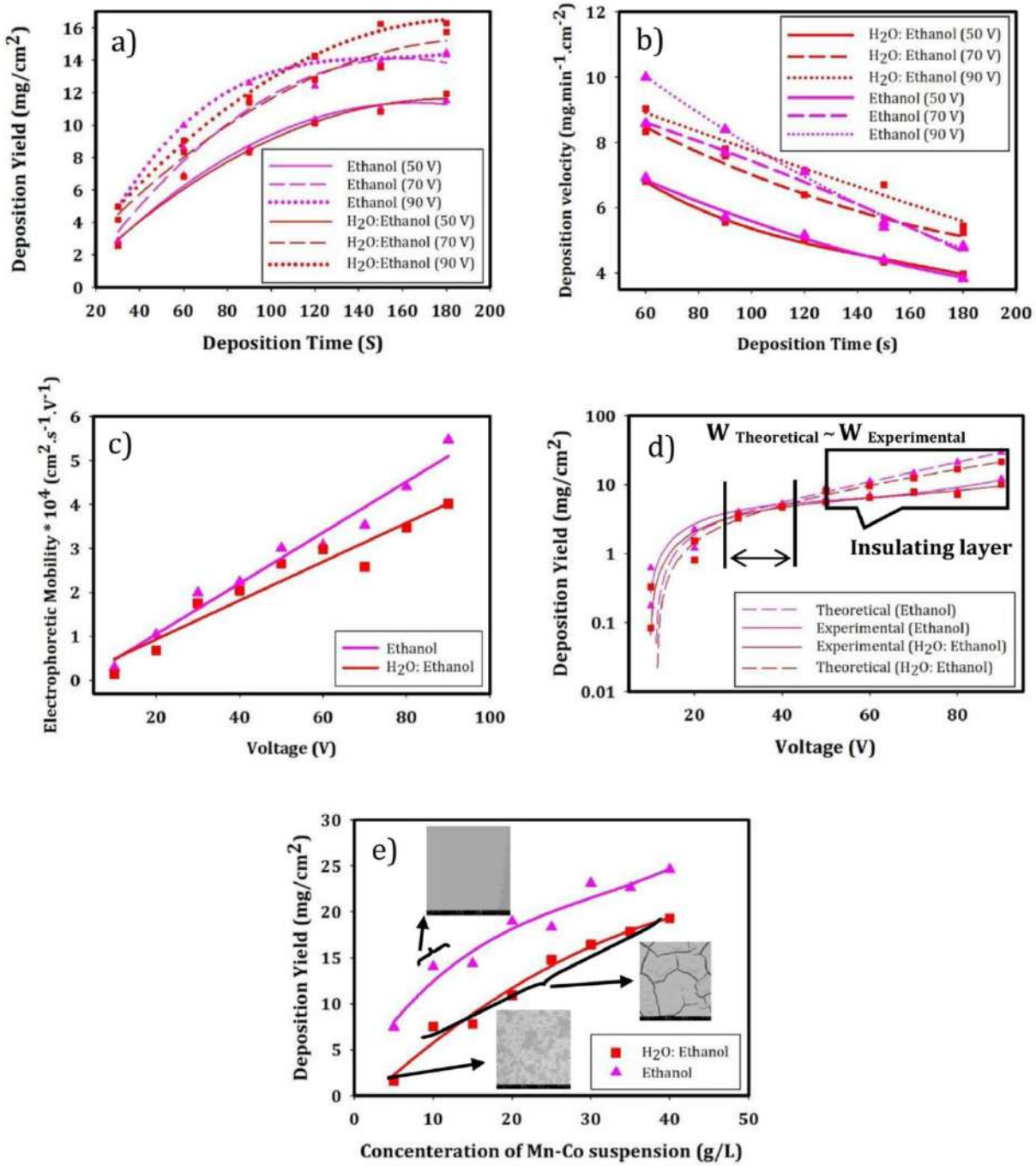

Fig. 5. a) Deposition yield, and b) Deposition velocity of Mn–Co particles versus deposition time at different voltages; c) Electrophoretic mobility, and d) Deposition yield (Theoretical and Experimental) of Mn–Co particles versus applied voltage; and e) Deposition yield variations of Mn–Co suspension as a function of solid concentration in H_2O: ethanol and pure ethanol solvents.

velocity (V) can be calculated by the following equation [67].

$$V = \frac{M_{t2} - M_{t1}}{A\Delta t} \tag{3}$$

Where V is the deposition velocity (mg·min^{-1} cm^{-2}), Δt (min) is the time interval, A (cm^2) is the deposition area, and M_{t2} and M_{t1} are the deposition masses at t2 and t1, respectively. Fig. 5b shows the variation in deposition velocity versus deposition time at different voltages in H_2O: ethanol and pure ethanol solvents. Regardless of the suspension media employed, the deposition velocity experiences a decline as time progresses at different voltages. This decrease is attributed to the growth of an insulating layer, resulting in a reduction in the conductive surface during the EPD process. A higher deposition velocity indicates a faster accumulation rate of discharged particles on Crofer 22 APU. However, it is observed that higher voltages result in reduced coating uniformity in both suspensions. The suspension prepared using ethanol solvent displays a higher deposition velocity compared to the suspension prepared with H_2O: ethanol solvent due to its elevated zeta potential.

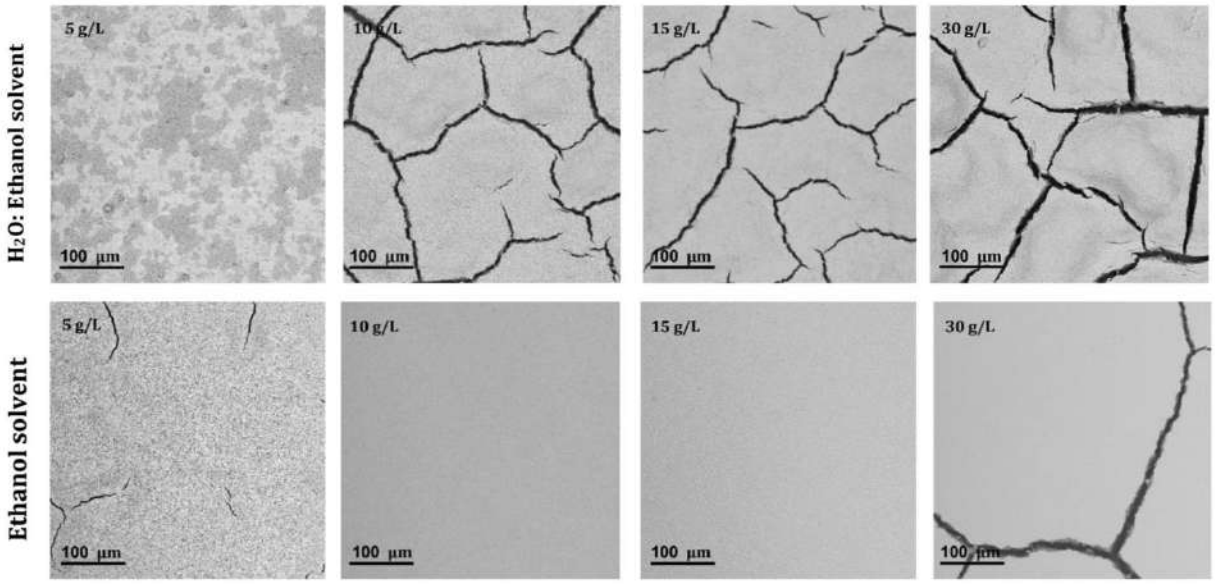

Fig. 6. SEM images of the surface of sintered Mn–Co spinel coatings with an iodine concentration of 0.5 g/L in H_2O: ethanol and pure ethanol solvents at various solid concentrations (5, 10, 15, and 30 g/L Mn–Co for each solvent).

Additionally, the deposition velocity in ethanol solvent at 90 V is greater than at 50 V and 70 V. This is because, at higher voltages, the formation of an insulating layer on the substrate occurs more rapidly.

3.2.2.3. Electrophoretic mobility. In order for particles to be effectively deposited, their electrophoretic mobility needs to be strong enough to overcome gravitational forces. The equation for determining the electrophoretic mobility of particles, derived from the Sarkar and Nicholson model, can be expressed as follows [68,69]:

$$\mu = \frac{Ln\left[1 - \frac{m_t}{m_0}\right]}{-At} \tag{4}$$

Where μ is the electrophoretic mobility ($cm^2 \cdot s^{-1}\ V^{-1}$), L is the distance between the anode and cathode (cm), A is the deposition area (cm^2), t is the deposition time, m_t is the deposition mass at time t, and m_0 is the initial deposition mass. Assuming that all particles reaching the electrode are deposited on its surface, equation (4) holds true. Fig. 5c illustrates the electrophoretic mobility of Mn–Co particles in H_2O: ethanol and pure ethanol solvents versus applied voltage for 1 min. When the voltage between the anode and cathode is increased, it leads to a growth in electrophoretic mobility. This happens because the increased voltage exerts a stronger force on the charged particles, causing them to move faster within the suspension. Comparing the electrophoretic mobility of Mn–Co particles in different solvents reveals that the electrophoretic mobility is higher for Mn–Co particles in pure ethanol solvent compared to H_2O: ethanol solvent. This difference is attributed to the thicker diffuse-double layer of Mn–Co particles in pure ethanol solvent. Additionally, at low voltages, the electrophoretic mobility of Mn–Co particles in both solvents is similar, but as the voltage increases, a significant difference between the two lines becomes apparent. At a voltage of 10 V in pure ethanol solvent, the Mn–Co particles exhibit a slow electrophoretic mobility ($0.29 \times 10^4\ cm^2 \cdot s^{-1}\ V^{-1}$), resulting in incomplete coverage of the substrate surface. However, by increasing the voltage to 20 V, the electrophoretic mobility of Mn–Co particles ($1.04 \times 10^4\ cm^2 \cdot s^{-1}\ V^{-1}$) increases, allowing for a uniform coating of Mn–Co on the substrate surface. In H2O: ethanol solvent, even at a voltage of 20 V, the substrate surface is not completely coated due to the relatively low electrophoretic mobility of Mn–Co particles ($0.68 \times 10^4\ cm^2 \cdot s^{-1}\ V^{-1}$). However, by further increasing the voltage to 30 V, the electrophoretic mobility of Mn–Co particles in H_2O: ethanol solvent increases ($1.77 \times 10^4\ cm^2 \cdot s^{-1}\ V^{-1}$), allowing for a uniform coating to be achieved on the substrate surface. Thus, to ensure complete coverage of the substrate surface, a minimum voltage of 20 V is necessary for pure ethanol solvent, while a minimum voltage of 30 V is required for H_2O: ethanol solvent.

3.2.2.4. Theoretical and experimental deposition yield. equation (5), derived from the Hamaker model, is used for estimating the deposition mass on the substrate in the EPD process and can be expressed as follows [70]:

$$W = f \int_{t_i}^{t_f} \mu E S C_s dt \tag{5}$$

Where W is the deposition mass (g), f is the efficiency factor ($f \leq 1$; assuming that all particles reaching the electrode are deposited on its surface, then $f = 1$), μ is the electrophoretic mobility ($cm^2 \cdot s^{-1} \cdot V^{-1}$), E is the electrical field (V/cm), C_s is the solid concentration (g/cm^3), S is the deposition area (cm^2), and t is the deposition time (s). By assuming that μ, E, C_s, and S remain constant over time, equation (5) is simplified as follows [62].

$$W = \mu E S C_s\, t \tag{6}$$

Fig. 5d displays the deposition yields of Mn–Co particles in ethanol and H_2O: ethanol solvents, as determined through both theoretical calculations and experimental measurements. In terms of theoretical and experimental findings, the deposition rate in both solvents is high between 10 V and 20 V because there is no insulating layer present on the substrate. Additionally, at voltage levels of 10 V and 20 V in ethanol and H_2O: ethanol solvents, respectively (as shown in Fig. 5c), the Mn–Co particles do not cover the entire substrate surface. This is because there isn't enough voltage to move the particles to the opposite electrode for deposition on the substrate. However, as the voltage is increased from 20 V to 90 V, the deposition rate decreases due to the formation of an insulating layer on the substrate. Beyond the voltage of 50 V, there is a substantial disparity in the deposition yield, as indicated by both theoretical and experimental data. This difference can be attributed to the rapid formation of an insulating layer at higher voltage levels.

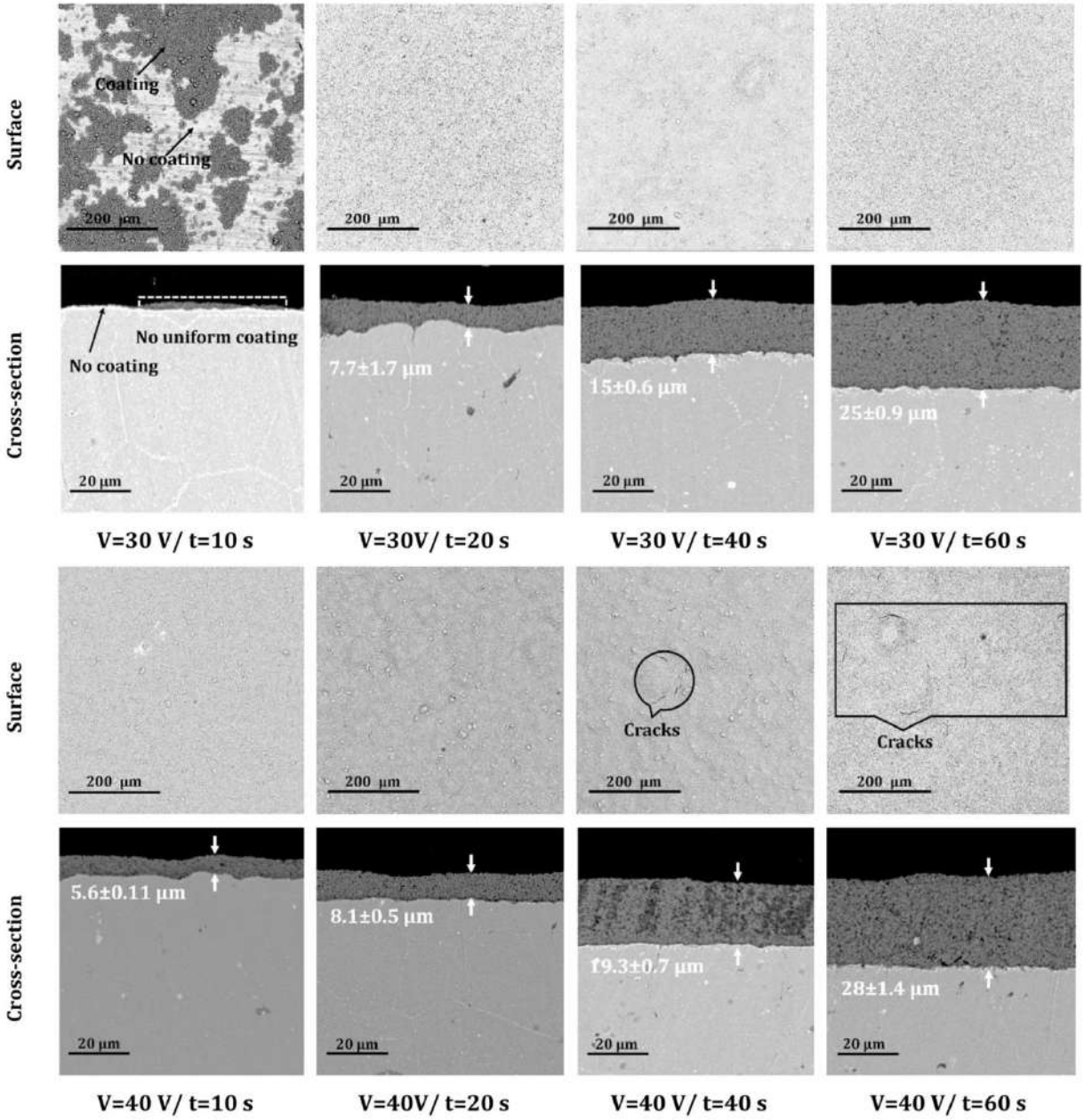

Fig. 7. SEM images of the Mn–Co sintered coating surface and cross-section at different voltages and deposition times in the H_2O: ethanol solvent.

Nevertheless, in the voltage range of 20 V–50 V, the deposition yield demonstrates negligible fluctuations, aligning with both theoretical predictions and experimental results. Consequently, it is feasible to calculate the deposition yield within this range.

3.2.3. *Concentration of solid and morphology of deposit*

Fig. 5e demonstrates the effect of solid concentration on the deposition yield of Mn–Co particles on a substrate in H_2O: ethanol and pure ethanol solvents. The results show that increasing the solid concentration from 5 g/L to 40 g/L of Mn–Co leads to an increase in deposition yield in both solvent systems. However, it is observed that the amount of deposition yield is much higher in pure ethanol compared to the H_2O: ethanol solvent. Furthermore, the quality of the coating in both solvent systems decreases as the solid concentration increases beyond 10 g/L and 15 g/L in H_2O: ethanol and pure ethanol solvents, respectively. The increased solid concentration of Mn–Co particles can lead to agglomeration in both H_2O: ethanol and pure ethanol solvents, resulting in thicker and non-uniform coatings. Similarly, in the pure ethanol solvent, the increased solid concentration can lead to the formation of cracks in the coating, contributing to the non-uniformity of the coating. These factors together can result in reduced coating density and quality. The deposition rate of Mn–Co particles is higher at higher concentrations, promoting particle agglomeration and reducing coating density. On the other hand, if the concentration is too low, below 5 g/L, the deposition rate may be very low, resulting in inadequate coating formation. Therefore, in this study, a concentration of 10 g/L Mn–Co particles is chosen as it provides a sufficient deposition rate while minimizing the risk of particle agglomeration and ensuring the formation of dense and uniform Mn–Co coatings on the substrate. Fig. 6 displays SEM images of the surface of sintered Mn–Co spinel coatings deposited using H_2O:

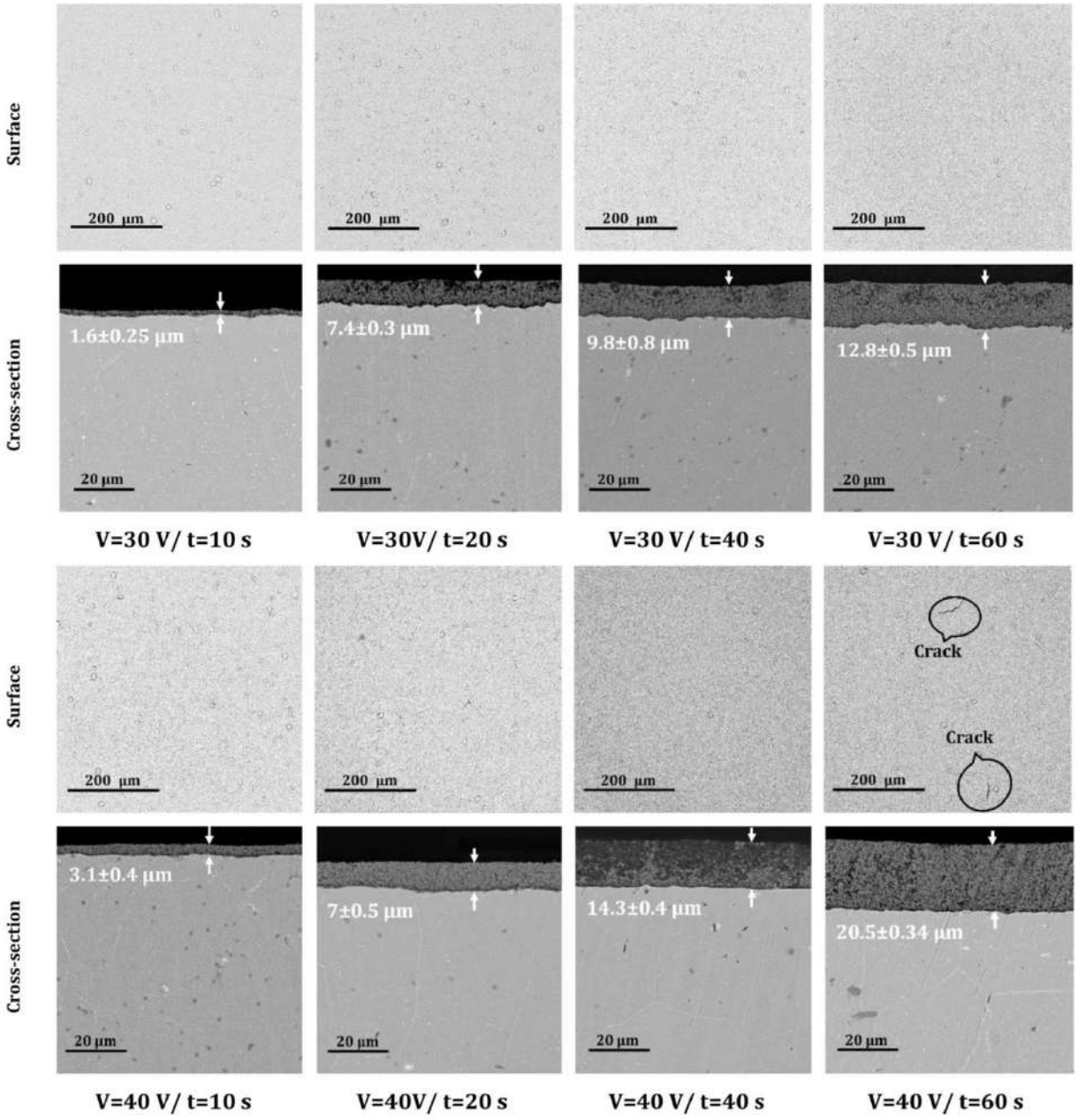

Fig. 8. SEM images of the Mn–Co sintered coating surface and cross-section at different voltages and deposition times in pure ethanol solvent.

ethanol solvent and compared to pure ethanol solvent at various solid concentrations. The results show that when using H_2O: ethanol as a solvent at a low solid concentration (5 g/L), there is a low deposition yield, leading to incomplete coverage of the substrate by Mn–Co particles in the suspension. Increasing the solid concentration (from 5 up to 40 g/L) leads to particle agglomeration, resulting in cracks on the coating surface and preventing the formation of a dense coating. During solvent drying, some nano cracks form on the coating, which later grow into larger micro-cracks during sintering at 800 °C for 2 h in static air. The solid concentration of the ethanol solvent appears to have a significant effect on the quality of the Mn–Co coating on the substrate. At a low solid concentration of 5 g/L, the coating is not dense, and there are small cracks on the surface. However, at higher solid concentrations of 10 g/L and 15 g/L, a uniform coating is formed on the substrate. Based on the results, the optimum solid concentration for achieving a sufficient deposition rate and a uniform and dense coating on the substrate is 10 g/L. At this concentration, the deposition yield is reasonable, and the quality of the coating is acceptable. It is also worth noting that increasing the solid concentration beyond 15 g/L leads to a higher deposition yield but results in cracks on the surface of the coating. This suggests that there is an upper limit for the ethanol solvent's solid concentration that can be used for depositing a high-quality Mn–Co coating on the substrate.

3.2.4. *Morphology of Mn–Co coating*

To prevent the formation of cracks on the Mn–Co coating surface, it is necessary to reduce both the applied voltage and the deposition time. This reduction results in a decrease in the thickness of the Mn–Co layer,

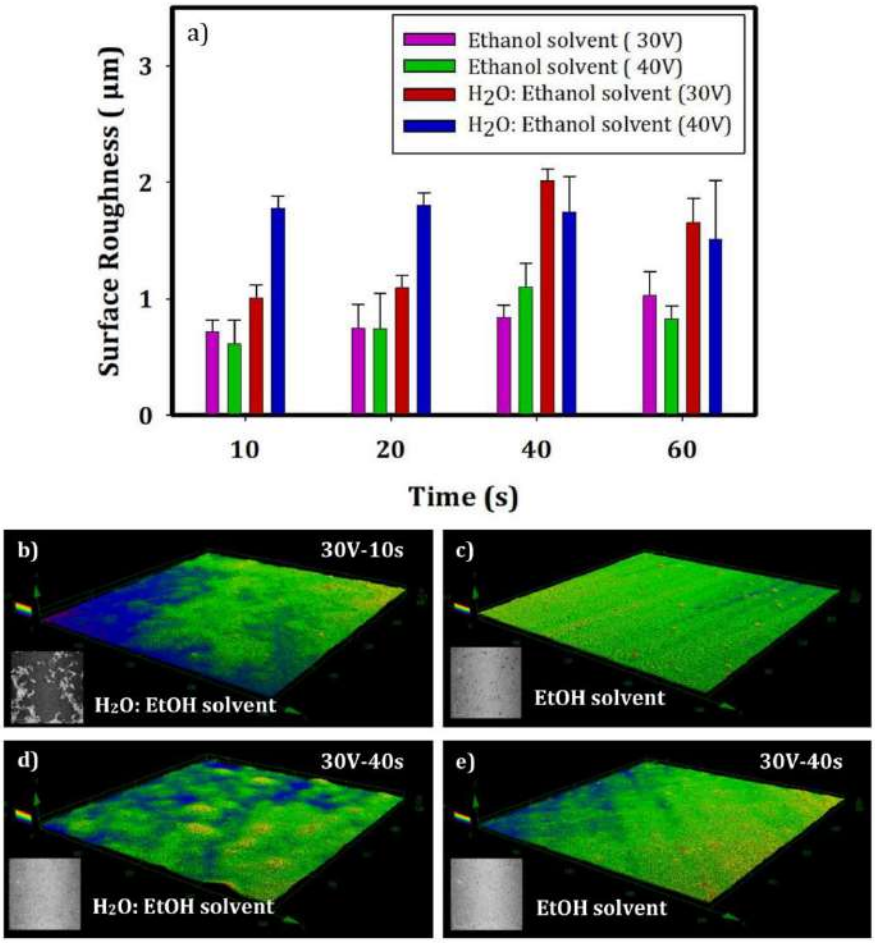

Fig. 9. a) Surface roughness of Mn–Co coatings at different voltages and deposition times in H_2O: ethanol and ethanol solvents; b, c, d, and e) 3D and 2D confocal microscopy images of sintered Mn–Co coatings.

ultimately leading to the achievement of a uniform coating with no cracks on the substrate. SEM images in Figs. 7 and 8 depict surface and cross-sectional views of sintered Mn–Co spinel coatings deposited at various voltages and deposition times in H_2O: ethanol and pure ethanol solvents. A comparison of Figs. 7 and 8 reveals that when using H_2O: ethanol solvent at 30V for 10s, the Mn–Co particles fail to cover the entire substrate due to insufficient time for complete surface coating. In both solvents, an increase in voltage from 30 to 40V enhances the mobility of Mn–Co particles in the solvent, resulting in an increased thickness of the Mn–Co coating on the substrate within the same deposition time. Similarly, extending the deposition time from 20 to 60s, while maintaining the same applied voltage, provides more opportunities for Mn–Co particles to deposit onto Crofer 22 APU. Consequently, the thickness of the Mn–Co coating on the substrate increases, leading to the presence of cracks in the Mn–Co coating layer. However, uniform Mn–Co coatings with strong adhesion between the coating and Crofer 22 APU are successfully achieved at various voltages and deposition times. Based on the observed coating thickness on the substrate, it can be concluded that applying voltages of 30V and 40V for a deposition time of 10s and 20s is appropriate for creating a protective layer on Crofer 22 APU in both H_2O: ethanol and pure ethanol solvents.

3.2.5. *Surface roughness of Mn–Co coating*

Fig. 9 illustrates the surface roughness and 3D and 2D confocal microscopy images of Mn–Co coatings at different voltages and deposition times in both solvents. The results indicate that the surface roughness of the Mn–Co coating is higher when deposited in the H_2O: ethanol solvent compared to the pure ethanol solvent at the same voltage and deposition time (as shown in Fig. 9d and e). This difference can be attributed to the agglomeration of Mn–Co powders in the H_2O: ethanol solvent, as depicted in Fig. 2c. In both solvents, extending the deposition time leads to an increase in the surface roughness of the Mn–Co coating. This phenomenon is explained by the fact that, at longer deposition times, Mn–Co particles in the suspension tend to deposit in specific preferred areas. Additionally, coarser and agglomerated particles have a higher chance of being deposited, resulting in an elevation of the surface roughness of the Mn–Co coating (as indicated in Fig. 9c and e). In H_2O: ethanol solvents, the surface roughness of the Mn–Co spinel coating becomes more pronounced when the voltage is raised from 30 to 40V at a shorter deposition time. This is attributed to the tendency of Mn–Co particles to agglomerate in the H_2O: ethanol solvent, making even a slight voltage difference have a significant impact on the surface roughness [24,71]. On the other hand, in pure ethanol solvent, the surface roughness of the Mn–Co coatings remains relatively unchanged with an increase in voltage, taking into account the standard deviation. The results of the 3D topography and surface roughness of the Mn–Co coating demonstrate that when using pure ethanol solvent, consistent and smooth layers are achieved. Furthermore, with a shorter deposition time, there is an increased likelihood of the Mn–Co particles in ethanol solvent forming a more homogeneous coating on the substrate.

4. Conclusion

In this study, electrophoretic deposition (EPD) proved to be a promising method for depositing the Mn–Co spinel coating on the surface of the Crofer 22 APU alloy. Suspension and process parameters were systematically evaluated to achieve a coating that is uniform, dense, smooth, and free of cracks. The analysis of particle size distribution, suspension stability, zeta potential, and suspension conductivity revealed that Mn–Co particles dispersed in pure ethanol solvent were well-suited for the deposition process. The stability behavior of Mn–Co particles in both H_2O: ethanol and ethanol suspensions appeared similar for a duration of 5 h. However, the results indicated that Mn–Co powders exhibited significantly greater agglomeration (approximately 7 times) when suspended in the H_2O: ethanol solvent compared to pure ethanol solvent. Additionally, the deposition yield was considerably higher in ethanol solvent than in H_2O: ethanol solvent, attributed to its elevated zeta potential. The conductivity of the H_2O: ethanol suspension was reported to be higher than that of pure ethanol, attributed to the additional presence of H^+ and OH^- ions in the suspension. Smooth and uniform Mn–Co spinel coatings in pure ethanol solvent were achieved at solid concentrations of 10 and 15 g/L. Microstructure and quality analysis of sintered Mn–Co coatings during oxidation treatment at 800 °C for 2 h showed that the coatings exhibited a uniform, smooth, and crack-free surface with high density. These desirable characteristics were obtained by depositing the coatings using pure ethanol as the solvent at applied voltages of 30 and 40V for 20 s, with a solid concentration of 10 g/L of Mn–Co particles and 0.5 g/L of iodine. The thickness and surface roughness of sintered Mn–Co coatings at applied voltages of 30 for 20 s in pure ethanol solvent were measured to be 7.4 ± 0.3 μm and 0.75 ± 0.5 μm, respectively.

CRediT author statement

O. Ekhlasiosgouei: Methodology, Investigation, Formal analysis, Data curation, Writing– original draft, Federico Smeacetto: Data curation, Writing-review and editing, and S. Molin: Conceptualization, Supervision, Writing-review and editing.

Declaration of competing interest

The authors declare that they have no known competing financial interests or personal relationships that could have appeared to influence the work reported in this paper.

References

[1] Zanchi E, Sabato AG, Molin S, Cempura G, Boccaccini AR, Smeacetto F. Recent advances on spinel-based protective coatings for solid oxide cell metallic interconnects produced by electrophoretic deposition. Mater Lett 2021;286:129229. https://doi.org/10.1016/j.matlet.2020.129229.

[2] Yang Z, Walker MS, Singh P, Stevenson JW, Norby T. Oxidation behavior of ferritic stainless steels under SOFC interconnect Exposure conditions. J Electrochem Soc 2004;151:B669. https://doi.org/10.1149/1.1810393.

[3] Talic B, Venkatachalam V, Hendriksen PV, Kiebach R. Comparison of MnCo2O4 coated Crofer 22 H, 441, 430 as interconnects for intermediate-temperature solid oxide fuel cell stacks. J Alloys Compd 2020;821:153229. https://doi.org/10.1016/j.jallcom.2019.153229.

[4] Vazquez-Navarro MD. Candidate interconnect materials: oxidation study of a Ni-based superalloy in pure oxygen at 800°C. ECS Proceedings Volumes 1999;19:749–58. https://doi.org/10.1149/199919.0749pv. 1999.

[5] Wu J, Liu X. Recent development of SOFC metallic interconnect. J Mater Sci Technol 2010;26:293–305. https://doi.org/10.1016/S1005-0302(10)60049-7.

[6] Shaigan N, Qu W, Ivey DG, Chen W. A review of recent progress in coatings, surface modifications and alloy developments for solid oxide fuel cell ferritic stainless steel interconnects. J Power Sources 2010;195:1529–42. https://doi.org/10.1016/j.jpowsour.2009.09.069.

[7] Talic B, Molin S, Wiik K, Hendriksen PV, Lein HL. Comparison of iron and copper doped manganese cobalt spinel oxides as protective coatings for solid oxide fuel cell interconnects. J Power Sources 2017;372:145–56. https://doi.org/10.1016/j.jpowsour.2017.10.060.

[8] Zanchi E, Talic B, Sabato AG, Molin S, Boccaccini AR, Smeacetto F. Electrophoretic co-deposition of Fe2O3 and Mn1,5Co1,5O4: processing and oxidation performance of Fe-doped Mn-Co coatings for solid oxide cell interconnects. J Eur Ceram Soc 2019;39:3768–77. https://doi.org/10.1016/j.jeurceramsoc.2019.05.024.

[9] Shen F, Lu K. Co3O4/Sm-Doped CeO2/Co3O4 Trilayer coating on AISI 441 interconnect for solid oxide fuel cells. ACS Appl Mater Interfaces 2017;9:6022–9. https://doi.org/10.1021/acsami.6b14562.

[10] Zanchi E, Ignaczak J, Molin S, Cempura G, Boccaccini AR, Smeacetto F. Electrophoretic co-deposition of Mn1.5Co1.5O4, Fe2O3 and CuO: Unravelling the effect of simultaneous addition of Cu and Fe on the microstructural, thermo-mechanical and corrosion properties of in-situ modified spinel coatings for solid oxide cell intercon. J Eur Ceram Soc 2022;42:3271–81. https://doi.org/10.1016/j.jeurceramsoc.2022.02.008.

[11] Zhu Z, Darl-Uzu C, Pal U, Gopalan S, Hussain AM, Dale N, Fukuyama Y, Miura Y, Miyoshi Y, Basu S. Comparison of Cu–Mn and Mn–Co spinel coatings for solid oxide fuel cell interconnects. Int J Hydrogen Energy 2022;47:36953–63. https://doi.org/10.1016/j.ijhydene.2022.08.239.

[12] Zhang X, You PF, Zhang HL, Yang XG, Luo MQ, Zeng C. Preparation and performances of Cu–Co spinel coating on ferritic stainless steel for solid oxide fuel cell interconnect. Int J Hydrogen Energy 2018;43:3273–9. https://doi.org/10.1016/j.ijhydene.2017.12.133.

[13] Liu K, Xu S, Shi J, Teng F, Yu X, Sun J. Impact of different atmospheres on oxidation and electrical performance of a solid oxide fuel cell interconnect with Co-containing protective coating. Energy Fuel 2020;34:8864–71. https://doi.org/10.1021/acs.energyfuels.0c01213.

[14] Jin Y, Sheng J, Hao G, Guo M, Hao W, Yang Z, Xiong X, Peng S. Highly dense (Mn, Co)3O4 spinel protective coating derived from Mn–Co metal precursors for SOFC interconnect applications. Int J Hydrogen Energy 2022;47:13960–8. https://doi.org/10.1016/j.ijhydene.2022.02.129.

[15] Larring Y, Norby T. Spinel and perovskite functional layers between Plansee metallic interconnect (Cr-5 wt % Fe-1 wt % Y[sub 2]O[sub 3]) and ceramic (La[sub 0.85]Sr[sub 0.15])[sub 0.91]MnO[sub 3] cathode materials for solid oxide fuel cells. J Electrochem Soc 2000;147:3251. https://doi.org/10.1149/1.1393891.

[16] Yang Z, Xia G, Nie Z, Templeton J, Stevenson JW. Ce-modified (Mn,Co) 3 O4 spinel coatings on ferritic stainless steels for SOFC interconnect applications. Electrochem Solid State Lett 2008;11. https://doi.org/10.1149/1.2929066.

[17] Stevenson JW, Yang ZG, Xia GG, Nie Z, Templeton JD. Long-term oxidation behavior of spinel-coated ferritic stainless steel for solid oxide fuel cell interconnect applications. J Power Sources 2013;231:256–63. https://doi.org/10.1016/j.jpowsour.2013.01.033.

[18] Ardigo MR, Popa I, Chevalier S, Girardon P, Perry F, Laucournet R, et al. Effect of coatings on long term behaviour of a commercial stainless steel for solid oxide electrolyser cell interconnect application in H2/H2O atmosphere. Int J Hydrogen Energy 2014;39:21673–7. https://doi.org/10.1016/j.ijhydene.2014.07.058.

[19] Molin S, Jasinski P, Mikkelsen L, Zhang W, Chen M, Hendriksen PV. Low temperature processed MnCo2O4 and MnCo1.8Fe0.2O4 as effective protective coatings for solid oxide fuel cell interconnects at 750 °C. J Power Sources 2016;336:408–18. https://doi.org/10.1016/j.jpowsour.2016.11.011.

[20] Palcut M, Mikkelsen L, Neufeld K, Chen M, Knibbe R, Hendriksen PV. Efficient dual layer interconnect coating for high temperature electrochemical devices. Int J Hydrogen Energy 2012;37:14501–10. https://doi.org/10.1016/j.ijhydene.2012.07.038.

[21] Wang R, Sun Z, Choi JP, Basu SN, Stevenson JW, Tucker MC. Ferritic stainless steel interconnects for protonic ceramic electrochemical cell stacks: oxidation behavior and protective coatings. Int J Hydrogen Energy 2019;44:25297–309. https://doi.org/10.1016/j.ijhydene.2019.08.041.

[22] Molin S, Sabato AG, Bindi M, Leone P, Cempura G, Salvo M, et al. Microstructural and electrical characterization of Mn-Co spinel protective coatings for solid oxide cell interconnects. J Eur Ceram Soc 2017;37:4781–91. https://doi.org/10.1016/j.jeurceramsoc.2017.07.011.

[23] Yoo J, Woo SK, Yu JH, Lee S, Park GW. La0.8Sr0.2MnO3 and (Mn1.5Co1.5)O4 double layer coated by electrophoretic deposition on Crofer22 APU for SOEC interconnect applications. Int J Hydrogen Energy 2009;34:1542–7. https://doi.org/10.1016/j.ijhydene.2008.12.005.

[24] Aznam I, Mah JCW, Muchtar A, Somalu MR, Ghazali MJ. Electrophoretic deposition of (Cu,Mn,Co)3O4 spinel coating on SUS430 ferritic stainless steel: process and performance evaluation for solid oxide fuel cell interconnect applications. J Eur Ceram Soc 2021;41:1360–73. https://doi.org/10.1016/j.jeurceramsoc.2020.09.074.

[25] Tan KH, Rahman HA, Taib H. Coating layer and influence of transition metal for ferritic stainless steel interconnector solid oxide fuel cell: a review. Int J Hydrogen Energy 2019;44:30591–605. https://doi.org/10.1016/j.ijhydene.2019.06.155.

[26] Sabato AG, Zanchi E, Molin S, Cempura G, Javed H, Herbrig K, et al. Mn-Co spinel coatings on Crofer 22 APU by electrophoretic deposition: up scaling, performance in SOFC stack at 850 °C and compositional modifications. J Eur Ceram Soc 2021;41:4496–504. https://doi.org/10.1016/j.jeurceramsoc.2021.03.030.

[27] Talic B, Molin S, Hendriksen PV, Lein HL. Effect of pre-oxidation on the oxidation resistance of Crofer 22 APU. Corrosion Sci 2018;138:189–99. https://doi.org/10.1016/j.corsci.2018.04.016.

[28] Wang R, Sun Z, Pal UB, Gopalan S, Basu SN. Mitigation of chromium poisoning of cathodes in solid oxide fuel cells employing CuMn1.8O4 spinel coating on metallic interconnect. J Power Sources 2018;376:100–10. https://doi.org/10.1016/j.jpowsour.2017.11.069.

[29] Sun Z, Wang R, Nikiforov AY, Gopalan S, Pal UB, Basu SN. CuMn1.8O4 protective coatings on metallic interconnects for prevention of Cr poisoning in solid oxide fuel cells. J Power Sources 2018;378:125–33. https://doi.org/10.1016/j.jpowsour.2017.12.031.

[30] Bednarz M, Molin S, Bobruk M, Stygar M, Długoń E, Sitarz M, et al. High-temperature oxidation of the Crofer 22 H ferritic steel with Mn1.45Co1.45Fe0.1O4 and Mn1.5Co1.5O4 spinel coatings under thermal cycling conditions and its properties. Mater Chem Phys 2019;225:227–38. https://doi.org/10.1016/j.matchemphys.2018.12.090.

[31] Tan KH, Rahman HA, Taib H. Ba0.5Sr0.5Co0.8Fe0.2O3−δ-Sm0.2Ce0.8O1.9 carbonate perovskite coating on ferritic stainless steel interconnect for low temperature solid oxide fuel cells. Mater Chem Phys 2020;254:123433. https://doi.org/10.1016/j.matchemphys.2020.123433.

[32] Ludwig GA, Korb MA, Lima DAS, Macías MA, Gauthier GH, Malfatti CF. Protective coatings for AISI 430 stainless steel at high temperatures using perovskite oxides La0.6Sr0.4CoO3 on spinel type oxide NiFe2O4. Ceram Int 2015;41:14561–73. https://doi.org/10.1016/j.ceramint.2015.07.173.

[33] Zhang Y, Zhang Y, Wu C, Yang Y, Li Q, Chen Y. Oxidation behavior and electrical properties of metal interconnects with Ce-doped Ni–Mn spinel coatings. Ceram Int 2022;48:9550–7. https://doi.org/10.1016/j.ceramint.2021.12.153.

[34] Shaigan N, Ivey DG, Chen W. Co/LaCrO3 composite coatings for AISI 430 stainless steel solid oxide fuel cell interconnects. J Power Sources 2008;185:331–7. https://doi.org/10.1016/j.jpowsour.2008.06.065.

[35] Shaigan N, Ivey DG, Chen W. Oxidation and electrical behavior of nickel/lanthanum chromite-coated stainless steel interconnects. J Power Sources 2008;183:651–9. https://doi.org/10.1016/j.jpowsour.2008.05.024.

[36] Shen F, Lu K. CoxFe1-x oxide coatings on metallic interconnects for solid oxide fuel cells. J Power Sources 2016;330:231–9. https://doi.org/10.1016/j.jpowsour.2016.09.018.

[37] Zhang HH, Zeng CL. Preparation and performances of Co-Mn spinel coating on a ferritic stainless steel interconnect material for solid oxide fuel cell application. J Power Sources 2014;252:122–9. https://doi.org/10.1016/j.jpowsour.2013.12.007.

[38] Tondo E, Boniardi M, Cannoletta D, De Riccardis MF, Bozzini B. Electrodeposition of yttria/cobalt oxide and yttria/gold coatings onto ferritic stainless steel for SOFC interconnects. J Power Sources 2010;195:4772–8. https://doi.org/10.1016/j.jpowsour.2010.02.055.

[39] Wu J, Jiang Y, Johnson C, Liu X. DC electrodeposition of Mn-Co alloys on stainless steels for SOFC interconnect application. J Power Sources 2008;177:376–85. https://doi.org/10.1016/j.jpowsour.2007.11.075.

[40] Jalilvand G, Faghihi-Sani MA. Fe doped Ni-Co spinel protective coating on ferritic stainless steel for SOFC interconnect application. Int J Hydrogen Energy 2013;38:12007–14. https://doi.org/10.1016/j.ijhydene.2013.06.105.

[41] Bik M, Stygar M, Jeleń P, Dąbrowa J, Leśniak M, Brylewski T, et al. Protective–conducting coatings based on black glasses (SiOC) for application in Solid Oxide Fuel Cells. Int J Hydrogen Energy 2017;42:27298–307. https://doi.org/10.1016/j.ijhydene.2017.09.069.

[42] Mousa Mirabad H, Nemati A, Faghihi-Sani MA, Fakouri Hasanabadi M, Abdoli H. Effect of YSZ sol-gel coating on interaction of Crofer22 APU with sealing glass for solid oxide fuel/electrolysis cell. J Alloys Compd 2020;847:156496. https://doi.org/10.1016/j.jallcom.2020.156496.

[43] Hua B, Zhang W, Wu J, Pu J, Chi B, Jian L. A promising NiCo2O4 protective coating for metallic interconnects of solid oxide fuel cells. J Power Sources 2010;195:7375–9. https://doi.org/10.1016/j.jpowsour.2010.05.031.

[44] Park BK, Lee JW, Lee SB, Lim TH, Park SJ, Park CO, et al. Cu- and Ni-doped Mn1.5Co1.5O4 spinel coatings on metallic interconnects for solid oxide fuel cells. Int J Hydrogen Energy 2013;38:12043–50. https://doi.org/10.1016/j.ijhydene.2013.07.025.

[45] Ou DR, Cheng M, Wang XL. Development of low-temperature sintered Mn-Co spinel coatings on Fe-Cr ferritic alloys for solid oxide fuel cell interconnect applications. J Power Sources 2013;236:200–6. https://doi.org/10.1016/j.jpowsour.2013.02.058.

[46] Grünwald N, Sebold D, Sohn YJ, Menzler NH, Vaßen R. Self-healing atmospheric plasma sprayed Mn1.0Co1.9Fe0.1O4 protective interconnector coatings for solid oxide fuel cells. J Power Sources 2017;363:185–92. https://doi.org/10.1016/j.jpowsour.2017.07.072.

[47] Waluyo NS, Park SS, Song RH, Lee SB, Lim TH, Hong JE, Ryu KH, Bin Im W, Lee JW. Protective coating based on manganese–copper oxide for solid oxide fuel cell interconnects: plasma spray coating and performance evaluation. Ceram Int 2018;44:11576–81. https://doi.org/10.1016/j.ceramint.2018.03.220.

[48] Chatterjee D, Biswas S. Development of chromium barrier coatings for solid oxide fuel cells. Int J Hydrogen Energy 2011;36:4530–9. https://doi.org/10.1016/j.ijhydene.2010.04.114.

[49] Wu W, Guan W, Wang G, Liu W, Zhang Q, Chen T, Wang WG. Evaluation of Ni80Cr20/(La0.75Sr 0.25)0.95MnO3 dual layer coating on SUS 430 stainless steel used as metallic interconnect for solid oxide fuel cells. Int J Hydrogen Energy 2014;39:996–1004. https://doi.org/10.1016/j.ijhydene.2013.10.094.

[50] Lacey R, Pramanick A, Lee JC, Il Jung J, Jiang B, Edwards DD, et al. Evaluation of Co and perovskite Cr-blocking thin films on SOFC interconnects. Solid State Ionics 2010;181:1294–302. https://doi.org/10.1016/j.ssi.2010.07.007.

[51] Besra L, Liu M. A review on fundamentals and applications of electrophoretic deposition (EPD). Prog Mater Sci 2007;52:1–61. https://doi.org/10.1016/j.pmatsci.2006.07.001.

[52] Lowrance YN, Azmi MA, Basar LM, Rahman HA. The influence of electrophoretic deposition (EPD) parameters on SS430 spinel coated characteristic. International Journal of Integrated Engineering 2021;13:258–64. https://doi.org/10.30880/ijie.2021.13.02.030.

[53] Bidabadi MHS, Siripongsakul T, Thublaor T, Wiman P, Chandra-ambhorn S. Oxidation and Cr-evaporation behavior of MnCo based spinel and composite coated AISI 430 steel. Surf Coating Technol 2022:434. https://doi.org/10.1016/j.surfcoat.2022.128176.

[54] Zanchi E, Sabato AG, Monterde MC, Bernadet L, Torrell M, Calero JA, Tarancón A, Smeacetto F. Electrophoretic deposition of MnCo2O4 coating on solid oxide cell interconnects manufactured through powder metallurgy. Mater Des 2023;227:111768. https://doi.org/10.1016/j.matdes.2023.111768.

[55] Mazur Ł, Koszelow D, Zajusz M, Łapiński M, Bik M, Zając P, Adamczyk A, Rutkowski P, Molin S, Brylewski T. Comparison of Cu1.3Mn1.7O4 spinels doped with Ni or Fe and synthesized via wet chemistry and solid-state reaction methods, designed as potential coating materials for metallic interconnects. J Eur Ceram Soc 2023;43:5557–74. https://doi.org/10.1016/j.jeurceramsoc.2023.05.015.

[56] Oh SU, Kim D, Lee IT, Choi CS, Lee JA, Heo YW, Lee JH. Electrophoretic deposition and low-temperature densification of Cu1.35Mn1.65O4 spinel for an interconnect protective coating in solid oxide fuel cells. Int J Hydrogen Energy 2022;47:33410–9. https://doi.org/10.1016/j.ijhydene.2022.07.259.

[57] Sabato AG, Molin S, Javed H, Zanchi E, Boccaccini AR, Smeacetto F. In-situ Cu-doped MnCo-spinel coatings for solid oxide cell interconnects processed by electrophoretic deposition. Ceram Int 2019;45:19148–57. https://doi.org/10.1016/j.ceramint.2019.06.161.

[58] Javed H, Saunders T, Reece MJ, Zanchi E, Sabato AG, Boccaccini AR, Smeacetto F. Pressure assisted flash sintering of Mn-Co based spinel coatings for solid oxide electrolysis cells (SOECs). Ceram Int 2021;47:17804–8. https://doi.org/10.1016/j.ceramint.2021.03.055.

[59] Zhu Z, Pal U, Gopalan S, Hussain AM, Dong S, Dale N, Fukuyama Y, Basu S. Alternating-current electrophoretic deposition of spinel coatings on porous metallic substrates for solid oxide fuel cell applications. Jom 2021;73:2764–70. https://doi.org/10.1007/s11837-021-04763-2.

[60] Mah JCW, Muchtar A, Somalu MR, Ghazali MJ. Metallic interconnects for solid oxide fuel cell: a review on protective coating and deposition techniques. Int J Hydrogen Energy 2017;42:9219–29. https://doi.org/10.1016/j.ijhydene.2016.03.195.

[61] Puranen J, Pihlatie M, Lagerbom J, Salminen T. Influence of powder composition and manufacturing method on electrical and chromium barrier properties of atmospheric plasma sprayed spinel coatings prepared from MnCo 2 O 4 and Mn 2 CoO 4 þ Co powders on Crofer 22 APU interconnectors. 2014. p. 9. https://doi.org/10.1016/j.ijhydene.2014.08.016.

[62] Ahmadi A, Mosallanejad B, Zare E. Highly efficient electrocatalysts fabricated via electrophoretic deposition for alcohol oxidation , oxygen reduction , hydrogen evolution , and oxygen evolution reactions. Int J Hydrogen Energy 2020;46:7263–83. https://doi.org/10.1016/j.ijhydene.2020.11.261.

[63] Oh S, Kim D, Lee I, Choi C, Lee J, Heo Y, Lee J. Electrophoretic deposition and low-temperature interconnect protective coating in solid oxide fuel cells. Int J Hydrogen Energy 2022;47:33410–9. https://doi.org/10.1016/j.ijhydene.2022.07.259.

[64] Zhu H, Zhang J, Cao W. Recent advances in spinel-based protective coatings produced by electrochemical method on metallic interconnects for solid oxide fuel cells. Int J Hydrogen Energy 2023;50:977–91. https://doi.org/10.1016/j.ijhydene.2023.09.242.

[65] Oskouyi OE, Maghsoudipour A, Shahmiri M, Hasheminiasari M. Preparation of YSZ electrolyte coating on conducting porous Ni–YSZ cermet by DC and pulsed constant voltage electrophoretic deposition process for SOFCs applications. J Alloys Compd 2019;795:361–9. https://doi.org/10.1016/j.jallcom.2019.04.334.

[66] Talic B, Falk-Windisch H, Venkatachalam V, Hendriksen PV, Wiik K, Lein HL. Effect of coating density on oxidation resistance and Cr vaporization from solid oxide fuel cell interconnects. J Power Sources 2017;354:57–67. https://doi.org/10.1016/j.jpowsour.2017.04.023.

[67] Guo X, Li X, Lai C, Li W, Zhang D, Xiong Z. Cathodic electrophoretic deposition of bismuth oxide (Bi 2 O 3) coatings and their photocatalytic activities. Appl Surf Sci 2015;331:455–62. https://doi.org/10.1016/j.apsusc.2015.01.034.

[68] Sarkar P, Nicholson PS. Electrophoretic deposition (EPD): Mechanisms, kinetics, and application to ceramics. J Am Ceram Soc 1996;79:1987–2002. https://doi.org/10.1111/j.1151-2916.1996.tb08929.x.

[69] Ferrari B, Moreno R. EPD kinetics: a review. J Eur Ceram Soc 2010;30:1069–78. https://doi.org/10.1016/j.jeurceramsoc.2009.08.022.

[70] Hamaker HC. Formation of a deposit by electrophoresis. Trans Faraday Soc 1940;36:279–87.

[71] Oskouyi OE, Shahmiri M, Maghsoudipour A, Hasheminiasari M. Pulsed constant voltage electrophoretic deposition of YSZ electrolyte coating on conducting porous Ni–YSZ cermet for SOFCs applications. J Alloys Compd 2019;785:220–7. https://doi.org/10.1016/j.jallcom.2019.01.166.

3.2. Manuscript II

Title: **Preparation of Mn-Co and Mn-Cu-Fe single-layer, and novel Mn-Co/Mn-Cu-Fe dual-layer spinel protective coatings on complex-shaped metallic interconnects by EPD method**

This study examined the potential of electrophoretic deposition (EPD) technique for applying dual-layer oxide spinel coatings of $MnCo_2O_4$/ $Mn_{1.7}CuFe_{0.3}O_4$ onto complex-shaped metallic interconnects. There has not been very limited research on complex-shaped metallic interconnects, which investigated the deposition of oxide spinel materials by EPD method. The study assessed various process parameters of EPD method aiming to achieve a coating that is uniform, dense, smooth, and crack-free on complex-shaped metallic interconnects. Two main reasons support the selection of a dual-layer oxide spinel coating for metallic interconnects. Firstly, the electrical conductivity of the $Mn_{1.7}CuFe_{0.3}O_4$ spinel coating is higher than that of the $MnCo_2O_4$ spinel coating. Therefore, it serves as an optimal outer layer, facilitating electrical conductivity between adjacent cells. Secondly, the $MnCo_2O_4$ spinel coating exhibits significantly higher oxidation resistance compared to the $Mn_{1.7}CuFe_{0.3}O_4$ spinel coating. As a result, it functions effectively as an inner layer, mitigating oxidation rates and preventing the migration and evaporation of chromium from the interconnects to the oxygen electrodes. This research highlights the applicability of EPD method for dual-layer oxide spinel coating on complex-shaped metallic interconnects.

The research highlighted are outlined as follows:

- A uniform and crack-free coating applied onto complex-shaped interconnects using EPD method.
- $MnCo_2O_4$/$Mn_{1.7}CuFe_{0.3}O_4$ dual-layer coating is a promising candidate for protective coatings.
- Dual-layer coating densification in reduction+ oxidation is higher than oxidation treatments.
- Dual-layer coating provides higher protection against Cr diffusion than single-layer coating.

Table 2. CRediT author statement of manuscript II.

Author	CRediT author statement	Signature
Omid Ekhlasiosgouei	Methodology, Investigation, Formal analysis, Data curation, Writing– original draft	Omid Ekhlasiosgouei
Maciej Bik	Investigation (Raman analysis), Formal analysis, Writing- review and editing	Maciej
Sebastian Molin	Resources, Conceptualization, Supervision, Writing- review and editing	Molin

International Journal of Hydrogen Energy 83 (2024) 563–576

Contents lists available at ScienceDirect

International Journal of Hydrogen Energy

journal homepage: www.elsevier.com/locate/he

Preparation of $MnCo_2O_4$ and $Mn_{1.7}CuFe_{0.3}O_4$ single-layer, and novel $MnCo_2O_4$/ $Mn_{1.7}CuFe_{0.3}O_4$ dual-layer spinel protective coatings on complex-shaped metallic interconnects by EPD method

Omid Ekhlasiosgouei [a,*], Maciej Bik [b], Sebastian Molin [a]

[a] Advanced Materials Center, Faculty of Electronics, Telecommunications and Informatics, Gdansk University of Technology, Gdansk, Poland
[b] Faculty of Materials Science and Ceramics, AGH University of Krakow, Krakow, Poland

ARTICLE INFO

Handling Editor: Ramazan Solmaz

Keywords:
Electrophoretic deposition
Complex-shaped metallic interconnect
Spinel
Dual-layer coating
Protective coating

ABSTRACT

Ceramic protective coatings applied to metallic interconnects play a vital role in solid oxide cells (SOCs) preventing interconnect degradation. In this study, uniform, dense, and crack-free single-layer coatings of $MnCo_2O_4$, $Mn_{1.7}CuFe_{0.3}O_4$, and dual-layer coatings of $MnCo_2O_4$/$Mn_{1.7}CuFe_{0.3}O_4$ spinel are deposited onto complex-shaped metallic interconnect using electrophoretic deposition (EPD) method. The porosity of sintered $MnCo_2O_4$ and $Mn_{1.7}CuFe_{0.3}O_4$ coatings in reduction treatment (1000 °C for 2h in H_2), followed by subsequent oxidation treatment (900 °C for 2h in air) is approximately 50% less than that of these coatings sintered in oxidation treatment (900 °C for 4h in air). The results indicate that the thickness of the sintered $MnCo_2O_4$, $Mn_{1.7}CuFe_{0.3}O_4$ single-layer, and $MnCo_2O_4$/$Mn_{1.7}CuFe_{0.3}O_4$ dual-layer coatings in reduction + oxidation treatments is 46.2%, 28.2%, and 23.1% denser, respectively, compared to sintered in oxidation treatment. Raman spectroscopy and Energy Dispersive Spectroscopy (EDS) analysis showed that in sintered dual-layer coatings subjected to reduction treatment followed by a subsequent oxidation treatment, exhibit a much more efficient interdiffusion processes throughout the thickness of the coating yielding the formation of a mixed $(Mn, Cu, Fe, Co)_3O_4$ spinel, comparing to dual-layer coatings undergoing only oxidation treatment. The dual-layer spinel coatings of $MnCo_2O_4$/ $Mn_{1.7}CuFe_{0.3}O_4$ present promising candidate for protective coatings on metallic interconnects.

1. Introduction

The interconnects play a crucial role in ensuring the reliable and continuous operation of the solid oxide cells (SOCs), providing electrical connections between individual cells and assisting in the distribution of reactant gases and thermal management [1–3]. In the context of SOCs applications, interconnects must possess specific properties to meet the demands of the operating environment: high electrical conductivity, chemical stability, thermal compatibility, and mechanical strength [4–7]. Commonly used interconnect materials include ferritic stainless steels, known for their high-temperature stability, corrosion resistance, and relatively low cost. Ferritic stainless steels, in particular, offer excellent mechanical properties and improved thermal expansion matched with the other cell components [8–10]. However, ongoing research focuses on the development of materials, such as protective coatings, to further improve interconnect performance and longevity [6]. The geometry of metallic interconnects in SOCs plays a significant role in ensuring the efficient and reliable operation of the fuel cell stack. The geometric design of these interconnects is carefully considered to optimize factors such as electrical performance, thermal management, gas distribution, and overall system integration [11,12]. Research focuses on improving electrical conductivity and addressing thermal compatibility issues. Furthermore, advancements are being made in interconnect fabrication techniques, including precision manufacturing processes and coatings, to optimize the overall performance and efficiency of SOC systems [9,10,13].

Coating of metallic interconnects is an essential aspect of SOC technology, aimed at improving the performance, durability, and reliability of these critical components [14–16]. Metallic interconnects require specialized coatings to address challenges such as oxidation, corrosion, and area-specific resistance (ASR) [17]. Coatings act as protective barriers, enhancing the interconnect's ability to withstand the harsh operating conditions of the fuel cell environment and improving its long-term performance [18,19]. Oxidation can lead to the formation

* Corresponding author.
E-mail address: omid.ekhlasiosgouei@pg.edu.pl (O. Ekhlasiosgouei).

https://doi.org/10.1016/j.ijhydene.2024.07.447
Received 30 June 2024; Received in revised form 29 July 2024; Accepted 30 July 2024
Available online 13 August 2024

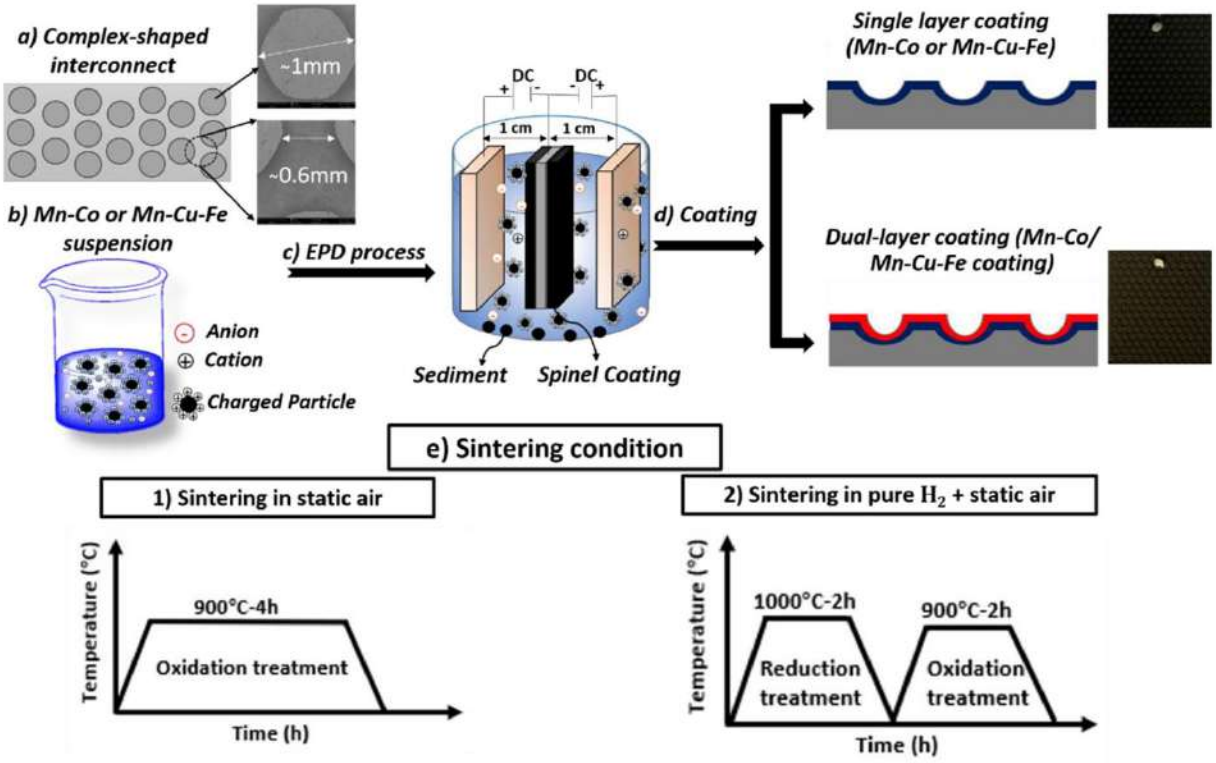

Fig. 1. The schematic illustration of a) complex-shaped metallic interconnects, b) electrostatic stabilization, c) EPD setup, d) Mn-Co, Mn-Cu-Fe single layer oxide spinel, and Mn-Co/Mn-Cu-Fe dual-layer oxide spinel coating on the complex-shaped interconnect, and e) sintering conditions in both oxidation treatment and reduction treatment, followed by a subsequent oxidation treatment.

Table 1
Spinel coating materials, suspension and process parameters of EPD method and sintering parameters for spinel coating on metallic interconnect.

Oxide spinel coating material	Substrate	Suspension condition			EPD condition			Sintering condition		
		Solvent	Solid load	I_2	Voltage (V)	Time (s)	Electrode's distance	Sample	Step 1: Reduction treatment (Pure H_2)	Step 2: Oxidation treatment (Static air)
Mn-Co single-layer coating	Crofer 22 APU (Complex-shaped)	Ethanol	10 g/L	0.5 g/L	40	60	10 mm	S1:	–	900 °C- 4h
								S4:	1000 °C- 2h	900 °C- 2h
Mn-Cu-Fe single-layer coating					60	420		S2:	–	900 °C- 4h
								S5:	1000 °C- 2h	900 °C- 2h
Mn-Co/Mn-Cu-Fe dual-layer coating					First layer: 40	First layer: 15		S3:	–	900 °C- 4h
					Second layer:60	Second layer:90		S6:	1000 °C- 2h	900 °C- 2h

of oxide scales on the surface of the interconnect, compromising its electrical conductivity and causing performance degradation [20]. Coatings play a vital role in reducing electrical resistance at the interfaces between the interconnect and adjacent fuel cell components. Coatings with high electrical conductivity can enhance the interconnect's performance by improving the electrical contact with the cell electrodes, leading to improved overall cell efficiency [14,21–23]. Various coating technologies for metallic interconnects in SOCs include electrophoretic deposition (EPD) [24–32], electrolytic deposition (ELD) [33–35], dip coating [36–38], plasma spraying [16,39–42], screen printing [43,44], spin coating [45,46], and sputtering [20,47–49]. Advanced ceramic materials, such as Mn-Co or Mn-Cu oxide spinel materials, are commonly used as coating materials due to their excellent thermal and chemical stability, electrical conductivity, and compatibility with the fuel cell environment [5,15,50–53].

Though many studies regarding protective coatings have been presented, only a very limited number of works have been carried out on complex-shaped interconnects. Zanchi et al. [54] indicated that electrophoretic deposition is a successful technique for applying $MnCo_2O_4$ spinel materials onto complex-shaped metallic interconnects. Furthermore, the samples coated with Mn-Co oxide spinel demonstrated a reduced degradation rate of area-specific resistance (1.2 mΩ cm^2/kh) and effectively limited the outward diffusion of chromium. Talic et al. [55] investigated the fabrication of $Mn_{1.5}Co_{1.5}O_4$ coating using the electrophoretic deposition method on Crofer 22H steel grid. The results showed that the sintered Mn-Co oxide spinel coating exhibited cracks on concave surfaces, while convex surfaces remained crack-free. These cracks can be attributed to the intricate interaction between factors such as the thickness of the coating, the sintering process, and the radius of curvature of the substrate. Additionally, the application of Mn-Co oxide spinel coating resulted in a reduced oxidation rate for the Crofer 22H grid exposed at 750 °C to an air atmosphere. Furthermore, the sintered

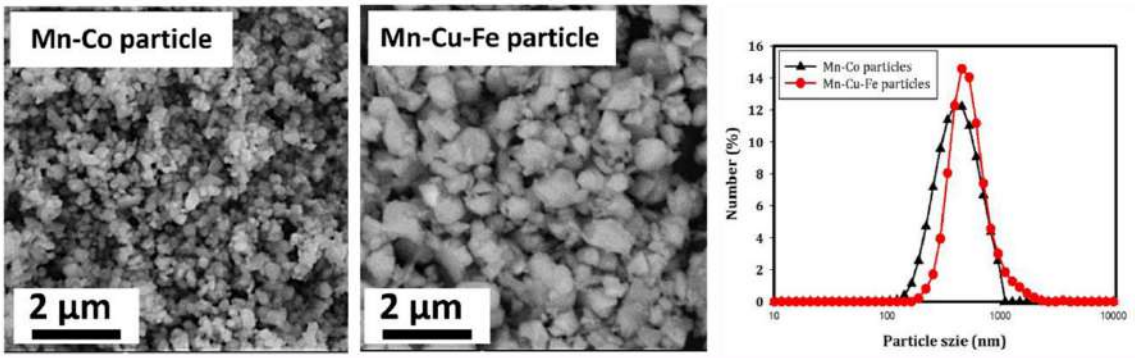

Suspension (EtOH solvent+ 10 g/l particles + 0.5 g/l iodine)	Average Particle Size (µm)	Zeta Potential (mV)	Suspension Conductivity (µS/cm)
Mn-Co Particles	0.40	16.5 ± 0.53	2.86 ± 0.71
Mn-Cu-Fe Particles	0.59	7.05 ± 0.28	6.01 ± 0.42

Fig. 2. SEM images, particle size distribution, and suspension properties (average particle size, zeta potential, and suspension conductivity) of both Mn-Co and Mn-Cu-Fe oxide spinel powders.

Mn-Co oxide spinel coating, subjected to reduction treatment, followed by a subsequent oxidation treatment exhibited increased density and a diminished propensity for crack formation compared to the coating sintered in oxidation treatment. Sun et al. [56] conducted research on a $CuMn_{1.8}O_4$ spinel coating, applying it to metallic flat plates and meshes through electrophoretic deposition. The results demonstrated superb coverage of the spinel coating on the mesh surface. However, it was observed that the coating thickness was greater at sharp corners compared to other areas, attributed to the increased local electrical field in those regions. Furthermore, upon comparing the coating morphology on flat surfaces and meshes, a similar structure was observed, except for the sharp corners.

Ignaczak et al. [57] conducted a study involving Mn-Co and Mn-Cu-Fe oxide spinel coatings on Crofer 22 APU using the EPD method. Their investigation focused on the impact of Fe addition on the structural and protective properties, including area-specific resistance (ASR) and oxidation rate, of these coatings. Results indicated that Mn-Cu-Fe oxide spinel exhibited higher electrical conductivity at 800 °C and 600 °C (20 S/cm and 40 S/cm, respectively) compared to Mn-Co oxide spinel. Additionally, the Mn-Cu-Fe oxide spinel coating showed a lower increase in ASR values during oxidation compared to the Mn-Co oxide spinel coating.

This study delves into the promising application of electrophoretic deposition (EPD) as a method for coating single and dual-layer configurations on complex-shaped metallic interconnects with $MnCo_2O_4$ and $Mn_{1.7}CuFe_{0.3}O_4$ spinel. There has not been very limited research on complex-shaped metallic interconnects, which investigated the deposition of oxide spinel materials by EPD method. Additionally, to achieve both satisfactory electrical conductivity and oxidation resistance simultaneously, we chose to employ novel dual-layer of $MnCo_2O_4$/$Mn_{1.7}CuFe_{0.3}O_4$ spinel coatings. The main objective is to attain uniform, smooth, dense, and crack-free spinel coatings on complex-shaped interconnects.

2. Experimental

2.1. Materials

In this research, a complex-shaped metallic interconnect was chosen as the substrate for applying a spinel coating using the EPD technique, as shown in Fig. 1a. The complex-shaped metallic interconnect (Cellconnex, Fiaxell, Switzerland) based on Crofer 22 APU stainless steel, consists of ~23 wt% Cr, ~0.5 wt% Mn, and the balance is Fe with minor alloying additions (La, Ti, Si, and Al). The interconnect sheets were cut with a laser into squares measuring 22 mm by 20 mm. Before applying the coating, the substrate underwent a cleaning process by immersing it in acetone and then ethanol (provided by OCH, Gliwice, Poland) using an ultrasonic bath for 30 min. Two types of spinel materials, namely commercial $MnCo_2O_4$ (labelled as "Mn-Co oxide spinel" material, supplied by Marion Technologies, France) and synthesized $Mn_{1.7}CuFe_{0.3}O_4$ (labelled as "Mn-Cu-Fe oxide spinel" material), were employed to deposit a conductive protective coating on the complex-shaped metallic interconnects. The $Mn_{1.7}CuFe_{0.3}O_4$ spinel material was synthesized using a modified Pechini method. This process involved mixing hydrated nitrate salts of manganese, copper, and iron with chelating agents and ethylene glycol, followed by heating and calcination. The resulting powders were ground and calcined again before being used for further studies. Additional information regarding the preparation of the synthesized $Mn_{1.7}CuFe_{0.3}O_4$ can be found in a preceding publication [34]. Ethanol served as the solvent, and iodine was used as a dispersing agent to create suspensions of Mn-Co and Mn-Cu-Fe oxide spinel materials for the EPD process.

2.2. Preparation of Mn-Co and Mn-Cu-Fe oxide spinel suspensions

The suspensions of Mn-Co and Mn-Cu-Fe oxide spinel materials, with solid concentrations of 10 g/L and 0.5 g/L iodine, were stabilized in ethanol solvent. Homogenization of Mn-Co and Mn-Cu-Fe oxide spinel powders in organic ethanol solvent was achieved through stirring and ultrasonic bath treatments for 45 min. Prior to EPD, these suspensions underwent an additional bath ultrasonic treatment for 5 min. The

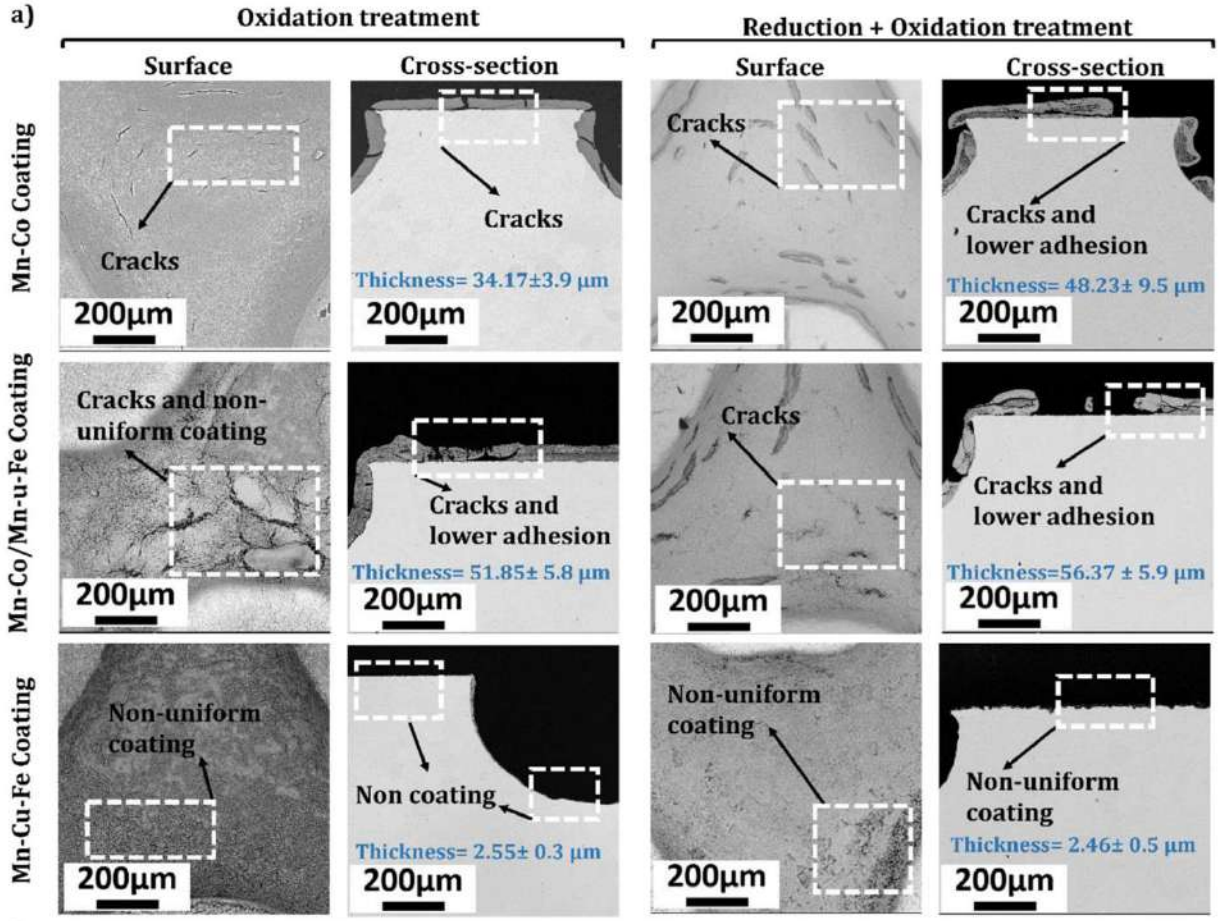

b)

Oxide spinel coating material	Substrate	Suspension condition			EPD condition			Sintering condition	
		Solvent	Solid load	I_2	Voltage (V)	Time (s)	Electrode's distance	Step 1: Reduction treatment (Pure H_2)	Step 2: Oxidation treatment (Static air)
Mn-Co	Crofer 22 APU (Complex-shaped)	Ethanol	10 g/L	0.5 g/L	90	100	10 mm	- 1000 °C- 2h	900 °C- 4h 900 °C- 2h
Mn-Cu-Fe					90	90		- 1000 °C- 2h	900 °C- 4h 900 °C- 2h
Mn-Co/Mn-Cu-Fe					First layer: 90 Second layer:90	First layer: 100 Second layer:90		- 1000 °C- 2h	900 °C- 4h 900 °C- 2h

Fig. 3. The microstructure of coatings prepared under non-optimized EPD conditions (resulting in non-uniform and cracked coatings on complex-shaped substrates): a) surface and cross-section SEM images of sintered Mn-Co, Mn-Cu-Fe single-layer oxide spinel, and Mn-Co/Mn-Cu-Fe dual-layer oxide spinel coatings in oxidation treatment and reduction treatment, followed by a subsequent oxidation treatment. b) Spinel coating materials, suspension, and process parameters of the EPD method, along with sintering parameters for spinel coating on complex-shaped metallic interconnects.

composition of spinel coating materials and suspension parameters for spinel coating on the complex-shaped metallic interconnect are presented in Table 1. Additionally, a schematic representation of stable Mn-Co and Mn-Cu-Fe oxide spinel powders in ethanol solvent is depicted in Fig. 1b.

2.3. DC electrophoretic deposition (EPD) process

To apply coatings of Mn-Co and Mn-Cu-Fe oxide spinel materials onto the substrate, the complex-shaped metallic interconnect served as the cathode, while Crofer 22 APU stainless steel functioned as the anode. The two electrodes were held in a vertical and parallel orientation during EPD process, with a fixed distance of 10 mm between them in the EPD cell. The process parameters for spinel single-layer and dual-layer coatings are detailed in Table 1. Additionally, a schematic representation of the EPD cell for single-layer and dual-layer coatings is illustrated in Fig. 1c. Additional information about the preparation of the suspension and the EPD process is available in a previous publication [58].

2.4. Sintering of single layer and dual-layer coatings

The single-layer oxide spinel coatings of Mn-Co, Mn-Cu-Fe, and the

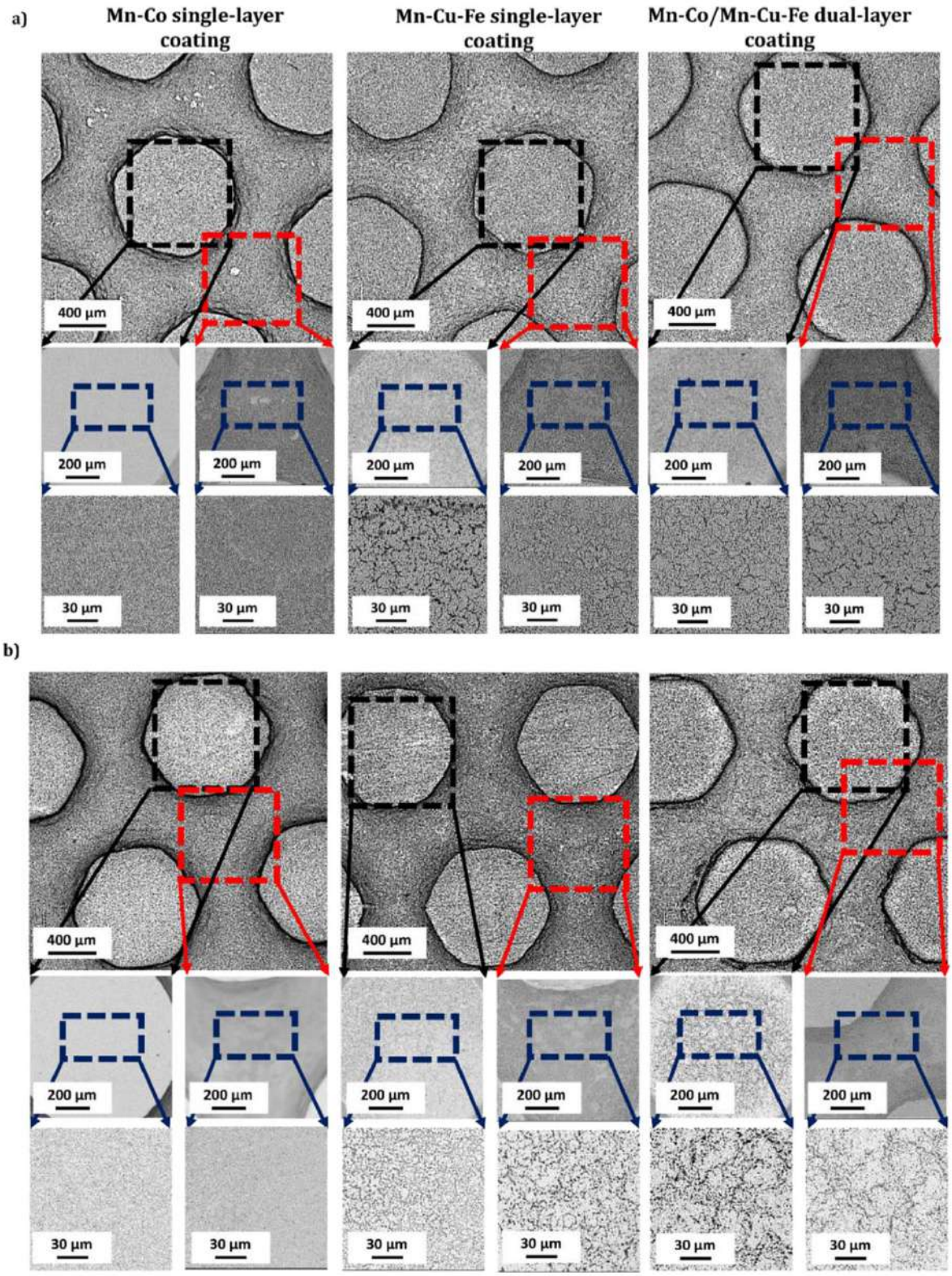

Fig. 4. OM, and SEM images of sintered Mn-Co, Mn-Cu-Fe single-layer coatings, and b) Mn-Co/Mn-Cu-Fe dual-layer oxide spinel coatings: a) in oxidation treatment, and b) reduction treatment, followed by a subsequent oxidation treatment.

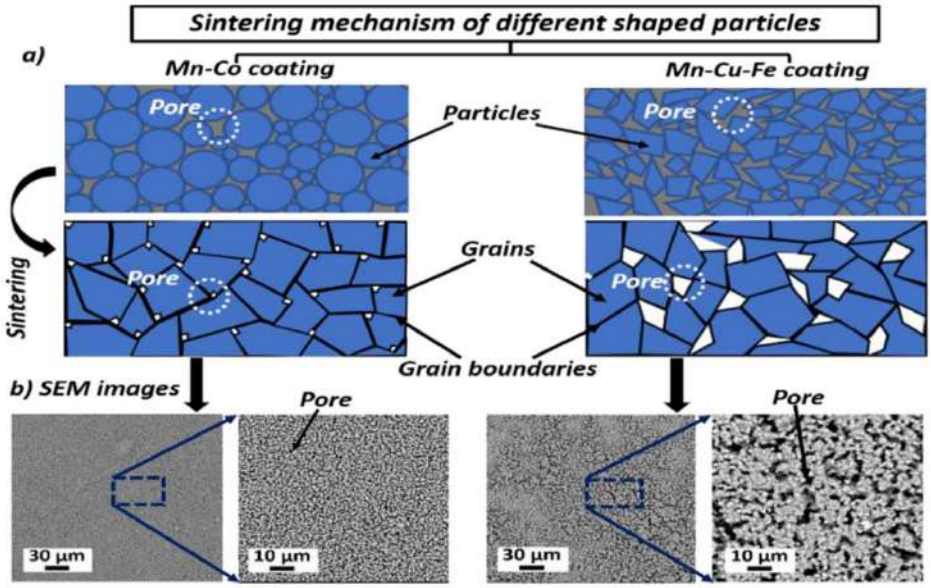

Fig. 5. a) Schematic of the sintering mechanism of particles with various shapes (Mn-Co and Mn-Cu-Fe oxide spinel particles), and b) surface SEM images of coatings at different magnifications.

dual-layer Mn-Co/Mn-Cu-Fe oxide spinel coating on the substrate, were dried at room temperature for 24 h. Following this, the coatings underwent sintering at different temperatures and durations in various atmospheres, as detailed in Table 1 and shown schematically in Fig. 1e. As shown in Fig. 1e, after applying Mn-Co, Mn-Cu-Fe single layer oxide spinel and Mn-Co/Mn-Cu-Fe dual-layer oxide spinel coatings, the samples underwent heat treatment using two distinct procedures. The initial group of samples underwent a single-step sintering process at 900 °C for 4 h in static air (oxidation treatment). The second set of samples underwent a two-step sintering process, involving an initial reduction treatment at 1000 °C for 2 h in flowing pure H_2 gas, followed by a subsequent oxidation treatment at 900 °C for 2 h in static air. The rate of heating and cooling in both the single-step sintering process and the two-step process was 3 °C/min.

2.5. Characterization

A Malvern Dynamic Light Scattering instrument (Zetasizer nano ZS, Malvern), was used to assess the particle size distribution, zeta potential, and suspension conductivity of Mn-Co and Mn-Cu-Fe oxide spinel particles in ethanol solvent. The surface and cross-sectional microstructure of the Mn-Co, Mn-Cu-Fe single layer oxide spinel, and Mn-Co/Mn-Cu-Fe dual-layer oxide spinel coatings were investigated using SEM with energy-dispersive X-ray spectroscopy (EDX) at an acceleration voltage of 20 kV. For cross-sectional analysis, the samples were embedded in epoxy resin under cold vacuum conditions, followed by grinding with SiC papers and polishing with 1 µm diamond slurry. Additionally, the confocal optical microscope (Olympus LEXT OLS4000) was employed to examine the surface microstructure of the sintered Mn-Co, Mn-Cu-Fe single layer oxide spinel, and Mn-Co/Mn-Cu-Fe dual-layer spinel oxide spinel coatings. The porosity of single-layer and dual-layer oxide spinel coatings was measured by ImageJ software. Phase composition was examined with Raman spectroscopy (namely Raman Confocal imaging) using a WITec alpha 300 M+ spectrometer, 785 nm excitation wavelength, with a laser spot of approximately 1064 nm in diameter, a spectral resolution of approximately 3 cm^{-1}, and a grating of 300 gr/mm. The technical data concerning measurements and their post-processing can be found in Ref. [59], as the measurements were conducted on pre-prepared cross sections in the same manner. The areas of constant width (3 µm) were tested, and their height (ranging from 36 to 38 µm) depended on the scale/coating thickness. The lateral resolution was 500 nm. The spectral range extracted during post-processing was equal to 112 ÷ 1000 cm^{-1}. In the case of a single $MnCo_2O_4$ protective layer, measured as a reference for dual coatings, point measurements were carried out using three different levels of laser power and 8 scans with a 20 s integration time.

3. Results and discussion

Fig. 2 illustrates SEM images, particle size distribution, and suspension characteristics of Mn-Co and Mn-Cu-Fe oxide spinel powders. As evident in the SEM images, the particle size of Mn-Cu-Fe oxide spinel powder is slightly greater than that of Mn-Co oxide spinel powder. Additionally, the morphology of Mn-Cu-Fe oxide spinel powders appears more disordered compared to Mn-Co oxide spinel powders. Moreover, both Mn-Co and Mn-Cu-Fe oxide spinel powders exhibit no agglomeration. According to the particle size distribution of Mn-Co and Mn-Cu-Fe oxide spinel powders in ethanol solvent, the narrow and monomodal distribution of spinel powders indicates that the particles in the suspension have similar sizes, implying an absence of agglomeration. Consequently, both Mn-Co and Mn-Cu-Fe oxide spinel powders demonstrate increased stability within the suspension. Additionally, the absence of particle agglomeration ensures a uniform and dense coating on the substrate. The average particle size of Mn-Co and Mn-Cu-Fe oxide spinel suspended in ethanol solvent measures 0.4 µm and 0.59 µm, respectively. Comparing SEM images and particle size averages reveals that the particle size average of Mn-Co oxide spinel powder is slightly smaller than that of Mn-Cu-Fe oxide spinel powder. To enhance the stability of powders in the solvent, iodine is introduced into the suspension to release H^+ ions. Subsequently, the powder surface absorbs these H^+ ions, leading to an increase in the thickness of the electrical double layer, or in other words, an increase in the zeta potential. Under identical suspension conditions, the zeta potential for Mn-Co and Mn-Cu-Fe oxide spinel particles in ethanol solvent is measured at 16.5 ± 0.53 and 7.05 ± 0.28 mV, respectively. Consequently, the stability of Mn-Co oxide spinel particles in ethanol solvent is higher compared to that of Mn-Cu-Fe oxide spinel particles because of their higher zeta potential. Elevating the suspension conductivity facilitates the movement of particles toward the opposite electrode, making it easier to

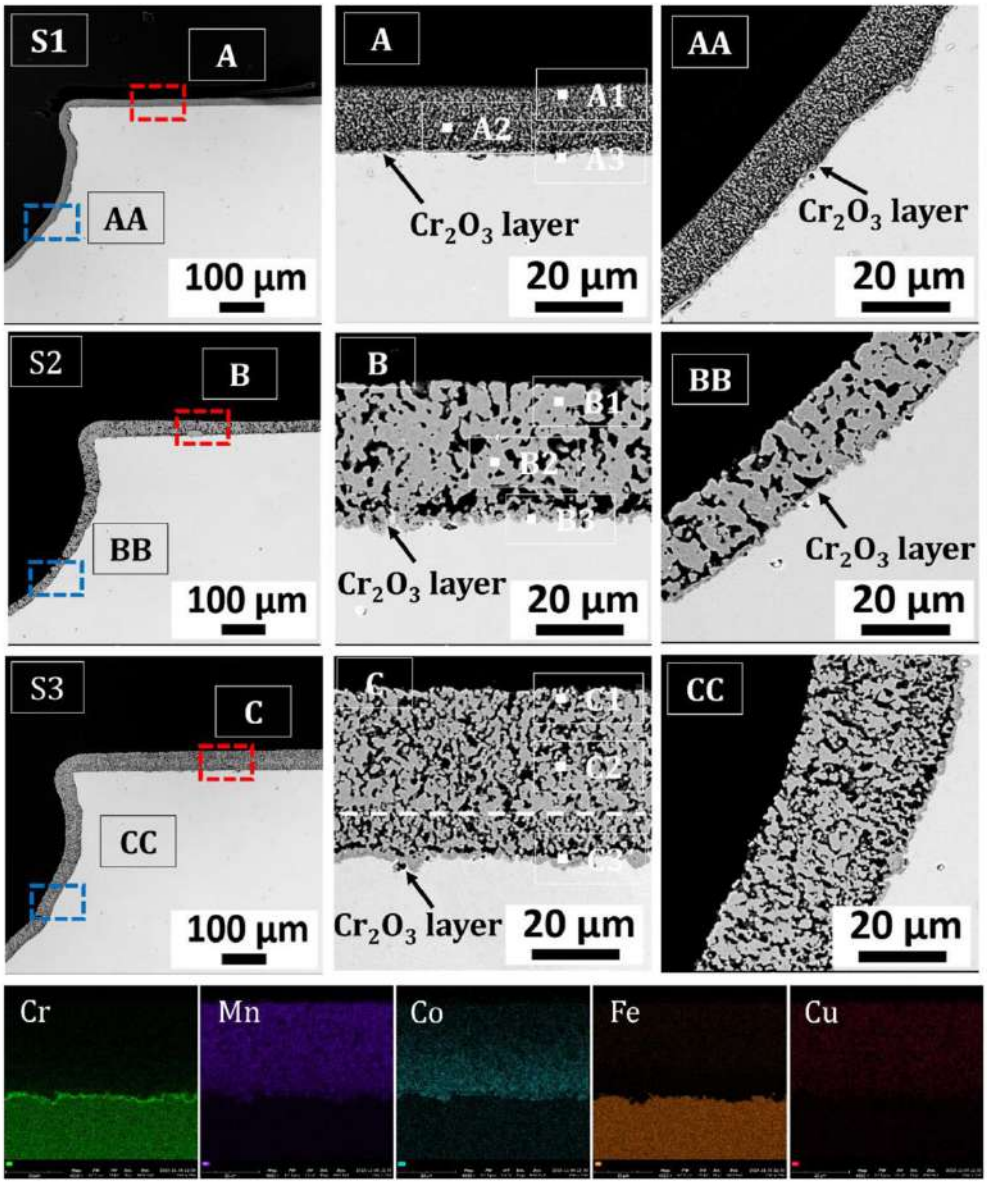

Fig. 6. SEM cross-section images sintered Mn-Co single-layer (S1), Mn-Cu-Fe single-layer (S2), and Mn-Co/Mn-Cu-Fe dual-layer (S3) oxide spinel coatings in oxidation treatment, EDX maps of Mn-Co/Mn-Cu-Fe dual-layer oxide spinel coating (from SEM cross-section of image C).

achieve a uniform and dense coating.

In our previous research, we deposited Mn-Co oxide spinel on flat Crofer 22 APU plates, describing the optimized deposition parameters. Unfortunately, the direct application of the process parameters developed for flat samples was not effective in the case of complex-shaped samples. This is an important but often overlooked problem in the use of EPD for larger-scale practical samples [58]. Using the parameters found previously led to low-quality samples in this investigation for complex-shaped metallic interconnects. Fig. 3a exhibits SEM images illustrating the surface and cross-sectional views of sintered Mn-Co, Mn-Cu-Fe single-layer oxide spinel, and Mn-Co/Mn-Cu-Fe dual-layer oxide spinel coatings subjected to oxidation and reduction treatment, followed by a subsequent oxidation treatment. Fig. 3b illustrates the characteristics of the suspension, process parameters, and sintering conditions employed in applying Mn-Co, Mn-Cu-Fe single-layer oxide spinel, and Mn-Co/Mn-Cu-Fe dual-layer oxide spinel coatings onto complex-shaped metallic interconnects through the EPD method. As indicated in Fig. 3a, the surface SEM images of sintered Mn-Co single-layer oxide spinel and Mn-Co/Mn-Cu-Fe dual-layer oxide spinel coatings exhibit cracks and a non-uniform coating on the substrate during oxidation treatment, likely attributed to a higher deposition yield on the substrate. Moreover, the size of cracks observed in the reduction treatment, followed by a subsequent oxidation treatment is greater than that in the oxidation treatment, a trend possibly associated with the varied thermal expansion coefficients of elements during the oxidation treatment. Cross-section SEM images of the sintered Mn-Co single-layer and Mn-Co/Mn-Cu-Fe dual-layer oxide spinel coatings in both sintering treatments reveal increased thickness due to higher applied voltages and deposition time, along with weak adhesion between the coating and substrate. Additionally, the deposition is non-uniform not only across the flat surface but also on edge and internal surfaces. The surface SEM images of sintered Mn-Cu-Fe single-layer coatings display a non-uniform

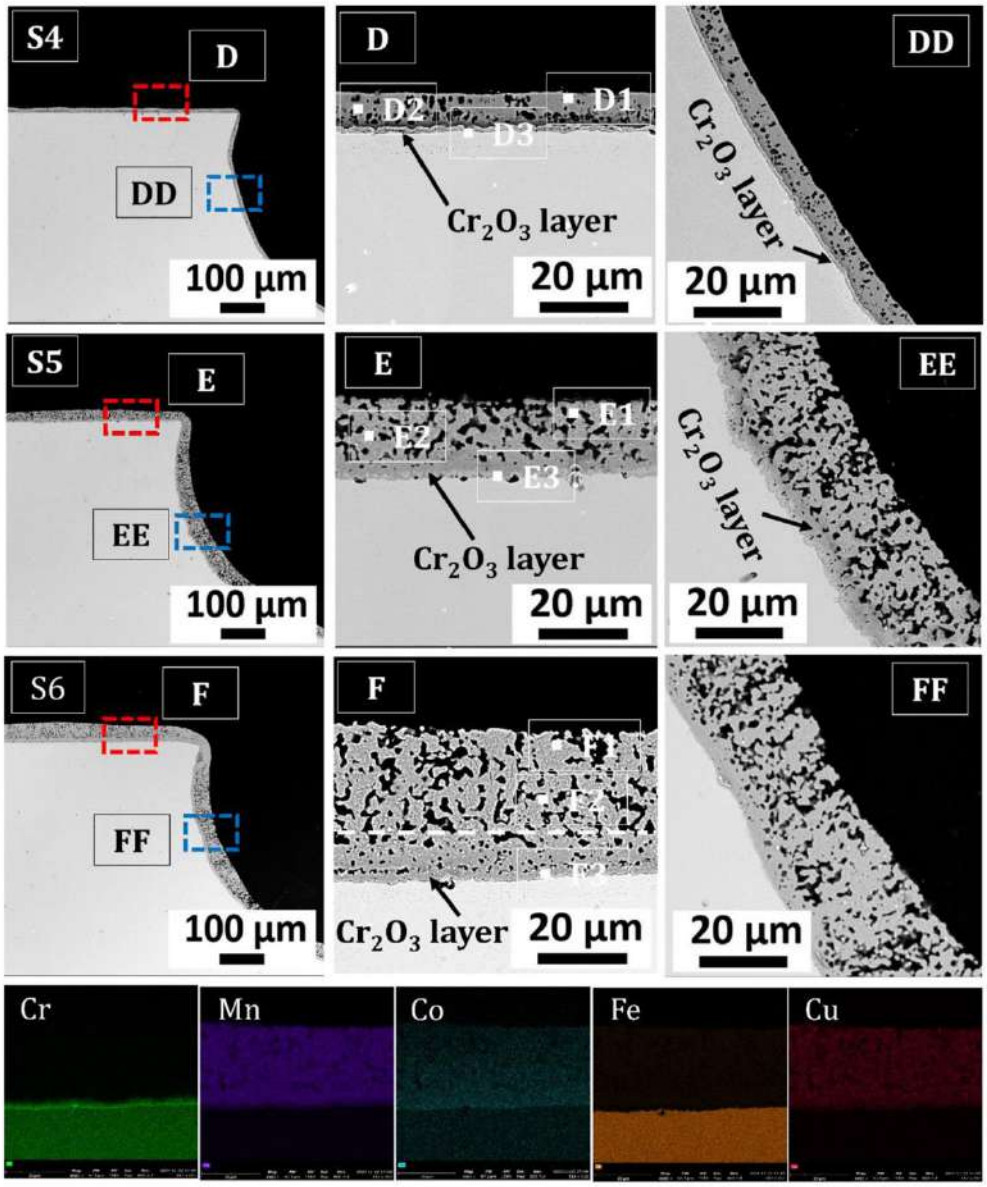

Fig. 7. SEM cross-section images sintered Mn-Co single-layer (S4), Mn-Cu-Fe single-layer (S5), and Mn-Co/Mn-Cu-Fe dual-layer (S6) oxide spinel coatings in reduction treatment, followed by a subsequent oxidation treatment, EDX maps of Mn-Co/Mn-Cu-Fe dual-layer oxide spinel coating (from SEM cross-section of image F).

coating on the substrate in both sintering treatments, attributed to a lower deposition yield. In other words, the chosen applied voltage and deposition time appear inadequate for achieving a uniform and dense coating on the metallic interconnects, as evident in the cross-section SEM images of the sintered Mn-Cu-Fe oxide spinel coating in both sintering treatments. To achieve a uniform and dense single-layer and dual-layer coating on complex-shaped metallic interconnects, the process parameters of the EPD method are optimized, as detailed in Table 1.

Evaluation based on OM images (Fig. 4a) indicates the successful deposition of a uniformly coated layer without cracks on complex-shaped metallic interconnects. Additionally, by appropriately selecting deposition time and applied voltage, the Mn-Co and Mn-Cu-Fe oxide spinel particles in the ethanol solvent effectively cover the entire substrate. According to the SEM images (Fig. 4a and b), the Mn-Co single-layer oxide spinel coating demonstrates higher uniformity and density compared to the Mn-Cu-Fe oxide single-layer spinel coating after sintering in both treatments. Conversely, both the Mn-Cu-Fe single-layer and Mn-Co/Mn-Cu-Fe dual-layer oxide spinel coatings do not display the same level of uniformity and density. This difference can be attributed to the shape of the synthesized Mn-Cu-Fe oxide spinel particles, as shown in Fig. 2. EPD proves to be an efficient technique for applying spinel materials onto complex-shaped metallic interconnects, both in the context of single-layer and double-layer configurations.

Fig. 5 displays a schematic of the sintering mechanism of Mn-Co and Mn-Cu-Fe oxide spinel particles with disordered shapes and different sintering onsets, along with surface SEM images of Mn-Co and Mn-Cu-Fe single-layer oxide spinel coatings on the substrate at different magnification. According to Fig. 5a, the schematic illustrates the pores on the surface of both Mn-Co and Mn-Cu-Fe oxide spinel coatings before and after sintering. Following sintering, there is a reduction in the porosity of

Table 2
Point EDS analysis of sintered single and dual-layer coatings in oxidation and reduction treatment, followed by a subsequent oxidation treatment at specific locations.

	Samples	Atomic concentration (At. %)					
		Point	Cr	Mn	Co	Cu	Fe
Oxidation treatment	Mn-Co oxide spinel coating	A1	0.17	13.44	25.41	–	–
		A2	0.25	12.37	24.01	–	–
		A3	5.01	15.54	25.86	–	–
	Mn-Cu-Fe oxide spinel coating	B1	0.34	19.02	–	9.92	3.87
		B2	2.86	18.07	–	9.47	3.67
		B3	4.95	16.08	–	10.02	1.74
	Mn-Co/ Mn-Cu-Fe oxide spinel coating	C1	0.25	16.56	1.51	6.47	3.00
		C2	0.84	11.93	3.92	4.79	2.27
		C3	2.61	11.90	4.91	3.98	4.91
Reduction + oxidation treatments	Mn-Co oxide spinel coating	D1	0.21	13.20	24.88	–	–
		D2	0.29	12.30	23.10	–	–
		D3	3.86	11.97	19.10	–	–
	Mn-Cu-Fe oxide spinel coating	E1	0.24	23.02	–	12.08	4.66
		E2	0.31	21.31	–	12.26	4.63
		E3	2.84	16.82	–	9.70	8.47
	Mn-Co/ Mn-Cu-Fe oxide spinel coating	F1	0.02	20.73	2.17	12.48	4.23
		F2	0.17	21.97	3.55	12.87	3.86
		F3	1.84	17.48	4.24	8.37	8.30

both coatings. However, the porosity of the Mn-Cu-Fe oxide spinel coating is higher and consists of larger pores compared to the Mn-Co oxide spinel coating. This difference is likely attributed to the particle shape. In Mn-Co oxide spinel powder, the particles exhibit a regular shape, whereas in Mn-Cu-Fe oxide spinel powder, the particle shape is more disordered, as demonstrated in Fig. 2. Consequently, after sintering, the Mn-Cu-Fe oxide spinel coating exhibits higher porosity compared to the Mn-Co oxide spinel coating. In accordance with Fig. 5b, surface SEM images of Mn-Co and Mn-Cu-Fe oxide spinel coatings reveal that the Mn-Cu-Fe oxide spinel coating exhibits greater porosity than the Mn-Co oxide spinel coating, attributable to the morphology of the Mn-Cu-Fe oxide spinel powder. Additionally, it is evident that there are no cracks on the surface of the Mn-Cu-Fe oxide spinel coating. Furthermore, surface SEM images of both Mn-Cu-Fe single-layer and Mn-Co/Mn-Cu-Fe dual-layer oxide spinel coatings in Fig. 4a and b indicate an absence of cracks. However, this observation may be linked to the higher and larger porosity of the Mn-Cu-Fe oxide spinel coating.

Based on the SEM cross-section images of sintered coatings in oxidation and reduction treatment, followed by a subsequent oxidation treatment (as shown in Figs. 6 and 7, respectively), the results indicate uniform, smooth, and crack-free deposition across the complex-shaped metallic interconnect surface, including flat, edge, and internal surfaces. Good adhesion is observed between both single and dual-layer coatings and the complex-shaped metallic interconnect. The analysis of cross-sectional images reveals that the density of single and dual-layer coatings significantly increases (porosity decreases) when subjected to reduction treatment, followed by a subsequent oxidation treatment compared to oxidation alone. The porosity percentages for sintered Mn-Co, Mn-Cu-Fe single-layer oxide spinel coatings, and Mn-Co/Mn-Cu-Fe dual-layer oxide spinel coatings in oxidation treatments are 56%, 23%, and 30%, respectively. Conversely, the porosity percentages for sintered Mn-Co, Mn-Cu-Fe single-layer oxide spinel coatings, and Mn-Co/Mn-Cu-Fe dual-layer oxide spinel coatings in reduction treatment, followed by a subsequent oxidation treatment are 25%, 20%, and 16%, respectively. This difference can be explained by increased diffusion of the Co elements in the metallic state followed by re-oxidation and densification [60]. The superior densification observed in the Mn-Cu-Fe oxide spinel coating compared to the Mn-Co oxide spinel coating can be attributed to the enhanced reactivity among its constituent elements (Mn, Cu, Fe). Additionally, EDX maps of dual-layer oxide spinel coatings are presented to provide a comprehensive understanding of the element distribution and elements diffusion processes. The elemental maps reveal a clear observation of chromium cation diffusion at the interface of sintered Mn-Co/Mn-Cu-Fe dual-layer oxide spinel coatings and the substrate during oxidation, and reduction treatment, followed by a subsequent oxidation treatment. Additionally, elemental maps for Fe, Co, Cu, and Mn show a consistent distribution of these elements after the sintering process. Elemental maps of sintered S1 and S4 (Mn-Co single-layer oxide spinel), S2 and S5 (Mn-Cu-Fe single-layer oxide spinel) in oxidation treatment (S1, and S2), and reduction treatment, followed by a subsequent oxidation treatment (S4, and S5) are presented in Fig. SI1 (supplementary materials).

To examine the distribution of elements within single and dual-layer coating and the diffusion of Cr element, the cross-section of the sample is analyzed using point analysis (Table 2). The results of the point analysis

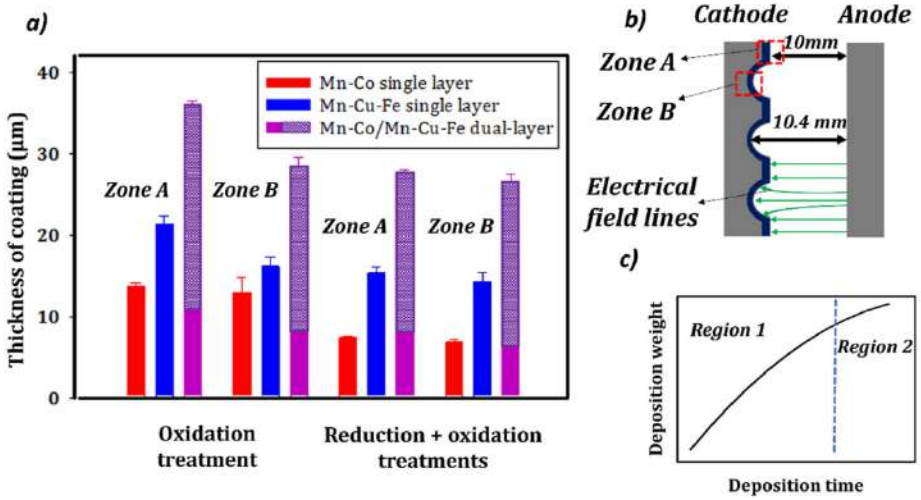

Fig. 8. a) thickness measurements of Mn-Co, Mn-Cu-Fe single-layer, and Mn-Co/Mn-Cu-Fe dual-layer oxide spinel coatings in Zone A and Zone B, b) scheme of coating on complex-shaped metallic interconnect in Zone A and Zone B, and c) graph depicting deposition yield versus deposition time.

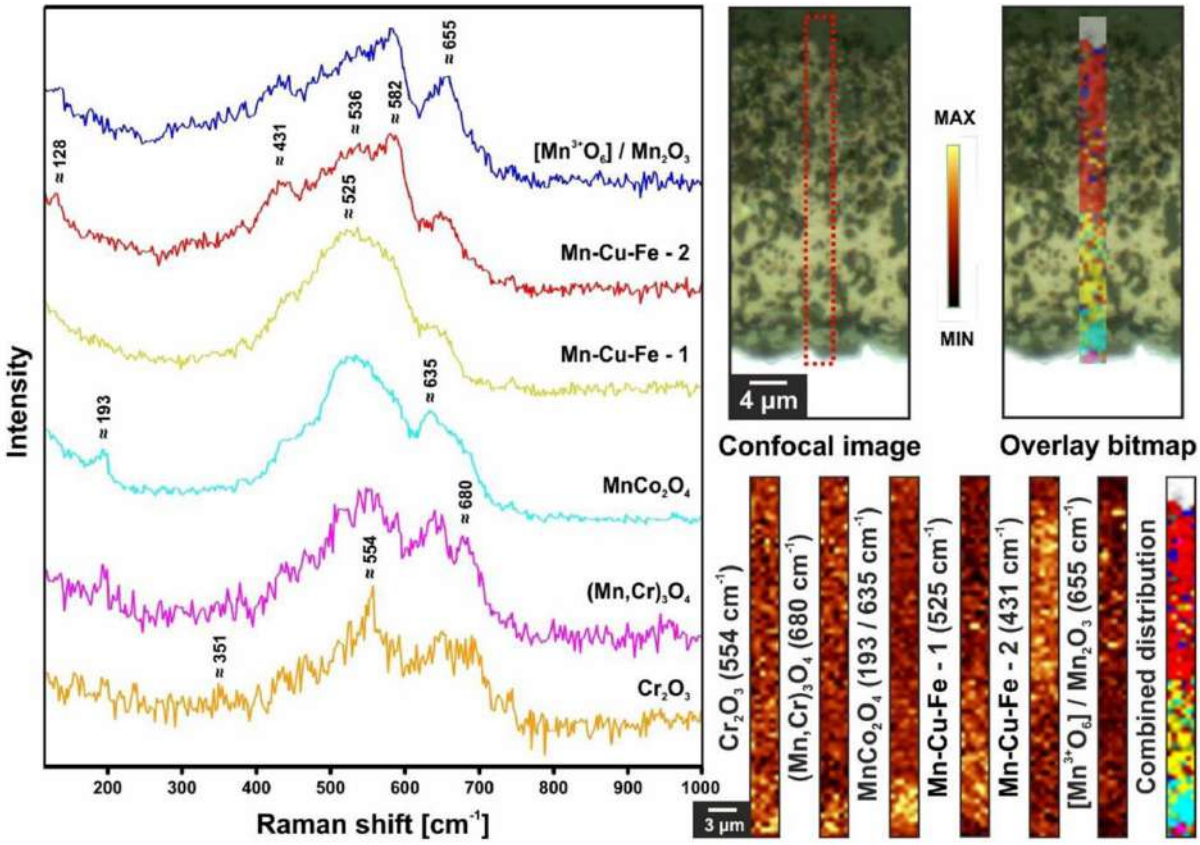

Fig. 9. Raman Confocal imaging of the cross section of as-coated Crofer 22APU steel with dual-layer oxide spinel coating sintered in oxidation environment. The following information concerns all Raman data - red square in confocal image corresponds to area investigated with Raman laser. Raman distribution images (obtained via the integration of the most characteristic band for the particular phase along with value of its Raman shift given in the brackets) are illustrated with the Raman spectra. Each spectrum was also marked with bands that can be unequivocally attributed to corresponding phase(s). (For interpretation of the references to colour in this figure legend, the reader is referred to the Web version of this article.)

indicate that, all types of coatings in reduction treatment, followed by a subsequent oxidation treatment exhibit lower values of Cr at the interaction layer between the coating and substrate compared to those sintered under oxidation treatment. This is evidenced by the comparison of points D3 vs. A3, E3 vs. B3, and F3 vs. C3 (as shown in Figs. 6 and 7). Based on point analysis conducted on both sintered single and dual-layer coatings in both sintering treatments, the Cr content is lower in the outer region compared to the inner region, as evidenced by the comparison of points A1 vs. A3, for example (as shown in Figs. 6 and 7). EDX line scan of sintered Mn-Co, Mn-Cu-Fe single-layer and Mn-Co/Mn-Cu-Fe dual-layer oxide spinel coatings in oxidation and reduction treatment, followed by a subsequent oxidation treatment are presented in Fig. SI2 (supplementary materials).

Fig. 8a presents measurements of the thickness of all coatings within Zone A (the flat part) and Zone B (the convex part). According to Fig. 8a, the thickness of all coatings is reduced in the case of reduction treatment, followed by a subsequent oxidation treatment compared to oxidation treatment. In addition, the differences in thickness between Mn-Co and Mn-Cu-Fe single-layer oxide spinel coatings under identical sintering conditions are influenced by the process parameters of EPD, such as applied voltage and deposition time. Achieving a uniformly coated Mn-Cu-Fe across the entire sample area requires higher voltage and deposition time compared to Mn-Co oxide spinel coating. According to Fig. 8b, the difference in coating thickness between Zone A and Zone B can be attributed to the non-uniform distribution of the electrical field and the varying distances between the anode and cathode. According to Fig. 8a and b, the thicknesses of the Mn-Co, Mn-Cu-Fe single-layer, and Mn-Co/Mn-Cu-Fe dual-layer oxide spinel coatings in Zone A are 6%, 24%, and 21% higher compared to Zone B at the same condition of EPD parameters. Furthermore, initially the coating builds up with higher deposition rate (region 1), whereas after the formation of certain thickness, which acts as an insulating layer on the substrate, the deposition yield remains constant (region 2). According to Fig. 8c, the variation in deposition yield as a function of deposition time in region 1 is much higher than in region 2. Consequently, in Zone A, the deposition yield remains constant after the formation of an insulating layer, even with an increase in deposition time. On the other hand, in Zone B, the deposition yield increases until the formation of an insulating layer across the entire substrate. Furthermore, the variation in coating thickness between both zones is not substantial, as shown in Fig. 8a.

Since Raman spectroscopy has already been proven by the authors to unravel many uncertainties in similar systems [59], herein Raman imaging revealed the presence of six different phases for dual-layer protective coatings (Fig. 9). Starting from the steel/coating interface, two phases forming thin interlayers, typical for Crofer 22APU steel, can be seen – Cr_2O_3, based on the presence of bands at approximately 351 and 554 cm^{-1} (the most characteristic) [61], as well as $(Mn,Cr)_3O_4$ spinel with a characteristic mode at approximately 680 cm^{-1} [62]. Above them, one can observe a distinctive layer in the confocal image that is built from $MnCo_2O_4$ (the first coating component), based on assigned bands at around 193 and 635 cm^{-1}. The position of the latter one, being at the same time the most characteristic mode, is noticeably shifted towards

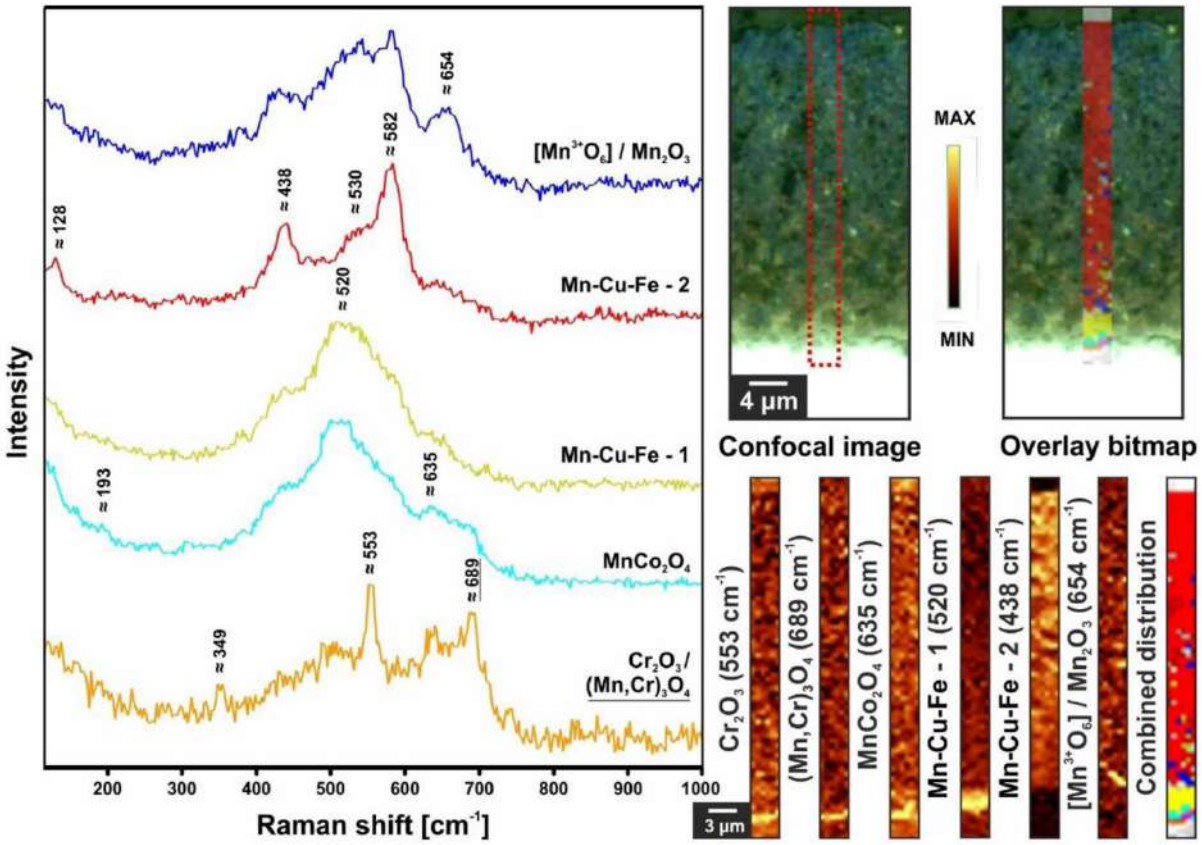

Fig. 10. Raman Confocal imaging of the cross section of as-coated Crofer 22APU steel with dual-layer coating sintered in reduction treatment, followed by a subsequent oxidation treatment environment (for Cr_2O_3 and Mn-Cr spinel one spectrum corresponds to both phases – underlined values refer to spinel phase).

lower Raman shift values compared to literature works [63,64]. It may result from the thermally-induced Jahn-Taller effect, typical for this spinel, which was also described by the authors in Ref. [59]. The dependence of the Raman spectrum of solely deposited $MnCo_2O_4$ on the laser power is illustrated in Fig. SI3 (supplementary materials). Another two layers that were revealed in distribution images (Fig. 9) are composed mainly of Mn-Cu-Fe spinel of different degrees of ordering. The inner, less ordered layer (labelled as "1") is illustrated with broad bands, with one distinctive, most intense mode at around 525 cm^{-1} [65], whereas the outer, more ordered layer (labelled as "2"), is illustrated with well-defined, narrower bands at approximately 128, 431 (the most characteristic), 536, and 582 cm^{-1} [65,66]. It is highly likely that such differences stem from mutual diffusion processes occurring during thermal treatment, resulting from Cu, Fe, and Co gradients in both coating components. Based on EDX mappings (Fig. 6), such interdiffusion occurs along the entire thickness of coating, however with the increased concentration of Co on spinals' interface. Therefore, the structure of the inner Mn-Cu-Fe layer ("1") may be altered by migrating cations from the $MnCo_2O_4$ spinel more severely, whereas the outer layer is less affected, hence more ordered and equilibrated. Moreover, the corresponding spectrum of $MnCo_2O_4$ is also dominated by the broad bands coming from the less ordered Mn-Cu-Fe spinel, indicating the formation of a reaction layer. Finally, an additional band at approximately 655 cm^{-1} increases in intensity locally within the outer layer ("Mn-Cu-Fe – 2"). This band originates from a higher share of Mn cations (highly probable Mn^{3+} - labelled as "$[Mn^{3+}O_6]$") present within the octahedral sites of the Mn-Cu-Fe spinel [66,67] or in the form of Mn_2O_3 (bixbyite – labelled as "Mn_2O_3") [68].

When using alternative treatment (reduction, followed by a subsequent oxidation), similar findings were reported (Fig. 10), but with some noteworthy differences. The most relevant one concern a much higher share of reacted (Mn, Cu, Fe, Co)$_3O_4$ spinel in favor of both $MnCo_2O_4$ and disordered Mn-Cu-Fe spinel, probably resulting from the reducing atmosphere during one step of the coating's sintering, leading to more pronounced diffusion processes. This is in very good agreement with EDS mapping analyses demonstrating a considerably smaller area of increased Co concentration in favor of Cu and Fe for reduction treatment, followed by a subsequent oxidation treatment (Fig. 7, S6 sample). Furthermore, bands assigned to the more ordered Mn-Cu-Fe spinel are even narrower and much better defined compared to specimens treated only in an oxidizing atmosphere that only further proves a higher efficiency of reduction treatment, followed by a subsequent oxidation treatment.

Fig. 11 depicts a schematic representation of the diffusion of elements and the formation of a chromium oxide, as well as (Mn,Cr)$_3O_4$ layers and reaction layer at the interface of stainless steel and coating. This occurs in the sintered Mn-Co/Mn-Cu-Fe dual-layer oxide spinel coating during oxidation treatment, and reduction treatment, followed by a subsequent oxidation treatment. According to Fig. 11, Cr elements diffuse from the substrate to the interface and react with oxygen to form the chromium oxide layer. Mn elements from the coating (high concentration of Mn element) migrate towards the Cr_2O_3 layer and undergo a reaction with Cr elements, resulting in the formation of the (Mn, Cr)$_3O_4$ reaction layer between the coating and the chromium oxide layer during both sintering treatments. For both types of treatments, the diffusion of Co, Mn, Cu, and Fe elements between the Mn-Co and Mn-Cu-Fe spinel coatings occurs along the entire thickness. However, during oxidation treatment, this process is especially enhanced at the interface

authors extend their gratitude to Dr. Piotr Jeleń from AGH University of Krakow for his assistance in Raman spectroscopy measurements.

Appendix A. Supplementary data

Supplementary data to this article can be found online at https://doi.org/10.1016/j.ijhydene.2024.07.447.

References

[1] Zanchi E, Sabato AG, Molin S, Cempura G, Boccaccini AR, Smeacetto F. Recent advances on spinel-based protective coatings for solid oxide cell metallic interconnects produced by electrophoretic deposition. Mater Lett 2021;286:129229. https://doi.org/10.1016/j.matlet.2020.129229.

[2] Zarabi Golkhatmi S, Asghar MI, Lund PD. A review on solid oxide fuel cell durability: latest progress, mechanisms, and study tools. Renew Sustain Energy Rev 2022;161:112339. https://doi.org/10.1016/j.rser.2022.112339.

[3] Zhu JH, Chesson DA, Yu YT. Review—(Mn,Co) 3 O 4 -based spinels for SOFC interconnect coating application. J Electrochem Soc 2021;168:114519. https://doi.org/10.1149/1945-7111/ac3a29.

[4] Zhang Y, Zhang Y, Wu C, Yang Y, Li Q, Chen Y. Oxidation behavior and electrical properties of metal interconnects with Ce-doped Ni–Mn spinel coatings. Ceram Int 2022;48:9550–7. https://doi.org/10.1016/j.ceramint.2021.12.153.

[5] Talic B, Venkatachalam V, Hendriksen PV, Kiebach R. Comparison of MnCo2O4 coated Crofer 22 H, 441, 430 as interconnects for intermediate-temperature solid oxide fuel cell stacks. J Alloys Compd 2020;821:153229. https://doi.org/10.1016/j.jallcom.2019.153229.

[6] Reddy MJ, Kamecki B, Talic B, Zanchi E, Smeacetto F, Hardy JS, et al. Experimental review of the performances of protective coatings for interconnects in solid oxide fuel cells. J Power Sources 2023;568. https://doi.org/10.1016/j.jpowsour.2023.232831.

[7] Talic B, Molin S, Hendriksen PV, Lein HL. Effect of pre-oxidation on the oxidation resistance of Crofer 22 APU. Corrosion Sci 2018;138:189–99. https://doi.org/10.1016/j.corsci.2018.04.016.

[8] Talic B, Molin S, Wiik K, Hendriksen PV, Lein HL. Comparison of iron and copper doped manganese cobalt spinel oxides as protective coatings for solid oxide fuel cell interconnects. J Power Sources 2017;372:145–56. https://doi.org/10.1016/j.jpowsour.2017.10.060.

[9] Zanchi E, Ignaczak J, Molin S, Cempura G, Boccaccini AR, Smeacetto F. Electrophoretic co-deposition of Mn1.5Co1.5O4, Fe2O3 and CuO: unravelling the effect of simultaneous addition of Cu and Fe on the microstructural, thermo-mechanical and corrosion properties of in-situ modified spinel coatings for solid oxide cell intercon. J Eur Ceram Soc 2022;42:3271–81. https://doi.org/10.1016/j.jeurceramsoc.2022.02.008.

[10] Shen F, Lu K. Co3O4/Sm-Doped CeO2/Co3O4 trilayer coating on AISI 441 interconnect for solid oxide fuel cells. ACS Appl Mater Interfaces 2017;9:6022–9. https://doi.org/10.1021/acsami.6b14562.

[11] Wu J, Liu X. Recent development of SOFC metallic interconnect. J Mater Sci Technol 2010;26:293–305. https://doi.org/10.1016/S1005-0302(10)60049-7.

[12] Shaigan N, Qu W, Ivey DG, Chen W. A review of recent progress in coatings, surface modifications and alloy developments for solid oxide fuel cell ferritic stainless steel interconnects. J Power Sources 2010;195:1529–42. https://doi.org/10.1016/j.jpowsour.2009.09.069.

[13] Zhu Z, Darl-Uzu C, Pal U, Gopalan S, Hussain AM, Dale N, et al. Comparison of Cu–Mn and Mn–Co spinel coatings for solid oxide fuel cell interconnects. Int J Hydrogen Energy 2022;47:36953–63. https://doi.org/10.1016/j.ijhydene.2022.08.239.

[14] Liu K, Xu S, Shi J, Teng F, Yu X, Sun J. Impact of different atmospheres on oxidation and electrical performance of a solid oxide fuel cell interconnect with Co-containing protective coating. Energy Fuel 2020;34:8864–71. https://doi.org/10.1021/acs.energyfuels.0c01213.

[15] Jin Y, Sheng J, Hao G, Guo M, Hao W, Yang Z, et al. Highly dense (Mn,Co)3O4 spinel protective coating derived from Mn–Co metal precursors for SOFC interconnect applications. Int J Hydrogen Energy 2022;47:13960–8. https://doi.org/10.1016/j.ijhydene.2022.02.129.

[16] Larring Y, Norby T. Spinel and perovskite functional layers between plansee metallic interconnect (Cr-5 wt % Fe-1 wt % Y[sub 2]O[sub 3]) and ceramic (La[sub 0.85]Sr[sub 0.15])[sub 0.91]MnO[sub 3] cathode materials for solid oxide fuel cells. J Electrochem Soc 2000;147:3251. https://doi.org/10.1149/1.1393891.

[17] Yang Z, Xia G, Nie Z, Templeton J, Stevenson JW. Ce-modified (Mn,Co) 3 O4 spinel coatings on ferritic stainless steels for SOFC interconnect applications. Electrochem Solid State Lett 2008;11. https://doi.org/10.1149/1.2929066.

[18] Talic B, Falk-Windisch H, Venkatachalam V, Hendriksen PV, Wiik K, Lein HL. Effect of coating density on oxidation resistance and Cr vaporization from solid oxide fuel cell interconnects. J Power Sources 2017;354:57–67. https://doi.org/10.1016/j.jpowsour.2017.04.023.

[19] Koszelow D, Makowska M, Marone F, Karczewski J, Jasiński P, Molin S. High temperature corrosion evaluation and lifetime prediction of porous Fe22Cr stainless steel in air in temperature range 700–900 °C. Corrosion Sci 2021;189. https://doi.org/10.1016/j.corsci.2021.109589.

[20] Molin S, Sabato AG, Bindi M, Leone P, Cempura G, Salvo M, et al. Microstructural and electrical characterization of Mn-Co spinel protective coatings for solid oxide cell interconnects. J Eur Ceram Soc 2017;37:4781–91. https://doi.org/10.1016/j.jeurceramsoc.2017.07.011.

[21] Zhang HH, Zeng CL. Preparation and performances of Co-Mn spinel coating on a ferritic stainless steel interconnect material for solid oxide fuel cell application. J Power Sources 2014;252:122–9. https://doi.org/10.1016/j.jpowsour.2013.12.007.

[22] Molin S, Jasinski P, Mikkelsen L, Zhang W, Chen M, Hendriksen PV. Low temperature processed MnCo2O4 and MnCo1.8Fe0.2O4 as effective protective coatings for solid oxide fuel cell interconnects at 750 °C. J Power Sources 2016;336:408–18. https://doi.org/10.1016/j.jpowsour.2016.11.011.

[23] Sabato AG, Zanchi E, Molin S, Cempura G, Javed H, Herbrig K, et al. Mn-Co spinel coatings on Crofer 22 APU by electrophoretic deposition: up scaling, performance in SOFC stack at 850 °C and compositional modifications. J Eur Ceram Soc 2021;41:4496–504. https://doi.org/10.1016/j.jeurceramsoc.2021.03.030.

[24] Oskouyi OE, Shahmiri M, Maghsoudipour A, Hasheminiasari M. Pulsed constant voltage electrophoretic deposition of YSZ electrolyte coating on conducting porous Ni–YSZ cermet for SOFCs applications. J Alloys Compd 2019;785:220–7. https://doi.org/10.1016/j.jallcom.2019.01.166.

[25] Oskouyi OE, Maghsoudipour A, Shahmiri M, Hasheminiasari M. Preparation of YSZ electrolyte coating on conducting porous Ni–YSZ cermet by DC and pulsed constant voltage electrophoretic deposition process for SOFCs applications. J Alloys Compd 2019;795:361–9. https://doi.org/10.1016/j.jallcom.2019.04.334.

[26] Yoo J, Woo SK, Yu JH, Lee S, Park GW. La0.8Sr0.2MnO3 and (Mn1.5Co1.5)O4 double layer coated by electrophoretic deposition on Crofer22 APU for SOEC interconnect applications. Int J Hydrogen Energy 2009;34:1542–7. https://doi.org/10.1016/j.ijhydene.2008.12.005.

[27] Aznam I, Mah JCW, Muchtar A, Somalu MR, Ghazali MJ. Electrophoretic deposition of (Cu,Mn,Co)3O4 spinel coating on SUS430 ferritic stainless steel: process and performance evaluation for solid oxide fuel cell interconnect applications. J Eur Ceram Soc 2021;41:1360–73. https://doi.org/10.1016/j.jeurceramsoc.2020.09.074.

[28] Tan KH, Rahman HA, Taib H. Coating layer and influence of transition metal for ferritic stainless steel interconnector solid oxide fuel cell: a review. Int J Hydrogen Energy 2019;44:30591–605. https://doi.org/10.1016/j.ijhydene.2019.06.155.

[29] Wang R, Sun Z, Choi JP, Basu SN, Stevenson JW, Tucker MC. Ferritic stainless steel interconnects for protonic ceramic electrochemical cell stacks: oxidation behavior and protective coatings. Int J Hydrogen Energy 2019;44:25297–309. https://doi.org/10.1016/j.ijhydene.2019.08.041.

[30] Wang R, Sun Z, Pal UB, Gopalan S, Basu SN. Mitigation of chromium poisoning of cathodes in solid oxide fuel cells employing CuMn1.8O4 spinel coating on metallic interconnect. J Power Sources 2018;376:100–10. https://doi.org/10.1016/j.jpowsour.2017.11.069.

[31] Sun Z, Gopalan S, Pal UB, Basu SN. Cu1.3Mn1.7O4 spinel coatings deposited by electrophoretic deposition on Crofer 22 APU substrates for solid oxide fuel cell applications. Surf Coating Technol 2017;323:49–57. https://doi.org/10.1016/j.surfcoat.2016.09.028.

[32] Bednarz M, Molin S, Bobruk M, Stygar M, Długoń E, Sitarz M, et al. High-temperature oxidation of the Crofer 22 H ferritic steel with Mn1.45Co1.45Fe0.1O4 and Mn1.5Co1.5O4 spinel coatings under thermal cycling conditions and its properties. Mater Chem Phys 2019;225:227–38. https://doi.org/10.1016/j.matchemphys.2018.12.090.

[33] Ludwig GA, Korb MA, Lima DAS, Macías MA, Gauthier GH, Malfatti CF. Protective coatings for AISI 430 stainless steel at high temperatures using perovskite oxides La0.6Sr0.4CoO3 on spinel type oxide NiFe2O4. Ceram Int 2015;41:14561–73. https://doi.org/10.1016/j.ceramint.2015.07.173.

[34] Tan KH, Rahman HA, Taib H. Ba0.5Sr0.5Co0.8Fe0.2O3−δ-Sm0.2Ce0.8O1.9 carbonate perovskite coating on ferritic stainless steel interconnect for low temperature solid oxide fuel cells. Mater Chem Phys 2020;254:123433. https://doi.org/10.1016/j.matchemphys.2020.123433.

[35] Shen F, Lu K. CoxFe1-x oxide coatings on metallic interconnects for solid oxide fuel cells. J Power Sources 2016;330:231–9. https://doi.org/10.1016/j.jpowsour.2016.09.018.

[36] Bik M, Stygar M, Jeleń P, Dąbrowa J, Leśniak M, Brylewski T, et al. Protective-conducting coatings based on black glasses (SiOC) for application in Solid Oxide Fuel Cells. Int J Hydrogen Energy 2017;42:27298–307. https://doi.org/10.1016/j.ijhydene.2017.09.069.

[37] Jalilvand G, Faghihi-Sani MA. Fe doped Ni-Co spinel protective coating on ferritic stainless steel for SOFC interconnect application. Int J Hydrogen Energy 2013;38:12007–14. https://doi.org/10.1016/j.ijhydene.2013.06.105.

[38] Mousa Mirabad H, Nemati A, Faghihi-Sani MA, Fakouri Hasanabadi M, Abdoli H. Effect of YSZ sol-gel coating on interaction of Crofer22 APU with sealing glass for solid oxide fuel/electrolysis cell. J Alloys Compd 2020;847:156496. https://doi.org/10.1016/j.jallcom.2020.156496.

[39] Wu W, Guan W, Wang G, Liu W, Zhang Q, Chen T, et al. Evaluation of Ni80Cr20/(La0.75Sr 0.25)0.95MnO3 dual layer coating on SUS 430 stainless steel used as metallic interconnect for solid oxide fuel cells. Int J Hydrogen Energy 2014;39:996–1004. https://doi.org/10.1016/j.ijhydene.2013.10.094.

[40] Chatterjee D, Biswas S. Development of chromium barrier coatings for solid oxide fuel cells. Int J Hydrogen Energy 2011;36:4530–9. https://doi.org/10.1016/j.ijhydene.2010.04.114.

[41] Waluyo NS, Park SS, Song RH, Lee SB, Lim TH, Hong JE, et al. Protective coating based on manganese–copper oxide for solid oxide fuel cell interconnects: plasma spray coating and performance evaluation. Ceram Int 2018;44:11576–81. https://doi.org/10.1016/j.ceramint.2018.03.220.

[42] Grünwald N, Sebold D, Sohn YJ, Menzler NH, Vaßen R. Self-healing atmospheric plasma sprayed Mn1.0Co1.9Fe0.1O4 protective interconnector coatings for solid

oxide fuel cells. J Power Sources 2017;363:185–92. https://doi.org/10.1016/j.jpowsour.2017.07.072.
[43] Lenka RK, Patro PK, Sharma J, Mahata T, Sinha PK. Evaluation of La0.75Sr0.25Cr0.5Mn0.5O3 protective coating on ferritic stainless steel interconnect for SOFC application. Int J Hydrogen Energy 2016;41:20365–72. https://doi.org/10.1016/j.ijhydene.2016.08.143.
[44] Unal FA, Mat MD, Demir I, Kaplan Y, Veziroglu N. Application of a coating mixture for solid oxide fuel cell interconnects. Int J Hydrogen Energy 2015;40:7689–93. https://doi.org/10.1016/j.ijhydene.2015.03.031.
[45] Saeidpour F, Ebrahimifar H. Effect of nanostructure Fe-Ni-Co spinel oxides/Y2O3 coatings on the high-temperature oxidation behavior of Crofer 22 APU stainless steel interconnect. Corrosion Sci 2021;182:109280. https://doi.org/10.1016/j.corsci.2021.109280.
[46] Zhu JH, Zhang Y, Basu A, Lu ZG, Paranthaman M, Lee DF, et al. LaCrO3-based coatings on ferritic stainless steel for solid oxide fuel cell interconnect applications. Surf Coating Technol 2004;177–178:65–72. https://doi.org/10.1016/j.surfcoat.2003.05.003.
[47] Hoyt KO, Gannon PE, White P, Tortop R, Ellingwood BJ, Khoshuei H. Oxidation behavior of (Co,Mn) 3O 4 coatings on preoxidized stainless steel for solid oxide fuel cell interconnects. Int J Hydrogen Energy 2012;37:518–29. https://doi.org/10.1016/j.ijhydene.2011.09.028.
[48] Geng S, Wang Q, Wang W, Zhu S, Wang F. Sputtered Ni coating on ferritic stainless steel for solid oxide fuel cell interconnect application. Int J Hydrogen Energy 2012;37:916–20. https://doi.org/10.1016/j.ijhydene.2011.03.160.
[49] Fu Q, Tietz F, Sebold D, Wessel E, Buchkremer HP. Magnetron-sputtered cobalt-based protective coatings on ferritic steels for solid oxide fuel cell interconnect applications. Corrosion Sci 2012;54:68–76. https://doi.org/10.1016/j.corsci.2011.08.051.
[50] Ignaczak J, Naumovich Y, Górnicka K, Jamroz J, Wróbel W, Karczewski J, et al. Preparation and characterisation of iron substituted Mn1.7Cu1.3-xFexO4 spinel oxides (x = 0, 0.1, 0.3, 0.5). J Eur Ceram Soc 2020;40:5920–9. https://doi.org/10.1016/j.jeurceramsoc.2020.07.001.
[51] Smeacetto F, De Miranda A, Cabanas Polo S, Molin S, Boccaccini D, Salvo M, et al. Electrophoretic deposition of Mn1.5Co1.5O4 on metallic interconnect and interaction with glass-ceramic sealant for solid oxide fuel cells application. J Power Sources 2015;280:379–86. https://doi.org/10.1016/j.jpowsour.2015.01.120.
[52] Zanchi E, Talic B, Sabato AG, Molin S, Boccaccini AR, Smeacetto F. Electrophoretic co-deposition of Fe2O3 and Mn1,5Co1,5O4: processing and oxidation performance of Fe-doped Mn-Co coatings for solid oxide cell interconnects. J Eur Ceram Soc 2019;39:3768–77. https://doi.org/10.1016/j.jeurceramsoc.2019.05.024.
[53] Stevenson JW, Yang ZG, Xia GG, Nie Z, Templeton JD. Long-term oxidation behavior of spinel-coated ferritic stainless steel for solid oxide fuel cell interconnect applications. J Power Sources 2013;231:256–63. https://doi.org/10.1016/j.jpowsour.2013.01.033.
[54] Zanchi E, Sabato AG, Monterde MC, Bernadet L, Torrell M, Calero JA, et al. Electrophoretic deposition of MnCo2O4 coating on solid oxide cell interconnects manufactured through powder metallurgy. Mater Des 2023;227:111768. https://doi.org/10.1016/j.matdes.2023.111768.
[55] Talic B, Wulff AC, Molin S, Andersen KB, Zielke P, Frandsen HL. Investigation of electrophoretic deposition as a method for coating complex shaped steel parts in solid oxide cell stacks. Surf Coating Technol 2019;380:1–8. https://doi.org/10.1016/j.surfcoat.2019.125093.
[56] Sun Z, Wang R, Nikiforov AY, Gopalan S, Pal UB, Basu SN. CuMn1.8O4 protective coatings on metallic interconnects for prevention of Cr poisoning in solid oxide fuel cells. J Power Sources 2018;378:125–33. https://doi.org/10.1016/j.jpowsour.2017.12.031.
[57] Ignaczak J, Zeng L, Sanchez DF, Makowska M, Górnicka K, Lankauf K, et al. Fe-modified Mn2CuO4 spinel oxides: coatings based on abundant elements for solid oxide cell interconnects. Int J Hydrogen Energy 2023;8. https://doi.org/10.1016/j.ijhydene.2023.06.041.
[58] Ekhlasiosgouei O, Smeacetto F, Molin S. Suspension and process parameters selection for electrophoretic deposition of Mn–Co spinel coating on steel interconnects. Int J Hydrogen Energy 2024;60:1054–67. https://doi.org/10.1016/j.ijhydene.2024.02.252.
[59] Mazur Ł, Ignaczak J, Bik M, Molin S, Sitarz M, Gil Aleksander, et al. Effectiveness of a dual surface modification of metallic interconnects for application in energy conversion devices. Int J Hydrogen Energy 2022;47:6295–311. https://doi.org/10.1016/j.ijhydene.2021.11.256.
[60] Bobruk M, Molin S, Chen M, Brylewski T, Hendriksen PV. Sintering of MnCo2O4 coatings prepared by electrophoretic deposition. Mater Lett 2018;213:394–8. https://doi.org/10.1016/j.matlet.2017.12.046.
[61] Mougin J, Le Bihan T, Lucazeau G. High-pressure study of Cr2O3 obtained by high-temperature oxidation by X-ray diffraction and Raman spectroscopy. J Phys Chem Solid 2001;62:553–63. https://doi.org/10.1016/S0022-3697(00)00215-8.
[62] Farrow RL, Mattern PL, Nagelberg AS. Characterization of surface oxides by Raman spectroscopy. Appl Phys Lett 1980;36:212–4. https://doi.org/10.1063/1.91429.
[63] Hosterman BD. Raman spectroscopic study of solid solution spinel oxides. 2011.
[64] Yuvaraj S, Vignesh A, Shanmugam S, Kalai Selvan R. Nitrogen-doped Multi-walled Carbon Nanotubes-MnCo2O4 microsphere as electrocatalyst for efficient oxygen reduction reaction. Int J Hydrogen Energy 2016;41:15199–207. https://doi.org/10.1016/j.ijhydene.2016.06.115.
[65] Lutz HD, Müller B, Steiner HJ. Lattice vibration spectra. LIX. Single crystal infrared and Raman studies of spinel type oxides. J Solid State Chem 1991;90:54–60. https://doi.org/10.1016/0022-4596(91)90171-D.
[66] Van Everbroeck T, Ciocarlan RG, Van Hoey W, Mertens M, Cool P. Copper-containing mixed metal oxides (Al, Fe, Mn) for application in three-way catalysis. Catalysts 2020;10:1–20. https://doi.org/10.3390/catal10111344.
[67] Yang X, Tang W, Liu Z, Makita Y, Ooi K. Synthesis of lithium-rich LixMn2O4 spinels by lithiation and heat-treatment of defective spinels. J Mater Chem 2002;12:489–95. https://doi.org/10.1039/b109463g.
[68] Shim SH, LaBounty D, Duffy TS. Raman spectra of bixbyite, Mn2O3, up to 40 GPa. Phys Chem Miner 2011;38:685–91. https://doi.org/10.1007/s00269-011-0441-4.

Supporting information

Preparation of $MnCo_2O_4$ and $Mn_{1.7}CuFe_{0.3}O_4$ single-layer, and novel $MnCo_2O_4$/ $Mn_{1.7}CuFe_{0.3}O_4$ dual-layer spinel protective coatings on complex-shaped metallic interconnects by EPD method

Omid Ekhlasiosgouei [a, 1], Maciej Bik[b], Sebastian Molin[a]

[a] Advanced Materials Center, Faculty of Electronics, Telecommunications and Informatics, Gdansk University of Technology, Gdansk, Poland

[b] Faculty of Materials Science and Ceramics, AGH University of Krakow, Krakow, Poland

Fig. SI1 shows SEM cross-section images and elemental maps of sintered S1 and S4 (Mn-Co single-layer oxide spinel coating), and S2 and S5 (Mn-Cu-Fe single-layer oxide spinel coating), in oxidation treatment (S1, and S2), and reduction + oxidation treatment (S4, and S5). The elemental maps reveal a clear chromium cations diffusion at the interface of sintered Mn-Co, and Mn-Cu-Fe single-layer oxide spinel coating and the substrate during oxidation, and reduction + oxidation treatments. Additionally, elemental maps for Fe, Co, Cu, and Mn show a consistent distribution of these elements after the sintering process.

[1] Corresponding author, Email address: omid.ekhlasiosgouei@pg.edu.pl

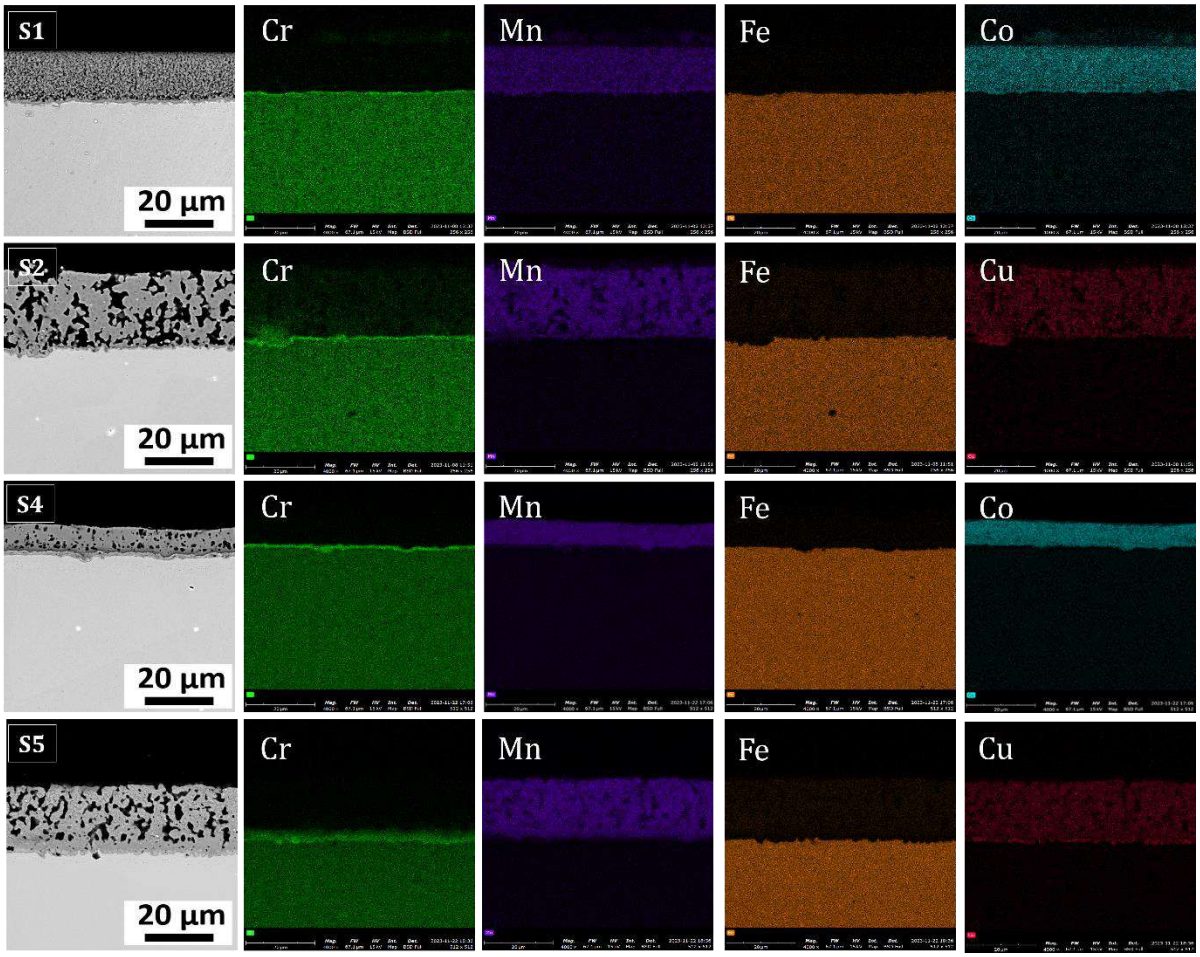

Fig. SI1. SEM cross-section images and EDS-X-ray elemental maps of sintered S1 and S4 (Mn-Co single-layer oxide spinel coating), and S2 and S5 (Mn-Cu-Fe single-layer oxide spinel coating) in oxidation treatment (S1, and S2), and reduction + oxidation treatment (S4, and S5).

Fig. SI2 shows the EDX line scan of sintered Mn-Co, Mn-Cu-Fe single and Mn-Co/Mn-Cu-Fe dual-layer coatings in oxidation and reduction+ oxidation treatments. The elemental line scan confirms that the oxide scale layer between the sintered single and dual-layer coatings in reduction + oxidation treatments and the alloy is thinner than that sintered in oxidation treatment. Consequently, it is anticipated to serve as a protective barrier, preventing the outward diffusion of cations and the inward diffusion of oxygen ions. Furthermore, the migration of Cr cation towards the outer surface is ascribed to the creation of an inner layer between the oxide scale and the coatings. This phenomenon occurs due to the presence of transition metals and the formation of chromium oxide on the alloy's surface. The findings

reveal that the concentration of Cr in the upper region is lower compared to the coating-alloy interface, suggesting that the sintered Mn-Co, Mn-Cu-Fe, and dual-layer Mn-Co/Mn-Cu-Fe coatings in reduction + oxidation treatments effectively prevent Cr evaporation and cathode poisoning.

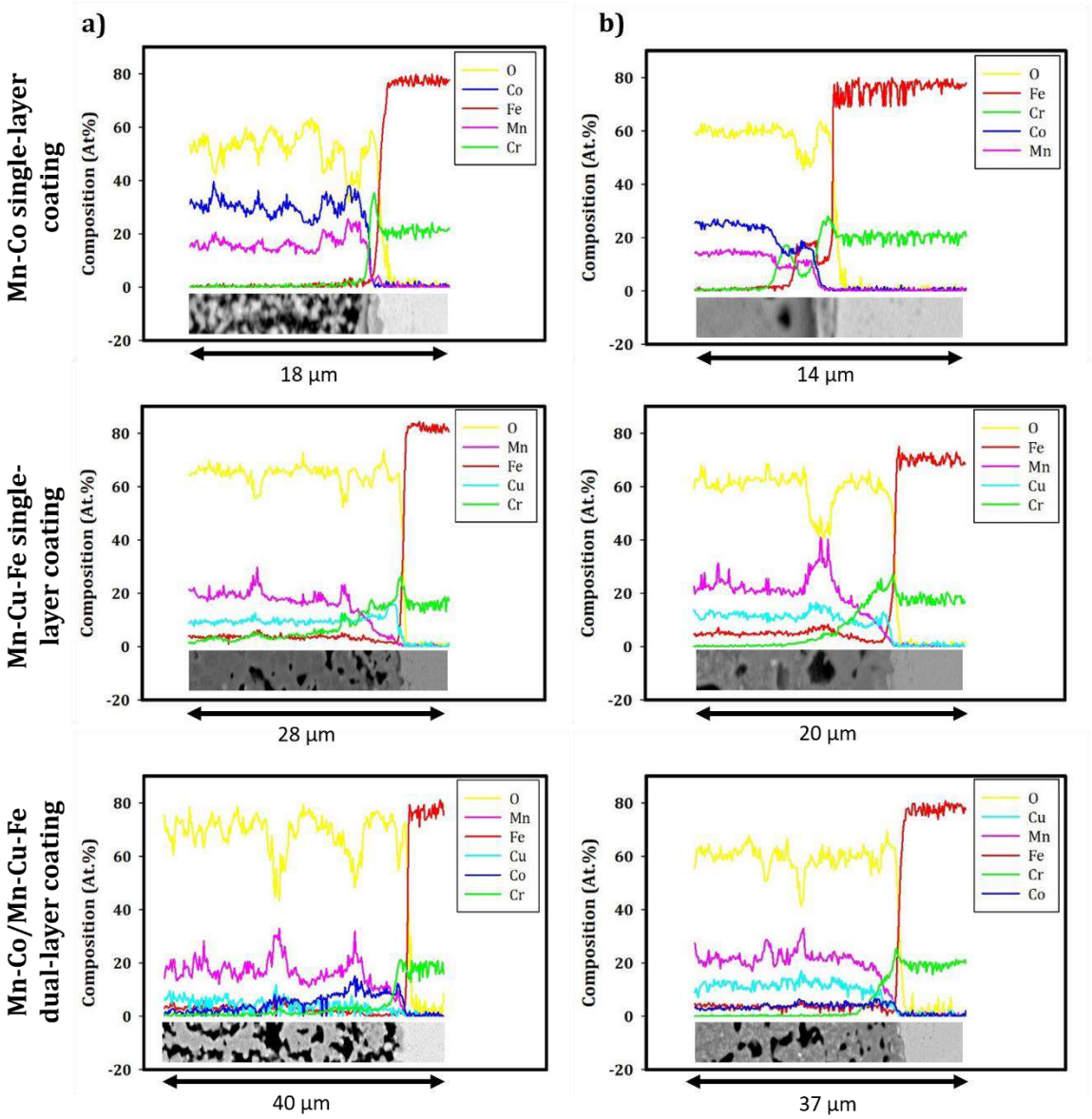

Fig. SI2. EDX line scan of sintered Mn-Co and Mn-Cu-Fe single and Mn-Co/Mn-Cu-Fe dual-layer coatings in: a) oxidation treatment and b) reduction+ oxidation treatments.

Fig. SI3 shows Raman spectra taken from cross section of $MnCo_2O_4$ layer on Crofer 22 APU steel using varying laser power.

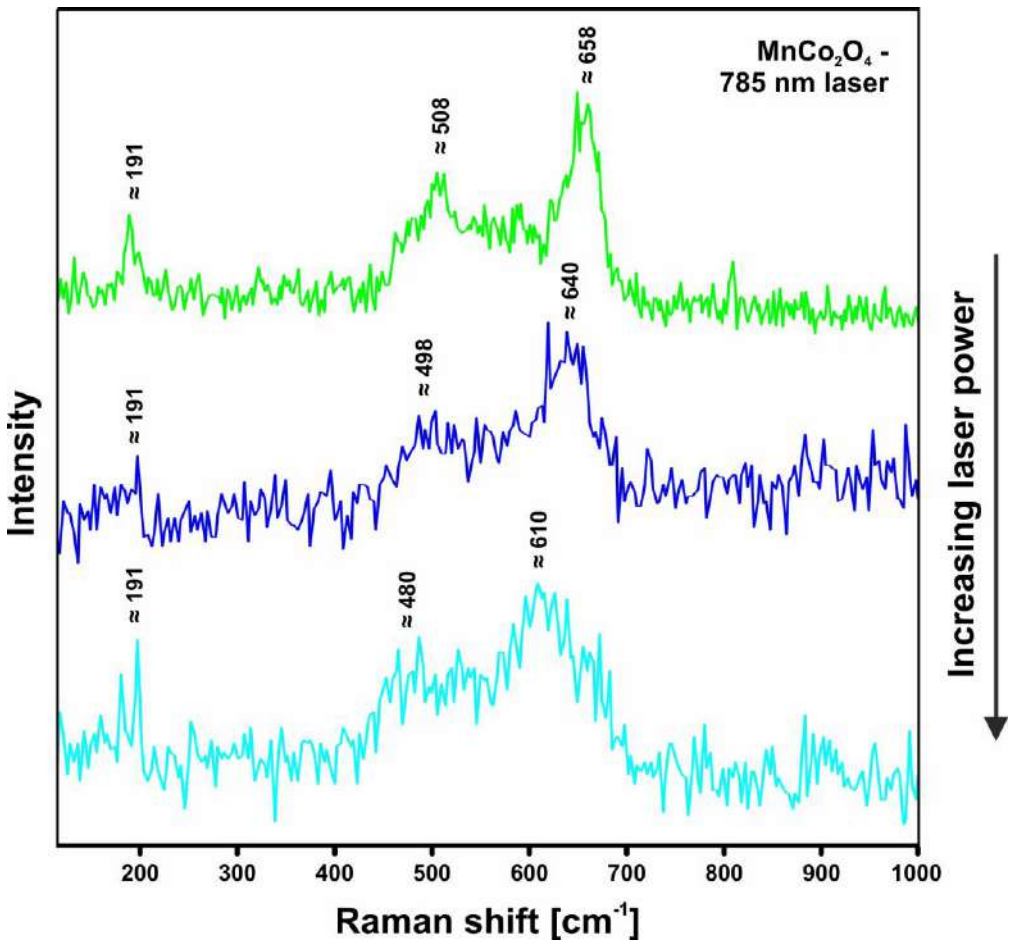

Fig. SI3. Raman spectra taken from cross section of $MnCo_2O_4$ layer on Crofer 22APU steel using varying laser power.

3.3. Manuscript III

Title: **Electrophoretic deposition of novel hybrid $MnCo_2O_4$: $Mn_{1.7}CuFe_{0.3}O_4$ spinel protective coating on stainless-steel metallic interconnects for SOFCs application**

This research investigated the potential of electrophoretic deposition (EPD) technique for applying hybrid spinel coatings of $MnCo_2O_4$: $Mn_{1.7}CuFe_{0.3}O_4$ with different ratios onto metallic interconnects to achieve a coating that is uniform, dense, smooth, and crack-free. There are two reasons behind the choice of novel hybrid spinel protective coatings for metallic interconnects, and the obtained results confirmed these reasons. Firstly, the electrical conductivity of $Mn_{1.7}CuFe_{0.3}O_4$ spinel coating is higher than that of $MnCo_2O_4$ spinel coating. Secondly, $MnCo_2O_4$ spinel coating exhibits lower Cr diffusion compared to the $Mn_{1.7}CuFe_{0.3}O_4$ spinel coating. As a result, in the hybrid coating, $Mn_{1.7}CuFe_{0.3}O_4$ spinel coating plays a crucial role in facilitating electrical conductivity between adjacent cells, and e $MnCo_2O_4$ spinel coating provides a protective layer to prevent the migration and evaporation of chromium from the interconnects to the oxygen electrodes. This highlights that the deposition of hybrid coatings presents a promising option for protective and conductive coatings on metallic interconnects.

The research highlighted are outlined as follows:

- A uniform, dense, and crack-free hybrid coating with different weight ratio applied onto stainless steel using EPD method.
- $MnCo_2O_4$: $Mn_{1.7}CuFe_{0.3}O_4$ hybrid coating is a promising candidate for protective coatings.
- Hybrid coating densification in reduction+ oxidation treatment is higher than oxidation treatments.
- Hybrid coating provides higher protection against Cr diffusion than Mn-Cu-Fe single-layer coating, but lower protection than the Mn-Co single-layer coating.
- The electrical conductivity of hybrid materials is higher than that of Mn-Co spinel material and lower than that of Mn-Cu-Fe spinel material.

Table 3. CRediT author statement of manuscript III.

Author	CRediT author statement	Signature
Omid Ekhlasiosgouei	Methodology, Investigation, Formal analysis, Data curation, Writing– original draft	
Maciej Bik	Investigation (Raman analysis), Formal analysis, Writing- review and editing	
Federico Smeacetto	Data curation, Writing- review and editing	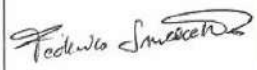
Piotr Jasinski	Data curation, Writing- review and editing	
Sebastian Molin	Resources, Conceptualization, Supervision, Writing- review and editing	

International Journal of Hydrogen Energy 158 (2025) 150569

Contents lists available at ScienceDirect

International Journal of Hydrogen Energy

journal homepage: www.elsevier.com/locate/he

Electrophoretic deposition of novel hybrid $MnCo_2O_4$: $Mn_{1.7}CuFe_{0.3}O_4$ spinel protective coating on stainless-steel metallic interconnects for SOFCs application

Omid Ekhlasiosgouei [a,*], Maciej Bik [b], Federico Smeacetto [c], Piotr Jasinski [a], Sebastian Molin [a]

[a] Advanced Materials Center, Faculty of Electronics, Telecommunications and Informatics, Gdansk University of Technology, Gdansk, Poland
[b] Faculty of Materials Science and Ceramics, AGH University of Krakow, Krakow, Poland
[c] Department of Applied Science and Technology, Politecnico di Torino, Italy

ARTICLE INFO

Handling Editor: Dr C O Colpan

Keywords:
Hybrid spinel coating
Interconnect
Electrophoretic deposition
Electrical conductivity
441 stainless steels

ABSTRACT

An innovative hybrid spinel coating, composed of $MnCo_2O_4$ and $Mn_{1.7}CuFe_{0.3}O_4$ spinel materials in varying ratios (1:0, 1:3, 1:1, 3:1, and 0:1 wt%), is applied on AISI 441 stainless-steel interconnects by electrophoretic deposition method, to improve electrical conductivity, and inhibit the migration and evaporation of chromium. Stainless steel have been coated with dense, uniform, and crack-free coatings using EPD method. The cross-sectional analysis reveals that the densification of hybrid coatings (1:1 wt%) sintered under reduction treatment (1000 °C for 2 h in H_2), followed by a subsequent oxidation treatment (900 °C for 2 h in air) is greater (29 %) than those sintered solely under oxidation treatment (900 °C for 4 h in air). What is more, Raman and XRD study suggests that the applied procedure provides a precise control over the phase composition of the hybrid coating materials. The electrical conductivity of the hybrid materials (1:1 wt%) is higher (45 %) than that of the $MnCo_2O_4$ spinel material but lower (36 %) than that of the $Mn_{1.7}CuFe_{0.3}O_4$ spinel material at 600 °C. The novel hybrid spinel coating presents a promising candidate for protective coating on metallic interconnects, due to its higher electrical conductivity, and higher sinterability as compared to Mn–Co spinel coating.

1. Introduction

Solid oxide cells (SOCs) possess the ability to generate electrical energy directly through the conversion of chemical energy and represent a noteworthy presence in the expanding energy market of today, being both environmentally friendly and efficient. They offer the capability to significantly reduce emissions of CO_2 and NO_x [1–4].

The ferritic stainless steels (FSSs), such as 430, 441 and Crofer 22 APU [1,4,5], are employed as metallic interconnects in intermediate temperature (600–800 °C) applications. Metallic interconnects act as links between individual cell, connecting the electrodes of one cell to the electrodes of an adjacent cell. They are designed to withstand aggressive conditions during solid oxide fuel cell (SOFC) and electrolysis (SOEC) operation and ensure electrical current flow through the entire fuel cell stack [4–6]. 441 stainless steel stands out as a promising choice for high-temperature applications due to its corrosion and oxidation resistance compared to other stainless steels. This enhanced resistance is crucial for ensuring long-term reliability and enduring service. The presence of Nb in the chemical composition of 441 stainless steel, along with the reduction of chromium carbides and intergranular corrosion, contributes positively to its exceptional resistance to high-temperature corrosion. Moreover, the alloy demonstrates remarkable high-temperature strength and matched thermal expansion coefficient (TEC) and high thermal conductivity within the fuel cell stack [2,3,6]. The metallic interconnects have drawn researchers' focus due to two key drawbacks, prompting efforts to extend the lifespan of SOCs: firstly, the presence of Cr may lead to fast Cr_2O_3 formation at high temperatures, and secondly, the evaporation of Cr-containing components such as $CrO_2(OH)_2$ can significantly decrease power output. Applying protective spinel coatings, such as Mn-Co [7–9], Mn-Cu [10–12], Ni-Co [13], Mn-Ni [14] and others, onto the surface of metallic interconnects can yield beneficial effects on their stability, thermal compatibility, electrical conductivity, and corrosion resistance at elevated temperatures. Indeed, these protective coatings play a crucial role in enhancing the

* Corresponding author.
E-mail address: omid.ekhlasiosgouei@pg.edu.pl (O. Ekhlasiosgouei).

https://doi.org/10.1016/j.ijhydene.2025.150569
Received 10 April 2025; Received in revised form 14 July 2025; Accepted 17 July 2025
Available online 19 July 2025

lifespan of metallic interconnects and SOCs [2,3,6]. Additionally, to further improve electrical and corrosion properties of oxide spinel, transition metals such as Cu, Ni, and Fe are doped into Mn–Co and Mn–Cu oxide spinel materials [11,14–19].

Several significant benefits of employing spinel ceramic protective coatings on the surface of ferritic stainless-steel interconnects include their reliable stability across various temperatures, maintenance of the original properties of the coated surface, effective barrier capabilities against gas molecules and corrosion-inducing agents, superior thermal stability, and resistance to chemical and physical degradation. Most importantly, their excellent electrical conductivity serves to prevent the formation of underlying oxide scales on the metallic interconnect surface, thus reducing electrical conductivity and mitigating chromium evaporation, a phenomenon known as chromium poisoning [2,3,7, 20–24]. There are several deposition methods for creating spinel protective coatings on the surface of metallic interconnects, including electrophoretic deposition (EPD) [8,15,16,25,26], magnetron sputtering [27], plasma spraying [28–31], electrolyte deposition [32–35], spin coating [13] and so on. EPD stands out as a cost-effective, environmentally friendly, efficient, and highly controllable method for generating uniform, dense, and adherent spinel protective coatings with desired thickness and chemical composition at room temperature within a short timeframe [36,37]. In the process of EPD, particles with positive charges within a stabilized suspension move towards the cathode under the influence of an applied electrical field, leading to the deposition of a dense and adherent ceramic coating on the cathode surface. The deposition yield can be controlled by adjusting the electrical field, deposition time, and suspension properties. Additionally, the EPD technique enables the deposition of multiple layers and gradient structures [36, 38–40]. In recent years, researchers have investigated the quality of doped and undoped spinel coatings (such as uniformity, densification, and crack-free) on stainless steel metallic interconnects using electrophoretic deposition method. In addition, the corrosion and electrical properties of undoped and doped coated stainless steel have been investigated. Sun et al. [41] applied $CuMn_{1.8}O_4$ spinel coatings to flat and mesh metallic interconnects using the electrophoretic method. Their findings indicated that the coating layer consisted of a mixture of Mn_3O_4 and the cubic spinel phase at room temperature, while it transformed into a pure cubic spinel phase when heated to 750–850 °C. These coated interconnects effectively functioned as Cr getters, successfully preventing Cr poisoning of the cathode. In addition, the ASR of the $CuMn_{1.8}O_4$ spinel coating on stainless steel metallic interconnects is approximately 17 mΩ cm^2 after 100 h of oxidation at 850 °C. Wang et al. [27] applied Mn–Co thin films onto the surface of Crofer22H to reduce electrical resistance and enhance corrosion resistance. Their findings demonstrated that the formation of Mn–Co spinel coatings along with a thin chromium layer led to improved electrical conductivity and anti-oxidation properties. The K_p values for uncoated stainless steel, Mn–Co, and 0.03 Cr/Mn–Co after 1000 h of oxidation at 800 °C in static air are 6.1×10^{-14}, 3.25×10^{-14}, and 3.08×10^{-14} g^2 cm^{-4} s^{-1}, respectively. Also, the ASR values of Mn–Co and 0.03 Cr/Mn–Co after 65 h at 800 °C are approximately 26 and 17 mΩ cm^2, respectively. Saeidpour et al. [13] observed that the application of Fe–Ni–Co spinel oxides/Y_2O_3 coatings as a barrier layer significantly reduced the oxidation rate of Crofer22-APU and enhanced the electrical conductivity of the surface scale compared to the bare steel. The weight gain of uncoated, Fe–Ni–Co, and Fe–Ni–Co/Y_2O_3 coatings on stainless steel after 500 h of oxidation at 800 °C in static air is approximately 0.3, 0.5, and 0.6 mg cm^{-2}, respectively. In addition, the electrical conductivity of uncoated, Fe–Ni–Co, and Fe–Ni–Co/Y_2O_3 coatings on stainless steel at 800 °C is 60.5, 165.5, and 215 S cm^{-1}, respectively. It was suggested that Mn–Co spinel coatings with lower manganese content exhibit excellent chromium barrier ability by reducing the outward diffusion channels for chromium [22]. Oh et al. [25] investigated the formation of $Cu_{1.35}Mn_{1.65}O_4$ spinel coatings on the surface of 460FC metallic interconnects. The deposited spinel coating resulted in a notable decrease in chromium poisoning and oxidation rate. The ASR value of uncoated stainless steel (460 FC) is around 170 mΩ cm^{-2} after 100 h of oxidation at 700 °C in air. In addition, the ASR value of $Cu_{1.35}Mn_{1.65}O_4$-coated stainless steel, prepared by EPD method at a voltage of 40 V for a deposition time of 60 s, is around 14 mΩ cm^2 after 1000 h at 700 °C. Aznam et al. [16] found that the application of deposited $(Cu–Mn–Co)_3O_4$ spinel coatings significantly reduced the oxidation rate of SUS430 steel and suppressed the chromium diffusion from the stainless steel intermetallic towards the cathode. Additionally, the deposited spinel coatings maintained stable electrical conductivity constant throughout a 200-h oxidation process. The weight gain of uncoated SUS430 stainless steel and $(Cu,Mn,Co)_3O_4$ spinel-coated stainless steel is around 0.8 and 0.1 mg cm^{-2}, respectively, after 200 h of oxidation at 800 °C in air. Sabato et al. [18] reported that the corrosion resistance of deposited Cu-doped $Mn_{1.5}Co_{1.5}O_4$ on Crofer22APU was approximately ten times greater than that of uncoated Crofer22APU. Their results showed that the K_p values for uncoated stainless steel, MnCo, 5Cu–MnCo, and 10Cu–MnCo spinel coatings on Crofer 22 APU stainless steel after 3000 h of oxidation in air at 800 °C are 6.11×10^{-14}, 0.53×10^{-14}, 0.71×10^{-14}, and 0.62×10^{-14} g^2 cm^{-4} s^{-1}, respectively. In addition, the ASR values of uncoated stainless steel and 5Cu–MnCo are around 30 and 12 mΩ cm^2, respectively. Zhang et al. [42] demonstrated that electrophoretically deposited $(Mn–Co)_3O_4$ spinel coatings, sintered in an H_2/H_2O atmosphere, exhibited a more enduring and stable performance due to the formation of a very thin chromia sub-scale and the inhibition of chromium diffusion, resulting in a reduction of area-specific resistance (ASR). The ASR values of sintered $(Mn,Co)_3O_4$ spinel coating in air and H_2/H_2O atmosphere, coated at a voltage of 400 V by EPD method, are around 17 and 40 mΩ cm^2, respectively. Zanchi et al. [7] studied the effect of simultaneous co-deposition of $Mn_{1.5}Co_{1.5}O_4$, Fe_2O_3 and CuO on the performance of Crofer 22 APU metallic interconnects. Their findings revealed that $Mn_{1.28}Co_{1.28}Fe_{0.15}Cu_{0.29}O_4$ spinel exhibited the most favorable corrosion resistance. The K_p values of uncoated Crofer 22 APU, MnCo, 5Fe–MnCo, and 10Fe–MnCo after 2000 h of oxidation at 750 °C in air are 26.9×10^{-15}, 14.5×10^{-15}, and 6.6×10^{-15}, and 6.6×10^{-15} g^2 cm^{-4}. s^{-1}, respectively. Furthermore, the presence of Cu and Fe resulted in an increase and decrease, respectively, in the coefficient of thermal expansion. Zhu et al. [43] conducted a comparison of the performance of various Cu–Mn and Mn–Co spinel coatings, including $CuMn_2O_4$, $CuNi_{0.2}Mn_{1.8}O_4$, $MnCo_2O_4$, and $MnFe_{0.34}Co_{1.66}O$, deposited on the surface of metallic interconnects. Their findings proposed that $CuNi_{0.2}Mn_{1.8}O_4$ spinel coating showed the highest electrical conductivity, the lowest ASR, and the highest resistance against the diffusion of Cr and O elements at intermediate temperatures. The ASR values of $MnFe_{0.34}Co_{1.66}O_4$, $MnCo_2O_4$, $CuMn_2O_4$, and $CuNi_{0.2}Mn_{1.8}O_4$ spinel coatings on stainless steel after 100 h of oxidation at 800 °C in static air are around 18, 16, 12, and 9 mΩ cm^2. Ajdys et al. [44] found that by increasing the fine powder fractions leading to the higher density of the $Mn_{1.5}Co_{1.5}O_4$ spinel layer, ASR was reduced by 65 % and the oxidation rate of metallic interconnects was decreased. Shirani Bidabadi et al. [45] examined the influence of Cu and Fe dopants on the performance of Mn–Co spinel coatings. Their results proposed that Cu-doped layers exhibited superior performance in terms of oxidation rate and chromium evaporation rate compared to Fe-doped layers. The K_p values of uncoated stainless steel (24h of oxidation), Mn–Co ($Mn_{1.25}Co_{1.75}O_4$, 24h of oxidation), 0.3 Cu-doped Mn–Co (24h of oxidation), 0.3 Fe-doped Mn–Co (504h of oxidation), and 0.1Cu–0.2Fe-doped Mn–Co (504h of oxidation) spinel coatings on AISI 430 stainless steel after oxidation in O_2–5 %H_2O atmosphere at 800 °C are 20.7×10^{-14}, 4.8×10^{-14}, 4.3×10^{-14}, 7.6×10^{-14}, and 6.5×10^{-14} g^2 cm^{-4} s^{-1}, respectively. Masi et al. [46] investigated the effect of Fe, Cu, and simultaneous Fe and Cu doping on the high temperature properties of Mn–Co spinel materials. Their findings proposed that Cu doping had a more beneficial effect on the thermal stability and densification of spinel materials compared to Fe doping. Additionally, Mn–Co spinel materials doped with Fe

exhibited greater thermal stability than those doped with Cu. Ma et al. [47] reported that dual doping of Cu and Y significantly increased the sintering properties, electrical conductivity and oxidation resistance of Crofer ferritic alloy as a metallic interconnect. Cu–Y dual-doped $(Mn–Co)_3O_4$ spinel coating demonstrated substantially lower ASR compared to coatings doped solely with Cu or Y. The K_p values of uncoated stainless steel, MnCo (Co_2MnO_4), 0.03 Cu-doped MnCo, 0.01 Y-doped MnCo, and 0.02Cu-0.02Y-doped MnCo spinel coating at 500 h of oxidation time are 4.6×10^{-15}, 3.5×10^{-15}, 3.4×10^{-15}, 5×10^{-16}, 4×10^{-16} $g^2\ cm^{-4}\ s^{-1}$, respectively. Mazur et al. [11] studied the influence of Ni and Fe doping on the high temperature behavior of Mn–Cu spinel coatings. Their finding indicated that higher levels of Ni doping increased electrical conductivity, while higher levels of Fe doping had the opposite effect.

The $MnCo_2O_4$ spinel coating exhibits reduced electrical conductivity at elevated temperatures compared to the $Mn_{1.7}CuFe_{0.3}O_4$ spinel coating. However, it showcases superior oxidation resistance under similar high-temperature conditions [48]. The utilization of innovative hybrid $MnCo_2O_4$: $Mn_{1.7}CuFe_{0.3}O_4$ spinel materials offers the potential to enhance both electrical conductivity and oxidation resistance simultaneously. This study investigates the microstructure of a novel hybrid $MnCo_2O_4$: $Mn_{1.7}CuFe_{0.3}O_4$ spinel coating, incorporating varying ratios of these spinel materials, applied to AISI 441 stainless-steel metallic interconnects by EPD method. The main objective is to examine the similar electrophoretic mobility of Mn–Co and Mn–Cu–Fe in an ethanol suspension stabilized by iodine, aiming to achieve a uniform distribution of individual components of $MnCo_2O_4$ ad $Mn_{1.7}CuFe_{0.3}O_4$ across the entire substrate. The secondary goal is to achieve uniform, smooth, dense, and crack-free hybrid spinel coatings on stainless steel interconnects. The third aim is to investigate the electrical conductivity and Cr diffusion of hybrid spinel coatings as compared to Mn–Co and Mn–Cu–Fe oxide spinel coatings.

2. Experimental

2.1. Materials

Metallic interconnects with a flat side were selected as substrates for applying a hybrid spinel coating using the EPD technique. The chemical composition of the examined AISI 441 stainless steels consists of 17.5–18.5 wt% Cr, 1 wt% Mn, Nb, and Si, 0.1–0.6 wt% Ti, 0.03 wt% C, 0.04 wt% P, and 0.02 wt% S, with the balance being Fe. The stainless-steel sheets were cut into 20 × 20 mm^2 with a thickness of 0.3 mm. Before applying the hybrid spinel coating, the substrates underwent a cleaning process involving immersion in acetone and then ethanol (provided by OCH, Gliwice, Poland) using an ultrasonic bath for 30 min to eliminate any contaminants. Two types of spinel materials were utilized: commercial $MnCo_2O_4$ (labelled as "Mn–Co oxide spinel" material) from Marion Technologie, France, and synthesized $Mn_{1.7}CuFe_{0.3}O_4$ (labelled as "Mn–Cu–Fe oxide spinel" material), serving as a conductive protective coating on stainless-steel interconnects. Further details about the preparation of the synthesized $Mn_{1.7}CuFe_{0.3}O_4$ can be found elsewhere [49]. Ethanol (absolute, 99.9 %) acted as the solvent, and iodine (provided by Chempur, mass molar: 253.81 g/mol, CAS: 7553-56-2) was employed as a dispersing agent to form suspensions of Mn–Co and Mn–Cu–Fe for the EPD process.

2.2. Preparation of Mn–Co/Mn–Cu–Fe suspension

The suspension, comprised of Mn–Co and Mn–Cu–Fe powders in different weight ratio (1:0, 0:1, 1:3, 1:1, and 3:1), with solid concentrations fixed at 10 g/L of spinel powder and 0.7 g/L iodine in ethanol as the solvent, was stabilized. Achieving uniformity of Mn–Co and Mn–Cu–Fe powders within the ethanol solvent involved subjecting them to a 45 min bath ultrasonic treatment. Before initiating the EPD process, an additional 5 min bath ultrasonic treatment was applied to enhance suspension stability. A detailed description of the proportions of spinel coating materials and suspension parameters for the hybrid spinel coating on the substrate is outlined in Table 1.

2.3. EPD process for hybrid spinel materials

In the deposition of Mn–Co, Mn–Cu–Fe, and hybrid coatings comprising Mn–Co and Mn–Cu–Fe spinel materials onto the substrate, AISI 441 stainless-steel interconnects were selected as a cathode, while two stainless steels were employed as the anode. The three electrodes were maintained in a vertical and parallel orientation throughout EPD process, with a fixed separation distance of 1 cm within EPD cell. The details regarding the process parameters for hybrid spinel coatings can be found in Table 1. Additionally, Fig. 1a provides a schematic representation of EPD cell designed for spinel coatings. Mn–Co, and Mn–Cu–Fe, and the hybrid spinel coatings applied to the substrates. Then, the spinel coatings were dried at room temperature for 24 h. Subsequently, these coatings underwent sintering at varied temperatures and durations in various atmospheres, as outlined in Table 1. The initial set of samples underwent a single-step sintering process at 900 °C for 4 h in a static air atmosphere (oxidation treatment). In contrast, the second set of samples underwent a two-step process, starting with an initial heat treatment at 1000 °C for 2 h in flowing pure H_2 gas (reduction treatment), followed by a subsequent treatment at 900 °C for 2 h in static air (oxidation treatment). The heating and cooling rate for both the single-step sintering process and the two-step process was set at 3 °C/min.

2.4. Preparation of spinel pellets

To investigate the structure, as well as the electrical conductivity of coating materials, pellets were formed out of powders of Mn–Co, Mn–Cu–Fe, and Mn–Co/Mn–Cu–Fe with varying ratios (1:3, 1:1, and 3:1 wt%), which were mixed in ethanol using a magnetic stirrer. The mixed powders underwent a 24 h drying process at 80 °C. Carboxymethyl cellulose (CMC) served as a binder for powder granulation, ensuring the formation of dense pellets. The powder was subjected to a uniaxial hydraulic press within a 13 mm (internal diameter) steel die. Following pressing, the pellets were dried for an additional 24 h at 80 °C before being sintered at 900 °C for 4 h in an air atmosphere, with a heating and cooling rate of 3 °C/min. Fig. 1b presents the schematic illustration of the preparation of the pellet sample.

2.5. Characterization

The evaluation of particle size distribution, zeta potential, and suspension conductivity of Mn–Co and Mn–Cu–Fe particles in an ethanol solvent was conducted using a Dynamic Light Scattering instrument (Zetasizer nano ZS, Malvern). X-ray diffraction was utilized to investigate the phase composition and crystal structure of the crushed pellets. The analysis was carried out at room temperature using a Bruker D2 phaser instrument with Cu-Kα radiation (1.5404 °A). Measurements were taken on rotating samples in a 2θ range from 10 to 80°, employing a step size of 0.01°, and with an accounting time of 0.2 s for each step. The phase composition of pellets was also examined with Raman spectroscopy using WITec alpha 300 M+ spectrometer, 785 nm excitation wavelength (laser spot of ca. 1064 nm in diameter), 3 cm^{-1} spectral resolution, grating 300 gr/mm. Each pellet was measured in five different, random spots across the pellets – for each point, 10 scans with 20 s integration time were used. WITec Project 5.3.1 software was used to record the spectra within $0 \div 3500\ cm^{-1}$, and OPUS 7.2. software was used to post-process them. Post-processing included averaging each five spectra of a particular pellet, cutting the resultant spectra within $60 \div 800\ cm^{-1}$ region (no important bands occurred within the remaining part), baseline correction using the polynomial function, as well as deconvolution using the Handke method [50], and

Table 1
Ratio of spinel coating materials, suspension and process parameters of EPD method and different sintering treatments for spinel coating on metallic interconnect.

The ratio of spinel coating material (Mn–Co: Mn–Cu–Fe)	Substrate	Suspension condition			EPD condition			Sintering condition	
		Solvent	Solid load	Iodine	Voltage (V)	Time (s)	Electrode's distance	Step 1: Reduction treatment (Pure H_2)	Step 2: Oxidation treatment (Static air)
1:0	AISI 441	Ethanol	10 g/L	0.7 g/L	40	50	10 mm	–	900 °C- 4h
								1000 °C- 2h	900 °C- 2h
1: 3								–	900 °C- 4h
								1000 °C- 2h	900 °C- 2h
1: 1								–	900 °C- 4h
								1000 °C- 2h	900 °C- 2h
3:1								–	900 °C- 4h
								1000 °C- 2h	900 °C- 2h
0:1								–	900 °C- 4h
								1000 °C- 2h	900 °C- 2h

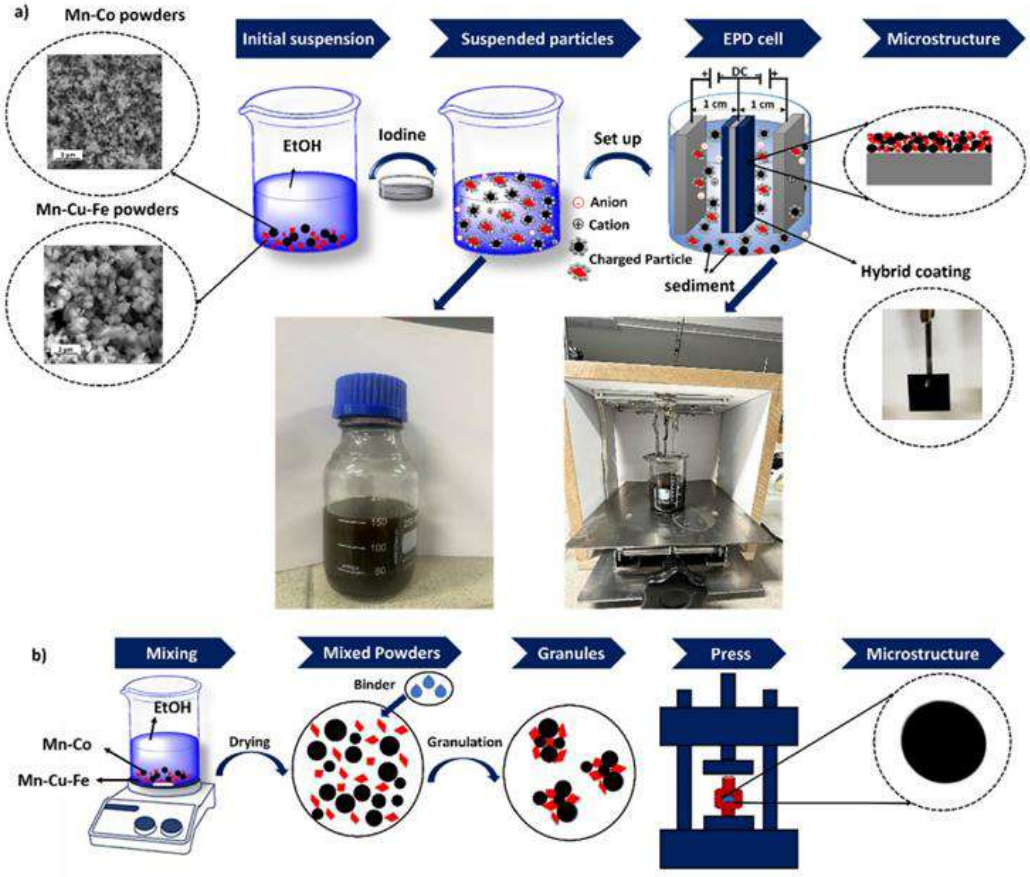

Fig. 1. a) the schematic illustration of initial suspension, electrostatic stabilization, and EPD set up, b) the schematic depiction of the procedure for preparing pellet samples.

Levenberg-Marquardt algorithm. A set of Gaussian-Lorentzian bands was used with an RMS error of ca. 0.05. The Peak Picking function was used to estimate the positions of all bands before and after the deconvolution process. The van der Pauw method was employed to examine the electrical conductivity of pellets made from spinel materials. The assessment of electrical conductivity was conducted in an air atmosphere over a temperature range from 800 °C to 200 °C, with decrements/steps of 50 °C. The electrical conductivity of pellets has an inverse relationship with pellet porosity. Consequently, the electrical conductivity data for different pellets were adjusted accordingly. The results regarding electrical conductivity are detailed, integrating corrections for porosity using the Bruggeman asymmetric modal equation [48]:

$$\sigma = \frac{\sigma_m}{(1-p)^{\frac{3}{2}}}$$

Where σ (S/cm) is corrected electrical conductivity, σ_m (S/cm) is measured electrical conductivity, and p is a sample-pore fraction. The

pellet's porosity was determined using Archimedes' principle (ASTM B962-13 standard).

The activation energy (E_a) for electrical conductivity can be determined using the Arrhenius equation.

$$\ln \sigma T = \frac{-E_a}{kT} + \ln \sigma_0$$

Where E_a (eV) is activation energy σ (S/cm) is electrical conductivity, T (K) is temperature, σ_0 is pre-exponential factor, and K ($8.617*10^{-5}$ eV/K) is Boltzmann's constant. The examination of the surface and cross-sectional microstructure of the hybrid spinel coatings subjected to both sintering treatments was investigated using Scanning Electron Microscopy (SEM) coupled with energy-dispersive X-ray spectroscopy (EDX) at an acceleration voltage of 15 kV. ThermoFisher Phenom XL microscope with backscatter detector (BSE) was used for all SEM/EDS analyses. For the cross-sectional analysis, the samples were embedded in epoxy resin under cold vacuum conditions, followed by a process involving grinding with SiC papers and polishing with 1 μm diamond slurry.

3. Results and discussion

3.1. Suspension and process parameters of EPD method

Fig. 2 illustrates the variations in zeta potential, suspension conductivity, and average particle size for Mn–Co and Mn–Cu–Fe suspensions in relation to iodine concentration (ranging from 0.1 to 1.1 g/L) and a solid concentration of 10 g/L. To maintain the stability of the powders in the ethanol solvent, iodine is added to release H^+ ions. Consequently, the particle surfaces absorb these ions, resulting in stability within the solvent. The absorption of H^+ ions around the particle surfaces, creating a positively charged surface, leads to the formation of a diffuse double layer (as shown in Fig. 1a). Fig. 2a depicts that, with an increase in iodine concentration from 0.1 to 0.9 g/L, the zeta potential initially rises and then declines in both suspensions. This is attributed to the extra amount of released H^+ ions in ethanol solvent, leading to a reduction in the thickness of the electrical double layer and, consequently, a decrease in the zeta potential. The objective is to achieve a homogeneous distribution of individual components of Mn–Co and Mn–Cu–Fe particles across the entire substrate by maintaining identical electrophoretic mobility for both in the ethanol suspension. The zeta potential results indicate that Mn–Co and Mn–Cu–Fe particles exhibit an identical zeta potential at an iodine concentration of 0.7 g/L, ensuring a homogeneous distribution of individual components on the substrate. Consequently, the deposition yield for Mn–Co, Mn–Cu–Fe, and Mn–Co: Mn–Cu–Fe (1:3, 1:1, and 3:1 wt%) suspensions is approximately at the same level, as depicted in Fig. 2d. Fig. 2b exhibits the conductivity of Mn–Co and Mn–Cu–Fe suspensions about iodine concentration, ranging from 0.1 to 1.1 g/L. As the iodine concentration increases in both suspensions, there is a corresponding rise in suspension conductivity, attributed to the elevated iodine concentration in the ethanol solvent. Fig. 2c depicts the average particle size of Mn–Co and Mn–Cu–Fe in ethanol solvent concerning iodine concentration (ranging from 0.1 to 1.1 g/L). The presence of particle agglomeration in the suspension can be associated with the solvent and disperser. As indicated in Fig. 2c, an increase in iodine concentration in both suspensions does not influence the average particle size; Mn–Co and Mn–Cu–Fe particles in the suspension exhibit similar sizes. Moreover, the average particle size of Mn–Cu–Fe is slightly higher than that of Mn–Co. Consequently, well-dispersed Mn–Co and Mn–Cu–Fe particles play a crucial role in achieving a uniform and dense coating on the substrate. Therefore, Mn–Co and Mn–Cu–Fe spinel particles in ethanol solvent at an iodine concentration of 0.7 g/L with a solid concentration of 10 g/L are suitable for obtaining a uniform, smooth, and crack-free hybrid coating on the stainless-steel substrate.

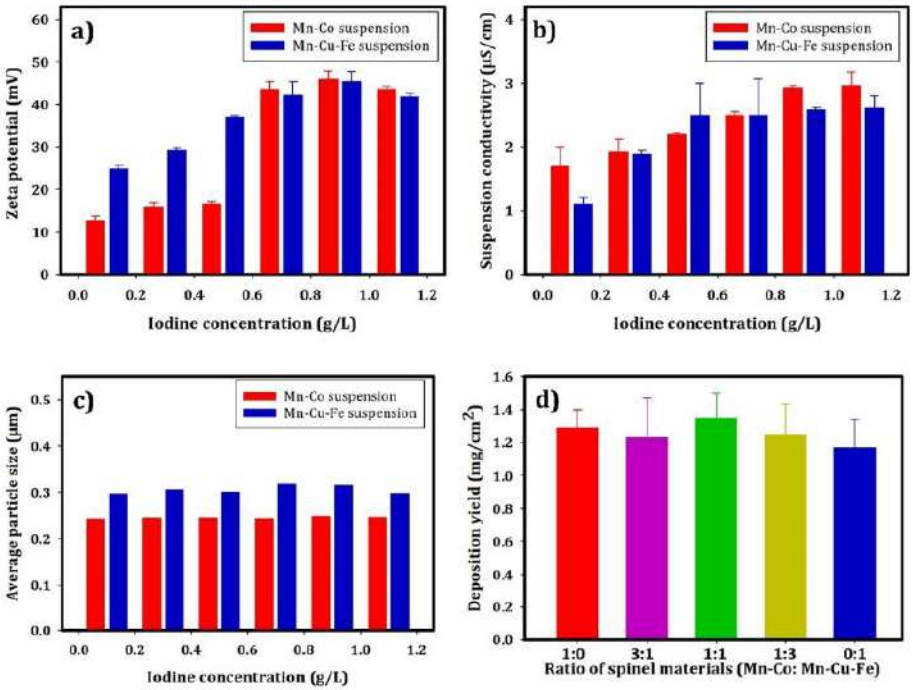

Fig. 2. a) zeta potential, b) suspension conductivity, c) average particle size of Mn–Co and Mn–Cu–Fe suspension versus iodine concentration, and d) deposition yield of Mn–Co, Mn–Cu–Fe, and Mn–Co: Mn–Cu–Fe (1:3, 1:1, and 3:1 wt%) suspensions.

3.2. Microstructure of hybrid coating on stainless-steel substrate

3.2.1. Surface microstructure

Fig. 3 illustrates SEM images of the surfaces of sintered spinel coatings containing Mn–Co: Mn–Cu–Fe at various weight ratios (1:0, 0:1, 1:3, 1:1, and 3:1) subjected to different sintering procedures. These treatments include oxidation treatment (in static air) and reduction (using pure H_2), followed by oxidation treatments (as outlined in Table 1). Comparing Fig. 3a and b reveals that the morphology of coatings subjected to reduction + oxidation treatments is denser compared to those treated only with oxidation. Furthermore, grain boundaries are more visible in coatings sintered with reduction + oxidation treatments. In essence, the compactness of coatings in reduction + oxidation treatments are higher than in oxidation treatments. Dense coatings subsequently prevent the diffusion of oxygen, thereby inhibiting the growth of a chromia layer between the coating and the substrate. The chemical composition and crystal structure are pivotal factors influencing the densification of spinel materials. The

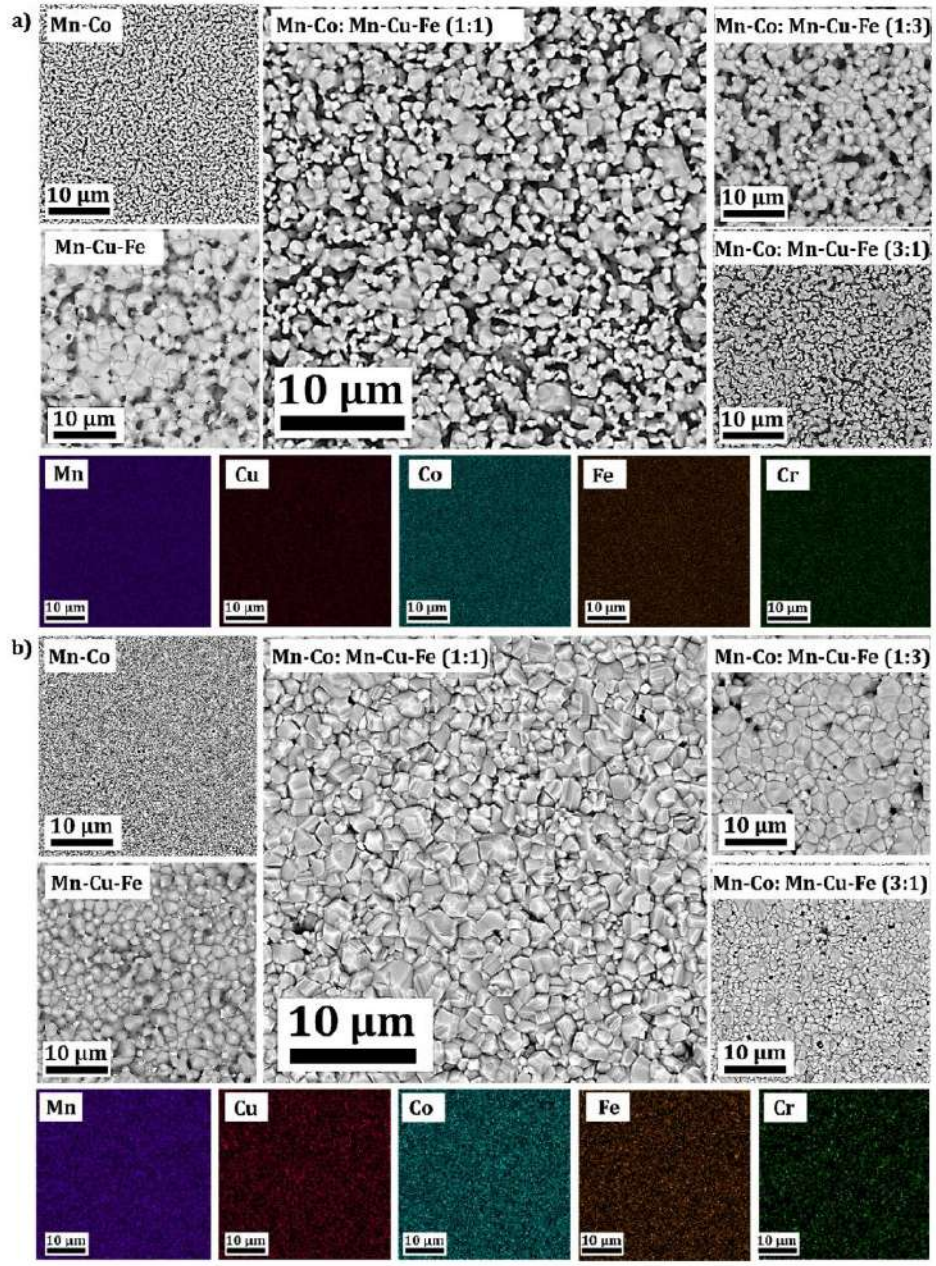

Fig. 3. SEM images of the surfaces of sintered coatings composed of Mn–Co and Mn–Cu–Fe at various weight percentages (1:0, 0:1, 1:3, 1:1, and 3:1) under different sintering conditions: a) oxidation treatment (in static air), and b) reduction (pure H_2) followed by oxidation treatment, and EDS-X-ray elemental maps showing the distribution of Mn, Cu, Co, and Fe for the sintered Mn–Co: Mn–Cu–Fe coating with a 1:1 weight ratio, both in oxidation and reduction + oxidation treatments.

higher densification of the Mn–Cu–Fe spinel coating compared to the Mn–Co spinel coating is attributed to the doping of Fe in the Mn–Cu oxide spinel structure, which lowers the sintering temperature and improves coating densification due to enhanced grain boundary diffusion. In addition, transition metals promote liquid-phase sintering and mass transport. The doping of transition metals in the spinel structure, due to differences in ionic radii and valence states, causes lattice strain and cation vacancies, which increase the diffusion rate, thereby improving densification through easier atomic movement. Moreover, increasing the ratio of Mn–Co spinel material leads to reduced densification of the hybrid material, attributable to the presence of Mn–Co spinel coating. In both sintering treatments, the densification of the Mn–Co: Mn–Cu–Fe (1:3 wt%) hybrid spinel coating is higher than that of Mn–Co and Mn–Cu–Fe, as well as other ratios of hybrid spinel coatings, due to the varying particle size distribution of the Mn–Co and Mn–Cu–Fe spinel materials. Particle size distribution plays a crucial role in achieving dense coatings. As indicated by Fig. 2c, the particle size distribution of the Mn–Cu–Fe spinel material is larger than that of the Mn–Co spinel material. During the EPD process, Mn–Co particles disperse among the Mn–Cu–Fe particles. As a result, during the sintering process, the higher sinterability of the Mn–Cu–Fe oxide spinel compared to the Mn–Co oxide spinel, along with the better distribution of both oxide spinel powders in the coating, leads to a decrease in the porosity of the hybrid coatings. Fig. 3a and b displays EDS-X-ray elemental maps illustrating the distribution of Mn, Cu, Co, and Fe for the sintered Mn–Co: Mn–Cu–Fe coating with a 1:1 weight ratio, in both oxidation and reduction + oxidation treatments. Based on Fig. 2d, the deposition yield of hybrid spinel coatings at various weight ratios of Mn–Co and Mn–Cu–Fe remains consistent due to their identical zeta potential. Consequently, the deposition yield of mixed particles exhibits a uniform distribution across all surface coatings. As indicated by the EDS-X-ray elemental map in both sintering treatments, the Mn–Co and Mn–Cu–Fe spinel materials are evenly distributed across the surface coatings during the EPD process.

3.2.2. Cross-section microstructure

Fig. 4 displays SEM images of the cross-sections of sintered Mn–Co: Mn–Cu–Fe spinel coatings at various weight ratios (1:0, 0:1, 1:3, 1:1, and 3:1) subjected to different sintering treatments. The results indicate that Mn–Co, Mn–Cu–Fe, and the hybrid spinel coatings with various ratios exhibit uniform, smooth, and crack-free on AISI 441 stainless steel interconnects in both sintering treatments. Comparing Fig. 4a and b reveals that the Mn–Cu–Fe spinel coating is denser than the Mn–Co spinel coating, and increasing the ratio of Mn–Co particles in the hybrid

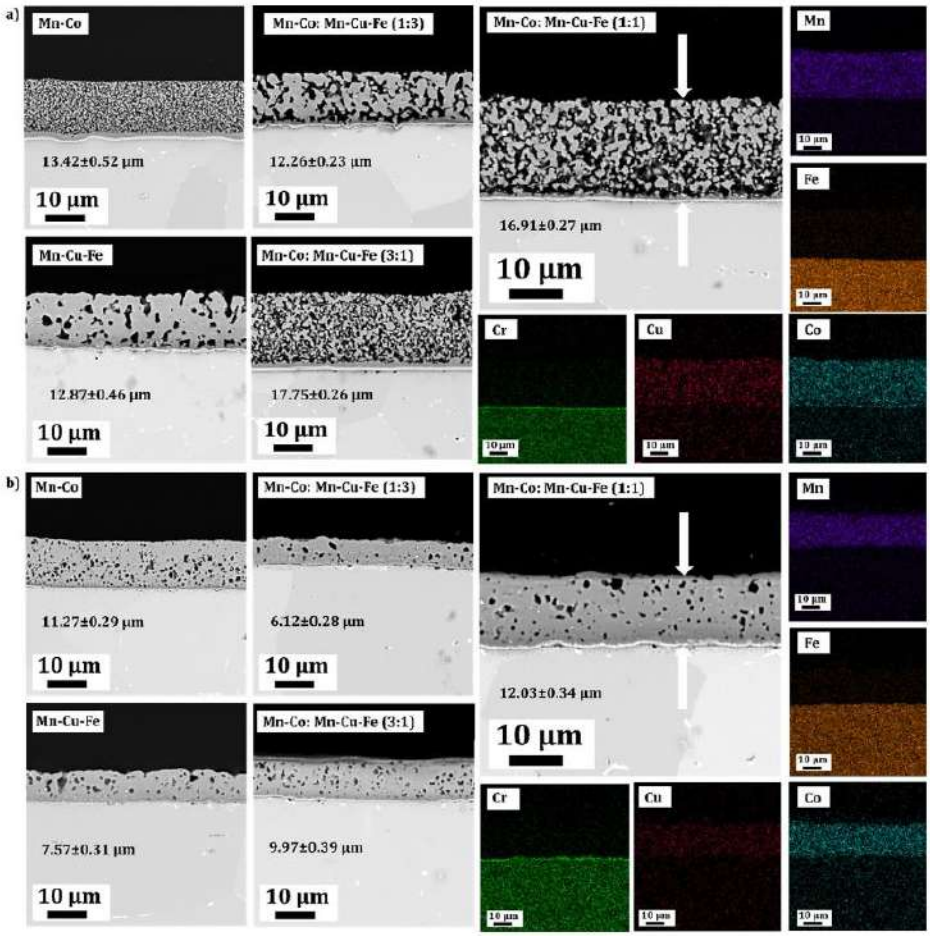

Fig. 4. Cross-section SEM images of sintered Mn–Co: Mn–Cu–Fe spinel coatings (at weight ratios of 1:0, 0:1, 1:3, 1:1, and 3:1) under different sintering treatments: a) oxidation and b) reduction + oxidation treatments, cross-section EDS-X-ray elemental maps of Mn–Co: Mn–Cu–Fe (at a 1:1 weight ratio) for both sintering treatments.

coating leads to decreased coating density. Additionally, the densification of Mn–Co, Mn–Cu–Fe, and the hybrid spinel coatings in reduction + oxidation treatments are higher than that in oxidation treatment. Comparison of coating thickness in both sintering treatments reveals approximately 16 %, 40 %, 50 %, 29 %, and 44 % shrinkage in the thickness direction for Mn–Co: Mn–Cu–Fe coatings at weight ratios of 1:0, 0:1, 1:3, 1:1, and 3:1, respectively. In essence, under the same EPD conditions, coating thickness in reduction + oxidation treatments are significantly lower than in oxidation treatment. Moreover, the densification of the hybrid coating (at a 1:3 wt% ratio) is higher than that of Mn–Co, Mn–Cu–Fe, and other ratios of hybrid spinel coatings due to the varying particle size distribution. Consequently, sintered coatings in reduction + oxidation treatments inhibit the formation of a chromia layer on the substrate. Fig. 4 depicts cross-section EDS-X-ray elemental maps of Mn–Co: Mn–Cu–Fe (at a 1:1 weight ratio) for both sintering treatments. The results indicate that the elements of hybrid spinel coatings at a 1:1 weight ratio in both sintering treatments are uniformly distributed across the entire deposited area during EPD process. Additionally, in both sintering treatments, chromium diffuses from the substrate to the interface of the coating and substrate, where it reacts with oxygen to form a chromia layer. Further analysis of the thickness of the chromia layer and element diffusion will be conducted using line scan and point analysis techniques.

3.2.3. Energy dispersive X-ray spectroscopy analysis

Fig. 5a and b shows the EDS point analysis results from samples cross-section for the outer (coating surface) and inner (interface of coating and substrate) regions of sintered Mn–Co coatings at various ratios in both sintering treatments. According to Fig. 5a and b, the findings reveal that the atomic concentration of the Cr element in the reduction + oxidation treatments is lower in both the outer and inner regions compared to the oxidation treatment. This is attributed to the increased densification of the coatings. Hence, this implies a slight occurrence of Cr diffusion during the reduction + oxidation treatments. Increasing the ratio of Mn–Cu–Fe oxide spinel material in mixed spinel materials leads to greater Cr diffusion at the interface between the coating and substrate under both sintering conditions. This can be attributed to the higher reactivity of Mn–Cu–Fe oxide spinel particles, which react with chromia more readily, forming a reaction layer. Additionally, when comparing Mn–Co and Mn–Cu–Fe oxide spinel coatings on stainless steel under both sintering conditions, the atomic concentration of Cr at the interface is lower in Mn–Co oxide spinel coating than in Mn–Cu–Fe oxide spinel coating. Point analysis results indicate that Mn–Co: Mn–Cu–Fe (3:1 and 1:1 wt%) oxide spinel coatings are effective candidates for preventing Cr diffusion from steel.

Fig. 5c and d illustrates the EDX line scan performed on sintered samples of Mn–Co, Mn–Cu–Fe, and Mn–Co: Mn–Cu–Fe (with a 1:1 weight ratio) subjected to oxidation treatment and reduction + oxidation treatments. Comparing Fig. 5c and d reveal that the chromia layer thickness for sintered spinel coatings of Mn–Co, Mn–Cu–Fe, and Mn–Co: Mn–Cu–Fe (1:1 wt%) in reduction + oxidation treatments are slightly lower than for those sintered in oxidation treatments, owing to the higher densification of coatings. Furthermore, the chromia layer thickness of sintered Mn–Co is lower than that of sintered Mn–Cu–Fe. Additionally, the chromia layer thickness of sintered Mn–Co: Mn–Cu–Fe spinel coatings, with a 1:1 weight ratio, is less than that of sintered Mn–Cu–Fe spinel coatings and greater than that of sintered Mn–Co spinel coatings. This disparity can be attributed to the differing shapes of Mn–Co and Mn–Cu–Fe spinel particles. The shape of commercial Mn–Co spinel powder is spherical, while the synthesized Mn–Cu–Fe spinel powder is non-spherical (as shown in Fig. 1a). When the powders are spherical (Mn–Co powder), they promote better packing and higher

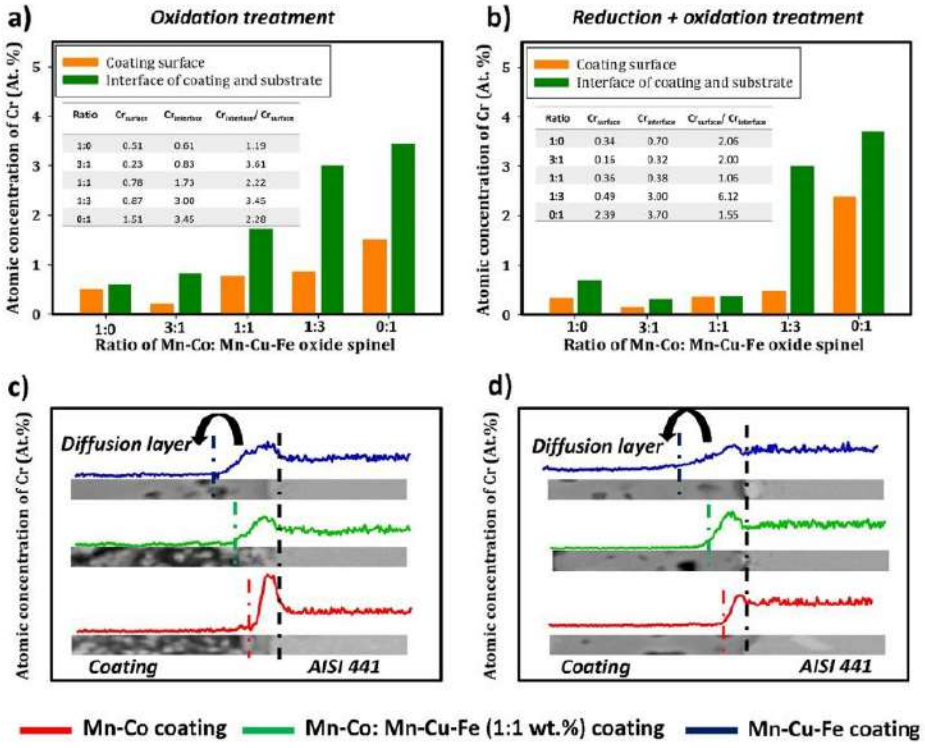

Fig. 5. a, and b) EDS point analysis results for the outer (coating surface) and inner (interface of coating and substrate) regions of sintered Mn–Co: Mn–Cu–Fe coatings (1:0, 3:1, 1:1, 3:1, and 0:1 wt%). c, and d). The EDX line scan on sintered samples of Mn–Co, Mn–Cu–Fe, and Mn–Co: Mn–Cu–Fe (with a ratio of 1:1 wt%): a, and c) under oxidation treatment, and b, and d) under reduction + oxidation treatments.

densification during sintering. On the other hand, Mn–Cu–Fe has higher sinterability compared to Mn–Co spinel materials. Accordingly, after sintering, the Mn–Cu–Fe coating contains more pores, through which Cr can diffuse to the surface of the coating.

3.3. Study of hybrid materials

3.3.1. Microstructural SEM/EDS analysis

The uniform distribution of Mn–Co and Mn–Cu–Fe spinel materials was examined using EDS-X-ray elemental mapping. Fig. 6 depicts the surface SEM images and the EDS-X-ray elemental mapping performed on pellets containing Mn–Co: Mn–Cu–Fe (with weight ratios of 1:1) spinel materials. Through the comparison of SEM images, it is apparent that Mn–Co spinel particles are dispersed among Mn–Cu–Fe spinel particles within hybrid pellets. Additionally, EDS-X-ray elemental mapping analysis aimed to verify the uniform distribution of particles throughout the entire pellet area after mixing. As shown in Fig. 1b, the Mn–Co and Mn–Cu–Fe spinel materials were mixed in ethanol solvent using a magnetic stirrer. The results show that the homogeneous dispersion of Mn, Co, Cu, and Fe elements from the Mn–Co and Mn–Cu–Fe spinel powders indicates that the mixing process was successful.

3.3.2. Phase structure

Fig. 7 illustrates X-ray diffraction (XRD) patterns for spinel materials, including Mn–Co, Mn–Cu–Fe oxide spinel materials, and a combination of Mn–Co: Mn–Cu–Fe with weight ratios of 1:3, 1:1, and 3:1. These samples underwent sintering at 900 °C for 4 h in a static air environment. According to XRD pattern of Mn–Co spinel material, only single phase of $MnCo_2O_4$ was identified (by X'Pert HighScore Plus Software) with crystal structure of cubic within the Fd-3m (227) space group (Reference code: 01-084-0482). Based on the XRD analysis of the Mn–Cu–Fe oxide spinel material, a dual-phase composition was detected. The first phase identified was Mn_2CuO_4, exhibiting a cubic crystal structure within the Fd-3m (227) space group (Reference code: 01-076-2296) and a tetragonal crystal structure within the I41/amd (141) space group (Reference code: 01-071-1142). The peaks slightly shifted due to the interdiffusion of $Fe^{2+}/^{3+}$ in both the cubic and tetragonal crystal structures, which most likely caused distortion of the crystal structure. The second phase identified was Mn_2O_3, displaying a tetragonal crystal structure (Reference code: 00-006-0540). In addition, three peaks were not detected in Mn–Cu–Fe oxide spinel materials. The XRD analysis of Mn–Co: Mn–Cu–Fe spinel materials with varying weight ratios of 3:1, 1:1, and 1:3 wt% revealed no additional phases upon combining the two oxide spinel materials. In a weight ratio of 1:3 wt% (Mn–Co: Mn–Cu–Fe oxide spinel material), and Mn_2O_3 was identified, similar to Mn–Cu–Fe oxide spinel materials. Based on the XRD patterns for the compositions of both materials at different ratios (3:1, 1:1, and 1:3 wt%), the peaks in the composition of spinel materials overlap with those of $MnCo_2O_4$ and $Mn_{1.7}CuFe_{0.3}O_4$ spinel materials. The peaks for the compositions of both spinel materials indicate a single phase of $MnCo_2O_4$ with a cubic crystal structure and Mn_2CuO_4 with both cubic and tetragonal crystal structures. Comparing the XRD patterns of the spinel compositions at different ratios with those of Mn–Co and Mn–Cu–Fe spinel materials reveals a slight shift in the peaks toward lower diffraction angles. This demonstrates that Mn, Fe, Cu, and Co cations occupy octahedral and tetrahedral positions, and the distortion of the crystal structure is due to interdiffusion between the two spinel materials. Fig. 7 shows the XRD pattern of different composition ratios of Mn–Co: Mn–Cu–Fe oxide spinel materials (1:0, 3:1, 1:1,1:3, 0:1 wt%) at specific diffraction angles (P1, P2, P3, P4, P5, and P6). When comparing the diffraction angles across various composition ratios of Mn–Co: Mn–Cu–Fe oxide spinel materials, it is evident that for Mn–Co: Mn–Cu–Fe (1:1 wt%) ratio, the diffraction angle of the mixed spinel materials is lower than that of Mn–Co: Mn–Cu–Fe (3:1 and 1:3 wt%) and Mn–Co and Mn–Cu–Fe oxide spinel materials. According to Bragg's equation, decreasing the diffraction angle increases the interplanar distance and lattice parameters. This can be attributed to the higher interdiffusion of Mn, Fe, Cu, and Co cations in Mn–Co: Mn–Cu–Fe (1:1 wt%) spinel materials compared to that in Mn–Co: Mn–Cu–Fe (1:0, 3:1, 1:3, and 0:1) spinel materials. For more details on the composition of spinel materials and

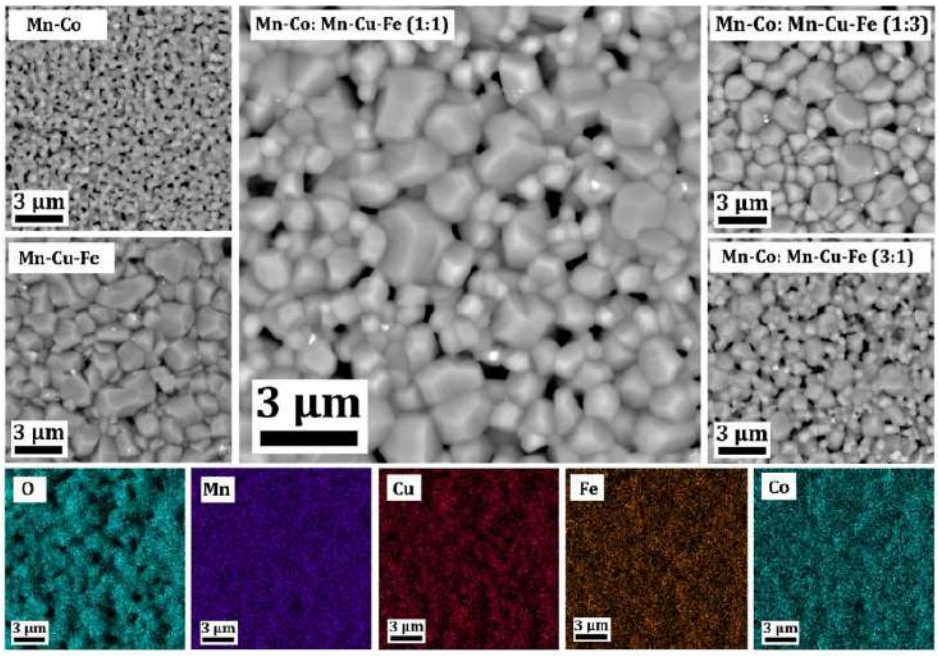

Fig. 6. The surface SEM images of pellets consisting of Mn–Co: Mn–Cu–Fe with various weight ratios (1:0, 0:1, 1:3, 1:1, and 3:1) sintered under oxidation treatment, alongside the EDS-X-ray elemental maps illustrating the composition of pellets with weight ratios of 1:1.

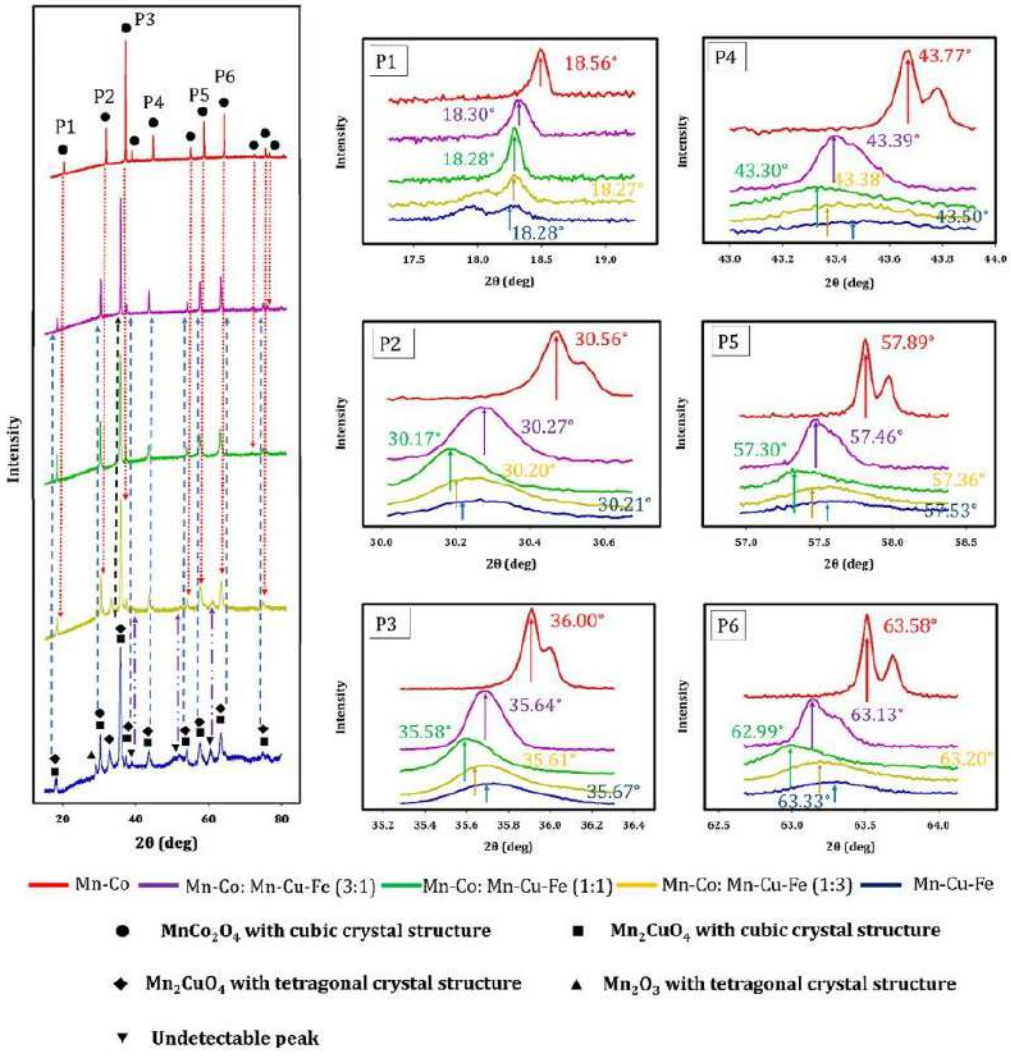

Fig. 7. The X-ray diffraction patterns of spinel materials, including Mn–Co, Mn–Cu–Fe, and Mn–Co: Mn–Cu–Fe with weight ratios of 1:3, 1:1, and 3:1 wt%, after undergoing the sintering process in an air atmosphere.

undetectable peaks in Mn–Cu–Fe oxide spinel material, Raman spectroscopy was used to further investigate the uncertain phase composition.

3.3.3. *Raman spectroscopy characterization*

Fig. 8 shows that Raman spectroscopy was used to qualitatively and quantitatively describe the investigated pellets in terms of their structure and volume ratios. Starting from the pellet made out of a single spinel, bands ca. 188, 475, 503, 590 and 663 cm^{-1} (the most characteristic) can be assigned to $MnCo_2O_4$ spinel phase [51,52]. The position of the most intense A_{1g} is slightly shifted towards lower Raman shift values when compared to other literature works [53,54], probably due to a thermally-induced Jahn-Taller effect typical for this spinel [55]. As for $Mn_{1.7}CuFe_{0.3}O_4$ specimen ten bands were recognized, but some of them 207, 304 (the most characteristic), 640 and 697 cm^{-1} can be assigned to Mn_2O_3 [56]. The others 93, 125, 441, 470, 538 and 584 cm^{-1} (the most characteristic) come from $Mn_{1.7}CuFe_{0.3}O_4$ [57,58]. In the case of Mn–Co: Mn–Cu–Fe (1:3 wt%), one can observe that additional bands coming from Mn–Co oxide spinel appeared compared to the spectrum of pure Mn–Cu–Fe spinel, but modes assigned to Mn–Cu–Fe spinel still dominate. What is more, bands ca. 300 and 640 cm^{-1} attributed to Mn_2O_3 are still visible, which is in a very good agreement with XRD patterns. For a 1:1 ratio, the expected increase in the intensity of a particular band assigned to Mn–Co spinel can be noticed, especially bands ca. 500 and 660 cm^{-1} comparing to band ca. 585 cm^{-1}. Furthermore, no Raman modes coming from Mn oxide are present, similarly to no peaks in XRD patterns. Such observations are highlighted much better for 3:1 ratio, as expected. Bands ca. 190, 500 and 660 cm^{-1} increased considerably in intensity, whereas Mn–Cu–Fe spinel modes can be barely noticed as single bands or even shoulders. However, to provide more accurate, quantitative approach, spectra deconvolution was provided within the most important 400 ÷ 700 cm^{-1} spectral region. In next step, I_{MnCo}/I_{MnCuFe} ratio for all five cases was calculated, where I_{MnCo} and I_{MnCuFe} stand for the sum of integral intensities of bands coming from Mn–Co and Mn–Cu–Fe oxide spinel, respectively. The obtained results (0.25, 0.44 and 0.71) suggest that Mn–Co: Mn–Cu–Fe ratios given in previous sections as 1:3, 1:1 and 3:1, respectively, were either exactly as expected, or very close to the presumed values. It

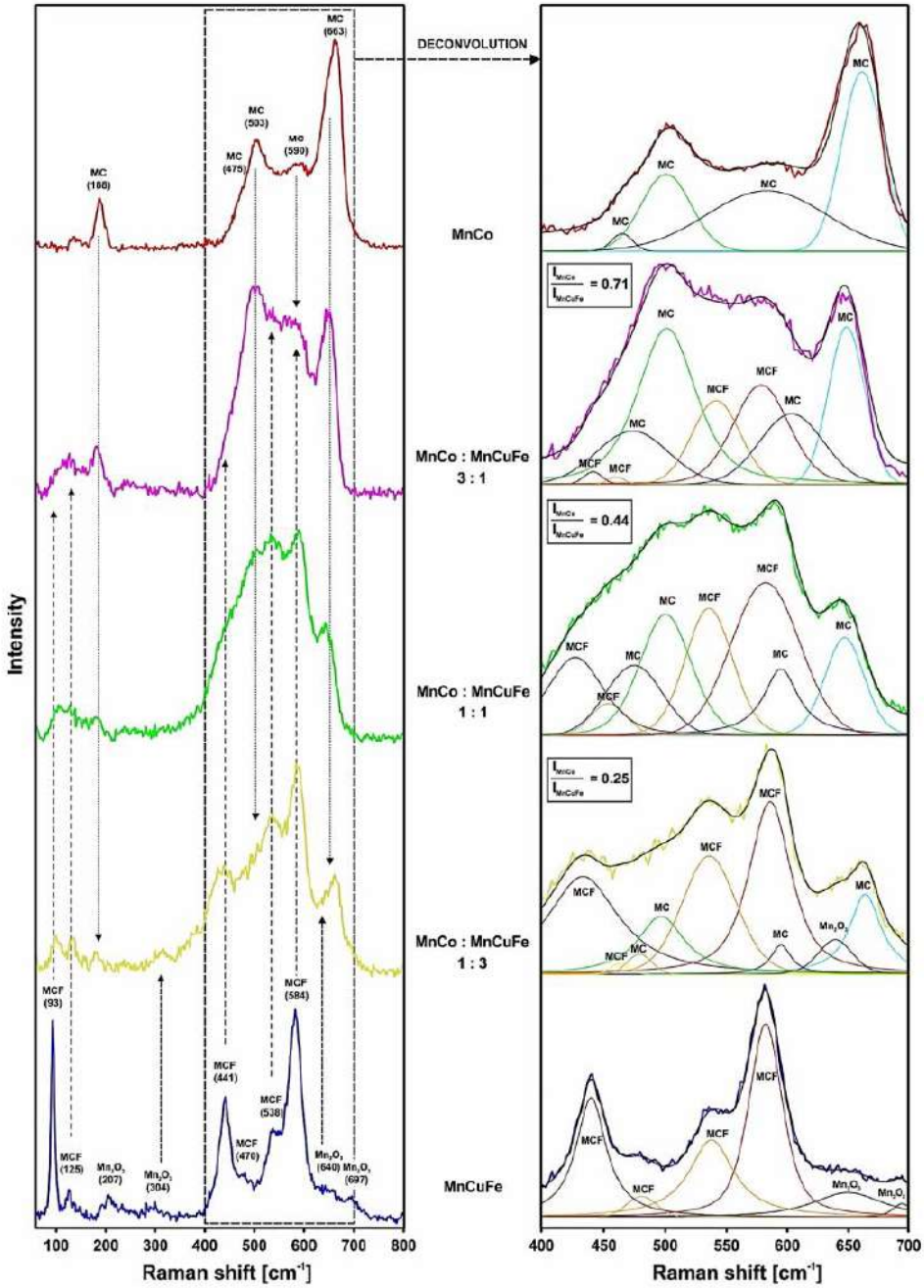

Fig. 8. Raman spectra of the investigated pellets. Arrows in the left image indicate the changes in the intensity of the particular bands. Right image illustrates the deconvoluted spectra with assignments of specific Raman modes.

indicates that procedures used in this work provide a very good control over the phase composition.

3.3.4. Shrinkage and porosity of hybrid materials

Fig. 9a displays the liner shrinkage percentage of pellets with varying ratios of Mn–Co to Mn–Cu–Fe spinel materials (1:0, 1:3, 1:1, 3:1, and 0:1 wt%) following sintering in static air at 900 °C for 4 h. The shrinkage percentage of Mn–Co spinel pellets is lower than that of Mn–Cu–Fe spinel pellets. Moreover, when comparing the different ratios of Mn–Co to Mn–Cu–Fe spinel pellets with pure Mn–Co and Mn–Cu–Fe spinel pellets, an increase in the proportion of Mn–Co spinel within the Mn–Cu–Fe spinel pellet led to a decrease in the shrinkage percentage.

Fig. 9b displays the porosity and bulk density of various spinel material ratios after sintering in a static air atmosphere at 900 °C for 4 h. The porosity of Mn–Co spinel pellets is higher than that of Mn–Cu–Fe spinel pellets. Additionally, increasing the ratio of Mn–Co spinel

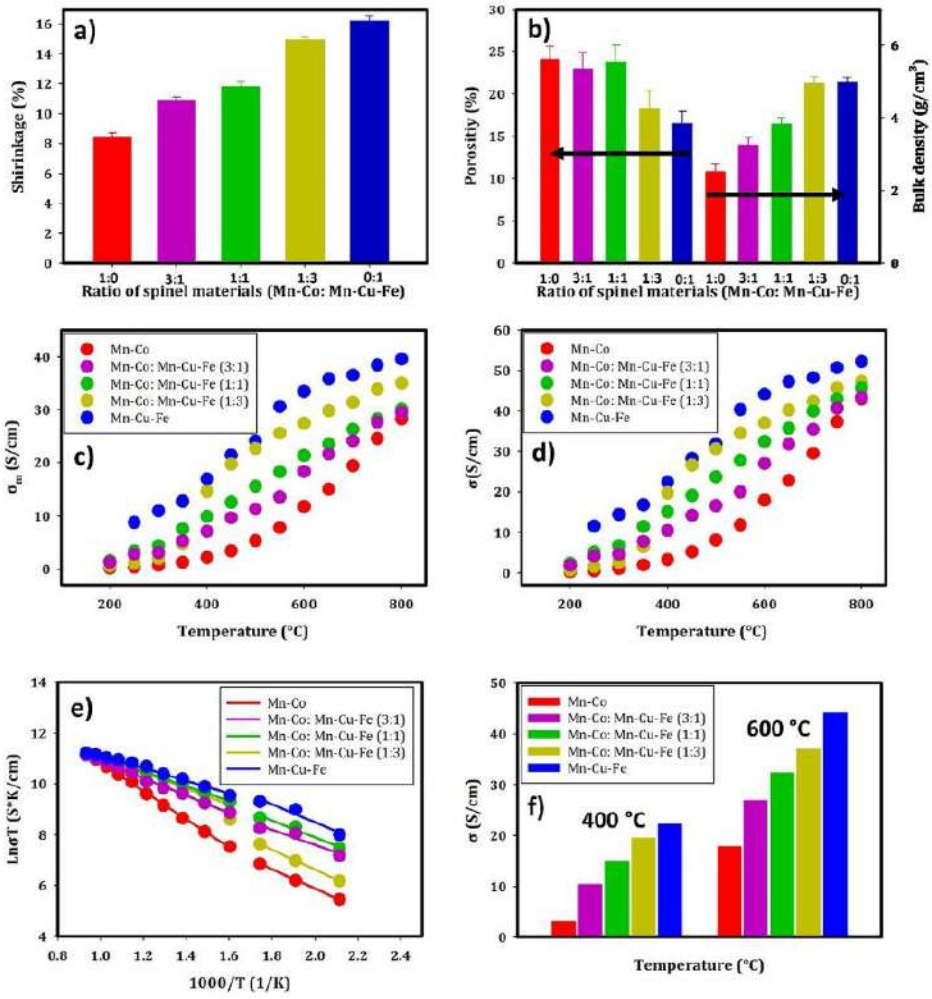

Fig. 9. a) Variation in pellet shrinkage with different proportions of spinel materials, b) Variation in the porosity and bulk density of pellets to different proportions of spinel materials, c) Electrical conductivity of pellets in correlation with temperature across various spinel material ratios, excluding porosity effects, d) Modifying the electrical conductivity of pellets with temperature, considering the influence of porosity, e) Arrhenius diagram depicting the relationship between pellet electrical conductivity and temperature for various ratios of spinel materials, and f) Electrical conductivity of pellets at different spinel material ratios at 400 °C and 600 °C.

material within Mn–Cu–Fe spinel pellets increases porosity. It is influenced by densification behavior and chemical composition. Mn–Cu–Fe pellets may achieve a higher level of densification under similar sintering conditions compared to Mn–Co pellets, resulting in reduced porosity. Moreover, Mn–Co coating exhibits enhanced densification during reduction + oxidation treatments compared to sintering in oxidation treatment (as depicted in Fig. 4a and b). This enhancement can be attributed to improved compatibility among its constituent elements (Mn, Cu, Fe). Additionally, there exists an inverse relationship between porosity and bulk density. As porosity increases, bulk density decreases, and vice versa. Comparing Fig. 9a and b reveals that the porosity percentage of Mn–Co spinel pellets is higher than that of Mn–Cu–Fe spinel pellets. Moreover, the densification of Mn–Co pellets is not notably significant. Consequently, the shrinkage percentage of Mn–Co spinel pellets does not exceed that of Mn–Cu–Fe spinel pellets.

3.3.5. *Electrical conductivity of hybrid materials*

The measurement of electrical conductivity is undertaken to gain insights into the electrical properties of spinel materials. The van der Pauw method was utilized to examine the electrical conductivity of spinel pellets. Fig. 9c illustrates the correlation between the electrical conductivity (σ_m) of pellets and temperature (200–800 °C) across different ratios of Mn–Co: Mn–Cu–Fe spinel materials (1:0, 1:3, 1:1, 3:1, and 0:1 wt%), excluding the influence of porosity. The results indicate that the electrical conductivity of Mn–Co spinel pellets is lower than that of Mn–Cu–Fe spinel pellets. Furthermore, the addition of Mn–Co spinel material to Mn–Cu–Fe spinel material results in a decrease in electrical conductivity. The electrical conductivity of Mn–Co, Mn–Co: Mn–Cu–Fe (3:1, 1:1, 1:3 wt%), and Mn–Cu–Fe oxide spinel materials at temperature of 600 °C is 17.96, 26.94, 32.40, 37.01, and 44.16 S/cm, respectively.

Fig. 9d illustrates the modification of pellet electrical conductivity with temperature across various ratios of Mn–Co: Mn–Cu–Fe spinel materials (1:0, 1:3, 1:1, 3:1, and 0:1 wt%) while considering the influence of porosity. After adjusting the electrical conductivity, the results indicate an increase in the electrical conductivity of pellets across different ratios. Additionally, the electrical conductivity of Mn–Co spinel material is lower than that of Mn–Cu–Fe spinel material. Moreover, increasing the ratio of Mn–Cu–Fe results in an increase in electrical

conductivity. It may be attributed to the presence of Fe dopant ions in Mn–Cu spinel material, which could increase its electrical conductivity by aiding the movement of charge carriers. Furthermore, the ion mobility within the crystal lattice of Mn–Cu–Fe spinel material may exceed that of Mn–Co spinel material, resulting in enhanced electrical conduction.

Fig. 9e illustrates an Arrhenius plot that depicts the correlation between pellet electrical conductivity and temperature across different ratios of spinel materials. The activation energy and pre-exponential factor were calculated for two temperatures, ranging 200–350 °C and 400–800 °C, and are detailed in Table 2.

The findings indicate that the activation energy of Mn–Cu–Fe spinel material decreases with higher temperatures. This is because elevated temperatures can increase the mobility of charge carriers within the Mn–Cu–Fe spinel material, making it easier for them to move and thereby lowering the activation energy needed for electrical conductivity. The activation energy of the Mn–Cu–Fe oxide spinel in this research is aligned with that of other studies [49,59]. Whereas the activation energy of Mn–Co spinel material decreases with lower temperature. At lower temperatures, this phenomenon is associated with a decrease in the motion of ions within the material. This diminished mobility restricts their capacity to surpass energy barriers, consequently leading to an increase in activation energy. The activation energy of the Mn–Co oxide spinel in this research is consistent with that reported in other study [49]. Furthermore, the addition of Mn–Co spinel material to Mn–Cu–Fe spinel material results in no significant disparity in activation energy between low and high temperatures.

Fig. 9f illustrates the electrical conductivity of pellets with varying ratios of spinel materials at 400 °C and 600 °C. At 800 °C, there are no significant differences observed among the different spinel material ratios (as shown in Fig. 9d). However, at 400 °C and 600 °C, significant variations are evident among the samples and temperatures. Consequently, Mn–Co and Mn–Co:M-Cu-Fe (3:1 wt%) spinel materials are recommended for intermediate temperature protective coatings, whereas Mn–Cu–Fe and Mn–Co:M-Cu-Fe (1:3 and 1:1 wt%) spinel materials are suitable for high temperature protective coatings.

4. Conclusions

The electrophoretic deposition (EPD) method proves to be highly effective for applying hybrid spinel materials onto metallic interconnects. These hybrid protective coatings play a critical role in preventing chromium migration, enhancing electrical conductivity compared to coatings made solely of Mn–Co or Mn–Cu–Fe spinel materials. Zeta potential and deposition yield are assessed to ensure the uniform distribution of Mn–Co and Mn–Cu–Fe spinel powders. Results indicate that the zeta potential and deposition yield of Mn–Co and Mn–Cu–Fe are approximately equal at 0.7 g/L iodine concentration. Consequently, hybrid spinel materials in varying ratios are uniformly deposited onto the metallic interconnect. The findings from a cross-sectional analysis of sintered hybrid spinel coatings under both sintering treatments indicate that densification is greater in coatings subjected to reduction + oxidation treatments compared to those sintered solely under oxidation treatment. In addition, mixing both oxide spinel powders in different ratios increased the sinterability, resulting in a highly densified coating compared to Mn–Co, and Mn–Cu–Fe oxide spinel coating. Furthermore, EDS mapping analysis reveals that during the EPD process, both Mn–Co and Mn–Cu–Fe spinel materials are uniformly deposited onto the substrate. The line scan analysis results indicate that the chromium diffusion from the substrate to the coating in hybrid spinel coatings is lower than in Mn–Cu–Fe spinel coatings and higher than in Mn–Co spinel coatings, for both sintering treatments. What is more, Raman studies proved applied EPD procedure and thermal treatment to be very efficient in the formation of coating materials of a well-defined phase composition. Furthermore, the electrical conductivity results demonstrate that the electrical conductivity of hybrid spinel materials is between that of Mn–Co and Mn–Cu–Fe oxide spinel material. The hybrid spinel coatings show promise for exhibiting high electrical conductivity, and increased sinterability compared to Mn–Co spinel material and low Cr diffusion compared to Mn–Cu–Fe spinel material. Therefore, Mn–Co: Mn–Cu–Fe (3:1, and 1:1 %) novel hybrid spinel coating emerges as a promising option for serving as a protective layer for stainless steels, and it will be explored further in upcoming studies.

Table 2
The activation energy and pre-exponential factor for different ratios of spinel material at two temperatures.

Spinel materials	Ratio (wt.%)	Temperature (°C)	E_a(eV)	$Ln\sigma_0$
Mn–Co: Mn–Cu–Fe	1:0	400–800	0.48	16.34
		200–350	0.33	13.49
	1:3	400–800	0.27	14.28
		200–350	0.34	14.49
	1:1	400–800	0.25	13.94
		200–350	0.29	14.59
	3:1	400–800	0.29	14.35
		200–350	0.26	13.61
	0:1	400–800	0.22	13.62
		200–350	0.31	15.64

CRediT authorship contribution statement

Omid Ekhlasiosgouei: Writing – original draft, Visualization, Validation, Software, Methodology, Investigation, Formal analysis, Data curation, Conceptualization. **Maciej Bik:** Writing – review & editing, Validation, Software, Methodology, Formal analysis, Data curation. **Federico Smeacetto:** Writing – review & editing, Validation, Data curation. **Piotr Jasinski:** Writing – review & editing, Validation, Resources, Data curation. **Sebastian Molin:** Writing – review & editing, Visualization, Validation, Supervision, Resources, Project administration, Methodology, Funding acquisition, Data curation, Conceptualization.

Declaration of interest statement

The authors declare that they have no known competing financial interests or personal relationships that could have appeared to influence the work reported in this paper.

Acknowledgement

This study received support from the National Science Centre (NCN) Opus project number 2023/49/B/ST8/03265: "Alternative to alloying: advanced protective coatings for low-cost alloys for solid oxide cell stack technology", which provided funding for the required experiments and analysis.

References

[1] Sreedhar I, Agarwal B, Goyal P, Singh SA. Recent advances in material and performance aspects of solid oxide fuel cells. J Electroanal Chem 2019;848:113315. https://doi.org/10.1016/j.jelechem.2019.113315.
[2] Mahato N, Banerjee A, Gupta A, Omar S, Balani K. Progress in material selection for solid oxide fuel cell technology: a review. Prog Mater Sci 2015;72:141–337. https://doi.org/10.1016/j.pmatsci.2015.01.001.
[3] Shaigan N, Qu W, Ivey DG, Chen W. A review of recent progress in coatings, surface modifications and alloy developments for solid oxide fuel cell ferritic stainless steel interconnects. J Power Sources 2010;195:1529–42. https://doi.org/10.1016/j.jpowsour.2009.09.069.
[4] Aznam I, Muchtar A, Somalu MR, Baharuddin NA, Rosli NAH. Advanced materials for heterogeneous catalysis: a comprehensive review of spinel materials for direct internal reforming of methane in solid oxide fuel cell. Chem Eng J 2023;471:144751. https://doi.org/10.1016/j.cej.2023.144751.
[5] Hassan MA, Bin Mamat O, Mehdi M. Review: influence of alloy addition and spinel coatings on Cr-based metallic interconnects of solid oxide fuel cells. Int J Hydrogen Energy 2020;45:25191–209. https://doi.org/10.1016/j.ijhydene.2020.06.234.

[6] Mao J, Wang E, Wang H, Ouyang M, Chen Y, Hu H, Lu L, Ren D, Liu Y. Progress in metal corrosion mechanism and protective coating technology for interconnect and metal support of solid oxide cells. Renew Sustain Energy Rev 2023;185. https://doi.org/10.1016/j.rser.2023.113597.
[7] Zanchi E, Talic B, Sabato AG, Molin S, Boccaccini AR, Smeacetto F. Electrophoretic co-deposition of Fe2O3 and Mn1,5Co1,5O4: processing and oxidation performance of Fe-doped Mn-Co coatings for solid oxide cell interconnects. J Eur Ceram Soc 2019;39:3768–77. https://doi.org/10.1016/j.jeurceramsoc.2019.05.024.
[8] Mirzaei M, Simchi A, Faghihi-Sani MA, Yazdanyar A. Electrophoretic deposition and sintering of a nanostructured manganese-cobalt spinel coating for solid oxide fuel cell interconnects. Ceram Int 2016;42:6648–56. https://doi.org/10.1016/j.ceramint.2016.01.012.
[9] Bobruk M, Molin S, Chen M, Brylewski T, Hendriksen PV. Sintering of MnCo2O4 coatings prepared by electrophoretic deposition. Mater Lett 2018;213:394–8. https://doi.org/10.1016/j.matlet.2017.12.046.
[10] Sun Z, Gopalan S, Pal UB, Basu SN. Cu1.3Mn1.7O4 spinel coatings deposited by electrophoretic deposition on Crofer 22 APU substrates for solid oxide fuel cell applications. Surf Coating Technol 2017;323:49–57. https://doi.org/10.1016/j.surfcoat.2016.09.028.
[11] Mazur Ł, Koszelow D, Zajusz M, Łapiński M, Bik M, Zając P, Adamczyk A, Rutkowski P, Molin S, Brylewski T. Comparison of Cu1.3Mn1.7O4 spinels doped with Ni or Fe and synthesized via wet chemistry and solid-state reaction methods, designed as potential coating materials for metallic interconnects. J Eur Ceram Soc 2023;43:5557–74. https://doi.org/10.1016/j.jeurceramsoc.2023.05.015.
[12] Guo PY, Pan JC, Wei PY, Shao Y, Qin C, Wang K, Wang YX, He Z, Wang DP, Yang LL, Zhang RN, Zhang JF. The formation of spinel CuxMn3-xO4 at 750 °C in the designed CuMn layers for solid oxide fuel cell applications. Surf Coating Technol 2023:464. https://doi.org/10.1016/j.surfcoat.2023.129467.
[13] Saeidpour F, Ebrahimifar H. Effect of nanostructure Fe-Ni-Co spinel oxides/Y2O3 coatings on the high-temperature oxidation behavior of Crofer 22 APU stainless steel interconnect. Corros Sci 2021;182:109280. https://doi.org/10.1016/j.corsci.2021.109280.
[14] Zhang Y, Zhang Y, Wu C, Yang Y, Li Q, Chen Y. Oxidation behavior and electrical properties of metal interconnects with Ce-doped Ni–Mn spinel coatings. Ceram Int 2022;48:9550–7. https://doi.org/10.1016/j.ceramint.2021.12.153.
[15] Qiao WQ, Li YW, Zhang YS, Wang MH, Li K, Li ZJ, Yang W. Cu- and Ce-doped MnCo2O4 spinel coatings on ferrite interconnects by electrophoretic deposition. Mater Today Commun 2024;38:108061. https://doi.org/10.1016/j.mtcomm.2024.108061.
[16] Aznam I, Mah JCW, Muchtar A, Somalu MR, Ghazali MJ. Electrophoretic deposition of (Cu,Mn,Co)3O4 spinel coating on SUS430 ferritic stainless steel: process and performance evaluation for solid oxide fuel cell interconnect applications. J Eur Ceram Soc 2021;41:1360–73. https://doi.org/10.1016/j.jeurceramsoc.2020.09.074.
[17] Zanchi E, Molin S, Sabato AG, Talic B, Cempura G, Boccaccini AR, Smeacetto F. Iron doped manganese cobaltite spinel coatings produced by electrophoretic co-deposition on interconnects for solid oxide cells | microfile:///F:/PhD Project/Articles/EPD Articles/EPD 3/power source 2.pdfstructural and electrical characterization. 2020. p. 455.
[18] Sabato AG, Molin S, Javed H, Zanchi E, Boccaccini AR, Smeacetto F. In-situ Cu-doped MnCo-spinel coatings for solid oxide cell interconnects processed by electrophoretic deposition. Ceram Int 2019;45:19148–57. https://doi.org/10.1016/j.ceramint.2019.06.161.
[19] Jin Q, Han L, Li N, Zhang T, Gao E, Yao M, Yao S, Wu Z, Li J, Zhu J, Wang W. Exploring the influence of chemical state of Cu species on CO-SCR performance in spinel-type CuM2O4 (M = Co, Mn, Fe, Ni, and Cr): the synergy between Cu2+ and surface oxygen vacancy. Fuel 2024;360:130553. https://doi.org/10.1016/j.fuel.2023.130553.
[20] Shaheen N, Chen Z, Nong Y, Su T, Yousaf M, Alomar M, Lu Y. Progress in nano-technology development and nano-material selection for low-temperature solid oxide fuel cell. J Alloys Compd 2024:977. https://doi.org/10.1016/j.jallcom.2023.173212.
[21] Horita T. Chromium poisoning for prolonged lifetime of electrodes in solid oxide fuel cells - review. Ceram Int 2021;47:7293–306. https://doi.org/10.1016/j.ceramint.2020.11.092.
[22] Gao J, Si X, Wang X, Li C, Qi J, Cao J. Exploring the effects of Mn content in the Mn-Co spinel coating on its formation and slowing the outward Cr diffusion. Corros Sci 2023;217:111156. https://doi.org/10.1016/j.corsci.2023.111156.
[23] Mah JCW, Muchtar A, Somalu MR, Ghazali MJ. Metallic interconnects for solid oxide fuel cell: a review on protective coating and deposition techniques. Int J Hydrogen Energy 2017;42:9219–29. https://doi.org/10.1016/j.ijhydene.2016.03.195.
[24] Reddy MJ, Kamecki B, Talic B, Zanchi E, Smeacetto F, Hardy JS, Choi JP, Mazur L, Vaßen R, Basu SN, Brylewski T, Svensson JE, Froitzheim J. Experimental review of the performances of protective coatings for interconnects in solid oxide fuel cells. J Power Sources 2023;568. https://doi.org/10.1016/j.jpowsour.2023.232931.
[25] Oh SU, Kim D, Lee IT, Choi CS, Lee JA, Heo YW, Lee JH. Electrophoretic deposition and low-temperature densification of Cu1.35Mn1.65O4 spinel for an interconnect protective coating in solid oxide fuel cells. Int J Hydrogen Energy 2022;47:33410–9. https://doi.org/10.1016/j.ijhydene.2022.07.259.
[26] Ekhlasiosgouei O, Smeacetto F, Molin S. Suspension and process parameters selection for electrophoretic deposition of Mn–Co spinel coating on steel interconnects. Int J Hydrogen Energy 2024;60:1054–67. https://doi.org/10.1016/j.ijhydene.2024.02.252.
[27] Wang B, Li K, Liu J, Yang T, Zhang N. Fabricating a MnCo coating to improve oxidation resistance and electrical conductivity of Crofer22H alloy as SOFC interconnect. Int J Hydrogen Energy 2024;50:1503–14. https://doi.org/10.1016/j.ijhydene.2023.11.014.
[28] Rednyk A, Musalek R, Tesar T, Medricky J, Tsepeleva A, Lukac F, Ctibor P, Sedlacek J, Chraska T. Liquid plasma spraying of NiO-YSZ anode layers applicable for SOFC. Mater Today Commun 2024;38:107855. https://doi.org/10.1016/j.mtcomm.2023.107855.
[29] Guski V, Verestek W, Rapp D, Schmauder S. Microstructural investigation of plasma sprayed ceramic coatings focusing on the effect of the splat boundary for SOFC sealing applications using peridynamics. Theor Appl Fract Mech 2021;112:102926. https://doi.org/10.1016/j.tafmec.2021.102926.
[30] N M, Santhy K, Rajasekaran B. The effect of strain induced phase transformation on the thermal expansion compatibility of plasma sprayed spinel coating on SOFC metallic interconnect – a study using in-situ high temperature X-ray diffraction. Int J Hydrogen Energy 2023;48:31767–78. https://doi.org/10.1016/j.ijhydene.2023.04.322.
[31] Chen X, Kou CC, Liao XJ, Li CX, Yang GJ, Huang K, Li CJ. Plasma-sprayed lanthanum-doped strontium titanate as an interconnect for solid oxide fuel cells: effects of powder size and process conditions. J Alloys Compd 2021;876:160212. https://doi.org/10.1016/j.jallcom.2021.160212.
[32] Zhou J, Hu X, Li J. Effect of Cu on the diffusion behavior and electrical properties of Ni-Co conversion coating for metallic interconnects in solid oxide fuel cells. J Alloys Compd 2021;887:161358. https://doi.org/10.1016/j.jallcom.2021.161358.
[33] Zhang X, You PF, Zhang HL, Yang XG, Luo MQ, Zeng C. Preparation and performances of Cu–Co spinel coating on ferritic stainless steel for solid oxide fuel cell interconnect. Int J Hydrogen Energy 2018;43:3273–9. https://doi.org/10.1016/j.ijhydene.2017.12.133.
[34] Cavichiolo LS, Nørby TH, Hald J, Pantleon K. Long-term effects of soft-chromising Ni-electroplated AISI 441 commodity steel for SOC stack interconnects. Corros Sci 2024;227. https://doi.org/10.1016/j.corsci.2023.111728.
[35] Lv Y, Geng S, Shi Z. Evaluation of electroplated copper coating on ferritic stainless steel for solid oxide fuel cells interconnects. J Alloys Compd 2017;726:269–75. https://doi.org/10.1016/j.jallcom.2017.07.318.
[36] Hu S, Li W, Finklea H, Liu X. A review of electrophoretic deposition of metal oxides and its application in solid oxide fuel cells. Adv Colloid Interface Sci 2020;276:102102. https://doi.org/10.1016/j.cis.2020.102102.
[37] Zhu H, Zhang J, Cao W. Recent advances in spinel-based protective coatings produced by electrochemical method on metallic interconnects for solid oxide fuel cells. Int J Hydrogen Energy 2024;50:977–91. https://doi.org/10.1016/j.ijhydene.2023.09.242.
[38] Oskouyi OE, Shahmiri M, Maghsoudipour A, Hasheminiasari M. Pulsed constant voltage electrophoretic deposition of YSZ electrolyte coating on conducting porous Ni–YSZ cermet for SOFCs applications. J Alloys Compd 2019;785:220–7. https://doi.org/10.1016/j.jallcom.2019.01.166.
[39] Oskouyi OE, Maghsoudipour A, Shahmiri M, Hasheminiasari M. Preparation of YSZ electrolyte coating on conducting porous Ni–YSZ cermet by DC and pulsed constant voltage electrophoretic deposition process for SOFCs applications. J Alloys Compd 2019;795:361–9. https://doi.org/10.1016/j.jallcom.2019.04.334.
[40] Ekhlasiosgouei O, Bik M, Molin S. Preparation of MnCo2O4 and Mn1.7CuFe0.3O4 single-layer, and novel MnCo2O4/Mn1.7CuFe0.3O4 dual-layer spinel protective coatings on complex-shaped metallic interconnects by EPD method. Int J Hydrogen Energy 2024;63:563–76. https://doi.org/10.1016/j.ijhydene.2024.07.447.
[41] Sun Z, Wang R, Nikiforov AY, Gopalan S, Pal UB, Basu SN. CuMn1.8O4 protective coatings on metallic interconnects for prevention of Cr-poisoning in solid oxide fuel cells. J Power Sources 2018;378:125–33. https://doi.org/10.1016/j.jpowsour.2017.12.031.
[42] Zhang H, Zhan Z, Liu X. Electrophoretic deposition of (Mn,Co)3O4 spinel coating for solid oxide fuel cell interconnects. J Power Sources 2011;196:8041–7. https://doi.org/10.1016/j.jpowsour.2011.05.053.
[43] Zhu Z, Darl-Uzu C, Pal U, Gopalan S, Hussain AM, Dale N, Fukuyama Y, Miura Y, Miyoshi Y, Basu S. Comparison of Cu–Mn and Mn–Co spinel coatings for solid oxide fuel cell interconnects. Int J Hydrogen Energy 2022;47:36953–63. https://doi.org/10.1016/j.ijhydene.2022.08.239.
[44] Ajdys L, Zurawska A, Kosiorek M, Naumovich Y, Zybert M, Wiecinska P, Chen M. Improving functional properties of protective coatings obtained by electrophoretic deposition on steel interconnects for solid oxide cells by tuning particle size distribution. Ceram Int 2023;49:33818–27. https://doi.org/10.1016/j.ceramint.2023.08.074.
[45] Bidabadi MHS, Siripongsakul T, Thublaor T, Wiman P, Chandra-ambhorn S. Oxidation and Cr-evaporation behavior of MnCo based spinel and composite coated AISI 430 steel. Surf Coating Technol 2022:434. https://doi.org/10.1016/j.surfcoat.2022.128176.
[46] Masi A, Bellusci M, McPhail SJ, Padella F, Reale P, Hong JE, Steinberger-Wilckens R, Carlini M. The effect of chemical composition on high temperature behaviour of Fe and Cu doped Mn-Co spinels. Ceram Int 2017;43:2829–35. https://doi.org/10.1016/j.ceramint.2016.11.135.
[47] Ma ZB, Wang MH, Zhang YS, Li K, Zhang MG, Yang W. Cu and Y doped (Co, Mn)3O4 spinel coatings on Crofer ferritic alloy by composite electrodeposition. Vacuum 2022;204:111352. https://doi.org/10.1016/j.vacuum.2022.111352.
[48] Ignaczak J, Zeng L, Sanchez DF, Makowska M, Górnicka K, Lankauf K, Karczewski J, Jasiński P, Molin S. Fe-modified Mn2CuO4 spinel oxides: coatings based on abundant elements for solid oxide cell interconnects. Int J Hydrogen Energy 2023;8. https://doi.org/10.1016/j.ijhydene.2023.06.041.
[49] Ignaczak J, Naumovich Y, Górnicka K, Jamroz J, Wróbel W, Karczewski J, Chen M, Jasiński P, Molin S. Preparation and characterisation of iron substituted

Mn1.7Cu1.3-xFexO4 spinel oxides (x = 0, 0.1, 0.3, 0.5). J Eur Ceram Soc 2020;40:5920–9. https://doi.org/10.1016/j.jeurceramsoc.2020.07.001.

[50] Handke M, Mozgawa W, Nocuń M. Specific features of the IR spectra of silicate glasses. J Mol Struct 1994;325:129–36. https://doi.org/10.1016/0022-2860(94)80028-6.

[51] Padmanathan N, Selladurai S. Mesoporous MnCo2O4 spinel oxide nanostructure synthesized by solvothermal technique for supercapacitor. Ionics 2014;20:479–87. https://doi.org/10.1007/s11581-013-1009-8.

[52] Yuvaraj S, Vignesh A, Shanmugam S, Kalai Selvan R. Nitrogen-doped Multi-walled Carbon Nanotubes-MnCo2O4 microsphere as electrocatalyst for efficient oxygen reduction reaction. Int J Hydrogen Energy 2016;41:15199–207. https://doi.org/10.1016/j.ijhydene.2016.06.115.

[53] Jayasubramaniyan S, Balasundari S, Rayjada PA, Kumar RA, Satyanarayana N, Muralidharan P. Enhanced electrochemical performance of MnCo2O4 nanorods synthesized via microwave hydrothermal method for supercapacitor applications. J Mater Sci Mater Electron 2018;29:21194–204. https://doi.org/10.1007/s10854-018-0269-5.

[54] Chen X, Cai S, Yu E, Li J, Chen J, Jia H. Photothermocatalytic performance of ACo 2 O 4 type spinel with light-enhanced mobilizable active oxygen species for toluene oxidation. Appl Surf Sci 2019;484:479–88. https://doi.org/10.1016/j.apsusc.2019.04.093.

[55] Hosterman BD. Raman spectroscopic study of solid solution spinel oxides. 2011.

[56] Shim SH, LaBounty D, Duffy TS. Raman spectra of bixbyite, Mn2O3, up to 40 GPa. Phys Chem Miner 2011;38:685–91. https://doi.org/10.1007/s00269-011-0441-4.

[57] Yang X, Tang W, Liu Z, Makita Y, Ooi K. Synthesis of lithium-rich LixMn2O4 spinels by lithiation and heat-treatment of defective spinels. J Mater Chem 2002;12:489–95. https://doi.org/10.1039/b109463g.

[58] Van Everbroeck T, Ciocarlan RG, Van Hoey W, Mertens M, Cool P. Copper-containing mixed metal oxides (Al, Fe, Mn) for application in three-way catalysis. Catalysts 2020;10:1–20. https://doi.org/10.3390/catal10111344.

[59] Waluyo NS, Park BK, Lee SB, Lim TH, Park SJ, Song RH, Lee JW. Mn,Cu)3O4-based conductive coatings as effective barriers to high-temperature oxidation of metallic interconnects for solid oxide fuel cells. J Solid State Electrochem 2014;18:445–52. https://doi.org/10.1007/s10008-013-2245-6.

4. Conclusion and future research directions

In this thesis, the research hypotheses have been validated. In addition, the conclusions of this thesis, along with potential directions for future research, are detailed as follows:

4.1. Conclusion

Electrophoretic deposition proves to be an efficient technique for applying single-layer, dual-layer, and hybrid coatings onto flat and complex-shaped stainless-steel surfaces, ensuring the formation of uniform, dense, and crack-free coatings. The detailed findings presented in this thesis are as follows:

- The stability of Mn-Co particles in both ethanol and H_2O: ethanol solvents exhibited similar behavior over a 5 h period. In the H_2O: ethanol solvent, Mn-Co particles tended to agglomerate, whereas in ethanol, the particles maintained a similar size. The zeta potential of Mn-Co particles in ethanol was significantly higher than that of particles in the H_2O: ethanol solvent. In addition, the suspension conductivity of Mn-Co particles was greater in the H_2O: ethanol solvent compared to ethanol.
- A uniform and dense coating was successfully achieved using ethanol as a solvent with a solid concentration of 10 g/L and an iodine concentration of 0.5 g/L. The Mn-Co coating was deposited at a voltage of 30 V for a duration of 20 s, resulting in a coating thickness of 7.4 ± 0.3 μm and a surface roughness of 0.75 ± 0.5 μm.
- The analysis of particle size distribution and zeta potential reveals that the Mn-Co oxide spinel suspension exhibits slightly smaller particle sizes and higher zeta potential than the Mn-Cu-Fe oxide spinel suspension. Additionally, the Mn-Co oxide spinel particles display a more regular morphology compared to the Mn-Cu-Fe oxide spinel particles.
- The results indicate that the thickness of the sintered $MnCo_2O_4$, $Mn_{1.7}CuFe_{0.3}O_4$ single-layer, and $MnCo_2O_4$/ $Mn_{1.7}CuFe_{0.3}O_4$ dual-layer coatings in reduction + oxidation treatments is 46.2%, 28.2%, and 23.1% denser, respectively, compared to sintered in oxidation treatment.
- The porosity of sintered $MnCo_2O_4$ and $Mn_{1.7}CuFe_{0.3}O_4$ coatings subjected to a reduction treatment followed by oxidation is approximately 50% lower compared to coatings sintered only in an oxidation treatment.

- Raman spectroscopy and Energy Dispersive Spectroscopy (EDS) analysis revealed that the sintered dual-layer coatings subjected to a reduction treatment followed by oxidation demonstrated a much more effective interdiffusion process throughout the coating's thickness, leading to the formation of a mixed (Mn, Cu, Fe, Co)$_3$O$_4$ spinel. This was in contrast to dual-layer coatings that underwent only oxidation treatment.
- Zeta potential and deposition yield were evaluated to confirm the uniform distribution of Mn-Co and Mn-Cu-Fe spinel powders. The results show that the zeta potential and deposition yield for both Mn-Co and Mn-Cu-Fe are nearly the same at an iodine concentration of 0.7 g/L.
- The findings from cross-sectional analysis of sintered hybrid spinel coatings under both sintering treatments indicate that densification is greater in coatings subjected to reduction + oxidation treatments compared to those sintered solely under oxidation treatment.
- The findings from cross-sectional analysis of sintered hybrid spinel coatings under both sintering treatments indicate that densification is greater in coatings subjected to reduction + oxidation treatments compared to those sintered solely under oxidation treatment.
- EDS mapping analysis reveals that during EPD process, both Mn-Co and Mn-Cu-Fe spinel materials are uniformly deposited onto the substrate.
- XRD result show that new phase in hybrid material was not detected.
- Raman studies proved applied EPD procedure and thermal treatment to be very efficient in the formation of coating materials of a well-defined phase composition.
- The electrical conductivity of the hybrid materials (1:1 wt.%) is higher than (45%) that of the $MnCo_2O_4$ spinel material but lower than (36%) that of the $Mn_{1.7}CuFe_{0.3}O_4$ spinel material at 600 °C.

4.2. Future research directions

The application of dual-layer and hybrid coatings offers a promising solution for providing both protective and conductive layers on metallic interconnects. To gain a deeper understanding of their long-term oxidation resistance, further research should focus on analyzing the microstructure of these coatings after oxidation, as well as evaluating the area-specific resistance (ASR) both before and after oxidation. Such studies are essential for

assessing the durability and performance of dual-layer and hybrid oxide spinel protective coatings over extended periods.

References

[1] P.S. and N.P. Bansal, Advances in Solid Oxide Fuel Cells IV, 2008.

[2] M. Singh, D. Zappa, E. Comini, Solid oxide fuel cell: Decade of progress, future perspectives and challenges, International Journal of Hydrogen Energy. 46 (2021) 27643–27674. https://doi.org/10.1016/j.ijhydene.2021.06.020.

[3] S. McIntosh, R.J. Gorte, Direct hydrocarbon solid oxide fuel cells, Chemical Reviews. 104 (2004) 4845–4865. https://doi.org/10.1021/cr020725g.

[4] A.B. Stambouli, E. Traversa, Solid oxide fuel cells (SOFCs): a review of an environmentally clean and efficient source of energy, 6 (2002) 433–455.

[5] J. Peng, J. Huang, X. long Wu, Y. wu Xu, H. Chen, X. Li, Solid oxide fuel cell (SOFC) performance evaluation, fault diagnosis and health control: A review, Journal of Power Sources. 505 (2021). https://doi.org/10.1016/j.jpowsour.2021.230058.

[6] W. Strickler, W.G. Carlson, CaO-Y,O,-ZrO, 47 (1963) 122–127.

[7] J.L. Hall, Cell components, 1987. https://doi.org/10.1016/s0031-9422(00)82398-5.

[8] C. Division, Phase relationships in the zirconia-yttria system, 10 (1975) 1527–1535.

[9] B.C.H. Steele, Appraisal of Ce 1 2 y Gd y O 2 2 y / 2 electrolytes for IT-SOFC operation at 500 8 C, 129 (2000) 95–110.

[10] S.C. Singhal, Solid Oxide Fuel Cells : Past , Present and Future, (n.d.). https://doi.org/10.1007/978-1-4471-4456-4.

[11] T. Setoguchi, K. Okamoto, K. Eguchi, H. Arai, SOLID-STATE SCIENCE AND TECHNOLOGY Effects of Anode Material and Fuel on Anodic Reaction of Solid Oxide Fuel Cells, 139 (1992) 2875–2880.

[12] C. Sun, U. Stimming, Recent anode advances in solid oxide fuel cells, Journal of Power Sources. 171 (2007) 247–260. https://doi.org/10.1016/j.jpowsour.2007.06.086.

[13] N.Q. Minh, R _-. -, 88 (1995).

[14] S.P. Jiang, A review of wet impregnation — An alternative method for the fabrication of high performance and nano-structured electrodes of solid oxide fuel cells, 418 (2006) 199–210. https://doi.org/10.1016/j.msea.2005.11.052.

[15] S.P. Jiang, Development of lanthanum strontium manganite perovskite cathode materials of solid oxide fuel cells : a review, 2008. https://doi.org/10.1007/s10853-008-2966-6.

[16] Y. Ji, J.A. Kilner, M.F. Carolan, Electrical properties and oxygen diffusion in yttria-stabilised zirconia (YSZ)– La 0 . 8 Sr 0 . 2 MnO 3 F d (LSM) composites, 176 (2005) 937–943. https://doi.org/10.1016/j.ssi.2004.11.019.

[17] S. Zarabi Golkhatmi, M.I. Asghar, P.D. Lund, A review on solid oxide fuel cell durability: Latest progress, mechanisms, and study tools, Renewable and Sustainable Energy Reviews. 161 (2022) 112339. https://doi.org/10.1016/j.rser.2022.112339.

[18] S.C. Singhal, Solid oxide fuel cells for stationary, mobile, and military applications, Solid State Ionics. 152–153 (2002) 405–410. https://doi.org/10.1016/S0167-2738(02)00349-1.

[19] J. Wu, X. Liu, Recent development of SOFC metallic interconnect, Journal of Materials Science and Technology. 26 (2010) 293–305. https://doi.org/10.1016/S1005-0302(10)60049-7.

[20] E. Zanchi, A.G. Sabato, S. Molin, G. Cempura, A.R. Boccaccini, F. Smeacetto, Recent advances on spinel-based protective coatings for solid oxide cell metallic interconnects produced by electrophoretic deposition, Materials Letters. 286 (2021) 129229. https://doi.org/10.1016/j.matlet.2020.129229.

[21] M.A. Hassan, O. Bin Mamat, M. Mehdi, Review: Influence of alloy addition and spinel coatings on Cr-based metallic interconnects of solid oxide fuel cells, International Journal of Hydrogen Energy. 45 (2020) 25191–25209. https://doi.org/10.1016/j.ijhydene.2020.06.234.

[22] Y. Pan, J. Wang, Z. Lu, R. Wang, Z. Xu, A review on the application of magnetron sputtering technologies for solid oxide fuel cell in reduction of the operating temperature, International Journal of Hydrogen Energy. 50 (2024) 1179–1193. https://doi.org/10.1016/j.ijhydene.2023.10.143.

[23] E. Zanchi, J. Ignaczak, B. Kamecki, P. Jasiński, S. Molin, A.R. Boccaccini, F. Smeacetto, Manganese–cobalt based spinel coatings processed by electrophoretic deposition method: The influence of sintering on degradation issues of solid oxide cell oxygen electrodes at 750 ◦c, Materials. 14 (2021). https://doi.org/10.3390/ma14143836.

[24] B. Talic, S. Molin, K. Wiik, P.V. Hendriksen, H.L. Lein, Comparison of iron and copper doped manganese cobalt spinel oxides as protective coatings for solid oxide fuel cell interconnects, Journal of Power Sources. 372 (2017) 145–156. https://doi.org/10.1016/j.jpowsour.2017.10.060.

[25] R. Wang, Z. Sun, U.B. Pal, S. Gopalan, S.N. Basu, Mitigation of chromium poisoning of cathodes in solid oxide fuel cells employing CuMn1.8O4 spinel coating on metallic interconnect, Journal of Power Sources. 376 (2018) 100–110. https://doi.org/10.1016/j.jpowsour.2017.11.069.

[26] B. Talic, A.C. Wulff, S. Molin, K.B. Andersen, P. Zielke, H.L. Frandsen, Investigation of electrophoretic deposition as a method for coating complex shaped steel parts in solid oxide cell stacks, Surface and Coatings Technology. 380 (2019) 1–8. https://doi.org/10.1016/j.surfcoat.2019.125093.

[27] R. Wang, Z. Sun, J.P. Choi, S.N. Basu, J.W. Stevenson, M.C. Tucker, Ferritic stainless steel interconnects for protonic ceramic electrochemical cell stacks: Oxidation behavior and protective coatings, International Journal of Hydrogen Energy. 44 (2019) 25297–25309. https://doi.org/10.1016/j.ijhydene.2019.08.041.

[28] I. Thaheem, D.W. Joh, T. Noh, H.N. Im, K.T. Lee, Physico-electrochemical properties and long-term stability of Mn1.45-0.5xCo1.45-0.5xCuxY0.1O4 spinel protective coatings on commercial metallic interconnects for solid oxide fuel cells, Journal of Industrial and Engineering Chemistry. 96 (2021) 315–321. https://doi.org/10.1016/j.jiec.2021.01.031.

[29] B. Hua, W. Zhang, J. Wu, J. Pu, B. Chi, L. Jian, A promising NiCo2O4 protective coating for metallic interconnects of solid oxide fuel cells, Journal of Power Sources. 195 (2010) 7375–7379. https://doi.org/10.1016/j.jpowsour.2010.05.031.

[30] N. Shaigan, D.G. Ivey, W. Chen, Oxidation and electrical behavior of nickel/lanthanum chromite-coated stainless steel interconnects, Journal of Power Sources. 183 (2008) 651–659. https://doi.org/10.1016/j.jpowsour.2008.05.024.

[31] B. Talic, P.V. Hendriksen, K. Wiik, H.L. Lein, Thermal expansion and electrical conductivity of Fe and Cu doped MnCo2O4 spinel, Solid State Ionics. 326 (2018) 90–99. https://doi.org/10.1016/j.ssi.2018.09.018.

[32] M. Bednarz, S. Molin, M. Bobruk, M. Stygar, E. Długoń, M. Sitarz, T. Brylewski, High-temperature oxidation of the Crofer 22 H ferritic steel with Mn1.45Co1.45Fe0.1O4 and Mn1.5Co1.5O4 spinel coatings under thermal cycling conditions and its properties, Materials Chemistry and Physics. 225 (2019) 227–238. https://doi.org/10.1016/j.matchemphys.2018.12.090.

[33] A.G. Sabato, E. Zanchi, S. Molin, G. Cempura, H. Javed, K. Herbrig, C. Walter, A.R. Boccaccini, F. Smeacetto, Mn-Co spinel coatings on Crofer 22 APU by electrophoretic deposition: Up scaling, performance in SOFC stack at 850 °C and compositional modifications, Journal of the European Ceramic Society. 41 (2021) 4496–4504. https://doi.org/10.1016/j.jeurceramsoc.2021.03.030.

[34] B. Talic, P.V. Hendriksen, K. Wiik, H.L. Lein, Thermal expansion and electrical conductivity of Fe and Cu doped MnCo2O4 spinel, Solid State Ionics. 326 (2018) 90–99. https://doi.org/10.1016/j.ssi.2018.09.018.

[35] L. Zhou, J.H. Mason, W. Li, X. Liu, Comprehensive review of chromium deposition and poisoning of solid oxide fuel cells (SOFCs) cathode materials, Renewable and Sustainable Energy Reviews. 134 (2020). https://doi.org/10.1016/j.rser.2020.110320.

[36] N.S. Waluyo, S.S. Park, R.H. Song, S.B. Lee, T.H. Lim, J.E. Hong, K.H. Ryu, W. Bin Im, J.W. Lee, Protective coating based on manganese–copper oxide for solid oxide fuel cell interconnects: Plasma spray coating and performance evaluation, Ceramics International. 44 (2018) 11576–11581. https://doi.org/10.1016/j.ceramint.2018.03.220.

[37] B. Talic, H. Falk-Windisch, V. Venkatachalam, P.V. Hendriksen, K. Wiik, H.L. Lein, Effect of coating density on oxidation resistance and Cr vaporization from solid oxide fuel cell interconnects, Journal of Power Sources. 354 (2017) 57–67. https://doi.org/10.1016/j.jpowsour.2017.04.023.

[38] J. Wu, Y. Jiang, C. Johnson, X. Liu, DC electrodeposition of Mn-Co alloys on stainless steels for SOFC interconnect application, Journal of Power Sources. 177 (2008) 376–385. https://doi.org/10.1016/j.jpowsour.2007.11.075.

[39] M. Palcut, L. Mikkelsen, K. Neufeld, M. Chen, R. Knibbe, P.V. Hendriksen, Efficient dual layer interconnect coating for high temperature electrochemical devices, International Journal of Hydrogen Energy. 37 (2012) 14501–14510. https://doi.org/10.1016/j.ijhydene.2012.07.038.

[40] Z. Zhu, U. Pal, S. Gopalan, A.M. Hussain, S. Dong, N. Dale, Y. Fukuyama, S. Basu, Alternating-Current Electrophoretic Deposition of Spinel Coatings on Porous Metallic Substrates for Solid Oxide Fuel Cell Applications, Jom. 73 (2021) 2764–2770. https://doi.org/10.1007/s11837-021-04763-2.

[41] M.J. Reddy, B. Kamecki, B. Talic, E. Zanchi, F. Smeacetto, J.S. Hardy, J.P. Choi, L. Mazur, R. Vasßen, S.N. Basu, T. Brylewski, J.E. Svensson, J. Froitzheim, Experimental review of the performances of protective coatings for interconnects in solid oxide fuel cells, Journal of Power Sources. 568 (2023). https://doi.org/10.1016/j.jpowsour.2023.232831.

[42] Y. Jin, J. Sheng, G. Hao, M. Guo, W. Hao, Z. Yang, X. Xiong, S. Peng, Highly dense (Mn,Co)3O4 spinel protective coating derived from Mn–Co metal precursors for SOFC interconnect applications, International Journal of Hydrogen Energy. 47 (2022) 13960–13968. https://doi.org/10.1016/j.ijhydene.2022.02.129.

[43] J. Mougin, T. Le Bihan, G. Lucazeau, High-pressure study of Cr2O3 obtained by high-temperature oxidation by X-ray diffraction and Raman spectroscopy, Journal of Physics and Chemistry of Solids. 62 (2001) 553–563. https://doi.org/10.1016/S0022-3697(00)00215-8.

[44] J.W. Stevenson, Z.G. Yang, G.G. Xia, Z. Nie, J.D. Templeton, Long-term oxidation behavior of spinel-coated ferritic stainless steel for solid oxide fuel cell interconnect applications, Journal of Power Sources. 231 (2013) 256–263. https://doi.org/10.1016/j.jpowsour.2013.01.033.

[45] M. Reisert, V. Berova, A. Aphale, P. Singh, M.C. Tucker, Oxidation of porous stainless steel supports for metal-supported solid oxide fuel cells, International Journal of Hydrogen Energy. 45 (2020) 30882–30897. https://doi.org/10.1016/j.ijhydene.2020.08.015.

[46] D. Koszelow, M. Makowska, F. Marone, J. Karczewski, P. Jasiński, S. Molin, High temperature corrosion evaluation and lifetime prediction of porous Fe22Cr stainless steel in air in temperature range 700–900 °C, Corrosion Science. 189 (2021). https://doi.org/10.1016/j.corsci.2021.109589.

[47] N.J. Magdefrau, L. Chen, E.Y. Sun, M. Aindow, Effects of alloy heat treatment on oxidation kinetics and scale morphology for crofer 22 APU, Journal of Power Sources. 241 (2013) 756–767. https://doi.org/10.1016/j.jpowsour.2013.03.181.

[48] E. Park, S. Taniguchi, T. Daio, J. Chou, K. Sasaki, Comparison of chromium poisoning among solid oxide fuel cell cathode materials, Solid State Ionics. 262 (2014) 421–427. https://doi.org/10.1016/j.ssi.2014.01.047.

[49] F. Shen, K. Lu, Co3O4/Sm-Doped CeO2/Co3O4 Trilayer Coating on AISI 441 Interconnect for Solid Oxide

Fuel Cells, ACS Applied Materials and Interfaces. 9 (2017) 6022–6029. https://doi.org/10.1021/acsami.6b14562.

[50] M.H.S. Bidabadi, T. Siripongsakul, T. Thublaor, P. Wiman, S. Chandra-ambhorn, Oxidation and Cr-evaporation behavior of MnCo based spinel and composite coated AISI 430 steel, Surface and Coatings Technology. 434 (2022). https://doi.org/10.1016/j.surfcoat.2022.128176.

[51] A.G. Sabato, S. Molin, H. Javed, E. Zanchi, A.R. Boccaccini, F. Smeacetto, In-situ Cu-doped MnCo-spinel coatings for solid oxide cell interconnects processed by electrophoretic deposition, Ceramics International. 45 (2019) 19148–19157. https://doi.org/10.1016/j.ceramint.2019.06.161.

[52] J. Yoo, S.K. Woo, J.H. Yu, S. Lee, G.W. Park, La0.8Sr0.2MnO3 and (Mn1.5Co1.5)O4 double layer coated by electrophoretic deposition on Crofer22 APU for SOEC interconnect applications, International Journal of Hydrogen Energy. 34 (2009) 1542–1547. https://doi.org/10.1016/j.ijhydene.2008.12.005.

[53] D. Liu, S. Geng, G. Chen, F. Wang, NiO/NiFe2O4 dual-layer coating on pre-oxidized SUS 430 steel interconnect, International Journal of Hydrogen Energy. 47 (2022) 21462–21471. https://doi.org/10.1016/j.ijhydene.2022.04.273.

[54] C. Goebel, R. Berger, C. Bernuy-Lopez, J. Westlinder, J.E. Svensson, J. Froitzheim, Long-term (4 year) degradation behavior of coated stainless steel 441 used for solid oxide fuel cell interconnect applications, Journal of Power Sources. 449 (2020). https://doi.org/10.1016/j.jpowsour.2019.227480.

[55] J.G. Grolig, J. Froitzheim, J.E. Svensson, Coated stainless steel 441 as interconnect material for solid oxide fuel cells: Evolution of electrical properties, Journal of Power Sources. 284 (2015) 321–327. https://doi.org/10.1016/j.jpowsour.2015.03.029.

[56] S. Molin, P. Jasinski, L. Mikkelsen, W. Zhang, M. Chen, P. V. Hendriksen, Low temperature processed MnCo2O4 and MnCo1.8Fe0.2O4 as effective protective coatings for solid oxide fuel cell interconnects at 750 °C, Journal of Power Sources. 336 (2016) 408–418. https://doi.org/10.1016/j.jpowsour.2016.11.011.

[57] Ł. Mazur, J. Ignaczak, M. Bik, S. Molin, M. Sitarz, Aleksander Gil, T. Brylewski, Effectiveness of a dual surface modification of metallic interconnects for application in energy conversion devices, International Journal of Hydrogen Energy. 47 (2022) 6295–6311. https://doi.org/10.1016/j.ijhydene.2021.11.256.

[58] J.C.W. Mah, A. Muchtar, M.R. Somalu, M.J. Ghazali, Metallic interconnects for solid oxide fuel cell: A review on protective coating and deposition techniques, International Journal of Hydrogen Energy. 42 (2017) 9219–9229. https://doi.org/10.1016/j.ijhydene.2016.03.195.

[59] Z. Sun, R. Wang, A.Y. Nikiforov, S. Gopalan, U.B. Pal, S.N. Basu, CuMn1.8O4 protective coatings on metallic interconnects for prevention of Cr-poisoning in solid oxide fuel cells, Journal of Power Sources. 378 (2018) 125–133. https://doi.org/10.1016/j.jpowsour.2017.12.031.

[60] A. Holt, P. Kofstad, Electrical conductivity and defect structure of Cr2O3. I. High temperatures (>~1000°C), Solid State Ionics. 69 (1994) 127–136. https://doi.org/https://doi.org/10.1016/0167-2738%2894%2990401-4.

[61] A. Holt, P. Kofstad, Electrical conductivity and defect structure of Cr2O3. II. Reduced temperatures (<~1000°C), Solid State Ionics. 69 (1994) 137–143. https://doi.org/https://doi.org/10.1016/0167-2738(94)90402-2.

[62] F. Cheng, J. Sun, Fabrication of a double-layered Co-Mn-O spinel coating on stainless steel via the double glow plasma alloying process and preoxidation treatment as SOFC interconnect, International Journal of Hydrogen Energy. 44 (2019) 18415–18424. https://doi.org/10.1016/j.ijhydene.2019.05.060.

[63] M. Wolff, A. Schwiers, K. Wilkner, D. Sebold, N.H. Menzler, Wet powder spraying – A versatile and highly effective technique for the application of spinel-type protective coatings on SOC interconnects, Journal of Power Sources. 592 (2024) 233931. https://doi.org/10.1016/j.jpowsour.2023.233931.

[64] Y. Zhang, Y. Zhang, C. Wu, Y. Yang, Q. Li, Y. Chen, Oxidation behavior and electrical properties of metal interconnects with Ce-doped Ni–Mn spinel coatings, Ceramics International. 48 (2022) 9550–9557. https://doi.org/10.1016/j.ceramint.2021.12.153.

[65] L. Agun, H.A. Rahman, S. Ahmad, A. Muchtar, Durability and stability of LSCF composite cathode for intermediate-low temperature of solid oxide fuel cell (IT-LT SOFC): Short Review, 893 (2014) 732–737. https://doi.org/10.4028/www.scientific.net/AMR.893.732.

[66] K.H. Tan, H.A. Rahman, H. Taib, Coating layer and influence of transition metal for ferritic stainless steel interconnector solid oxide fuel cell: A review, International Journal of Hydrogen Energy. 44 (2019) 30591–30605. https://doi.org/10.1016/j.ijhydene.2019.06.155.

[67] J. Ignaczak, Y. Naumovich, K. Górnicka, J. Jamroz, W. Wróbel, J. Karczewski, M. Chen, P. Jasiński, S. Molin, Preparation and characterisation of iron substituted Mn1.7Cu1.3-xFexO4 spinel oxides (x = 0, 0.1, 0.3, 0.5), Journal of the European Ceramic Society. 40 (2020) 5920–5929. https://doi.org/10.1016/j.jeurceramsoc.2020.07.001.

[68] H.L. Anthony Petric, Electrical Conductivity and Thermal Expansion of Spinels at Elevated Temperatures, Journal of the American Ceramic Society. 90 (2007) 1515–1520. https://doi.org/10.1111/j.1551-2916.2007.01522.x.

[69] B.K. Park, J.W. Lee, S.B. Lee, T.H. Lim, S.J. Park, C.O. Park, R.H. Song, Cu- and Ni-doped Mn1.5Co1.5O4 spinel coatings on metallic interconnects for solid oxide fuel cells, International Journal of Hydrogen Energy. 38 (2013) 12043–12050. https://doi.org/10.1016/j.ijhydene.2013.07.025.

[70] S.T. Hashemi, A. Masoud, M. Askari, P.E. Gannon, applications, Materials Research Bulletin. 102 (2018) 180–185. https://doi.org/10.1016/j.materresbull.2018.02.040.

[71] O. Characteristics, F. Cell, M. Interconnects, Oxidation Characteristics and Electrical Properties of Doped Mn-Co Spinel Reaction Layer for Solid Oxide Fuel Cell Metal Interconnects, (2018). https://doi.org/10.3390/coatings8010042.

[72] Z. Sun, S. Gopalan, U.B. Pal, S.N. Basu, Cu1.3Mn1.7O4 spinel coatings deposited by electrophoretic deposition on Crofer 22 APU substrates for solid oxide fuel cell applications, Surface and Coatings Technology. 323 (2017) 49–57. https://doi.org/10.1016/j.surfcoat.2016.09.028.

[73] Æ.P. Holtappels, Æ.T. Graule, T. Nakamura, Æ.L.J. Gauckler, Materials design for perovskite SOFC cathodes, (2009) 985–999. https://doi.org/10.1007/s00706-009-0153-3.

[74] M. Tsai, C. Chu, S. Lee, La0.6Sr0.4Co0.2Fe0.8O3 protective coatings for solid oxide fuel cell interconnect deposited by screen printing, Journal of Alloys and Compounds. 489 (2010) 576–581. https://doi.org/10.1016/j.jallcom.2009.09.114.

[75] Z. Yang, G. Xia, G.D. Maupin, J.W. Stevenson, Conductive protection layers on oxidation resistant alloys for SOFC interconnect applications, 201 (2006) 4476–4483. https://doi.org/10.1016/j.surfcoat.2006.08.082.

[76] K.O. Hoyt, P.E. Gannon, P. White, R. Tortop, B.J. Ellingwood, H. Khoshuei, Oxidation behavior of (Co,Mn) 3O 4 coatings on preoxidized stainless steel for solid oxide fuel cell interconnects, International Journal of Hydrogen Energy. 37 (2012) 518–529. https://doi.org/10.1016/j.ijhydene.2011.09.028.

[77] A. Kruk, M. Stygar, T. Brylewski, Mn – Co spinel protective – conductive coating on AL453 ferritic stainless steel for IT-SOFC interconnect applications, Journal of Solid State Electrochemistry. (2013) 993–1003. https://doi.org/10.1007/s10008-012-1952-8.

[78] M. Mirzaei, A. Simchi, A. Yazdanyar, Electrophoretic deposition and sintering of a nanostructured manganese–cobalt spinel coating for solid oxide fuel cell interconnects, Ceramics International. 42 (2016) 6648–6656. https://doi.org/10.1016/j.ceramint.2016.01.012.

[79] H. Zhang, Z. Zhan, X. Liu, Electrophoretic deposition of (Mn,Co)3O4 spinel coating for solid oxide fuel cell interconnects, Journal of Power Sources. 196 (2011) 8041–8047.

https://doi.org/10.1016/j.jpowsour.2011.05.053.

[80] N. Shaigan, D.G. Ivey, W. Chen, Co/LaCrO3 composite coatings for AISI 430 stainless steel solid oxide fuel cell interconnects, Journal of Power Sources. 185 (2008) 331–337. https://doi.org/10.1016/j.jpowsour.2008.06.065.

[81] G. Cabouro, G. Caboche, S. Chevalier, P. Piccardo, Opportunity of metallic interconnects for ITSOFC : Reactivity and electrical property, Journal of Power Sources. 156 (2006) 39–44. https://doi.org/10.1016/j.jpowsour.2005.08.039.

[82] A. Conductor, T. Nogami, D.P. Sai, B. Singh, R.K. Singh, I. Coatings, Y. Gong, Y. Zhu, Use of SOFC Metallic Interconnfile:///C:/Users/ASUS/Desktop/Int J Applied Ceramic Tech - 2013 - Zhang - Fabrication of Mn Co Spinel Coatings on Crofer 22 APU Stainless Steel by.pdfect Coated with Spinel Protective Layers using the APS Technology, (2007).

[83] Y. Zhang, A. Javed, M. Zhou, S. Liang, Fabrication of Mn – Co Spinel Coatings on Crofer 22 APU Stainless Steel by Electrophoretic Deposition for Interconnect Applications in Solid Oxide Fuel Cells, 341 (2014) 332–341. https://doi.org/10.1111/ijac.12013.

[84] P. Paknahad, M. Askari, M. Ghorbanzadeh, Abstract, Journal of Power Sources. (2014). https://doi.org/10.1016/j.jpowsour.2014.04.122.

[85] L. Besra, M. Liu, A review on fundamentals and applications of electrophoretic deposition (EPD), Progress in Materials Science. 52 (2007) 1–61. https://doi.org/10.1016/j.pmatsci.2006.07.001.

[86] N.J. Magdefrau, L. Chen, E.Y. Sun, M. Aindow, The effect of Mn1.5Co1.5O4 coatings on the development of near surface microstructure for Haynes 230 oxidized at 800°C in air, Surface and Coatings Technology. 242 (2014) 109–117. https://doi.org/https://doi.org/10.1016/j.surfcoat.2014.01.025.

[87] Å.H. Persson, L. Mikkelsen, P. V Hendriksen, M.A.J. Somers, Interaction mechanisms between slurry coatings and solid oxide fuel cell interconnect alloys during high temperature oxidation, Journal of Alloys and Compounds. 521 (2012) 16–29. https://doi.org/https://doi.org/10.1016/j.jallcom.2011.12.095.

[88] S. Lee, J. Hong, H. Kim, J. Son, J. Lee, B. Kim, H. Lee, K. Joong, Highly Dense Mn-Co Spinel Coating for Protection of Metallic Interconnect of Solid Oxide Fuel Cells Highly Dense Mn-Co Spinel Coating for Protection of Metallic Interconnect of Solid Oxide Fuel Cells, (2014). https://doi.org/10.1149/2.0541414jes.

[89] S.R. Akanda, N.J. Kidner, M.E. Walter, Spinel coatings on metallic interconnects: Effect of reduction heat treatment on performance, Surface and Coatings Technology. 253 (2014) 255–260. https://doi.org/https://doi.org/10.1016/j.surfcoat.2014.05.049.

[90] E. Zanchi, A.G. Sabato, M.C. Monterde, L. Bernadet, M. Torrell, J.A. Calero, A. Tarancón, F. Smeacetto, Electrophoretic deposition of MnCo2O4 coating on solid oxide cell interconnects manufactured through powder metallurgy, Materials and Design. 227 (2023) 111768. https://doi.org/10.1016/j.matdes.2023.111768.

[91] D.R. Ou, M. Cheng, X.L. Wang, Development of low-temperature sintered Mn-Co spinel coatings on Fe-Cr ferritic alloys for solid oxide fuel cell interconnect applications, Journal of Power Sources. 236 (2013) 200–206. https://doi.org/10.1016/j.jpowsour.2013.02.058.

[92] Y. Shao, H. Zhu, X. Zhang, P.Y. Guo, C. Qin, K. Wang, Y.X. Wang, Z. He, D.P. Wang, L.L. Yang, N. Liu, Z.Z. Dong, Design and competitive growth of different spinels at 750 °C for the multi-component CuCoMnFe alloy coatings, Surface and Coatings Technology. 479 (2024). https://doi.org/10.1016/j.surfcoat.2024.130507.

[93] Z. Ranjbar-Nouri, M. Soltanieh, S. Rastegari, Applying the protective CuMn2O4 spinel coating on AISI-430 ferritic stainless steel used as solid oxide fuel cell interconnects, Surface and Coatings Technology. 334 (2018) 365–372. https://doi.org/10.1016/j.surfcoat.2017.11.036.

[94] E. Zanchi, J. Ignaczak, S. Molin, G. Cempura, A.R. Boccaccini, F. Smeacetto, Electrophoretic co-deposition of Mn1.5Co1.5O4, Fe2O3 and CuO: Unravelling the effect of simultaneous addition of Cu and Fe on the microstructural, thermo-mechanical and corrosion properties of in-situ modified spinel coatings for solid oxide cell intercon, Journal of the European Ceramic Society. 42 (2022) 3271–3281. https://doi.org/10.1016/j.jeurceramsoc.2022.02.008.

[95] Ł. Mazur, D. Koszelow, M. Zajusz, M. Łapiński, M. Bik, P. Zając, A. Adamczyk, P. Rutkowski, S. Molin, T. Brylewski, Comparison of Cu1.3Mn1.7O4 spinels doped with Ni or Fe and synthesized via wet chemistry and solid-state reaction methods, designed as potential coating materials for metallic interconnects, Journal of the European Ceramic Society. 43 (2023) 5557–5574. https://doi.org/10.1016/j.jeurceramsoc.2023.05.015.

[96] W.Q. Qiao, Y.W. Li, Y.S. Zhang, M.H. Wang, K. Li, Z.J. Li, W. Yang, Cu- and Ce-doped MnCo2O4 spinel coatings on ferrite interconnects by electrophoretic deposition, Materials Today Communications. 38 (2024) 108061. https://doi.org/10.1016/j.mtcomm.2024.108061.

[97] L. Du, J. Li, Q. Liao, N. Qin, D. Bao, Ce-doping at Mn site to enhance resistive switching performance of spinel MnCo2O4 resistive random access memory devices, Ceramics International. 50 (2024) 20495–20503. https://doi.org/10.1016/j.ceramint.2024.03.171.

[98] Z. Zhu, C. Darl-uzu, U. Pal, S. Gopalan, A.M. Hussain, N. Dale, Y. Fukuyama, Y. Miura, Y. Miyoshi, S. Basu, ScienceDirect Comparison of Cu e Mn and Mn e Co spinel coatings for solid oxide fuel cell interconnects, International Journal of Hydrogen Energy. 47 (2022) 36953–36963. https://doi.org/10.1016/j.ijhydene.2022.08.239.

[99] G.A. Ludwig, M.A. Korb, D.A.S. Lima, M.A. Macías, G.H. Gauthier, C.F. Malfatti, Protective coatings for AISI 430 stainless steel at high temperatures using perovskite oxides La0.6Sr0.4CoO3 on spinel type oxide NiFe2O4, Ceramics International. 41 (2015) 14561–14573. https://doi.org/10.1016/j.ceramint.2015.07.173.

[100] K.H. Tan, H.A. Rahman, H. Taib, Ba0.5Sr0.5Co0.8Fe0.2O3−δ-Sm0.2Ce0.8O1.9 carbonate perovskite coating on ferritic stainless steel interconnect for low temperature solid oxide fuel cells, Materials Chemistry and Physics. 254 (2020) 123433. https://doi.org/10.1016/j.matchemphys.2020.123433.

[101] F. Shen, K. Lu, CoxFe1-x oxide coatings on metallic interconnects for solid oxide fuel cells, Journal of Power Sources. 330 (2016) 231–239. https://doi.org/10.1016/j.jpowsour.2016.09.018.

[102] T. Brylewski, S. Molin, M. Marczyński, Mazur, K. Domaradzki, O. Kryshtal, A. Gil, Influence of Gd deposition on the oxidation behavior and electrical properties of a layered system consisting of Crofer 22 APU and MnCo2O4 spinel, International Journal of Hydrogen Energy. 46 (2021) 6775–6791. https://doi.org/10.1016/j.ijhydene.2020.11.169.

[103] M. Bik, M. Stygar, P. Jeleń, J. Dąbrowa, M. Leśniak, T. Brylewski, M. Sitarz, Protective-conducting coatings based on black glasses (SiOC) for application in Solid Oxide Fuel Cells, International Journal of Hydrogen Energy. 42 (2017) 27298–27307. https://doi.org/10.1016/j.ijhydene.2017.09.069.

[104] H. Mousa Mirabad, A. Nemati, M.A. Faghihi-Sani, M. Fakouri Hasanabadi, H. Abdoli, Effect of YSZ sol-gel coating on interaction of Crofer22 APU with sealing glass for solid oxide fuel/electrolysis cell, Journal of Alloys and Compounds. 847 (2020) 156496. https://doi.org/10.1016/j.jallcom.2020.156496.

[105] G. Jalilvand, M.A. Faghihi-Sani, Fe doped Ni-Co spinel protective coating on ferritic stainless steel for SOFC interconnect application, International Journal of Hydrogen Energy. 38 (2013) 12007–12014. https://doi.org/10.1016/j.ijhydene.2013.06.105.

[106] Z. Shen, J. Rong, X. Yu, MnxCo3-xO4 spinel coatings: Controlled synthesis and high temperature oxidation resistance behavior, Ceramics International. 46 (2020) 5821–5827. https://doi.org/10.1016/j.ceramint.2019.11.032.

[107] W. Wu, W. Guan, G. Wang, W. Liu, Q. Zhang, T. Chen, W.G. Wang, Evaluation of Ni80Cr20/(La0.75Sr 0.25)0.95MnO3 dual layer coating on SUS 430 stainless steel used as metallic interconnect for solid

oxide fuel cells, International Journal of Hydrogen Energy. 39 (2014) 996–1004. https://doi.org/10.1016/j.ijhydene.2013.10.094.

[108] D. Chatterjee, S. Biswas, Development of chromium barrier coatings for solid oxide fuel cells, International Journal of Hydrogen Energy. 36 (2011) 4530–4539. https://doi.org/10.1016/j.ijhydene.2010.04.114.

[109] J. Mao, E. Wang, H. Wang, M. Ouyang, Y. Chen, H. Hu, L. Lu, D. Ren, Y. Liu, Progress in metal corrosion mechanism and protective coating technology for interconnect and metal support of solid oxide cells, Renewable and Sustainable Energy Reviews. 185 (2023). https://doi.org/10.1016/j.rser.2023.113597.

[110] N. Grünwald, D. Sebold, Y.J. Sohn, N.H. Menzler, R. Vaßen, Self-healing atmospheric plasma sprayed Mn1.0Co1.9Fe0.1O4 protective interconnector coatings for solid oxide fuel cells, Journal of Power Sources. 363 (2017) 185–192. https://doi.org/10.1016/j.jpowsour.2017.07.072.

[111] F.A. Unal, M.D. Mat, I. Demir, Y. Kaplan, N. Veziroglu, Application of a coating mixture for solid oxide fuel cell interconnects, International Journal of Hydrogen Energy. 40 (2015) 7689–7693. https://doi.org/10.1016/j.ijhydene.2015.03.031.

[112] S.M. Mohamed, M.M.S. Sanad, T. Mattar, M.F. El-Shahat, C. Rossignol, L. Dessemond, K. Zaidat, S. Obbade, The structural, thermal and electrochemical properties of MnFe1−x-yCuxNiyCoO4 spinel protective layers in interconnects of solid oxide fuel cells (SOFCs), Journal of Alloys and Compounds. 923 (2022). https://doi.org/10.1016/j.jallcom.2022.166351.

[113] R.K. Lenka, P.K. Patro, J. Sharma, T. Mahata, P.K. Sinha, Evaluation of La0.75Sr0.25Cr0.5Mn0.5O3 protective coating on ferritic stainless steel interconnect for SOFC application, International Journal of Hydrogen Energy. 41 (2016) 20365–20372. https://doi.org/10.1016/j.ijhydene.2016.08.143.

[114] H.P. Tseng, T.Y. Yung, C.K. Liu, Y.N. Cheng, R.Y. Lee, Oxidation characteristics and electrical properties of La- or Ce-doped MnCo2O4 as protective layer on SUS441 for metallic interconnects in solid oxide fuel cells, International Journal of Hydrogen Energy. 45 (2020) 12555–12564. https://doi.org/10.1016/j.ijhydene.2020.02.178.

[115] B. Talic, V. Venkatachalam, P.V. Hendriksen, R. Kiebach, Comparison of MnCo2O4 coated Crofer 22 H, 441, 430 as interconnects for intermediate-temperature solid oxide fuel cell stacks, Journal of Alloys and Compounds. 821 (2020) 153229. https://doi.org/10.1016/j.jallcom.2019.153229.

[116] E. Zanchi, B. Talic, A.G. Sabato, S. Molin, A.R. Boccaccini, F. Smeacetto, Electrophoretic co-deposition of Fe2O3 and Mn1,5Co1,5O4: Processing and oxidation performance of Fe-doped Mn-Co coatings for solid oxide cell interconnects, Journal of the European Ceramic Society. 39 (2019) 3768–3777. https://doi.org/10.1016/j.jeurceramsoc.2019.05.024.

[117] Z. Zhu, C. Darl-Uzu, U. Pal, S. Gopalan, A.M. Hussain, N. Dale, Y. Fukuyama, Y. Miura, Y. Miyoshi, S. Basu, Comparison of Cu–Mn and Mn–Co spinel coatings for solid oxide fuel cell interconnects, International Journal of Hydrogen Energy. 47 (2022) 36953–36963. https://doi.org/10.1016/j.ijhydene.2022.08.239.

[118] Y.N. Lowrance, M.A. Azmi, L.M. Basar, H.A. Rahman, The Influence of Electrophoretic Deposition (EPD) Parameters on SS430 Spinel Coated Characteristic, International Journal of Integrated Engineering. 13 (2021) 258–264. https://doi.org/10.30880/ijie.2021.13.02.030.

[119] I. Aznam, J.C.W. Mah, A. Muchtar, M.R. Somalu, M.J. Ghazali, Electrophoretic deposition of (Cu,Mn,Co)3O4 spinel coating on SUS430 ferritic stainless steel: Process and performance evaluation for solid oxide fuel cell interconnect applications, Journal of the European Ceramic Society. 41 (2021) 1360–1373. https://doi.org/10.1016/j.jeurceramsoc.2020.09.074.

[120] B. Talic, A.C. Wulff, S. Molin, K.B. Andersen, P. Zielke, H.L. Frandsen, Investigation of electrophoretic deposition as a method for coating complex shaped steel parts in solid oxide cell stacks, Surface and Coatings Technology. 380 (2019) 1–8. https://doi.org/10.1016/j.surfcoat.2019.125093.

[121] F. Shen, M. Reisert, R. Wang, P. Singh, M.C. Tucker, Assessment of Protective Coatings for Metal-Supported Solid Oxide Electrolysis Cells, ACS Applied Energy Materials. 5 (2022) 9383–9391. https://doi.org/10.1021/acsaem.2c00655.

Figures

Tables